UCSF
UC San Francisco Electronic Theses and Dissertations

Title

A Multiscale Approach to Link Organ-Level Biomechanics with Tissue-Level Mechanobiology of a Bone-Periodontal Ligament-Tooth Fibrous Joint

Permalink

https://escholarship.org/uc/item/78z7543h

Author

Jang, Andrew Timothy

Publication Date

2015

Supplemental Material

https://escholarship.org/uc/item/78z7543h#supplemental

Peer reviewed|Thesis/dissertation

A Multiscale Approach to Link Organ-Level Biomechanics with
Tissue-Level Mechanobiology of a
Bone-Periodontal Ligament-Tooth Fibrous Joint

by

Andrew Timothy Jang

DISSERTATION

Submitted in partial satisfaction of the requirements for the degree of

DOCTOR OF PHILOSOPHY

in

Oral and Craniofacial Sciences

in the

GRADUATE DIVISION

of the

UNIVERSITY OF CALIFORNIA, SAN FRANCISCO

DEDICATION

      I dedicate this dissertation to my family – my parents, Drs. Corey and Gail Jang, and my little baby sister, Dr. Patrice Jang. Your spiritual encouragement, prayers, and home-baked goods sustained me throughout my entire PhD journey.

      I also dedicate this dissertation to my beautiful fiancée, Elisha Eng [Jang]. Words cannot describe the appreciation that I have for all of her physical, emotional, and spiritual support. I wish I could make her a coauthor of my dissertation, but this is the next best thing.

ACKNOWELDGEMENTS

I would like to express my sincere gratitude to the individuals and groups who were instrumental during my journey as a PhD trainee:

First and foremost, I would like to acknowledge the many years of guidance and support from my mentor and principle investigator, Dr. Sunita Ho, who taught me the art of science. She consistently pushed me to better myself and encouraged me to not settle for mediocracy. It was truly a blessing to be under her mentorship for the past 7 years, and I look forward to many more years of friendship and intellectual collaboration.

I would also like to thank the current and past members of Dr. Sunita Ho's lab who not only contributed to my academic and scientific achievements, but also made lab fun.

I also thank my dissertation committee, Dr. Jeffery Lotz, Dr. Mark Ryder, and Dr. Samuel Webb, for taking time out of their busy schedules to provide feedback on my dissertation.

A special thanks to Xradia Inc. (now Carl Zeiss X-ray microscopy) for their financial support. I would like to especially acknowledge Kevin Fahey, Arno Merkle, Luke Hunter, and Sergey Etchin for their guidance with the µ-XCT and *in situ* loading device.

Within the Department of Preventive and Restorative Dental Sciences, Division of Biomaterials and Bioengineering, I would like to thank Dr. Grayson Marshall and Dr. Sally Marshall for their mentorship and unwavering encouragement. I would also like to extend recognition to Grace Nonomura for her laboratory support and to the late Larry Watanabe, for introducing me to Dr. Ho and getting me started on my research path at UCSF.

I would also like to acknowledge the support of specific individuals in the Oral and Craniofacial Sciences (OCS) Group. A special thanks to Roger Mraz for his guidance in

navigating through the program as well as the dozens of cookies shared with me throughout the years. Thanks to Kathryn Gabriel for the administrative work to help keep me funded. Additional recognition for Dr. Pamela DenBesten, Dr. Ralph Marcucio, Dr. Caroline Shiboski, and Dr. Stefan Habelitz for the dedication to the program and the tremendous amount of work spent on maintaining the T32 institutional training grant which supported me and my fellow OCS students.

I want to recognize the support from Richard Prevost from LaVision for his help with the digital volume correlation software, as well as the guidance from Dr. Virginia Altoe and Dr. Shawl Aloni from Lawrence Berkeley National Laboratory regarding transmission electron microscopy.

Finally, I would like to acknowledge the Journal of Visualized Experiments and Elsevier B.V. for their permission to use the following publications within this dissertation.

- For chapter 3: Jang, A.T., Lin, J.D., Seo, Y., Etchin, S., Merkle, A., Fahey, K., and Ho, S.P. (2014). In situ Compressive Loading and Correlative Noninvasive Imaging of the Bone-periodontal Ligament-tooth Fibrous Joint. J. Vis. Exp.

- For Chapter 5: Jang, A.T., Merkle, A.P., Fahey, K.P., Gansky, S.A., and Ho, S.P. (2015). Multiscale biomechanical responses of adapted bone–periodontal ligament–tooth fibrous joints. Bone *81*, 196–207.

A Multiscale Approach to Link Organ-Level Biomechanics with Tissue-Level Mechanobiology of a Bone-Periodontal Ligament-Tooth Fibrous Joint

Andrew Timothy Jang

ABSTRACT

Similar to other tissues in the body, the dentoalveolar complex is constantly subjected to functional loads (physiological, parafunctional, and therapeutic). As loads are applied, teeth undergo micromotion within respective alveolar sockets. The micromotion results in local deformations within the softer vascularized and innervated periodontal ligament (PDL), and subsequently within the surrounding harder alveolar bone and mineralized tissues of a tooth. Over prolonged loading, the resulting adaptation to local strains is thought to be due to an activation of a cascade of biological events that occur at multiple length scales. These biological events identified as modeling and remodeling processes within respective tissues subsequently guide the local tissue morphology/architecture and material properties, and in turn the overall biomechanics of the dentoalveolar complex. The cascade of biological events is a part of a local feedback loop or autoregulation and does not reach a plateau in its activity level until an optimization in biochemical and physicochemical properties is achieved to accommodate the functional demands.

In this study, load-mediated adaptation of the vascularized and innervated complex was investigated from a mechanics and materials perspective. This approach was sought as particularly the complex contains both hard-soft and hard-hard tissue interfaces all of which are uniquely designed to transmit mechanical forces while minimizing fracture and

failure particularly in bone and tooth. Of note are the functionally graded entheses, which are the insertion sites of the PDL into the adjacent alveolar bone and cementum tissues and serve as focal regions for strain concentrations and hotspots for the cellular processes leading to modeling and remodeling of all tissues related to the bone-PDL-tooth complex.

The central objective of this dissertation was to investigate, from a multiscale perspective, the shift in functional adaptation of the bone-PDL-tooth fibrous joint in response to reduced functional load by using a small-scale animal model. **It was hypothesized that function-related strains at the bone-PDL and cementum-PDL interfaces stimulate cells to form or resorb mineral by creating a localized micro-niche**. To test this hypothesis, two specific aims were formed: Specific Aim 1: Test the hypothesis that the adaptation of the bone-PDL-tooth fibrous joint to reduced functional loads is temporal and is tissue-specific (mineralized and/or unmineralized). Specific Aim 2: Test the hypothesis that organ level joint mechanics directly influence physiological drift of teeth through the mechanobiological response to site-specific deformations within the functional space. To investigate temporal adaptation to reduced functional loads in Aim 1, approach taken was focused on mapping biomechanics, and tissue related physicochemical properties at different length scales (multiscale) using complementary methods including: X-ray microscopy, micro/nanoindentation, histology and immunohistochemistry, and transmission electron microscopy (TEM) techniques. Organ-level adaptations at a macroscale were characterized by analyzing shift in joint morphology and were correlated to joint biomechanics. Tissue-level adaptation was measured by mapping shifts in deformations of respective tissues which were evaluated

using digital volume correlation (DVC). Tissue-level adaptations were also determined by using indentation methods to measure changes in local tissue hardness and elastic modulus. In specific Aim 2, the organ-level biomechanics was correlated with localized biochemical shifts within tissues and at the hard-soft tissue interfaces by staining for tartrate resistance acid phosphatase (TRAP), alkaline phosphatase (ALP), and immunogold labelling for bone sialoprotein (BSP) and osteocalcin (OC) macromolecular localization. Overall, the information gathered from this multidisciplinary approach was used to correlate the biomechanical events at an organ level with localized adaptations at the tissue and cellular levels.

Results specific to Aim 1 highlighted the importance of age by indicating that the shift in biomechanics due to reduced functional loads adaptation of the fibrous joint in younger mammals is significant compared to older mammals. Rats subjected to reduced functional loads illustrated that adaptations within the PDL resulted in a significant reduction in functional space and an increase in joint stiffness at younger ages. At an older age, differences included alveolar bone adaptations in the form of a decrease in bone volume fraction (form) and a decrease in elastic modulus (material properties). In line with the classical theories on the functional history of mineralized tissues, results from this study demonstrated that the observed temporal adaptations within the dentoalveolar complex are registered as a functional history in tissues and joints. Overall, these results highlight an optimization paradigm within the context of joint biomechanics, in that, adaptation observed at a macroscale is due to the coupled effect of a change in organ-level morphology as a result of a change in functional shape (hypothesized to be primarily driven through the modulation of cementum) and shifts in physicochemical properties of

tissues including that of alveolar bone within the dentoalveolar complex. Specific to Aim 2, the use of *in situ* imaging and modeling of the changes in the PDL-space in an intact oral and craniofacial complex revealed the effect of a natural tilt of the tooth in the distal direction within a single mastication cycle. Within the functional space, compressive and shear strains were computationally determined and found to be primarily concentrated on the distal side of the tooth. Both these strains correlated spatially with sites of increased alveolar bone resorption as determined through TRAP staining and TEM. Of particular interest was that the site-specific distal TRAP activity was reduced when the animals were given softer diets. These results collectively lead to the hypothesis that the physiological distal drift in rodents in part is driven as a response to mastication forces through the site-specific resorption and apposition, thus sculpting the alveolar bone socket to accommodate functional demands.

Overall, the findings using a multiscale approach to highlight load-mediated adaptions of the bone-PDL-tooth fibrous joint fit into the larger continuum of functional adaptation of the oral and craniofacial complex. This was enabled through development of methodologies specific to *in situ* mechanical testing coupled with experimental mechanics to correlate organ-level biomechanics with tissue-level strains. Tissue-level strains specific to the PDL and alveolar bone were correlated with local biochemical expressions. Additionally, insights from this study indicated that by correlating organ-level biomechanics with tissue-level mechanobiology, functional loads are needed to sculpt the bony tissues. The insights gathered included that the growth of a load bearing organ not limited to the oral and craniofacial complex can be modulated by shaping tissues and this in turn is done by regulating magnitude, frequency of load and the age at

which these stimuli were given. Lastly, the validated technology can be adapted to develop experimental models, however under *ex vivo* conditions, to highlight the local effects within tissues as a result of therapeutic treatments or parafunctional habits on the bone-PDL-tooth fibrous joint within the larger biomechanical continuum containing the temporomandibular joint (TMJ).

TABLE OF CONTENTS

LIST OF TABLES

LIST OF FIGURES

CHAPTER 3. *IN SITU* COMPRESSIVE LOADING AND CORRELATIVE NONINVASIVE IMAGING OF THE BONE-PERIODONTAL LIGAMENT-TOOTH FIBROUS JOINT

CHAPTER 4. STRAIN MAPPING AND CORRELATIVE MICROSCOPY OF THE ALVEOLAR BONE IN A BONE-PDL-TOOTH FIBROUS JOINT

CHAPTER 5. MULTISCALE BIOMECHANICAL RESPONSES OF ADAPTED BONE-PERIODONTAL LIGAMENT-TOOTH FIBROUS JOINTS

CHAPTER 6. ADAPTATION OF THE BIOMECHANICALLY ACTIVE INTERRADICULAR ALVEOLAR BONE TO REDUCED FUNCTIONAL LOADS

CHAPTER 7. AN OVERVIEW OF BIOMECHANICS AND MECHANOBIOLOGICALLY RELATED EVENTS IN THE BONE-PERIODONTAL LIGAMENT-TOOTH FIBROUS JOINT

CHAPTER 1. INTRODUCTION

1.1.   Dissertation motivation and clinical significance

Mechanical forces are fundamental for development, growth, and maturation of tissues and organs (Carter, 1984; Carter et al., 1996). From a development standpoint, stiffness gradients in tissues polarize, differentiate, organize and prompt migration of cells consequently resulting in the synthesis of organic and inorganic constituents to construct extracellular matrices (ECM) (Ingber, 1997). In most vertebrates, after birth, forces continue to play a role and are a part of a closed loop containing phases of growth and tissue maturation as the body optimizes to address the mechanical environment. While functional loads serve as a key factor in tissue maintenance and health, shifts in "functional quality" were characterized as one of the main etiological factors for observed pathological states. This philosophy continues to be leveraged by clinicians for treatments that include distraction osteogenesis, and that which is more specific to the bone-periodontal ligament (PDL)-tooth complex are orthodontic interventions.   Clinical manifestations of adaptations due to shifts in magnitude and frequency of mechanical loads include disuse induced osteoporosis due to paralysis (Mohr et al., 2014) or from microgravity (Morey and Baylink, 1978; Wronski and Morey, 1983; Turner et al., 1985; Shaw et al., 1988), and manipulation of bone growth patterns through the use of aforementioned therapeutic loads (e.g. osteogenic distraction and orthodontics) (Ga, 1987; Chin and Toth, 1996).

The oral and craniofacial organ system is subjected to multiple loads including speech, intracranial pressure, and mastication (chewing). Of particular interest in this

dissertation are forces generated within the PDL between the tooth and alveolar bone as a result from mastication of harder and softer foods. The effects of magnitude and frequency as a result of chewing on harder and softer foods throughout the craniofacial complex has been well documented (Hylander, 1985; Kiliaridis et al., 1985; Hylander and Johnson, 1992, 1997). Over the years, the biomechanical apparatus and behaviors responsible for mastication have been studied using several different animal models ranging from developing stages (Herring and Wineski, 1986; Weijs et al., 1987; Herring et al., 1991; Langenbach et al., 1991, 1992; Westneat and Hal, 1992; Xiaofeng et al., 1994; Langenbach et al., 2001) to adulthood (Ravosa, 1991; Cole III, 1992; Ravosa, 1996, 1996, 1999; Biknevicius and Leigh, 1997; Ravosa, 1998; Vinyard and Ravosa, 1998; Taylor et al., 2006). Many studies have linked functional loads as a direct impetus for adaptations in cranial shape and pathology in the maxilla (Yamamoto, 1996), as well as its individual constituents (**Fig. 1.1**) including the sutures (Ten Cate et al., 1977; Herring and Mucci, 1991; Mao, 2002; Popowics and Herring, 2007; Katebi et al., 2012), temporomandibular joint (TMJ) (Copray et al., 1985; Mao et al., 1998; Agarwal et al., 2001), and dentoalveolar complex (Short and Johnson, 1990; Gibson et al., 1992; Popowics et al., 2009; Mavropoulos et al., 2010). While the concept of a relationship between the mechanical strains developed from mastication and the resulting morphology is longstanding (Endo, 1966; Hylander, 1985; Vinyard et al., 2008), there still lies a gap between cause and effect relationship, that is, a link that would fill the gap between adaptive processes and commonly observed clinical outcomes.

The oral and craniofacial complex is an organ system comprising of various organs that include the bone-PDL-tooth fibrous joint, cranial and palatal sutures, and the temporal

2

mandibular diarthrodial joint. Although chewing forces directly act on the bone-PDL-tooth complex, other organs of the craniofacial complex also are affected by the same forces. This presents a challenge in identifying the direct causality of functional loads and decoupling their effect as related to the resulting adaptation in tissues related to specific organs (Hylander et al., 1991). Although the work within this dissertation is on the dentoalveolar complex located within oral cavity, it provides insights into a larger continuum of functional adaptation of the craniofacial complex. To systematically investigate functional adaptation, a multiscale approach using guiding principles from mechanical engineering, materials science, and biomechanics were taken to map spatiotemporal functional adaptation within the dentoalveolar complex of the oral cavity. The remainder of this chapter will describe current dogmas and shortcomings surrounding the studies on functional adaptation of the dentoalveolar complex subsequently leading to the objectives of this dissertation.

1.2. The dentoalveolar complex and functional adaptation

Specifically, within the oral cavity, functional loads exist primarily in the form of mastication, i.e. chewing loads and are accommodated by the bone- PDL-tooth complex or gomphosis (Nanci, 2007; Ho et al., 2010a). This region is unique compared to other joints, in that, it is both innervated and vascularized, and is dynamic in response to both physiological and non-physiological loads (Moxham and Berkovitz, 1982; Berkovitz, 1990; Nanci, 2007). Additionally, several interfaces between soft-hard (PDL-bone and PDL-cementum) and hard-hard (cementum-dentin) tissues lie within a relatively small space (~100-200 µm) allowing for high resolution microscopy techniques to fully capture the region in its entirety. Alterations to functional loads below or above the physiological

threshold (hypo function and hyper function) have been shown to cause significant changes in root and bone morphology (Steigman et al., 1989; Niver et al., 2011), and can promote an altered overall biomechanics of the complex. These fundamental concepts continue to be exploited to investigate bone dynamics for bone regeneration (distraction osteogenesis (Chin and Toth, 1996)) and/or cause tooth movement (orthodontics (Asbell, 1990)). Within the context of this dissertation, the dentoalveolar complex is divided into three regions: tooth, alveolar bone, and PDL (Nanci, 2007) (**Fig. 1.2**). The tooth is further divided into three distinct mineralized tissues that include enamel, dentin, and cementum.

The alveolar bone: Alveolar bone contains about 60% inorganic mineral (with the remaining 40% being organic and water) and supports the tooth during mastication (chewing). Within the context of the central objective of this dissertation, that is, load-mediated adaptation of the bone-PDL-tooth complex, the interradicular bone and interdental bone are of particular interest. In general, a molar contains a furcation between its roots and straddles on interradicular bone. As a result, the interradicular bone is thought to be the main recipient of vertical loads during a chewing cycle. Interdental bone exists between the teeth and is primarily deformed during the rotational motion of tooth when loaded. While alveolar bone is fundamentally similar to long bones, recent studies have identified key differences based on identification of different progenitors (Matsubara et al., 2005; Aghaloo et al., 2010; Reichert et al., 2013) as well as organization of collagen (Matsuura et al., 2014). Despite the differences in their origins, it is likely that the X-ray attenuating lamina dura in direct contact with the PDL can be analogous to cortical bone, while the less X-ray attenuating trabecular parts that define the alveoli could be similar to the trabeculae of cancellous bone.

As a whole, bony tissue by far has been the most compressively studied tissue with respect to functional adaptation. The idea that mechanical forces shape the architecture of the skeleton dates back to the 19th century (Meyer, 1867; Roux, 1905). One of the earlier relationships between force and resulting tissue/organ architecture was drawn with Julius Wolff's initial relationship between function and adaptation as related to architecture within long bones from a mathematical perspective (Wolff, 1892, 1986). From his original publications, (translated from German by Rash and Burke): "Every change in the form and function of bones, or of their function alone, is followed by certain definite changes in their internal architecture and equally definite secondary alteration in their external conformation, in accordance with mathematical laws" (Wolff, 1892). This implies that there is an effect of mechanical forces on external and internal architectures of bone, but the statement did not elaborate on the mechanobiological processes related to architectural changes identified as adaptations. This concept was later expanded by introducing bone metabolism through modeling (a change in external bone shape) and remodeling (natural turnover of bone) related activities and a feedback loop (mechanostat) was identified by connecting the change in bone mass with the mechanical usage (Frost, 1964, 1987; Turner and Burr, 1993; Turner et al., 1995).

Bone can undergo changes within three states based on a comparison between the mechanical stimulation (MS) and "normal load" (NL) (**Fig. 1.3**). Normal load has been compared to a "lazy zone" in which the tissue is optimized for its mechanical environment. Under a normal state, the MS is in the approximate range of the NL (MS=NL) which results in the formation and resorption rates being proportional (Carter, 1984). As such, there is minimal net change within bone leading to no changes in form or material properties.

5

Under a disuse state (MS<NL), the balance of formation and resorption rates tilt in favor of resorption through a combination of decreases in formation and increases in resorption, or decreases in formation only. The net result is a decrease in bone turnover, bone mineralization, and a decrease in the volumetric density of tissues. When the mechanical stimulation is greater than the normal load, the net balance between resorption and formation is in favor of formation. However, upon increasing load rate, this pattern increases to the point in which the mechanical stimulation exceeds the ultimate strength of the material resulting in fracture, injury, and subsequently wound-healing induced inflammation. In addition to the magnitude and rate of loading, it has been shown experimentally that developing bone has increased sensitivity to shifts in cyclic loads compared to mature adult bone (Carter, 1984, 1987). This has led to the importance of the ability of tissues to register the history of load when predicting its adaptive response to a history of micro damage (Carter, 1984).

As mentioned above, the natural turnover of bone is thought to be a combination of two processes – formation and resorption. Cells responsible for the mineralization of bone are osteocytes and osteoblasts. Osteoblasts primarily originate from mesenchymal stem cells and are typically found lining the periosteum (Pittenger et al., 1999). Initially, the osteoblasts begin the process of bone formation by secreting matrix products that construct osteoid which is essentially the mineralizing organic substructure (mainly type I collagen) of bone and provides for the tensile strength of the bone in its entirety (Urist et al., 1983; Miller and Parker, 1984). The parallel laydown of inorganic on and in between the organic constituents to form the osteoid is due to the deposition of apatite within the organic matrix and to provide bone with its compressive strength. Studies showing

fluorochrome labeling of new bone formation have identified that bone growth adds structure to external bone also known as "appositional bone growth" (Frost et al., 1961). As the appositional bone growth continues, osteoblasts are eventually encapsulated within the new bone formation and are converted into osteocytes. Osteocytes are contained within the bone in small "homes" called lacunae and are connected to each other by a canalicular network, an avenue for nutrient distribution and intercanalicular signaling (Baud, 1968) necessary for maintenance of bone. While osteocytes are commonly referred to as "inactive osteoblasts" as they are thought to mineralize the surrounding bone tissue throughout the lifespan of an organism and are capable of signal transmission over distances along the cross-section and length of bone (Civitelli, 2008; Noble, 2008). However, there still remain many questions regarding formation and resorption events at the PDL-bone and PDL-cementum entheses – the critical attachment sites without which load-bearing function is significantly impaired.

Resorption of bone primarily occurs through osteoclast function (von Kölliker, 1873; Nijweide et al., 1986). Osteoclasts are derived from fusion of several monocytes (Teitelbaum, 2000). While osteoclasts are not produced directly from osteoblasts, it has been shown that the maturation of osteoclasts requires the presence of osteoblasts which signal for osteoclast differentiation through the expression of macrophage colony-stimulating factor (M-CSF) and receptor for activation of nuclear factor kappa B (NK-κβ) (RANKL) (Yasuda et al., 1998). Osteoprotegerin (OPG which is also produced by osteoblasts acts as a decoy receptor for RANKL decreasing osteoclastogenesis highlighting the osteoblast as a central cell for the regulation of resorption activities of bone in addition to bone formation (Teitelbaum, 2000). The resorption process of bone

through osteoclast occurs resulting in resorption lacunae (also known as "Howship's lacunae") with a ruffled pattern. Following osteoclast attachment with the mineralized tissue, the osteoclast proceeds to demineralize the inorganic bone through localized acidification (Boyle et al., 2003). Degradation of the organic matrix occurs through the secretion of several matrix metalloproteases (MMP's) including MMP-9, 10, 12, 13, and 14 (Okada et al., 1995; Sato et al., 1997). Under the bone remodeling paradigm, the processes of bone formation and resorption occurs in succession, eventually replacing about 10% of an adult human's skeletal system per year (Wheeless, 1996).

While genetic triggers are in part responsible for the regulation of bone resorption and formation, epigenetic signals in the form of active (in addition to passive stretch due to development related growth) mechanical stimulation have been shown to guide the differentiation and activities of osteoblasts and osteoclasts. Within *in vitro* conditions, mesenchymal stem cells were shown to differentiate into a different progeny solely based on the elastic modulus of the construct on which the cells were seeded (Engler et al., 2006). These findings identify the cell's mechanical interaction with the ECM as a crucial factor for signaling differentiation. After differentiation, loading type (magnitude and frequency) has been shown necessary for the expression and activity of alkaline phosphatase *in vitro* (Roelofsen et al., 1995) in both osteoblasts and osteoblast progenitor cells. Mechanical stimulation has also been shown to inhibit osteoclastic bone resorption within *in vitro* experiments (Roelofsen et al., 1995; Klein-Nulend et al., 2005). *In vivo*, mechanical stimulations are felt through both the ECM-cell and cell-cell attachments as the bony tissue is deformed (Wang et al., 1993; Bonewald, 2006). Additionally, as mechanical stimulation also occurs from shear on the cellular membranes of osteocytes

and osteoblasts the resulting movement of interstitial fluid that travels within the canalicular network, triggers a communication between osteocytes (Cowin et al., 1991; S et al., 1994).   While both osteocytes and osteoblasts have been shown to react to mechanical stimulation, it is believed that the osteocyte network is in direct control of both osteoblast recruitment and activity (Bonewald, 2006). Specifically, studies have shown that mechanical stimulation of the bone *in vivo* leads to the reduction of sclerostin which is an inhibitor of bone formation by osteoblasts (Robling et al., 2008) as well as an increase in nitric oxide which is an earlier mediator for bone formation (Fox et al., 1996).

Since the role of fluid flow through the bony networks play an important role for mechanotransduction, researchers have addressed the temporal nature of bone adaptation in response to mechanical stimuli. In 1998, C.H. Turner characterized three rules pertaining to the dynamic component of functional adaptation (Turner, 1998). Turner's first rule was that "bone adaptation is driven by dynamic loading". While this rule coincides with the dynamic nature that accompanies most external activities (e.g. running and chewing), experimental evidence has shown that both loading frequency and strain rates are important mediators of functional adaptation within bone (Turner et al., 1994a, 1994b, 1995). Therefore, both loading magnitude and frequency play an important role and must be considered when modeling functional adaptations.   The second law characterizes the diminishing return by stating that "only a short duration of mechanical loading is necessary to initiate an adaptive response. Extending the loading duration has a diminishing effect on further bone adaptation." This concept was best demonstrated through experiments involving long durations of repeated activities (Lanyon, 1992; Umemura et al., 1997). While this concept does apply in part to alveolar bone, the plastic

nature of alveolar bone (e.g. relapse in orthodontic treatment) indicates that other processes or rules may also apply. While an increased duration of an isolated activity did increase the bone mass, it was found that the response (either with increased resorption or formation) was not proportional to the time over which the input signal was given. When placed in context with the third rule, "bone cells accommodate to a customary mechanical loading environment, making them less responsive to routine [routine – a customary signal becoming routine in nature or acting as the same stimulus over a prolonged period] loading signals", it can be concluded that functional adaptation would be best achieved as a dynamic function (e.g. a stimulus which increases either in frequency or magnitude over time). Additionally, these last two rules also predict a reduction in the adaptive response as a function of age which is important when designing and interpreting the effect of age-related adaptation.

Using these fundamental concepts, adaptation within the dentoalveolar complex has also been studied in the oral cavity using shifts in both therapeutic (orthodontic) loading and physiological function as experimental variables. Using orthodontic forces, experiments have identified osteogenesis on the tension side of these forces, while the opposing compression side resulted in elevated osteoclastic activity (Rygh, 1976; Rygh et al., 1986). In response to reduced physiological loads using soft diets, alveolar bone exhibited osteoporotic changes with reduced levels of bone density compared to those fed harder foods (Thongudomporn et al., 2009). Although mainly seen in the developing ages, this form of adaptation has also been observed in fully grown adults (Mavropoulos et al., 2010). While many similarities exist between bone found in the alveolar process

and skeletal bone, caution should be taken when comparing functional adaptation within each of these tissues.

The tooth and its adaptation: The tooth encapsulates the pulp, nerves and blood vessels. From a materials standpoint, enamel of the crown is composed of highly organized hydroxyapatite crystals (95% inorganic mineral and 5% organic and water components) and is considered harder than cementum, bone and dentin. During mastication, enamel comes into frequent contact with food particles and enamel from the opposing dentition. The substructure supporting enamel is made of dentin, which is composed of 70% mineral by weight and 30% organic and water components. Cementum is a mineralized tissue, which primarily covers the root surface of a tooth. Due to its architecture and chemical composition, cementum is the softest of the mineralized tissues of the tooth and is composed of approximately 45-50% inorganic mineral and 50-55% organic and water components, although the ratio is not the same with age (Kumar, 2014).

With respect to the dentoalveolar complex, cementum is a highly dynamic tissue and serves as the primary tissue attaching the tooth to the periodontium (Bosshardt and Selvig, 1997). Like other mineralized tissues, studies have identified spatial and temporal shifts in the composition of mineral content (Bosshardt and Selvig, 1997; Jang et al., 2014a), as well as in the ratio of its elemental makeup (Nakata et al., 1972; Hals and Selvig, 1977; Nakagaki et al., 1985; Murakami et al., 1987; Bosshardt and Selvig, 1997). Studies have also identified shifts in the growth rate of cementum over time (Bosshardt and Selvig, 1997; Jang et al., 2014a). While the increase in cementum growth was largely correlated to regions of increased function within the tooth (i.e. tooth furcation and tooth

apex) and is known as secondary cementum, the functional adaptive capacity of cementum and its progenitor cells are unknown (Foster et al., 2007). Various matrix molecules representative of bone were also identified in cementum, however, several molecules specific to cementum were recently discussed. Regardless, the structure-function relationship of these molecules as related to formation and resorption of cementum matrix (Salmon et al., 2013) let alone their behavior in the presence of mechanical loads is a wide topic of research.

The periodontal ligament and its functional adaptation: Tissues within the functional space separating the bone and tooth are primarily made up of collagen bundles (mainly type I and III) (Berkovitz, 1990), and contain other elastic fibers such as oxytalan and elastin (Nanci and Bosshardt, 2006). It has been hypothesized that the fiber bundle orientation is thought to play a role in optimizing strains and resulting functional stresses (Moxham and Berkovitz, 1982; Berkovitz, 1990; Benjamin et al., 2006; Tanaka et al., 2006). On the other hand, the ground substance within the interstitium of the PDL, containing proteoglycans that interact with interstitial fluid produce a viscous (time-related) and a hydrostatic response during function (Embery et al., 1995; Natali et al., 2004). Cells (fibroblasts, osteoblasts, osteoclasts, progenitor cells) in local regions sense the strains through ECM-cell interactions (integrin-matrix) and cell-cell interactions (tight junctions) and respond through gene transcription, promoting collagen fibril turnover, forming and resorbing minerals, and ultimately tissue adaptation (Shore et al., 1985; Ingber, 2003, 2005, 2006; Wang et al., 2009). In turn, the adapted tissues can alter overall biomechanics and cellular responses eliciting a feedback loop in perpetuity under prolonged loading (**Fig. 1.4**) however, as described earlier can reach a plateau in this

biomechanical behavior.

From a biological perspective, the tissues and enthesial organs (PDL-bone and PDL-cementum interfaces) within the narrow functional space of the dentoalveolar complex are ideal for studying functional adaptation as this space is characterized by a rich vasculature allowing nutrients and progenitor cells (Saffar et al., 1997; Ochareon and Herring, 2011) to enter and irrigate the tissues and their interfaces. *In vitro* studies on PDL cells have demonstrated a bias in the alignment direction of the cells with respect to the applied loads (Bellows et al., 1982) as well as a promotion of differentiation to osseous tissues (Kawarizadeh et al., 2003; Kanzaki et al., 2006). *In vivo* experiments have correlated the size, density and mineralization of Sharpey's fibers with the magnitude of occlusal loading in rat periodontium (Short and Johnson, 1990; Silva and Merzel, 2004). Additionally, it also was noted that the stiffness of the PDL attachment in mini-pigs increases dramatically once erupting teeth have reached occlusion and gained occlusal function (Popowics et al., 2009).

The enthesial organs, PDL-bone and PDL-cementum graded interfaces: The interface between two tissues with dissimilar material properties, such as bone and PDL, and cementum and PDL are of particular importance when studying the mechanics of the dentoalveolar complex. From a materials and mechanics perspective, these interfaces would initiate localized regions of increased strain and stress gradients, depending on the material types (Boresi et al., 1993) and this concept was well illustrated and is applied to fabricate functionally graded materials (Suresh and Mortensen, 1998; Suresh, 2001). The functionally graded interfaces concept and materials thereof when applied to the dentoalveolar complex illustrates the nature's optimization of properties to accommodate

occlusal forces generated from mastication which are transmitted through several different materials—from enamel to alveolar bone via a chain of interfaces that lie between discrete materials, such as enamel → dentin → cementum → PDL → and subsequently to the alveolar bone. The interfaces between these tissues are unique as they are designed to transmit forces between tissues while minimizing material failure. Interfaces or junctions identified in the tooth include, the dentin-enamel junction (DEJ) (Marshall et al., 2003), dentin-cementum junction (CDJ) (Ho et al., 2004), and the PDL entheses (Ho et al., 2010a). From a materials perspective, the "quality" of the interfaces determines the degree of both stress and strain concentrations (dependent on the differential in stiffness variation of the interfacing tissues) due to cyclic chewing forces and can lead to mechanical failure when fatigue limits are exceeded (Thomopoulos et al., 2006). Within the fibrous joint of the dentoalveolar complex, the attachments of the PDL with cementum and alveolar bone would also create localized regions of increased strain gradients resulting from tension, compression and shear components related to occlusal load (Thomopoulos et al., 2006; Benjamin et al., 2006; Lu and Thomopoulos, 2013)**.**

Transition between soft tissue PDL and hard tissue bone occurs through a mechanically and chemically integrated transition zone most often identified as an interface between two visually discrete tissues. In contrast to many other joints within the body whose bony tissue and ligament are separated by a layer of cartilage, the dentoalveolar complex is classified as a fibrous joint with fibrous entheses. At a tissue level, the PDL fibers directly insert themselves into the cementum and alveolar bone forming "tethered ends" (Ho et al., 2010a). The collagen fibers of the PDL change their orientation from radial to circumferential and become gradually more mineralized when

approaching the harder tissues. The combination of structural and elemental changes allows for elastic graded interfaces necessary to distribute large and cyclic functional loads.

The "plastic" bone-PDL-cementum complex: Maintenance of 150-380 μm of PDL-space within humans is a requirement for optimum function of the dynamic bone-PDL-tooth fibrous joint (Hurng et al., 2011). Factors that can alter the width of the functional space in a dynamic complex include age, disease, extraneous mechanical loads (Hurng et al., 2011). While age and disease are also regarded as active players of tissue adaptation, in this study, we will specifically investigate effects of reduced functional loads on biomechanical performance of the organ and correlate them with local strains and biochemical expressions. Several groups have already studied the biomechanics within the PDL-space while others have analyzed the cellular response within these tissues as well as quantified the physicochemical differences within adapted tissues (Johnson, 1990; Chiba and Komatsu, 1993; Natali et al., 2004; Tanaka et al., 2006; Ho et al., 2010a). However, few groups have been able to correlate the micro level biomechanical strains within the PDL-space to the biological events leading to tissue adaptation. Within other mechanically loaded joints, the interface between the soft and hard tissues contains a higher potential to buildup internal stresses in harder elements and strains in softer elements which are felt by the tissue specific cells and the progenitors that reside in PDL, bone and possibly in cementum. Hence, it is conceivable that these biomechanical/mechanobiological coupling processes are dependent on the attachment/integration of the softer PDL with the harder cementum and bone. However, mechanical strains are amplified at the PDL-bone and PDL-cementum interfaces and are

proposed to be stimuli for cell differentiation to regulate formation of cementoid and osteoid layers, and subsequently the needed functional space to facilitate tooth micromotion in the socket (Lee et al., 2015).

Functional loads promote "plasticity" and rapid tissue adaptation within the load-bearing tissues. At a broader scale, the mechanistic definition of plasticity is the link between mechanical stress and strain-induced biology within tissues and their interfaces. This concept is all the more relevant in the bone-PDL-tooth joint, because the complex forms a continuum from both a mechanical and a biological perspective. A mechanical continuum exists as a strain/stress distribution interface between the PDL-bone and PDL-cementum depending on the primary and secondary tissues being softer or harder that are responsible for absorbing/resisting the functional loads. A biological continuum exists due to vascularization within this joint that allows for rapid distribution of nutrients needed to maintain tissue vitality and adaptation as well as a healthy functional space within the joint.

Functional loads within the oral cavity and the craniofacial complex: In general, functional loads within the oral cavity can be divided into several types: physiological, pathological, and therapeutic. Physiological functional loads are primarily from mastication (chewing) which are used to degrade food particles into smaller digestible bits. Within humans, the loads are about 200N (Lieberman, 2011) and about 10-15N in rats (Nies and Young Ro, 2004). While there exist a range in direction, magnitude, and frequency for physiological loads, load that exists beyond the healthy range would be considered pathologic by nature. A common pathological load is a dramatic increase in magnitude and/or frequency (load rate) and examples include

bruxism or primary occlusal trauma leading to joint injury and localized inflammation of the dentoalveolar complex (Itoiz et al., 1963; Hallmon, 1999). In addition, "normal loads" applied to a compromised dentoalveolar complex can result in a traumatic inflammatory response and is referred to as "secondary occlusal trauma" (Hallmon, 1999). Examples of directional pathological loads include external impacts leading to tooth avulsion. Finally, within the dentoalveolar complex clinicians have used loads as a therapeutic tool (e.g. orthodontics) to reposition teeth to facilitate optimum occlusal loading, but thus far has been limited to esthetics (Asbell, 1990) causing root shortening through resorption. It is thought that in order to prevent a traumatic injury, the orthodontic loads are usually in the order of 25-500g (Cornelis et al., 2007), but based on literature specific to long bone, the magnitude and the rate at which the load is applied is equally important (Turner, 1998).

As is the case with musculoskeletal bone, the primary source of physiological function related to mastication loads primarily depend on the efficiency of masseter, temporalis, and medial pterygoid muscles but are also affected by the configuration of the mandible as well as the nature of the occlusal plane (Ahlgren and Öwall, 1970; Okane et al., 1979). These loads have been measured to average around a range of 200 N within the molar region during normal mastication, but have been shown to peak at 2000 N during non-physiological loading (example: pathological grinding) (Braun et al., 1995, 1996). Long term effects of hypofunction and hyperfunction loads can also lead to dramatic changes within the PDL, bone and cementum (Steigman et al., 1989; Johnson, 1990; Kaneko et al., 2001; Niver et al., 2011). However, the cause of these changes from an organ to a tissue level is minimally investigated and least understood, with several

research works that focus mostly on cell responses and intracellular pathways challenging the relevance of cell-based study in the context of organ function.

Within the oral and craniofacial complex, the chewing loads are transferred throughout several tissues of the tooth with different material properties, that include the PDL and the surrounding alveolar bone (Weijs and de Jongh, 1977; Nanci, 2007). Functional loads on a single bone-PDL-tooth organ can be approximated as cyclic loads on the crown in the axial direction (Parfitt, 1960). The tooth accommodates for these loads through its translational and rotational movements within the bony socket (Christiansen and Burstone, 1969). The PDL *per se* accommodates the loads by allowing micro motion of the tooth within the bony socket. While the principal direction of occlusal load on molars is vertical in rats and humans, the motion of the tooth is heavily influenced by the interdigitating contacts from the opposing dentition and the motion of the TMJ producing both translational (vertical and horizontal) and rotation. Within the bone-PDL-tooth complex *per se* several investigators have highlighted the rotation of the tooth (Qian et al., 2009; Naveh et al., 2012a; Lin et al., 2013), the first being Christiansen and Burstone (Christiansen and Burstone, 1969). Since then, researchers have highlighted this motion as being a combination of both vertical as well as rotational movements which could all occur in parallel (Chattah et al., 2009; Qian et al., 2009; Naveh et al., 2012a; Lin et al., 2013). Lin et al., described it as "screw-like" motion within the socket which in turn creates shear dominated deformations within the PDL. The cumulative effect of these deformations include pullout forces near the PDL-bone and PDL-cementum interfaces (Ho et al., 2010a; Hurng et al., 2011) not necessarily in directly opposite regions. The macroscale tooth movement results in localized strains in the PDL fibers and movement

of interstitial fluid through ground substance as a concerted viscoelastic response (Chiba and Komatsu, 1993; Benjamin et al., 2002; Natali et al., 2002, 2004; Benjamin et al., 2006; Tanaka et al., 2006; Ho et al., 2010a). Cells inhabiting the PDL matrix feel the strain through integrin-matrix and cell-cell interactions (Wang et al., 1993; Lehoux and Tedgui, 2003; Wang, 2006). Intracellular responses to these strains are the transcription of genes and the production of biochemical signals, which take the form of matrix-related proteins that modulate turnover of both mineralized tissues and the PDL. Overall, this sequence of events creates a closed loop that can either prompt or resorb mineral, regardless to meet the functional demands, promoting tissue and organ adaptation over prolonged periods of loading. These adaptive processes are deeply interconnected at different hierarchical levels and are manifested at the cell, tissue, and organ levels.

As teeth are loaded under both physiological and non-physiological conditions, pullout forces are generated within the soft-hard tissue interfaces, which then impart a detectable strain on nearby cells. It is important to note that as a mechanical continuum, multiple cell types are affected across the entire PDL-space due to tissue deformation. As a result, the crosstalk between several cell types that either promote mineralization or resorption can be altered. Cells include cytes, clasts, and blasts, which can be tissue-specific, i.e. related to cementum or alveolar bone. The conversion of mechanical stimulation to a biochemical signal (mechanotransduction) can occur through mechanosensitive genes such as OSX, and the expression of proteins through mechanosensitive pathways (e.g. postulated mechanosensitive protein is BSP), or through other postulated mechanosensitive proteins such as DMP1 (George et al., 1993; Nakashima et al., 2002; Papachroni et al., 2009; Qin et al., 2007). Hence, investigating

and mapping the mechanobiological factors within the microniche of the PDL-cementum and PDL-bone will allow us to develop a deeper understanding of the underlying mechanisms surrounding hard-soft tissue interface regeneration – a major challenge in restoring normal organ function.

Active and passive forces: From a biomechanics perspective, the types of forces which act on an organism are classified as either active or passive (Turner and Burr, 1993; Ingber, 1997). During development and functional growth, passive forces are primarily derived from the innate tension within cells and their attachment within other cells while active forces are defined as forces generated within the tissues and felt by the cells as a reaction from muscle contraction due to function imposed on the organ. *In vitro and in vivo* experiments have shown that these intrinsic forces are crucial for guiding cell polarity, differentiation, and migration, which are all key factors for various stages of development (Lee et al., 2015), while active forces have been shown to shape the supporting softer and harder structural elements (Carter and Beaupré, 2007). The combined responses of active and passive forces provide necessary input to guide tissue growth beyond the years of development and continue throughout the life of an organism. Specific to the dentoalveolar complex, intrinsic forces play a role in the initial formation of the PDL complex. Since the main source of active force within the dentoalveolar complex is from mastication, passive forces will play a major role in the initial formation and development of the bone-PDL-tooth complex from birth until weaning (about 3-4 weeks). Even after the tooth has erupted, the PDL complex is still forming the dentoalveolar complex will continue to form as secondary cementum also continues to deposit and the thickness of which increases with age (Nanci, 2007; Jang et al., 2014a). Therefore, at

any given time post-weaning, the combined effect from both the passive and active forces should be acknowledged although there is no standard procedure to decouple the two types of forces within an animal model. Appositional growth will be enhanced and continue to play a role in functional adaptation of the joint, albeit in a reduced capacity in normal physiological conditions. The enlargement of the muscles of mastication over age translates to increases in the magnitude of active forces on the joint. The active forces will remain at a plateau until the muscles begin to atrophy in which the active forces on the bone-PDL-tooth joint could decrease with age resulting in resorption activities in bone, and continuing apposition of cementum in the bone-PDL-tooth complex (Nanci, 2007).

1.3. Rationale for an *in vivo* model

In vivo modeling of functional adaptation of the dentoalveolar complex is commonly done in rats due to mastication habits and high throughput systems albeit limited existence of transgenic models. Each dental quadrant in a rat (2-hemimandibular and 2-hemimaxillary complexes) consists of three molars and a single continuously growing incisor in any given hemi-mandible or maxilla. Due to the dissimilarities between the rat and human dentition, experiments on rat mastication is often limited to modeling the mastication effects on the molars from the perspective of delineating site-specific regenerative potential within the bone-PDL-tooth complex (Lin et al., 2014; Lee et al., 2015).

Prior to the work described within this dissertation, several groups have investigated the effects of functional adaptation by manipulating or inducing physiological (Thomas and Peyton, 1983; Kiliaridis et al., 1985; Hiiemäe, 2004; Tanaka et al., 2007; Kingsmill et al., 2010; Niver et al., 2011), therapeutic (Bondevik, 1980; King et al., 1991;

Alhashimi et al., 2000), and pathological loads (Mavropoulos et al., 2004a; Enokida et al., 2005; Wada et al., 2008) (**Table 1.1**). The analysis of physiological chewing behavior of a normal rat was done by Hiiemäe, et al. (Hiiemäe and Ardran, 1968; Hiiemäe and Houston, 1971), in which the complex patterns of the animal when given different types of food was described in great detail. Among the conclusions from these studies was the observation that the behavior of the rat changed its chewing habits when eating a softer pudding compared to the normal hard pellet diet. Chewing habits were later correlated to the mastication of food with softer consistency where mastication loads which increased in frequency but decreased in magnitude (Thomas and Peyton, 1983). Groups have commonly modeled pathological variations in normal functional load by either placing an impedance on the occlusal surface (e.g. bite blocks) (Mavropoulos et al., 2004a; Enokida et al., 2005) or causing hypofunction by using an unopposed tooth molar model. It was shown that this decrease in functional loads resulted in shifts in bone volume density (Kingsmill et al., 2010) as well as shifts within the mandibular growth (Mavropoulos et al., 2004b). As orthodontics is common and represents therapeutic loads, animal models using orthodontic loads are mainly achieved through the use of orthodontic springs and orthodontic appliances (Bondevik, 1980; King et al., 1991; Grandfield et al., 2015). Common results have identified site specific shifts in inflammatory factors such as IL-1β, IL-6, TNF-α (Alhashimi et al., 2000, 2001), and changes in bone growth rate and direction (Bondevik, 1980; King et al., 1991; Grandfield et al., 2015). Within the context of occlusal loads, results obtained from reduced functional load model (Hiiemäe, 2004) will be discussed, the protocol of which was

successfully followed, however, adapted by our group (Niver et al., 2011) by keeping the nutrients the same and making powder chow from hard pellets normally given to rats.

1.4. Overall hypothesis and objectives

In this dissertation, the intensity and specificity of the functional adaptation processes within the dentoalveolar complex will be investigated by mapping shifts in mechanical strains and as a result, shifts in biochemical expressions to physicochemical tissue manifestation leading to overall changes in organ biomechanics. Hence, it **was *hypothesized that function-related strains at the PDL-bone and PDL-cementum interfaces stimulate cells to form or resorb mineral by creating a localized micro-niche***. Prior to the discussion of specific objectives, following chapters will detail the multifaceted approach to quantify changes in the biomechanical, biomaterial, and biochemical properties of the region. A schematic describing the multiscale breakdown of experiments is presented in **Figure 1.5**. General methodologies will be described in chapter 2. Since significant advancements in technology were made within our group within the context of this project, separate chapters describing the protocol and expected results for the *in situ* loading of a rat hemimandible (Chapter 3) and the measurement of alveolar bone deformation using digital volume correlation (DVC) (Chapter 4) will be presented. Chapters 5-7 will follow and will include investigating the aforementioned central hypothesis from a hierarchical perspective.

The following sections will list chapter titles and sub-objectives for chapters 5-7:

CHAPTER 5. MULTISCALE BIOMECHANICAL RESPONSES OF ADAPTED BONE-PERIODONTAL LIGAMENT-TOOTH FIBROUS JOINTS

1) Identify the shift in joint stiffness due to reduced function

2) Correlate the shift in joint biomechanics to a shift in physicochemical properties of tissues within joints exposed to reduced function

CHAPTER 6. ADAPTATION OF ALVEOLAR BONE TO REDUCED FUNCTIONAL LOADS

1) Demonstrate from a mechanics of materials perspective that interradicular interface with the tooth serves as a focal point for organ-level biomechanics

2) Correlate shifts in functional load with changes in formation/resorption dynamics within alveolar bone

3) Characterize adaptations in morphology and material properties of bone when exposed to reduced mastication forces

CHAPTER 7. AN OVERVIEW OF BIOMECHANICS AND MECHANOBIOLOGICALLY RELATED EVENTS IN THE BONE-PERIODONTAL LIGAMENT-TOOTH FIBROUS JOINT

1) To further improve the current mastication model by including the interdigitation between the maxillary and mandibular molars by accounting for the axis of rotation using the TMJ.

2) To implement an "artificial PDL tether method" by using the tooth movement within the socket as an input source in order to model the deformations within the PDL.

3) To relate growth and resorption markers at the PDL-bone and PDL-cementum tethered interfaces with their respective tether strains within the realm of a loaded fibrous joint.

1.5.   Figures and tables

Figure 1.1. A. Cranial and palatal sutures of a craniofacial complex. B. The oral and
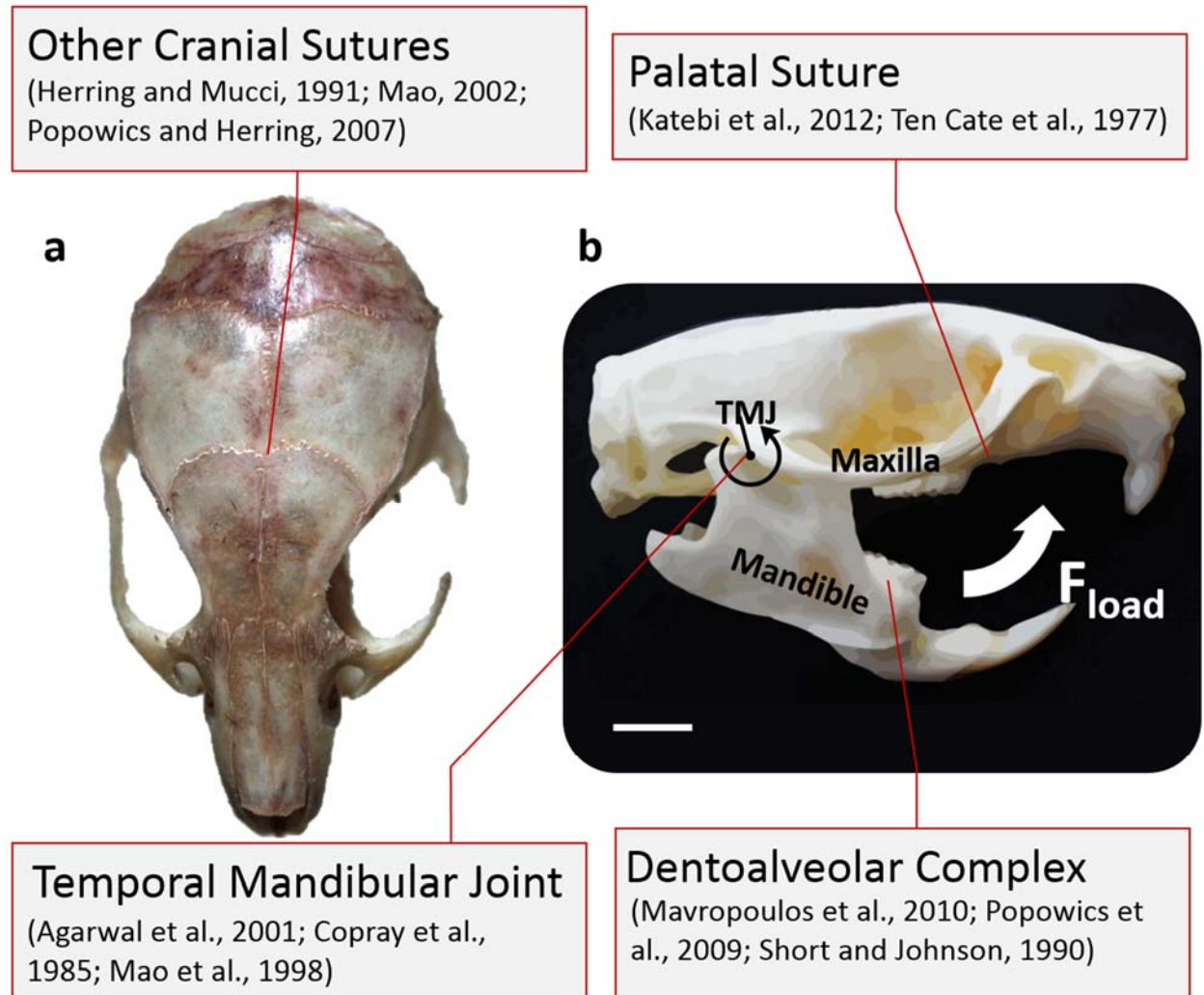
craniofacial organ system illustrating mandibular and maxillary complexes along with the

temporomandibular joint (TMJ).
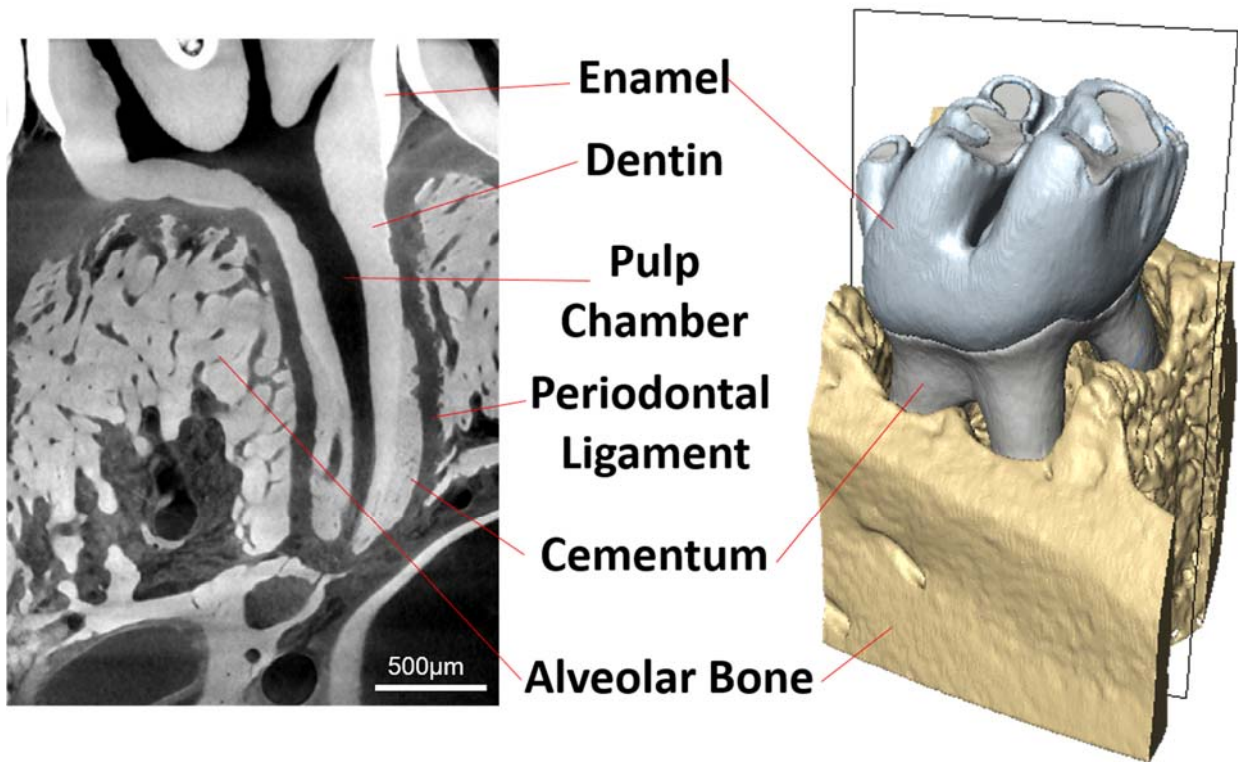
Figure 1.2. μ-XCT virtual section of a rat mandibular second molar including PDL stained with phosphotungstic acid and a 3D layout of the bone-tooth complex. Hard and soft tissues have been appropriately labeled.
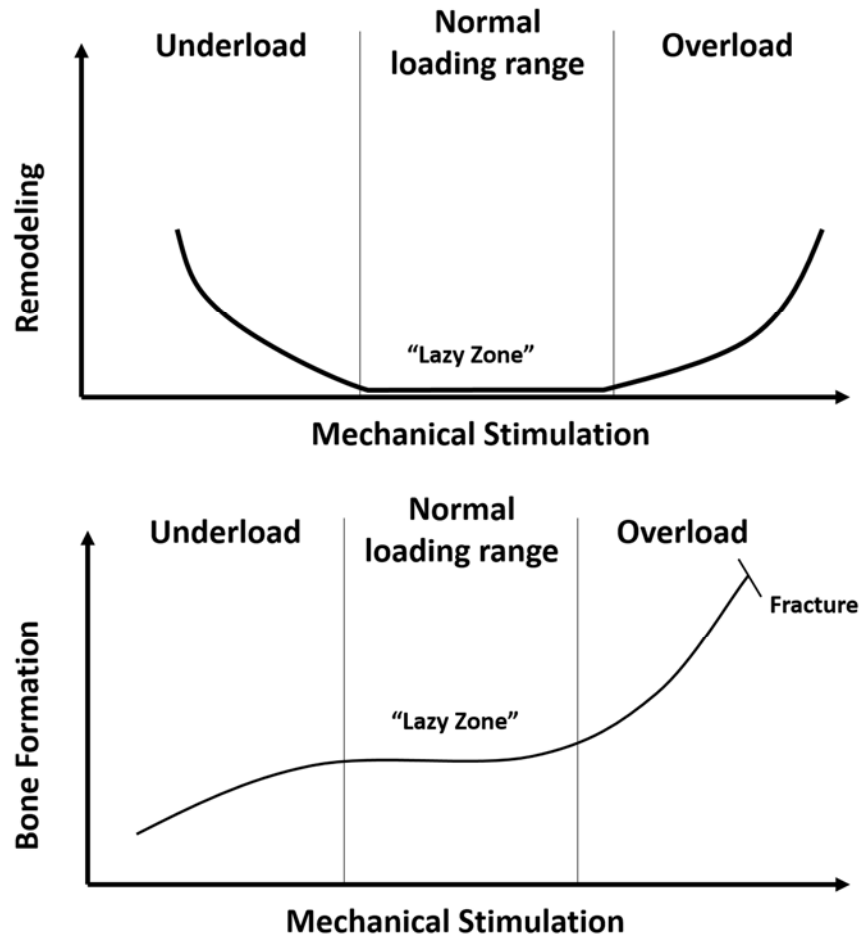
Figure 1.3. Top and bottom figures illustrate relationships between mechanical stimulation, bone formation, and bone resorption. Remodeling (resorption and formation) and modeling (formation) activities are affected differently by mechanical stimulation. Mechanical stimulation = f(magnitude of load, frequency of load). When the bone is underused (i.e. disuse), formation is inhibited, however remodeling activities within this region results in bone loss. Within normal loading range, remodeling activities maintain constant bone volume. Additionally, at higher stimulation levels, osteoblast activation will increase leading to additional appositional formation. Past a certain threshold, these loads become traumatic, leading to material failure through micro-cracks and tissue fracture with long term atrophy effects (adapted from Turner, *et al.* 1998).
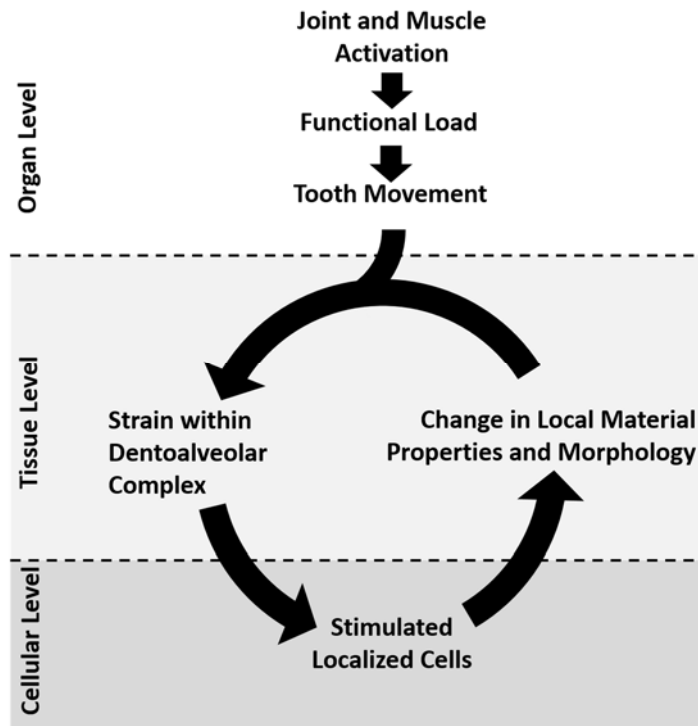
Figure 1.4. Hierarchical considerations causing load-mediated adaptation of a dentoalveolar complex. At an organ level, physiological functional loads normally originate from muscles of mastication and interdigitation of teeth. The resulting reactionary forces on teeth are accommodated by tooth movement within the alveolar socket. At a tissue level, tooth movement causes local deformations, primarily within the PDL and subsequently within the alveolar bone and tooth. Cells within tissues sense the localized strains and respond by shifting the regulation of bone and cementum dynamics. The cumulative effects of these local shifts result in broader change in respective tissues and their material properties and morphologies. This adapted structure will respond differently to the same initial tooth movement resulting in a modified distribution of local tissue strains. This cycle will continue until an optimization of material properties and structure are attained to accommodate the functional demands.
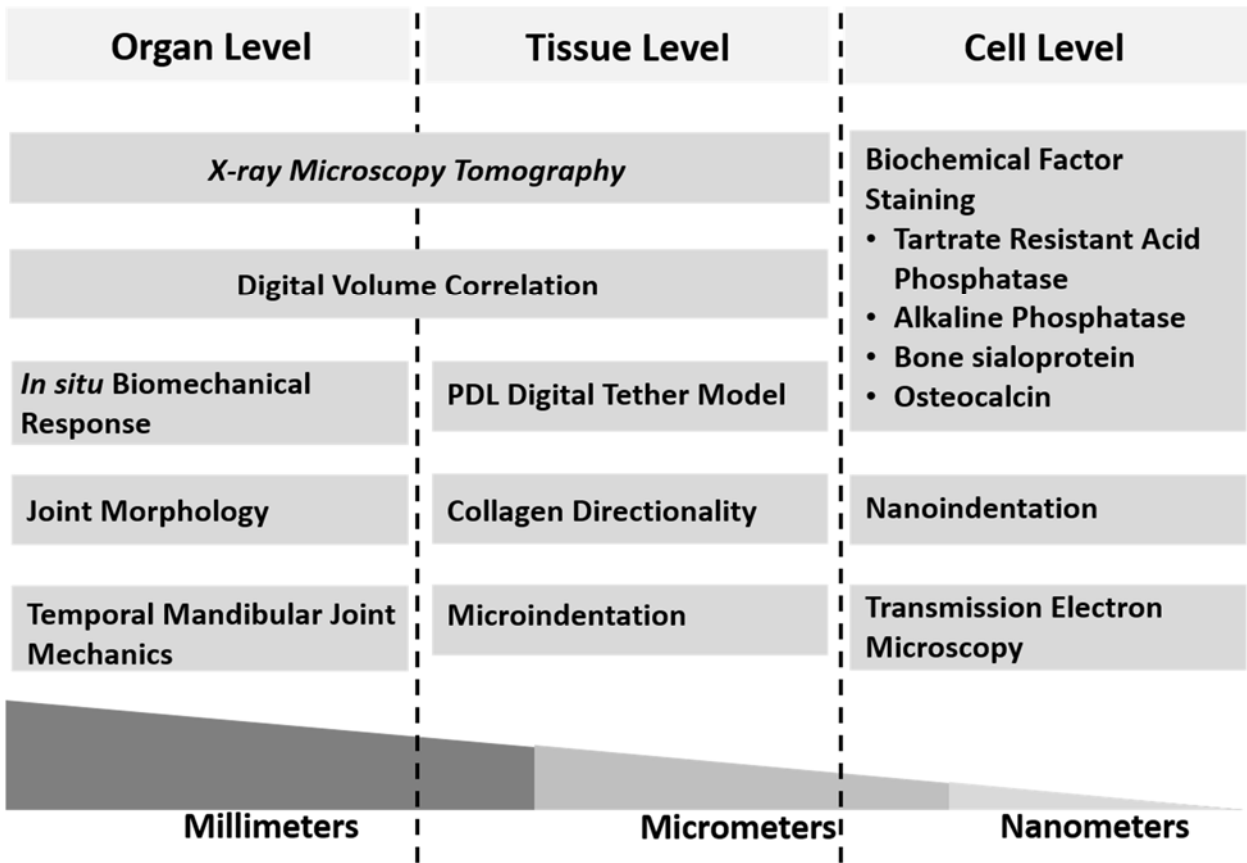
Figure 1.5. Multiscale approach (ranging from organ to tissue levels) and associated experimental methods used in this study.

Author	Year	Animal Model	Load Adaptation	Methods	Observations
Peyton	1983	rat	physiologic	soft diet – pudding	decreased bite Force
Kiliaridis	1985	rat	physiologic	soft diet - food mixed with water	skull became more orthocranial in shape - no change in skull volume - decrease growth rate of angle mandible
Hiiemäe	2004	rat	physiologic	soft diet – liquid	increase bite rate
Tanaka	2007	rat	physiologic	soft diet - crushed pellets	no change in body weight; mineralization in trabecular bone of condyle - lower. Higher mineralization in cortical bone in anterior and posterior area
Kingsmill	2010	rat	physiologic	soft diet - powered chow as paste	decreased bone volume, mineral density, alcian blue staining (GAG)
Niver	2011	rat	physiologic	soft diet – powder	decreased attenuation lines (μ-XCT) , decreased hardness (microindentation)
Bondevik	1980	rat	therapeutic	orthodontic appliance	narrowing of PDL-space, cell free zones - recovery after 1-2 weeks
King	1991	rat	therapeutic	springs	dental drift complementary to loads
Alhashimi	2000	rat	therapeutic	ortho spring	Change in expression of IL-1β, IL-6, TNF-α
Mavropoulos	2004	rat	pathologic	porridge (bite block)	altered bone volume density
Enokida	2005	rat	pathologic	hypofunction - recovery (bite plates on incisors)	Change in histomorphometry and RANKL distribution
Wada	2008	rat	pathologic	hypofunction	elastic property and bone formation (fluorochrome)

Table 1.1. Previous works illustrate the outcomes of the dentoalveolar complex in rats exposed to various types of functional loads.

CHAPTER 2. GENERAL EXPERIMENTAL METHODS

2.1.   Introduction

Within this chapter the protocols for the reduced loading on a small-scale animal model such as a rat and various methods that were applied to investigate the objectives will be described in detail.   Due to the multiscale and interdisciplinary nature of this research (see **Fig. 1.4**), several testing methodologies and assays will be used at the levels of bone-PDL-tooth organ, tissues and the interfaces that makeup the organ (see Fig. 1.2).

2.2   Reduced functional load on a rat

Within chapters 5 and 6, the effects of reduced physiological functional loads were analyzed by replacing hard pellet diet with a soft powder chow of equivalent nutrition (Niver et al., 2011). All experimental protocols were compliant and followed the guidelines of the Institutional Animal Care and Use Committee (IACUC) (Niver et al., 2011). Sprague Dawley male rats (Charles River Laboratories, Inc., Wilmington, MA) were divided into two groups: hard diet (HD; N=30) and soft diet (SD; N=30). Animals were received at 4 weeks of age when weaning of the pups is generally initiated. Hard diet (control), which is the normal pellet chow (PicoLab 5058, LabDiet, Deans Animal Feeds, Redwood City, CA, USA) was given to one-half of the set of rats while the SD group (reduced functional load group) was given a finely pulverized version of the control pellet. Powdered diets were pulverized and sifted on a regular basis to ensure a constant powder-like consistency. To analyze the effect of age on load adaptation, animals were grown to 8, 12, 16, 20, or 24 weeks (N=6 in each group) respectively. Animal weights were taken

and documented twice a week per IACUC standards. No extreme weight loss of animals was observed. Once animals were grown to a desired age, each animal was euthanized by carbon dioxide asphyxiation and bilateral thoracotomy. Hemimandibles were harvested, and right hemimandibles were used for *in situ* loading for organ biomechanics, X-ray microscopy (XRM) of unloaded and loaded organs for strain-mapping using digital volume correlation (chapter 4 and chapter 6), microindentation and nanoindentation for tissue properties (chapters 5 and 6), specifically of bone and cementum hard tissues. Left hemimandibles were preserved for histology (hematoxylin and eosin, picrosirius red stains) and immunohistochemistry (tartrate acid resistant phosphatase (TRAP), alkaline phosphatase (ALP), and immunogold labelling (bone sialoprotein – a postulated mechanosensitive protein) (chapter 7).

2.3. Histology

2.3.1. Tissue preparation for conventional histology, immunohistochemistry, (Lin et al., 2014) and immunogold labelling (Chen et al., 2015)

Harvested hemimandibles were prepared for histology using protocols previously described (Lin et al., 2014). Intact hemimandibles were processed through a combination of decalcification and fixation using a mixed solution of 0.5M ethylenediaminetetraacetic acid (EDTA) and 2% paraformaldehyde for 3 weeks (Doherty et al., 2010). Specimens were checked regularly to ensure decalcification to facilitate sectioning for histology, and epitope recognition for immunohistochemistry and immunogold labelling. Demineralized specimens were dehydrated through a series (80%, 95%, and 100%) of Flex alcohol (Richard-Allan Scientific, Kalamazoo, MI) before embedding in paraffin (Tissue Prep-II, Fisher Scientific, Fair Lawn, NJ).   Sagittal sections were cut from the embedded

specimens using a rotary microtome (HM 325 Rotary Microtome, Thermo Scientific, Waltham, MA, USA). Sectioned specimens were mounted on statically charged slides (Superfrost Plus Fisher Scientific, Waltham, MA, USA). Prior to staining, sections were deparaffinized using xylene and rehydrated through a reverse series of ethanol (100%, 95%, and 80%). These sections were used to stain with H&E and PSR stains.

For cryosectioning, sections were placed in a 15% solution of sucrose for 2-3 hours then a 30% solution of sucrose overnight. Primed specimens were then embedded in an OCT solution (Scigen Inc. Gardena, CA, USA) and flash frozen using a combination of ethanol and dry ice. Sectioning on frozen blocks was performed using a rotary microtome and placed on charged slides. Sections slides were rehydrated by bringing frozen sections to room temperature for 30 minutes and washing slides twice in 1x phosphate buffer solution for 4 minutes each. These sections were used to perform site-specific immunohistochemistry to localize ALP and TRAP expressions within tissues. Visualization of local expressions was facilitated by performing light microscopy on stained sections.

For ultrasectioning, intact specimens were dissected and fixed overnight in 10% neutral buffered formalin (NBF, Richard-Allan Scientific, Kalamazoo, MI). Each specimen was washed twice in 1X phosphate-buffered saline (PBS) and then dehydrated using graded (50-100%) ethanol solutions. The specimen kept in 100% ethanol was scanned using a μ-CT (MicroXCT-200, Carl Zeiss Microscopy, Pleasanton, CA) followed by infiltration of the specimen with LR-white resin (Electron Microscopy Sciences, Hatfield, PA). The infiltrated specimen was kept in a gelatin capsule (Electron Microscopy Sciences) and polymerized for 2 days at 60°C. 90-100 nm thick tissue sections were cut

with an ultramicrotome (Reichert Ultracut E, Leica Microsystems, Inc., Buffalo Grove, IL) and were collected on formvar/carbon-coated Ni grids (Electron Microscopy Sciences). Site-specific protein localization at a nanoscale was performed through immunogold labeling of thin sections on grids (Chen et al., 2015) and visualization facilitated by a transmission electron microscope (TEM).

2.3.2. Picrosirius red (PSR) staining to determine directionality of collagen fiber bundles (Lin et al., 2014)

Rehydrated sections were stained using a combination of Sirius red F3B (C.I. 35782) and picric acid (American MasterTech Scientific Co., Lodi, CA). Specimens were imaged using polarized light microscopy (BX 51, Olympus America Inc., San Diego, CA) using Image Pro Plus v6.0 (Media Cybernetics, Inc., Silver Spring, MD) for image acquisition. A Fourier component analysis was done using a modified version of ImageJ to measure directionality of the PDL fibers (Fiji – created by Jean-Yves Tinevez (Tinevez, 2015))

2.3.3. Tartrate resistant acid phosphatase (TRAP) staining (Erlebacher and Derynck, 1996) to determine the location of osteoclasts

Rehydrated sections were selected and incubated in a solution of 0.2M sodium acetate and 50mM L-(+)-tartaric acid at pH 5.0 (Sigma-Aldrich, St Louis, MO, USA) for 20 minutes at room temperature (25°C). Following the 20 minutes of incubation, 0.5 mg/ml napthol AS-MX phosphate and 1.1 mg/mL fast red TR salt was added to the sodium acetate buffer. Solution and slides were then incubated at room temperature for 1-4 hours at body temperature (37°C), regularly checking for proper TRAP staining (note: for cryosectioned specimens, about 15 minutes of incubation is required for this step).

Following TRAP staining, specimens were rinsed in distilled water and counterstained in a batch of fresh Mayer's hematoxylin for a minimum of 10 seconds (longer if solution is old). Sections were then rinsed again in tap water and mounted.

2.3.4. Alkaline phosphatase (ALP) staining (Yoshiki et al., 1972; Miao and Scutt, 2002)

Rehydrated sections were selected and incubated in a solution of Trismaleate buffer solution (100mM, pH 9.2) with 1% MgCl overnight. Fresh solutions were made of 100mM Trismaleate buffer (without the 1% MgCl) and added napthol AS-MX phosphate (0.2 mg/mL) and fast red TR salt (0.4 mg/mL) for 15-20 minutes (for cryosections – longer if staining paraffin sections). Sections that were stained with ALP were counterstained with Meyer's hematoxylin for 10 seconds, rinsed in tap water and mounted with immunomount.

2.4. Structural analysis

2.4.1. X-ray microscopy (XRM) to generate X-ray tomograms (Herber et al., 2012; Lin et al., 2013)

Intact specimens designated for XRM tomography were immediately placed in a tris-buffered solution supplemented with 50μg/mL of penicillin/streptomycin (UCSF cell culture facility, San Francisco, CA, USA) (Chiba and Komatsu, 1993). Specimens were scanned (Micro XCT-200, Xradia, Inc., Pleasanton, CA, USA) in hydrated conditions using tris-buffered solution. Refer to **Table 2.1** for scanning parameters. Care was taken to scan all specimens as soon as possible in order to reduce the amount of tissue alteration due to storage. Acquired images were reconstructed using XMReconstructor (v8.1.6599, Xradia Inc., Pleasanton, USA).

2.4.2. Joint and bone morphometric analyses (Parfitt, 1988; Bouxsein et al., 2010; Lee et al., 2013)

Joint and bone morphometrics included functional space measurements (Lee et al., 2013) and bone volume fraction (BVF) calculations (Parfitt, 1988; Bouxsein et al., 2010). Functional space measurements were taken on reconstructed tomograms using 3D viewer (Xradia 3D viewer v1.1.6, Xradia Inc., Pleasanton, CA, USA). Following the identification of standard virtual slices within each specimen, a series of 10 measurements were taken measuring the distance between the interradicular crest of the alveolar bone and the furcation of the tooth.

BVF was calculated using sub volumes identified within the tomograms. Intensity based segmentation was done in Avizo (Avizo 9.0.0, FEI, Hillsboro, OR, USA) to separate bone from non-bony tissues producing a binary label of the bone. Within the context of this dissertation, BVF was defined as the ratio of bone volume to total volume (total volume = bone volume + endosteal space). Since the general shape of the bone was irregular, the total volume of the bone was approximated by taking the segmented image of the bone and applying a digital closing algorithm (Dougherty et al., 2003) to include all the internal holes within the bone (Avizo 9.0.0). BVF values were then calculated by taking the volume of the unclosed binary image and dividing it by the "morphologically closed" binary label.

2.4.3. Immunogold labelling of bone sialoprotein

The ultrasections from infiltrated blocks were decalcified with 4% EDTA solution twice for 20 min each time in an incubator. Decalcified sections were washed twice using Milli-Q water, twice with PBS, and were treated with a blocking agent containing 2.5%

bovine serum albumin (BSA, Sigma-Aldrich) in PBS for 10 min. Grids were incubated in primary antibody solution (1:20 dilution in PBS) at 4°C overnight. After washing three times with PBS, sections were treated again with 2.5% BSA for 10 min then incubated in a 10-nm-diameter protein G-gold nanoparticle solution (Electron Microscopy Sciences, Hatfield, PA) for 1 hr. at room temperature. Following washing three times with PBS, grids were rinsed with Milli-Q water and air-dried overnight. No counterstaining was applied to the sections. The sections were examined using a transmission electron microscope (JEOL USA, Inc., Peabody, MA) operated at an accelerating voltage of 100 keV.

2.5. Materials testing

2.5.1. Local hardness evaluation using microindentation (Ho et al., 2004)

Following imaging and *in situ* mechanical testing (see chapter 3 for *in situ* mechanical testing protocol), sagittal sections were made with a rotary saw and diamond blade (ISOMET, Buehler Ltd, IL, USA) using the center of the occlusal plane as an orthogonal reference. Sliced specimens were then embedded in epoxy. The exposed surface of the bone-PDL-tooth complex was then polished using a series of fine diamond suspension slurries with a final suspension grade of 0.25 µm (Buehler Ltd, Lake Bluff, IL). Knoop hardness microindentation (10s, 20gf, dry conditions) was performed on secondary cementum of the second molar and the accompanying interdental alveolar bone and interradicular alveolar bone. Microindentation was performed as per ASTM E384-99 standard (ASTM - E04 Committee, 1999).

2.5.2. Elastic modulus evaluation under wet conditions using nanoindentation technique

Epoxy embedded hemimandible sections prepared for microindentation (see section 2.4.1) were also used for nanoindentation (Nanoscan 4D, Nanounity, Moscow, Russia) under wet conditions. Following hydration of the specimen with deionized water for 1 hr., specimens were indented using a Berkovich tip (2000µN force). Rows of indents were placed on the interradicular bone of the second molar with about 16µm of spacing between indents. The reduced elastic modulus (E_r) was calculated using the Oliver-Pharr method (Oliver and Pharr, 1992).

2.6. Tables

Optical Magnification	KVP	Voxel Size*	Exposure time**	Projections**
2x	75	~7 µm	4-16 sec	2000
4x	75	~3.5 µm	1-7 sec	2000
10x	75	~1.5 µm	7-30 sec	2000

*in addition to optical magnification voxel size also depends on the distance between the source-rotation axis and detector-rotational axis
**exposure time and projections depend on the desired image quality and the amount of material outside the "field of view"

Table 2.1. XCT Parameters

CHAPTER 3. *IN SITU* COMPRESSIVE LOADING AND CORRELATIVE NONINVASIVE IMAGING OF THE BONE-PERIODONTAL LIGAMENT-TOOTH FIBROUS JOINT

This work was published in Journal of Visual Experimentations in 2014. To see the accompanying video please visit (http://www.jove.com/video/51147/in-situ-compressive-loading-correlative-noninvasive-imaging-bone). Additionally, it was written in a language suitable and as required by JOVE.

3.1. Abstract

This study demonstrates a novel biomechanics testing protocol. The advantage of this protocol includes the use of an *in situ* loading device coupled to a high resolution X-ray microscope, thus enabling visualization of internal structural elements under simulated physiological loads and wet conditions. Experimental specimens will include intact bone-periodontal ligament (PDL)-tooth fibrous joints. Results will illustrate three important features of the protocol as they can be applied to organ level biomechanics: 1) reactionary force vs. displacement: tooth displacement within the alveolar socket and its reactionary response to loading, 2) three-dimensional (3D) spatial configuration and morphometrics: geometric relationship of the tooth with the alveolar socket, and 3) changes in readouts 1 and 2 due to a change in loading axis, *i.e.* from concentric to eccentric loads. Efficacy of the proposed protocol will be evaluated by coupling mechanical testing readouts to 3D morphometrics and overall biomechanics of the joint. In addition, this technique will emphasize on the need to equilibrate experimental conditions, specifically reactionary loads prior to acquiring tomograms of fibrous joints. It should be noted that the proposed protocol is limited to testing specimens under *ex vivo*

conditions, and that use of contrast agents to visualize soft tissue mechanical response could lead to erroneous conclusions about tissue and organ-level biomechanics.

3.2. Introduction

Several experimental methods continue to be used to investigate the biomechanics of diarthrodial and fibrous joints. Methods specific to the tooth organ biomechanics include the use of strain gauges (Jantarat et al., 2001a, 2001b; Popowics et al., 2009), photoelasticity methods (Asundi and Kishen, 2000, 2001), Moiré interferometry (Wang and Weiner, 1997; Wood et al., 2003), electronic speckle pattern interferometry (Dong-Xu et al., 2011), and digital image correlation (DIC) (Zhang and Arola, 2004; Li et al., 2009; Qian et al., 2009; Zhang et al., 2009; Lin et al., 2014). In this study, the innovative approach includes noninvasive imaging using X-rays to expose the internal structures of a fibrous joint (mineralized tissues and their interfaces consisting of softer zones, and interfacing tissues such as ligaments) at loads equivalent to *in vivo* conditions. An *in situ* loading device coupled to a micro-X-ray microscope will be used. The load-time and load-displacement curves will be collected as the molar of interest within a freshly harvested rat hemi-mandible is loaded. The main goal of the approach presented in this study is to emphasize the effect of three-dimensional morphology of tooth-bone by comparing conditions at: 1) no load and when loaded, and when 2) concentrically and eccentrically loaded. Eliminating the need for cut specimens, and to perform experiments on whole intact organs under wet conditions will allow for maximum preservation of the 3D stress state. This opens a new area of investigation in understanding dynamic processes of the complex under various loading scenarios.

In this study, the methods for testing PDL biomechanics within an intact fibrous joint of a Sprague Dawley rat, a joint considered as an optimum bioengineering model system will be detailed. Experiments will include simulation of mastication loads under

42

hydrated conditions in order to highlight three important features of the joint as they relate to organ level biomechanics. The three points will include: 1) reactionary force vs. displacement: tooth displacement within the alveolar socket and its reactionary response to loading, 2) three-dimensional (3D) spatial configuration and morphometrics: geometric relationship of the tooth with the alveolar socket, and 3) changes in readouts 1 and 2 due to a change in loading axis, i.e. from concentric to eccentric loads. The three fundamental readouts of the proposed technique can be applied to investigate the adaptive nature of joints in vertebrates either due to changes in functional demands, and/or disease. Changes in the aforementioned readouts, specifically the correlation between reactionary loads with displacement, and resulting reactionary load-time and load-displacement curves at different loading rates can be applied to highlight overall changes in joint biomechanics. Efficacy of the proposed protocol will be evaluated by coupling mechanical testing readouts to 3D morphometrics and overall biomechanics of the joint.

3.3. Protocol (a narrative; http://www.jove.com/video/51147/in-situ-compressive-loading-correlative-noninvasive-imaging-bone**)**

Animal housing and euthanasia: All animals used in this demonstration were housed under pathogen-free conditions in accordance to the guidelines of the Institutional Animal Care and Use Committee (IACUC) and the National Institute of Health (NIH). Provide animals with standard hard-pellet rat chow and water *ad lib.* Euthanize animals via a two-step method of carbon dioxide asphyxiation, bilateral thoracotomy in accordance with the standard protocol of UCSF as approved by IACUC. Perform biomechanical testing within 24 hours of animal sacrifice to avoid tissue degradation.

3.3.1. Preparation and dissection of a rat mandible or maxilla

1. Remove rat mandibles by gently severing membranous tissue and muscle tissue attachments while preserving the entire mandible, including the coronoid process and the condylar process (**Fig. 3.1**)(Huelke and Castelli, 1965).

2. Separate hemimandibles by carefully cutting the fibrous tissue of mandibular symphysis with a scalpel blade.

   *Note: The coronary and condylar processes, and ramus of the mandible (**Fig. 3.1**) should be removed if they physically obstruct biomechanical testing of the 2nd molar.*

3. Cut the incisors without exposing the pulp chamber as not to hinder loading of the molar.

3.3.2. Specimen preparation for *in situ* compressive loading (Fig. 3.2)

1. Immobilize the specimen on a steel stub by using a material that is significantly stiffer than the experimental specimen prior to loading it in an *in situ* loading device (**Fig. 3.2a**).

   Note: Polymethylmethacrylate (PMMA) was used to immobilize the specimen in this study and excess, if any, was removed using a dental explorer.

2. Align the occlusal surface of the molar(s) of interest parallel with the AFM metal specimen disc using a straight edge in both planes (i.e. mesial-distal and buccal-lingual).

3. Create a trough with a blunt instrument surrounding the molars.

   Note: This space should serve as a "moat" to contain excess liquid and maintain tissue hydration during in situ loading.

4. Prepare the tooth surface to build up for concentric (**Fig. 3.2b**) or eccentric (**Fig. 3.2c**) loading using a dental composite. Etch the surface of the tooth of interest with 35% phosphoric acid gel on occlusal surface for 15 sec.

5. Rinse the etchant thoroughly with deionized water and dry the surface using an air/water syringe or a compressed-air canister. With an explorer, spread a drop of the bonding agent into open cusps in a thin layer. Cure the composite with a dental curing light.

   Note: All steps involving composites should be performed without direct light from a lamp. Such conditions would undesirably accelerate the polymerization process, and could prevent proper placement of the composite. Room lighting is acceptable.

6. Remove excess bonding agent from adjacent teeth with a fine scalpel or razor blade.

7. Place flowable dental composite on the surface following the preparation of the surface and spread it into grooves of the molar(s) of interest using a dental explorer.

8. Expose the composite to dental curing light for 30 sec.

9. Mold an occlusal buildup of about 3-4 mm using a dental resin composite, from the occlusal plane of the molar(s) of interest and light cure for 30 sec.

10. Reduce the top of the composite buildup to a flat surface parallel to enable a consistent loading scheme across all specimens by using a straight edge and a high speed hand piece.

Note: During biomechanical testing, other specimens should be stored in tris-phosphate buffered solution (TBS) with 50 mg/ml penicillin, and streptomycin

3.3.3. Loading device drift and stiffness, material property differentiating capability, *in situ* loading of the fibrous joint

1. Secure the specimen with the composite buildup on the anvil of the loading stage, and test for uniform loading as shown in **Figure 3.2b**.

2. Place an articulating paper on the surface of the composite followed by loading the specimen to a finite load to check for concentric or eccentric loading (**Fig. 3.2b and 3.c**).

3. Place TBS-soaked Kimwipe around the specimen to ensure specimen hydration. Make a trough around the specimen and fill it with TBS to keep the organ hydrated during imaging.

4. Input peak load and displacement rate into the Deben software to compress the molar to a desired peak load at a displacement rate following immobilization of the hemimandible.

   Note: Typical readouts should include a reactionary load as the material is compressed over time (load transducer sensitivity = 0.1 N). From load-time and displacement-time, a load-displacement curve for the compressed material should be obtained (Chiba and Komatsu, 1993; Natali et al., 2008; Naveh et al., 2012a). *Using the data collected from the loading cycles, various properties of the joint can also be determined. The stiffness of the joint should be calculated by taking the slope of the linear portion (approximately the last*

30% of the data) of the loading phase of the load vs. displacement curve (Lin et al., 2013)*.*

3.3.4. Staining of soft tissue, the PDL, with phosphotungstic acid (PTA)

Note: To enhance X-ray attenuation contrast, the PDL should be stained with 5% PTA solution (Metscher, 2009)*.*

1. Backfill PTA staining solution into a clean 1.8 ml glass carpule and place loaded carpule into syringe.

2. Inject solution slowly (5 min/carpule) into the PDL-space of adjacent teeth to prevent structural damage to periodontal tissues surrounding molar of interest.

   Note: The above steps should be repeated until about 5 full carpules (9 ml) of solution are injected and allowed to flow into the surrounding tissues. The prepped specimens can also be soaked overnight in the remaining PTA solution (8 hr).

3.3.5. Recommended µ-XCT scanning settings

1. Perform µ-XCT with the following scanning settings: (see **Table 3.1**)

3.4. Representative results

Estimation of loading device "backlash", "pushback", stiffness, and system drift under a constant load

Backlash: Between loading and unloading portions of the cycle, there exists a pause of 3 seconds during which gears reverse within the motor before true unloading commences, i.e. as the specimen pulls away from the top jaw (**Fig. 3.3**). This period is referred to as a backlash in the system, which represents a segment of time when the

system is attempting to switch from closing to opening of the jaws. It should be noted that all load cycles will contain a similar backlash response regardless of specimen or loading conditions (**Fig. 3.4**). A normal load vs. time curve obtained using a rigid body is shown in **Figure. 3.3a and 3.3b** highlighting the loading, unloading, and backlash regions at two different loads of 6 N and 16 N. A normal load vs. displacement curve highlighting the corresponding three segments is shown in **Figure 3.3c**.

Pushback: While all backlash periods occur within the same 3 sec time frame, the reactionary response and as a result the shape of the backlash region could change depending on the specimen. By testing the system using a rigid body (**Fig. 3.3**), the steepest and highest drop in reactionary load was observed when compared to the bone-PDL-tooth complex and polydimethylsiloxane (PDMS). However, the fibrous joint illustrated a significant drop in reactionary load during backlash phase compared to PDMS. PDMS (**Fig. 3.4**) specimens appeared to have the least drop (no difference between the 1:05 and 1:25 crosslinker densities - **Fig. 3.4A**).

Stiffness: Stiffness of the loading device when tested against rigid body was significantly higher than that of the complex and PDMS specimens. These data validate the effectiveness of the loading device to highlight changes in biomechanics of the bone-PDL-tooth complex and softer materials (**Fig. 3.4b**).

Visualizing soft and hard tissue structures within the intact bone-PDL-tooth complex using μ-XCT: In an unstained, but hydrated fibrous joint, attenuation of hard tissue features, including alveolar bone, cementum, enamel, and dentin were highlighted (**Fig. 3.5a and 3.5b**). However, spaces that contained predominantly softer organic tissues were transparent to X-rays, leaving the PDL-space relatively "empty" (black).

Specimens treated with PTA showed increased contrast within the PDL-space, thus highlighting features representative of the PDL and gingival tissues (**Fig. 3.5c-f**). Scanning at a higher magnification revealed PDL as a fibrous network between the tooth and bone.

Reactionary force vs. displacement: biomechanical response of the fibrous joint during *in situ* loading: Compared with concentric loading, eccentric loading pattern on a similar specimen showed increased displacement of the tooth within the joint for a given reactionary load (**Fig. 3.6a**). However, for fibrous joints treated with PTA no significant differences in the overall biomechanics were observed regardless of the loading condition (**Fig. 3.6b**). In the untreated but eccentrically loaded system, the increased displacement of the root into the alveolar socket can be correlated to lower stiffness as seen in the load-displacement curves (**Fig. 3.6c**). While there could be a natural variance leading to a range of biomechanical responses of fibrous joints harvested within control groups, PTA-treated fibrous joints exhibited increased stiffness and displaced less within the socket compared to untreated counterparts for a given reactionary peak load. However, there was no detectable change in shape or duration of the backlash phase of the load cycle between untreated and PTA treated specimens.

Three-dimensional spatial configuration and morphometrics: mapping the bone-tooth configuration under loaded conditions using μ-XCT: Virtual slices taken from tomograms were compared to illustrate 1) tooth movement within the socket, 2) tooth-bone association both in 2D and 3D, 3) the extent of movement due to eccentric compared to concentric loading. Tooth movement was highlighted by superimposition of similar virtual slices at no load and at load and generating gif movies. While both loading

49

schemes caused the tooth to displace vertically within the joint, an eccentric loading configuration (**Fig. 3.7b and 3.7c**) caused an additional rotational effect of the tooth with the roots rotating distally resulting in decreased PDL space along the distal sides of the roots compared with concentric loading scans (**Fig. 3.7 and 3.8**). Although the PTA-stained PDL was more attenuating (**Fig. 3.5**), the movement of the tooth within alveolar socket in the PTA treated joints was less pronounced and correlated with the biomechanical data (**Fig. 3.6b and 3.6c**).

3.5.   Discussion

The first step in establishing this protocol involved evaluating the stiffness of the loading frame by using a rigid body. Based on the results, the stiffness was significantly higher enabling the use of the loading device for further testing of specimens with significantly lower stiffness values. The second step highlighted the ability of the instrument to distinguish different stiffness values by using two phases of the loading-unloading curve generated by using a rigid body, PDMS materials of different crosslink densities, and fibrous joints. The stiffness from the loading phase and pushback during the backlash phase were used to identify the resistance of the material to loading and recovery of the material following unloading (**Fig. 3.3 and 3.4**). The third and fourth steps of the protocol were to correlate the changes in load-displacement curves obtained from the loading device to the *in situ* imaging done with the use of X-rays (**Fig. 3.5**). This involved loading the joints and obtaining tomograms at no load and load, under concentric and eccentric conditions respectively. The protocol demonstrated that by changing the loading axis differences in levels of PDL-compression can be highlighted (**Fig. 3.6 and 3.7**). In this discussion we will first highlight instrument features and challenges that

should be adequately understood and met prior to biomechanical testing of the bone-PDL-tooth complex.

3.5.1. Challenges of experimental setup

Composite buildup: While the protocol itself is relatively straightforward, there are several steps that must be done with great care. One of the biggest challenges was to ensure that excess composite material did not overflow to adjacent teeth, which would then mechanically link multiple teeth and misrepresent the joint mechanics of a single tooth. Since significant manual dexterity and knowledge of dental tools proved to be useful for this procedure, preparation of specimens for loading was primarily performed by dental students and dentists with the assistance of optical magnification.

Consistent loading scheme: Another important detail for biomechanical testing was to ensure a consistent loading scheme. The contact area between the jaw of *the in situ* loading device and opposing surface of the composite proved to be very crucial to the experiment. This is because mechanics of the fibrous joint can change as a result of the area of contact, which was simulated in this study by using concentric and eccentric (unbalanced) loads. The scenario presented in this study mimics possible changes in occlusion of mammalian teeth, which could result in a change in tooth movement within the alveolar socket (**Fig. 3.5**). While it is understood that the proposed testing mechanism does not mimic physiological mastication cycle, it presents itself as a standard testing method. By creating a composite buildup with a surface parallel to the jaw of the loading stage, we were able to generate a consistent loading pattern. This standard testing method can be used to identify changes in biomechanics of the bone-PDL-tooth complexes from various experimental groups.

Sensitivity of the *in situ* loading device: The experimental protocol describes methods for validating detection limits of the *in situ* loading device using three different specimens, of which two can be considered as standard materials. The stiffness of the loading frame when tested with aluminum was significantly higher with negligible contribution to the observed mechanical behavior of various PDMS specimens, and the biomechanical response of a fibrous joint. While all the specimens tested had a backlash period of ~3 sec, the shape of the backlash portion slightly varied (**Fig. 3.4a**) with the type of specimen. Rigid specimens exhibited a sharp decrease in reactionary load (**Fig. 3.3a and 3.4a**) while softer specimens did not exhibit a sharp decrease (**Fig. 3.4a**). It can be argued that the difference in backlash behavior is attributed to the ability of the specimen to push back on the gears during gear reversal. The push back effect on the gears could manifest into a lower drop in the peak reactionary response of the material as the jaw starts to move away from the specimen. Thus, the backlash segment can be exploited to gain insights to material property. Stiffness values of PDMS calculated from load displacement curves were in agreement with literature values (Hemae, 1967), and the range of stiffness for the crosslinked PDMS was within the range of the bone-PDL-tooth complex. Hence, the *in situ* loading device is suitable for measuring the displacement and reactionary response of the tooth as it is compressed into the alveolar socket. The reactionary response can be from softer and/or harder constituents. The dominance of the softer constituent over the harder can be identified by loading incrementally and imaging, followed by digitally correlating the no load to loaded conditions to identify strain-dominated regions within the bone-PDL-tooth complex (Lin et al., 2013).

Principal component of mastication is in the axial direction: Similar to humans, the mastication cycle of rats involve the free motion of the mandible to chew food (Hunt et al., 1970; Komatsu et al., 2007). While this motion has been mapped to include many different directions such as lateral movements, the principal component of load is thought to be in the axial direction (Hunt et al., 1970). Therefore, the simulated *in situ* loads in axial direction were placed either concentrically or eccentrically (**Fig. 3.2**).

Experimental factors that could affect results related to organ level biomechanics: The advantage of coupling X-ray microscopy with *in situ* loading is that the load-displacement curve can be correlated to the spatial association of the tooth with the alveolar socket, form of the root and the alveolar surface, and the narrowing and widening of the PDL-space under load. The correlation and complementary evaluation provides a holistic approach to determine organ biomechanics. In the past, it was only postulated that the mechanics of an organ and/or tissues can prompt the load-displacement behavior. This protocol illustrated that the association of the moving members when under load can also be a defining characteristic of observed stiffness. Any changes observed within the first 5-8 N is thought to be contributed by the quality of the PDL an initial conformational change within the collagen and interstitial fluid exchange with minimum resistance to load; this region has been referred to as the "uncrimping" region (Quintarelli et al., 1971a). Loads higher than 7 N could be contributed by tooth, bone, the strain-hardening effects of the periodontal ligament, and the interfaces attaching the tissues. Once the PDL-space is minimized and as the PDL undergoes strain hardening, hard tissue interactions between the tooth and bony socket arise at the interradicular region resulting in a steeper load to displacement slope. In addition to material recovery, the

backlash of the loading device can be exploited to investigate the viscoelastic nature of the PDL without altering the joint as was done in other studies (Chiba and Komatsu, 1993; Lin et al., 2013).

The general regions within the load displacement curves correlate to some events within the joint. The above events are the common denominators between the two loading schemes. However, the differences between concentric and eccentric load-displacement profiles and corresponding tomograms highlighted the influence of load direction on the overall organ biomechanics. The main source of these differences was the introduction of a tooth rotation as it displaces within the joint, causing the compression of PDL spaces at specific areas. It is understood that normal physiological loads are applied on the tooth in several directions including those that introduce rotational tooth movement. However, it is recommended that a concentric loading scheme be used as a standard loading scheme due to the difficulty of applying a "standard" eccentric load across all specimens. As such this experimental protocol can be used to differentiate biomechanical differences between adapted and nonadapted systems.

One of the drawbacks of using higher energy X-rays is that they are minimally absorbed by softer tissues and produced inadequate contrast. The PDL is transparent to X-rays and as a result necessitates the use of contrast agents. PTA enhances the contrasts of soft tissues by directly staining (Crabtree and Murphy, 1979; Quintarelli et al., 1971b, 1973) and allowing for visualization by using X-rays. Hence, by using the contrast agents, visible deformation within stained soft tissue regions between loaded and unloaded tomographies was observed; however higher magnification (at least 10X) is recommended for analysis (data not shown). A limitation of the staining protocol included

the use of ethanol, a mild fixative (Crabtree and Murphy, 1979) which could have altered the stiffness of the PDL and overall joint mechanics leading to erroneous conclusions.

3.6. Conclusions

This study highlights a novel testing protocol to analyze the biomechanical response of an intact bone-PDL-tooth fibrous joint, but under *ex vivo* conditions. The described experimental method including post analyses of data can be used to measure effects of experimental variables (i.e. disease, growth factors, age, and therapeutic molecules) on the mechanics of the bone-PDL-tooth fibrous joint. Additionally, results from these experiments will serve as a baseline for which relationships between variations at the macroscale organ level can be related to specific changes at the tissue and cellular levels. Limitations of the protocol include, imaging under *ex vivo* conditions, use of contrast agents, and loss in spatial accuracy between surfaces of the tooth and alveolar socket due to tissue relaxation during longer acquisition times necessary for tomogram generation.

3.7. Figures and tables
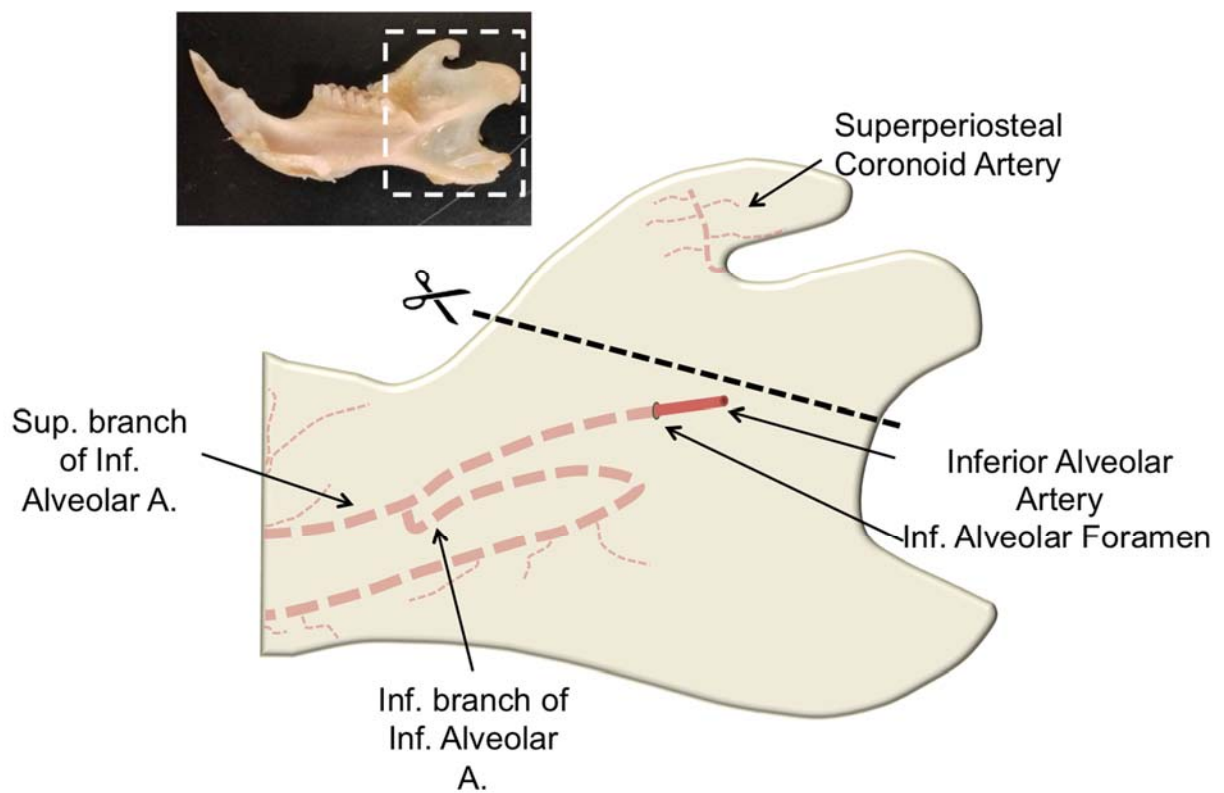
Figure 3.1. An adapted illustration (Huelke and Castelli, 1965) of key locations when preparing the hemimandible for biomechanical testing. Shown within the inset is a hemimandible.
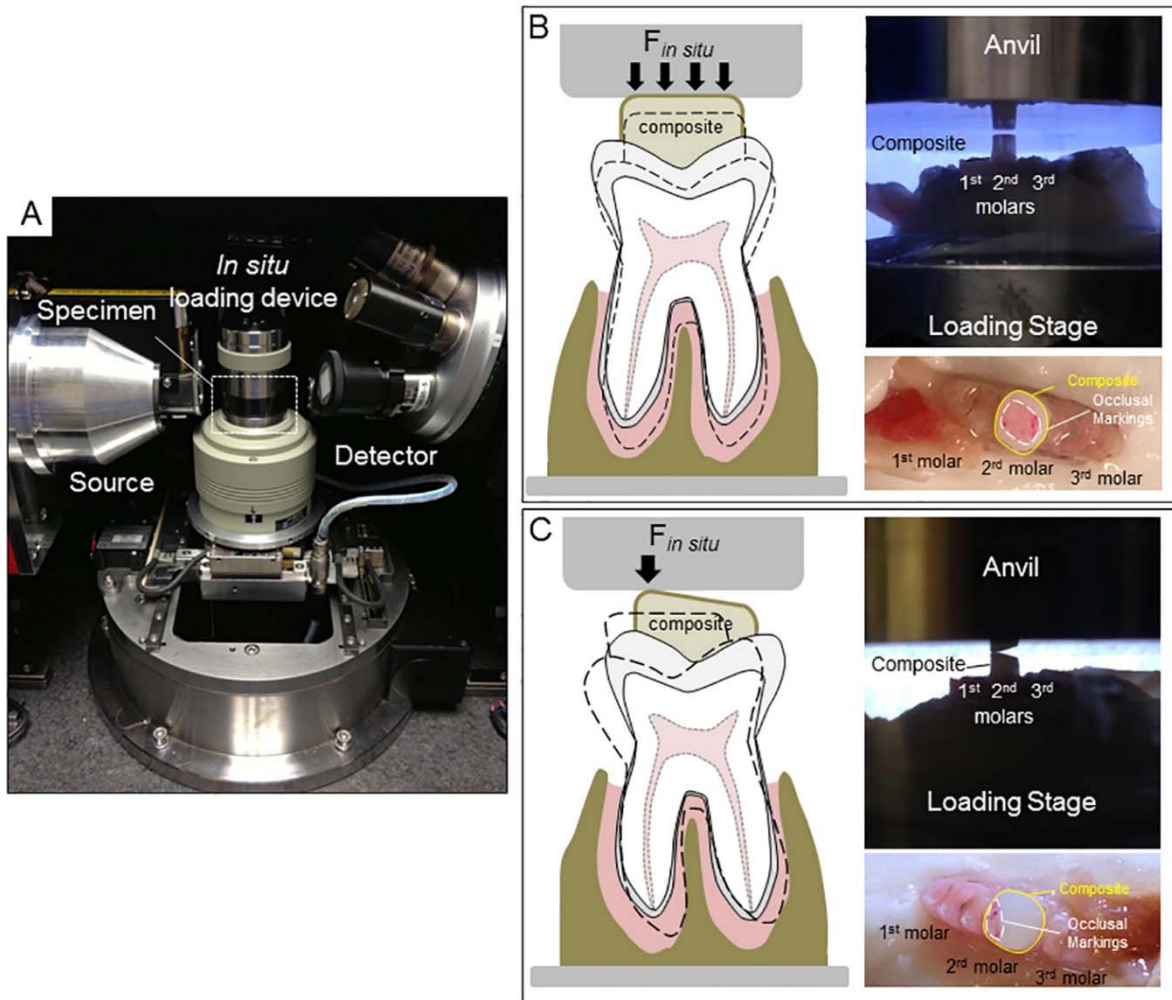
Figure 3.2. (a) An image of an *in situ* loading device on a custom holder within the micro-X-ray computed tomography (µ-XCT) unit. Concentric (b) and eccentric (c) loading conditions determined by the type of contact between the anvil and the composite surface are illustrated in the form of schematics, and the corresponding experimental setups (region corresponds to that highlighted by the white box in (a) respectively. Marks from articulating paper confirm initial contact area between the anvil and the dental composite.
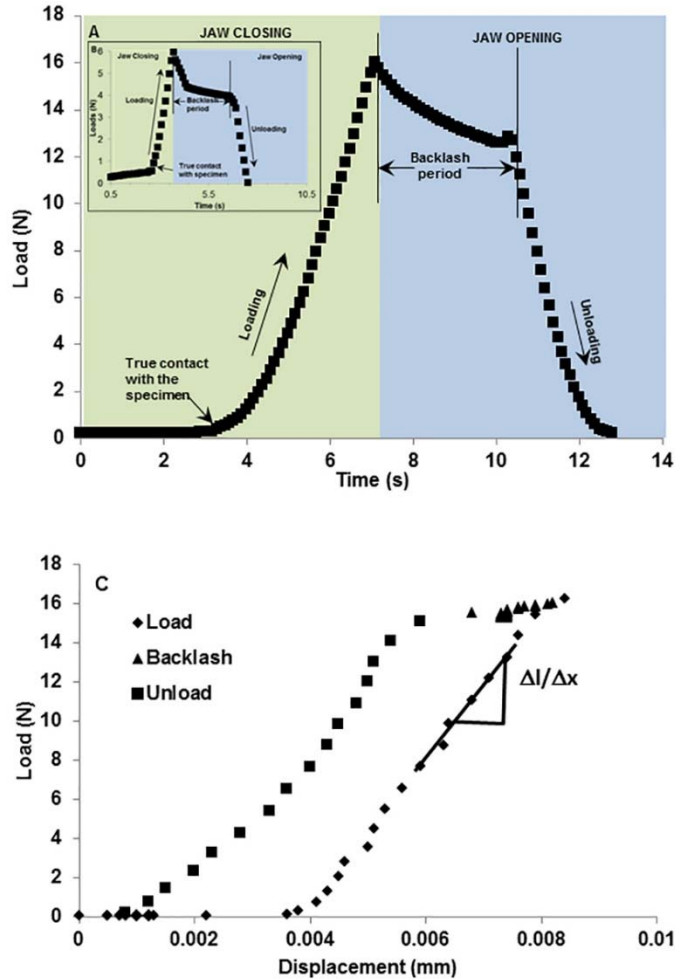
Figure 3.3. Representative load-time curve illustrating system "backlash". Load vs. time using a rigid body illustrates backlash period as an event between closing and opening of the anvils. The green region indicates loading period where anvils are approaching (green region) to load a rigid body to 15 N (a) and 5 N (b, inset). The blue region indicates an unloading period where the anvils are retracting from each other. However due to the lack of instantaneous motor response due to time taken by gear reversal, there lies a back lash period of ~3 sec. During this time the load decreases approximately by 2 N before true unloading occurs. Loading and unloading events can be related to load vs. displacement graphs (c) which shows minimal displacement during the backlash period.
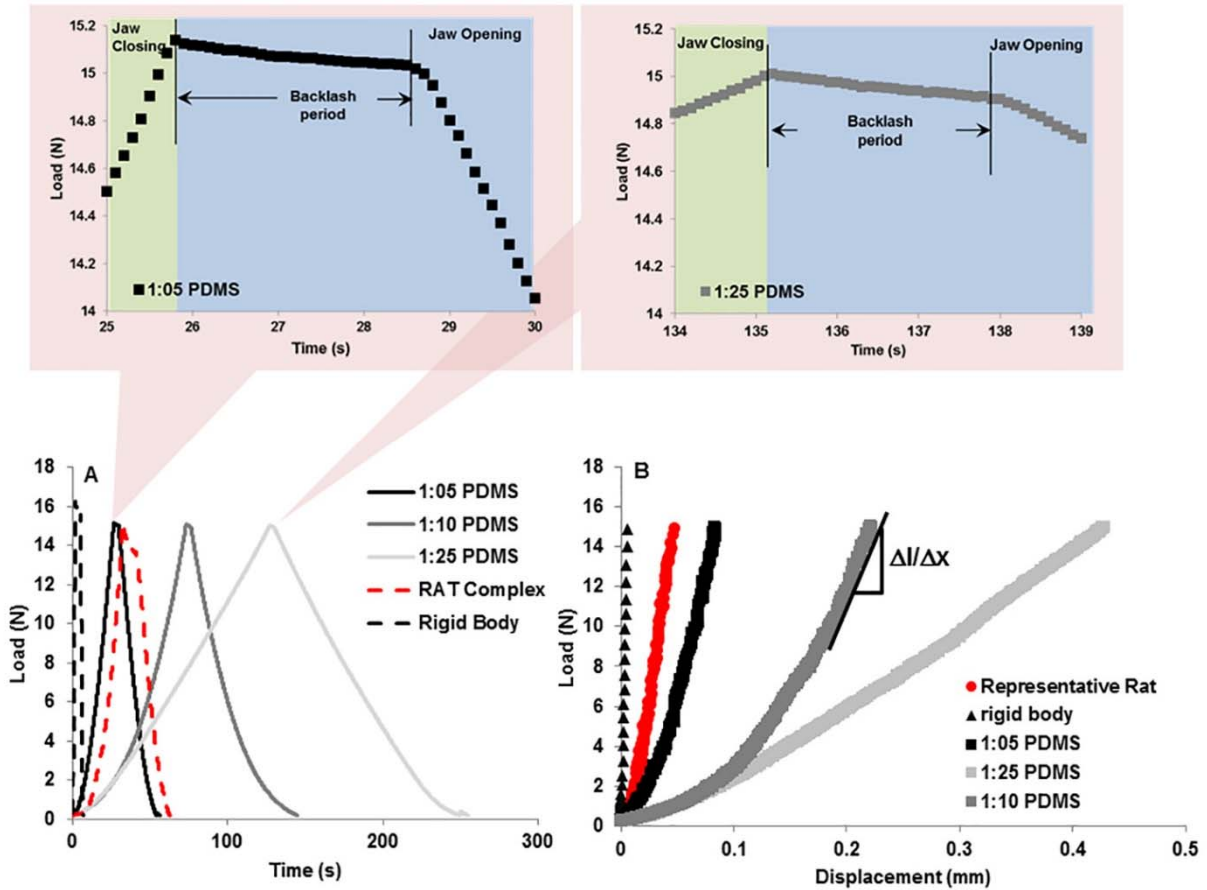
Figure 3.4. Representative load-displacement curves and "pushback" effect using PDMS. Bottom curves: Load-time relationships between PDMS of decreasing monomer to cross-linker ratios reveal the ability of the *in situ* loading unit to detect differences in material properties. Top curves, left and right illustrate the change in backlash of the system due to material recovery. The left and right when compared illustrate the same effect, indicating that the recovery difference between 1:25 and 1:05 PDMS is minimal or is not within the detection limits of the loading device. b) Load-displacement curves for varying materials including rigid body aluminum, experimental specimen, and the 3 PDMS specimens. It is the slope of the 30% linear part of the loading curve that was used to calculate stiffness of the material.
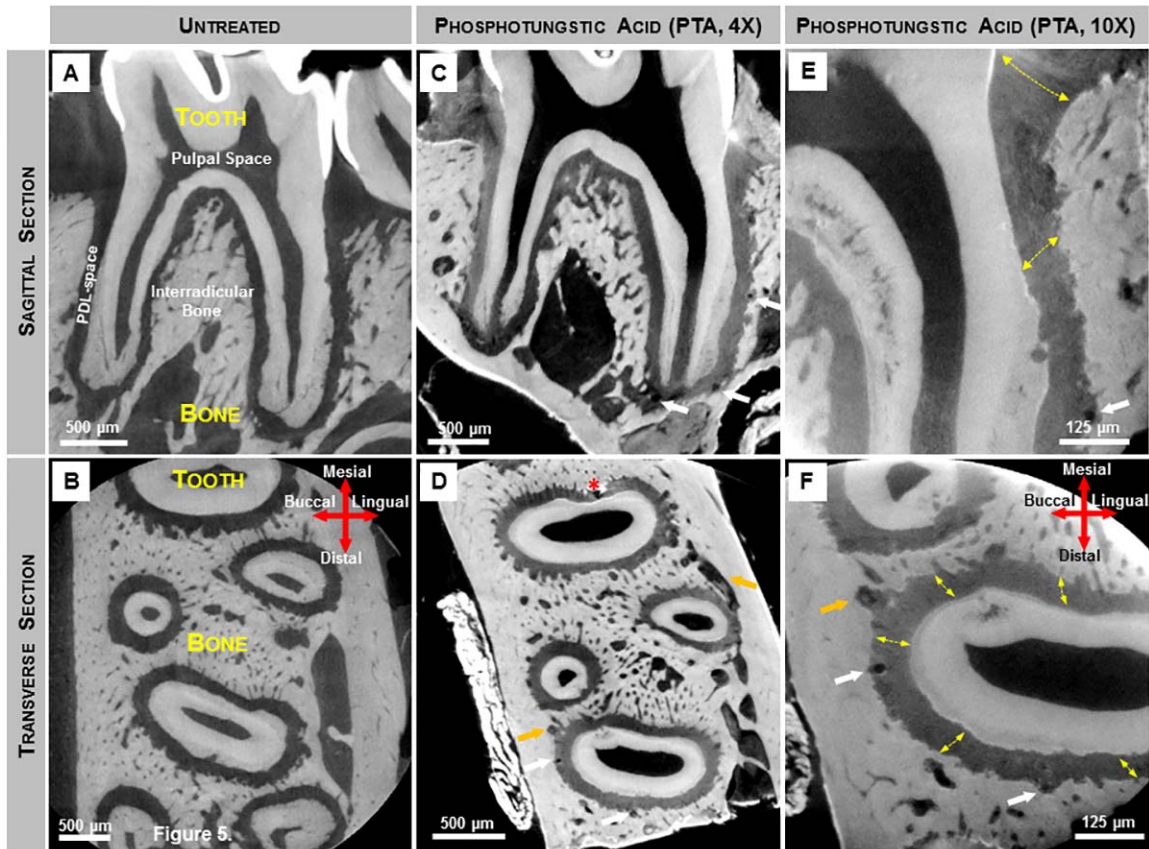
Figure 3.5. X-ray virtual sections of mandibular second molars stained for PDL structure enhancement. (a, b) Grey scale values within untreated molars indicate X-ray attenuation of various tissues including the softer regions within the complex. However, nonmineralized tissues such as PDL were not highlighted due to its minimal attenuating characteristics of X-ray energy at 75 kVp. (c-f) Following PTA staining the attenuating characteristics of the softer PDL were enhanced and details within the PDL were visualized using an X-ray microscopy. Thus, 2D virtual sagittal (c-4X magnification, e-10X magnification) and transverse (d-4X magnification, f-10X magnification) sections revealed PDL fiber orientation (yellow arrows). The lumen of blood vessels within endosteal spaces (orange arrows) and the PDL (white arrows) appear as dark circular structures, while the pulpal space remains unstained. Artifacts created during the staining procedure are also noted (d, red asterisks).
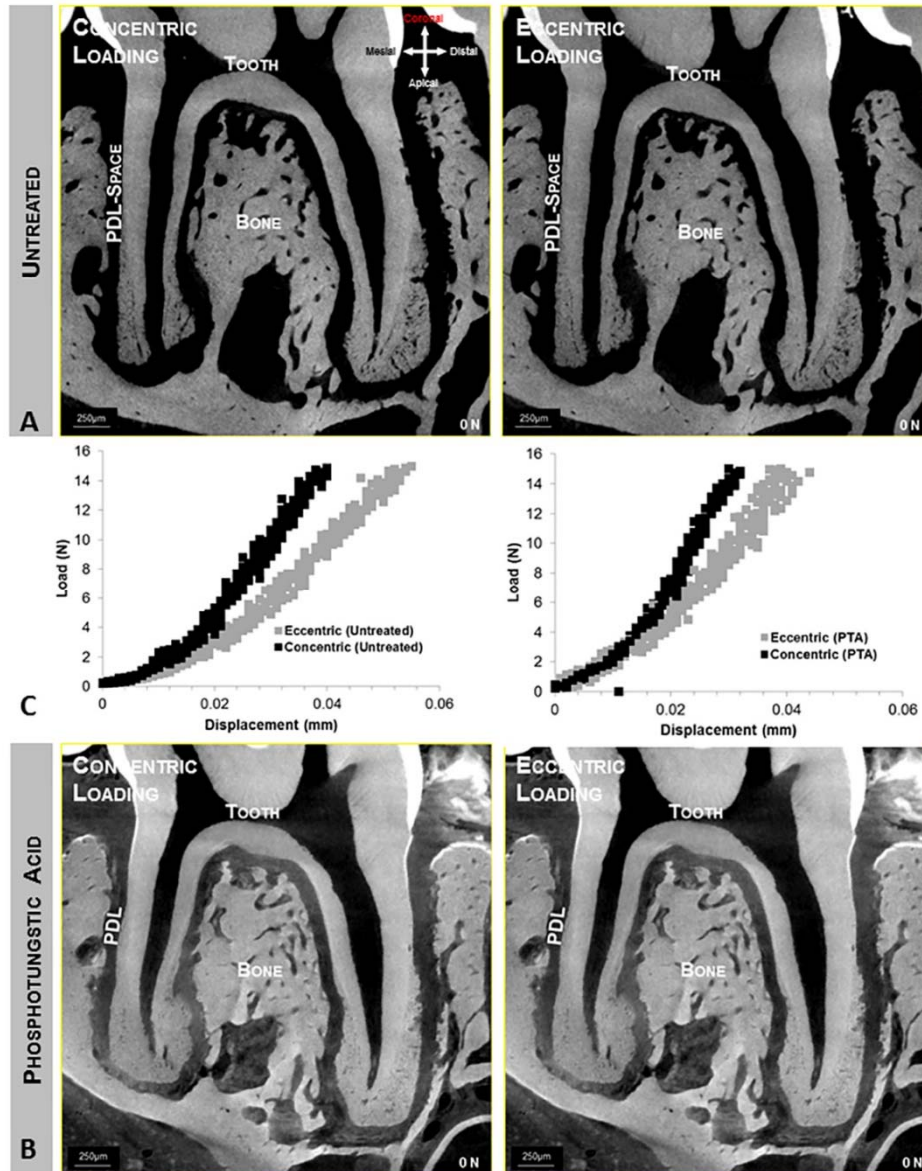
Figure 3.6. Concentrically and eccentrically loaded specimens. Top (a) and bottom panels (b) illustrate quick time movies of tooth-bone relationship at no load and when loaded to 15 N, concentrically and eccentrically respectively. Top and bottom panels illustrate bone-tooth association when untreated (a) and stained (b) conditions. Center panel (c) illustrates different load-displacement behaviors between eccentrically and concentrically (left curves) loaded complexes, and stained and unstained (right curves) complexes
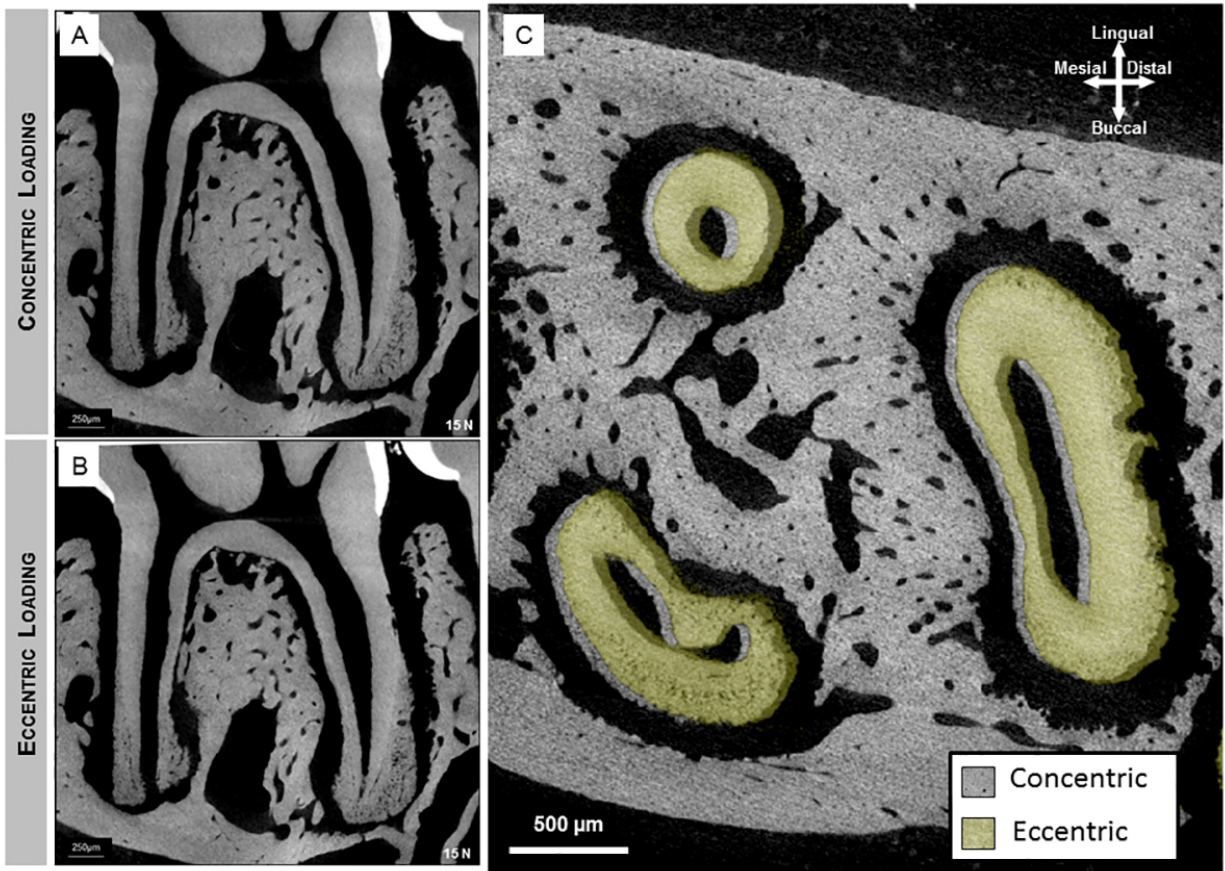
Figure 3.7. Sagittal section of 2nd molar illustrates the association of the tooth with the alveolar socket when loaded concentrically (a) and eccentrically (b). Majority of compression was seen within interradicular (arrow heads) and apical (arrows) regions. When compared to virtual sections of the tooth in eccentric loading (b), the additional rotational component of the tooth motion causes increased compression to the distal side of the mesial root. Overlaid transverse sections revealed distal translation and clockwise rotational movement of the tooth (green roots) relative to a concentrically loaded tooth (gray).
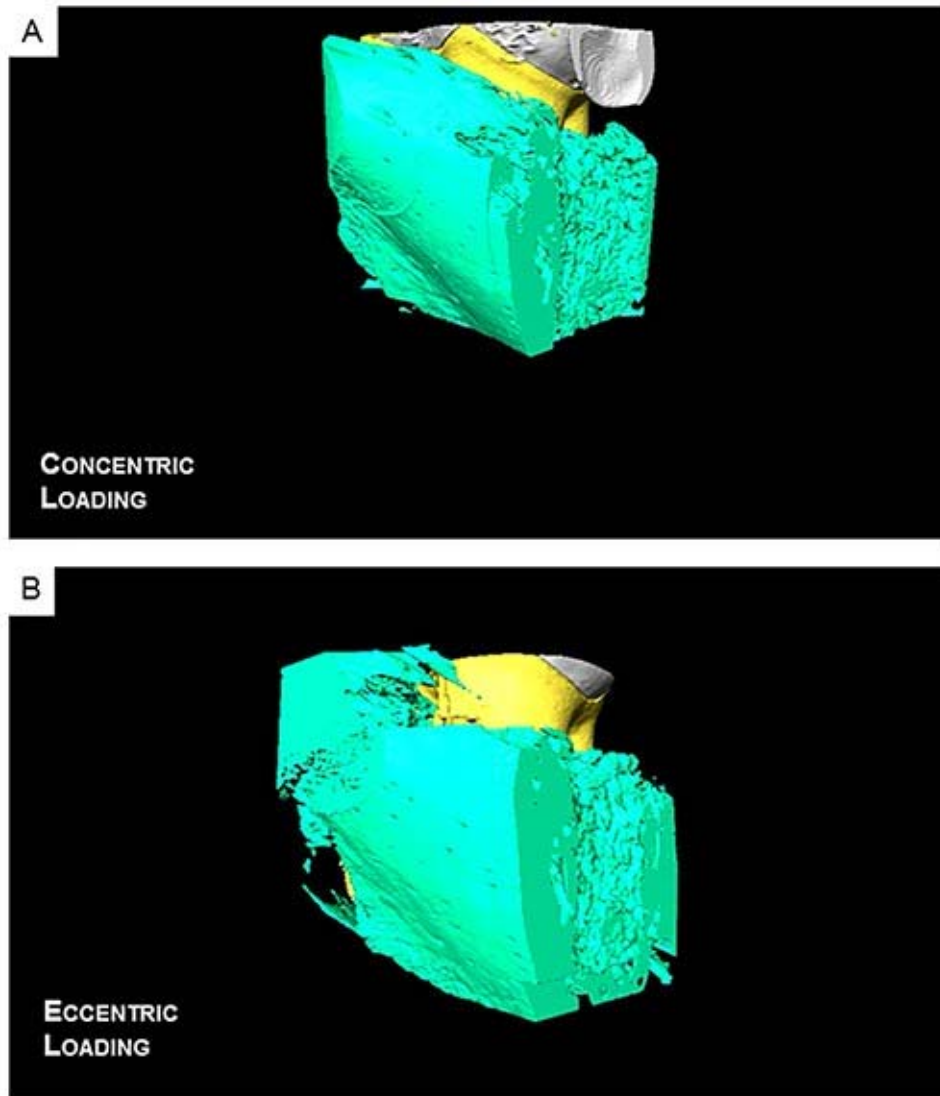
Figure 3.8. Reconstructed 3D movies reveal a decreased PDL-space within the distal side of the root when eccentrically loaded (a) compared to a concentrically loaded complex (b). Please refer to the publication website for movie files http://www.jove.com/video/51147/in-situ-compressive-loading-correlative-noninvasive-imaging-bone.

Property	Value
Objective magnification used	4x, 10x
Tomography projections	1,800 images
X-ray tube voltage	75 kVp (50 kVp for PTA stained samples)
X-ray tube power	8 W
Exposure Time	~8-25 seconds*
Voxel side length	~4 μm (4X objective),~2 μm (10X objective) **

* Exposure time can vary based on the geometry and optical density of the specimen and X-ray tube voltage.
** Actual pixel resolution will slightly differ based on the configuration of the source, specimen, and detector.

Table 3.1. Recommended μ-XCT Scanning Settings

CHAPTER 4. STRAIN MAPPING AND CORRELATIVE MICROSCOPY OF THE ALVEOLAR BONE IN A BONE-PDL-TOOTH FIBROUS JOINT

4.1 Abstract

Objectives: In this study, we will detail a method to calculate strains within interradicular alveolar bone by using digital volume correlation (DVC) on high resolution X-ray tomograms of intact bone-PDL-tooth fibrous joints. The effects of loading schemes (concentric and eccentric) and optical magnification on the resulting strain in alveolar bone, with the potential to correlate deformation gradients with information from other complementary techniques across length scales will be investigated. Strain maps will be correlated with structural and site-specific mechanical properties obtained from other imaging modalities that include atomic force microscopy (AFM) and AFM-based nanoindentation techniques on the same specimen.

Methods: Intact hemimandibles were harvested from male Sprague Dawley rats and biomechanical testing using an *in situ* load cell coupled to an XRM tomography unit was performed. X-ray tomograms were taken at no load and loaded conditions. DVC was used to calculate deformations within alveolar bone. Comparison of strain maps as a result of different loading schemes (concentric vs. eccentric) and at different magnifications (4X.vs.10X) were performed. Preprocessing methods to increase signal to noise ratio, and optimization of parameters for DVC were identified using a homogenous material such as polydimethylsiloxane (PDMS). Virtual sections from X-ray computed tomograms and strain maps from DVC solutions were aligned with topography data as obtained using an AFM, and reduced elastic modulus grid as determined by nanoindentation technique to correlate datasets of the same section within one specimen.

Results: Strain map of a concentrically loaded bone was different, however, illustrated similar ranges in strains when loaded eccentrically. Strain maps of homogenous materials (PDMS) resulting from DVC on tomograms at different magnifications were similar. However, the strain maps of heterogeneous materials at lower and higher magnification were different. Correlation of datasets produced a spatial alignment of strain space with structure, X-ray attenuation and site-specific elastic modulus values of similar region.

Significance: The DVC experimental mechanics technique illustrated a dependence of strain on optical magnification specifically for heterogeneous materials such as bone. The results at higher optical magnification highlight the potential for extracting deformation at higher spatial resolutions. Correlation of data spaces from different complementary techniques is plausible and could provide insights into processes that lead to functional adaptation, albeit differences in spatial resolutions of respective techniques.

4.2. Graphical abstract

a) Schematic of bone-tooth complex digitally reduced to illustrate tooth and alveolar bone configuration for *in situ* biomechanical testing. b) The furcation of the tooth saddles on interradicular bone and was identified as the region with the greatest reduction in functional space. c) The digital volume correlation (DVC) method was used to visualize differences in distributions of maximum normal strain within interradicular bone of rats adapted to hard and soft diets. d) From a multiscale perspective, changes in physical cues on organs resulting from the mechanical environment are transmitted through tissues to initiate biological responses in cells that over time can be related to biochemical processes leading to adaptations.

4.3.   Introduction

Digital volume correlation (DVC) is a powerful experimental mechanics technique that builds upon acquisition and processing of images from objects of various shapes and sizes.   Fundamentally, it is a 3D extrusion of a 2D technique known as digital image correlation (DIC) (Bay et al., 1999; Verhulp et al., 2004; Zauel et al., 2005; Hardisty and Whyne, 2009).   In principle, the DVC algorithm correlates identical features between images taken at no load to that taken at loaded conditions.   Deformations resulting from loads including mechanical and thermal loads are subsequently displayed as strains within volumes of materials (Bing et al., 2009).   DVC holds several advantages over other experimental mechanics techniques, as it can evaluate strain gradients within materials while preserving the architecture of the specimen.   Compared with the widely used finite element method, the advantage of using DVC is that it can accommodate any shape (geometry) or anisotropic configuration and does not require constitutive properties of materials to calculate deformations.   However, a hybrid of DVC and FEM (Evans and Holt, 2009) can leverage upon the advantages of the two techniques, thus providing accurate strains (DVC) and stresses (FEA) with limited assumptions about constitutive properties of heterogeneous and anisotropic materials (Evans and Holt, 2009).

DVC technique relies on feature tracking within images. As a result, DVC was used to measure deformations however, within smaller specimens reduced from organs (Bay et al., 1999).   DVC was applied after the specimens containing regions of interest were trimmed to a fundamental geometry, such as cubes or cuboids, and subsequently strains due to the action of uniform loads were evaluated.   Specifically, the arrangement and density of trabeculae within cancellous bone isolated from long bone and similar

68

structures have been proved ideal for the technique (Bay et al., 1999; Smith et al., 2002; Gillard et al., 2014). While these experiments succeeded in measuring deformation within a specimen reduced to a simple geometry, the effect of form induced strain within an "intact organ" can also be investigated with the current state-of-the-art technology. Hence, developments in technology have challenged the reductionist approach by performing biomechanics of intact organs using an *in situ* loading device coupled to an imaging microscope (Naveh et al., 2012a; Lin et al., 2013; Jang et al., 2014b). Advances in X-ray microscopy techniques have allowed for high resolution images (micron and submicron voxel size) of intact specimens at low and high magnifications thus maintaining structural/mechanical integrities of surrounding tissues, subsequently challenging the limits of DVC. Therefore, there is the ability to measure strain fields in tissues at relatively higher resolution and within the context of organ biomechanics without compromising the integrity of organ and its tissues (Scout-and-Zoom^{TM}).

As mentioned, digital correlation of volumes requires a minimum density of trackable features. The resolving power of strain (coarse or fine gradients) using DVC depends on density of trackable features which in turn are dependent on the magnification of the lens and resolving capacity of the detector in a microscope. Interfacing post-processing of acquired data from a nondestructive imaging modality such as X-ray microscopy with DVC, allows for strains gradients to be correlated with mineral densities gradients in volumes of tissues. Additionally, limited studies have attempted to preserve and investigate the effect of form-derived strain using DVC, which is a step away from the reductionist approach and closer to a holistic approach (Thompson, 1961).

Tissue mechanics in the realm of organ biomechanics can be evaluated through optical reduction approach as a result of decrease field of view at a higher magnification. Depending on the magnification, the strains due to loads can be derived from form and/or intrinsic properties of tissues from uncompromised organs/structures. Hence, optically reduced images can provide material-mediated strains thereby insights into local biological events and adaptive processes by which tissues change their form to accommodate organ function. The objectives of the study include: (1) to investigate the contribution of magnification on resulting strains within volumes of alveolar bone of the bone-PDL-tooth fibrous joint; (2) compare tissue strains evaluated at lower and higher magnifications (use of a holistic approach through Scout-and-Zoom™); (3) demonstrate an approach to correlate material-derived strain with physicochemical properties of materials using complementary analytical techniques on the same specimen. Prior to implementing DVC on biological specimens, optimization including noise calculation and validation of the technique will also be discussed.

4.4. Materials and methods

Flow chart provided in **Figure 4.1** highlights the following subsections. Calculations involving noise floor, parameter optimization for DVC, and validation of DVC (**Supplemental Fig. 4.1-4.4**) are provided as supplemental material. Subsequently, strains within volumes of PDMS and alveolar bone of the bone-PDL-tooth fibrous joint at various loading schemes are shown in **Supplemental Figures 4.S5-4.S8**.

4.4.1. X-ray imaging of a mechanically loaded bone-PDL-tooth fibrous joint

All animal experimental protocols followed the guidelines of the Institutional Animal Care and Use Committee (IACUC). Biomechanical testing was performed on intact hemi-

mandibles harvested from Sprague Dawley rats using *in situ* mechanical loading device coupled to an X-ray microscope (XRM) (MicroXCT-200, Carl Zeiss X-ray Microscopy, Pleasanton, California) (Lin et al., 2013; Jang et al., 2014b). Molars were loaded at a displacement rate of 1 mm/min to a peak reactionary load of 15N or 20N. Following compression of the specimen to a targeted peak load, the jaws of the loading cell were held stationary to allow for the internal structures to equilibrate. After reaching a steady state in load (~1 hr), the specimens were scanned at 4X and 10X magnifications (75KVp, 7 second exposure, 2000 projections). Tomograms were taken at no load (0N) and loaded (15N or 20N) states. For comparison, specimens were loaded and scanned at 4X magnification under concentric and eccentric conditions, and at 4X and 10X magnifications for concentric loading scheme only. Between each scan of the loaded state, specimens were unloaded and rehydrated for 45 minutes. The flowchart for pre- and post-image processing is show in **Figure 4.1** with each validated step described in detail within the supplemental information.

4.4.2. Post processing of X-ray scans prior to DVC calculations

Reconstructed tomograms were further processed to optimize parameters for accurate strain calculation. The order of data processing involved, increasing the signal to noise ratio by filtering data at no load and loaded conditions (anisotropic diffusion) (Perona and Malik, 1990) within Avizo (Avizo 8.1.0, FEI, Germany) to remove "salt and pepper" noise while preserving features to be recognized by the DVC software (**Fig. 4.1 and 4.S1a**); removal of spurious noise related to body movement (translation) through rigid body registration by using alveolar bone as a reference (**Fig. 4.1 and 4.S1b**), and cropping (no data) with regions of no interest masked (intensity value was set to zero)

prior to performing digital correlation (see supplemental materials). Finally, the tooth was digitally removed from the image space by using intensity segmentation method (**Fig. 4.1 and 4.S1c**) in Avizo.

4.4.3. Validation of DVC using polydimethylsiloxane with trackable features

Polydimethylsiloxane (PDMS) was used to validate DVC solution on data acquired using our imaging and processing methods (see supplemental information). PDMS (1:30 crosslinker/base ratio) specimens of known dimensions and mechanical properties were fabricated (**Fig. 4.2a**). Glass beads (50 µm in diameter) were added as trackable features within PDMS for DVC at no load and loaded conditions. The setup of the specimen within the *in situ* load cell is shown in **Figure 4.2a**. Tomograms of the PDMS specimen were taken at 0N (unloaded) and at 5N (loaded) and were digitally correlated to solve for deformation (DaVis, LaVision). Strains were calculated as a differential of the displacement vectors.

4.4.4. Site-specific mechanical property determination by using AFM-based nanoindentation technique

Modulus mapping was performed by using AFM-based nanoindentation under wet conditions as previously described (1000 µN) (Ho et al., 2004) to calculate reduced elastic modulus (E_r) (Oliver and Pharr, 1992). Nanoindents were spaced at 5 ☐m in parallel rows to form a 200 µm x 75 µm grid on the region of interest. Topography images from the nanoindenter under wet conditions were also taken to assist with data space correlation.

4.4.5. Visualization of strain maps and correlation with physical and chemical properties

Strain maps produced through DVC were imported and visualized using Avizo image analysis software. Data correlation from multiple techniques on the same specimen was accomplished by registering across different data spaces as acquired using different techniques. The light microscope image was used as a reference to register topography obtained from AFM and the virtual section obtained from X-ray tomography. The landmarks as identified in the region of interest were used to overlap data spaces across analytical techniques, Image registration algorithms and data extraction was done using a custom code written in MATLAB. Line profiles of all data spaces were extracted and compared.

4.5. Results

4.5.1. Digital volume correlation of a concentric and eccentrically loaded bone-PDL-tooth joint

The strains within PDMS were uniform and as expected. PDMS illustrated similar ranges in strain at 2X and 4X (**Fig. 4.2**). *In situ* loading of a joint either concentrically or eccentrically produced different configurations of the tooth relative to the alveolar socket (**Fig. 4.3a and 4.3b**), and changes in the distribution of strain. Specifically noted is the additive effect of the eccentrically loaded tooth that illustrated higher deformations within the interradicular, apical, and interdental regions of the alveolar bone (**Fig. 4.3c-f, Fig. 4.S7**).

4.5.2. Effects of magnification on strain calculations

Comparisons of DVC calculated strain distributions from images taken at magnifications of 4X (**Fig. 4.4a**) and 10X (**Fig. 4.4b**) are shown. Respective to the 4X solution, the 10X solution had similar strain gradients (i.e. fulcrum has higher strain values

compared to internal bone regions). However, slight discrepancies in strain within the same region do exist between the two magnifications as seen from the (**Fig. 4.4a and b**) volumetric strain distributions (**Fig. 4.4c-d and 4.S8**).

4.5.3. Correlative techniques between nanoindentation and DVC

Light microscopy images and equivalent virtual sections from XRM/strain space are shown in **Figure 4.5a**. The region used for modulus mapping is seen in **Figure 4.5b** with equivalent regions being shown for X-ray microscopy, AFM topography image, nanoindentation, and DVC solutions which are all aligned (**Fig. 4.5b**). The graph in **Figure 4.5c** highlights the correlation which can be done by sampling data from the same location across each of the aligned data spaces (arrows spanning each plane) allowing for relationships to be drawn across different microscopy techniques.

4.6. Discussion

While the use of DVC to analyze deformations within specific tissues is not novel, the methods outlined within attempt to push the boundaries of correlative microscopy and biomechanical testing demonstrating: (1) an influence of magnification on the digital volume correlation solution, (2) the ability to detect changes in strain distribution resulting from different loading schemes, and (3) a workflow to directly correlate results from different imaging modalities. Results within this study illustrate a new approach to analyze multiple techniques in tandem to provide direct relationships between mechanical stimulation and the biological response.

The computational background surrounding DVC calculations has been described and verified in previous publications (Bay et al., 1999; Gillard et al., 2014). From an applications perspective, the fundamental principle surrounding DVC calculations

involves breaking the image into smaller segments identified as interrogation windows and tracking features within each window relative to no load conditions. Therefore, care must be taken prior to running the DVC algorithm to maximize the signal to noise ratio for each image since noise can be misinterpreted as a "feature" when calculating displacement and subsequently strain. Additionally, the threshold to adjust interrogation window size is based on minimum number of features (about 3). Since the number of "quality features" is based on the imaging modality and magnification (and in part the distribution of detectable features within a specimen) the resolution threshold limit is a variable and can be high. Considering the fundamental basis of DVC calculations, several image processing techniques were used to enhance the signal to noise ratio of the image to reduce the probability of the DVC software using noise when calculating deformations within volumes of tissues. Since the signal to noise ratio is enhanced by increasing real feature detection and decreasing random noise, anisotropic diffusion was used as it preserved the edges of features while eliminating the random (i.e. salt and pepper) noise (**Fig. 4.S1a**) (Perona and Malik, 1990). The second step involved finding an appropriate interrogation window size to define the accuracy of strains. The resulting strains in tissues are crucial for providing insights to relevant biological output while maintaining accuracy within the calculations and can be linked to strain-adaptive nature of load bearing tissues. Increasing the number of interrogation windows will increase the ability of DVC solution to resolve gradients, however choosing a small interrogation window will decrease the density of trackable features specifically at a lower magnification thereby decreasing the accuracy of the solution. Additionally, the overlap between interrogation windows may also be adjusted to increase the spatial resolution of the DVC

solution. Previous authors have used a 50% overlap (Gillard et al., 2014; Du et al., 2015).

It should be noted that even though an increase in overlap can increase the spatial

resolution of strain solution, amount of additional information gained by increasing the

overlap beyond 50% is questionable as the interrogation window would become

significantly larger than the gauge length.

Within the described workflow, the primary sources of noise within the image are

generated during acquisition and reconstruction. Therefore, the first objective of using

PDMS was to provide a fundamental and straight forward system to test the noise floor

which otherwise will lead to erroneous strains not necessarily due to deformation of the

specimen. This noise tends to be particularly high in images with low signal to noise

ratios. As it is a common practice with DVC, noise floor calculation within a setup are

done by taking identical consecutive scans and performing the strain calculations

(Verhulp et al., 2004; Gillard et al., 2014). In this particular study, using PDMS and the

apparatus as discussed in materials and methods, the strain calculations is about 0.1%

which was significantly lower than the strain measured from compression (3-4%) (**Fig.**

4.S3b). After comparing noise floor calculations at several interrogation window sizes,

64x64x64 voxel window with a 50% overlap was chosen as an optimal size as it gave the

best balance between a low noise floor and a high spatial resolution. However, it should

be noted that the noise floor and optimal window size will depend on the imaging

conditions as well as the density of features within a specimen. For example, the

conditions that appear to be accurate for PDMS need not be the same conditions for

bone. Therefore, a separate plot for interrogation window size and noise floor was

generated at different magnifications of alveolar bone (4X and 10X) and was compared to PDMS (**Fig. 4.S3**).

Additionally, the minimum fraction of valid pixel (mfvp) is another influential parameter which must be predefined within the DVC software when processing masked images. The primary concern about having a mfvp <100% is that the points for which the gauge length may not be representative of the true center of the interrogation window. This would lead to inaccuracies in gauge length and strain calculations. In future, an adaptive interrogation windows mapping feature to help overcome these shortcomings is necessary. Ideally all interrogation windows would be placed within regions that do not include masked regions (i.e. mfvp = 100%). However, due to the complex geometry of some specimens such as those identified in this study, excluding regions with mfvp < 100% would result in the significant loss of data. In this study, several different mfvp values were tested and it was found that 25% returned the best balance between data confidence and data loss (Du et al., 2015).

Validation was performed by verifying DVC solution against an FEA solution. Using PDMS geometry and its deformation state as the boundary conditions, a similar range and distribution of strains were seen within the specimen (**Fig. 4.S3**). While FEA is generally accepted to verify DVC, it is only effective where deformations are described. The applications of DVC to "intact" bone-PDL-tooth space allows for a more realistic effect of load types (eccentric vs. concentric) while accounting for joint morphology. In this study, the effect of load type in an intact joint is demonstrated by comparing strains produced by a concentric with an eccentric loading scheme, however loaded to the same magnitude (**Fig. 4.3a**). Despite identical magnitudes, a difference in strains within bone

was registered in joints loaded eccentrically and concentrically (**Fig. 4.3b**). However, an emphasis on the accuracy of the results as perceived by the DVC technique was demonstrated through optimization of parameters specifically accounting for minimum valid pixel (**Fig. 4.3c-f and 4.S7**). The results underline the capacity of the DVC software to test different loading states and to be able to accurately study the maps should clinically relevant scenarios be investigated.

Results produced in this study were not limited to strain maps. Considering the deformation calculated by DVC, the calculated strain is divided into two different types: form-derived deformation and material-derived deformation. Both types of deformation are coupled when calculating strains. While the pattern is accurate, the relative differences in strains could be dependent on magnification at which the specimens were scanned and in turn the hierarchical level being considered within the holistic approach sought in this study. It is difficult to decouple form- and material property-derived deformations from a single calculation. Using a higher or lower objective magnification can shift the influence bias of the DVC calculations towards form-derived strain (lower magnification) or material-derived strain (higher magnification). It is important to recognize that within a particular specimen if the size of the trackable features is the same at various magnifications; it is likely that form-derived strain will be same as material-property derived strain. In the likelihood that this will not be the case, which is what it is most of the time, it is conceivable for strains to be not the same within regions of interest at different magnifications. The two specimens that were tested (PDMS and alveolar bone) showcase examples of specimens which are homogenous and has a low hierarchical organization (PDMS) compared to alveolar bone, which has multiple

hierarchal organizational levels and may be only detectable at certain magnifications. Because differences in trackable features are dependent on magnification from the perspective of DVC, it is possible to see differences in strain calculations due to differences in size and quantity of trackable features at a magnification in alveolar bone (**Fig. 4.4**) vs. PDMS for which the DVC solutions were similar (**Fig. 4.2b and c**). The primary reason for the magnification-dependent differences in calculated strain fundamentally originates from the increased capacity of the higher magnification objective to detect smaller features (i.e. 10X magnification can resolve osteocyte lacunae effectively than 4x) within a particular bony structure. This differs from a lower magnification objective which can only detect and utilize the macroscopic structure of bone for strain calculations. In an ideal case, even higher magnification system would be preferred to highlight material-derived strain (e.g. 20x or 40x), which can be done by reducing the specimen to increase the signal to noise ratio for a reliable DVC. Imaging at a higher magnification would allow direct alignment of data from tissue strain to biological effectors (e.g. tissue material properties, biochemical factors, and mineral density) into a unified coordinate system in ways that questions related to mechanobiology (**Fig. 4.5**) can be investigated. However, it is important to recognize these limitations in both imaging resolution and resolving power from post analysis such that the observed results are not misinterpreted (Zebaze and Seeman, 2015).

Resolving power is critical as it also plays a primary role when correlating data spaces across a variety of microscopy techniques. First, landmark registration method used to register the data requires the user to input several equivalent points between the data sets with a higher level of precision. In the case of bone, internal endosteal

morphology and the lacunae were used as landmarks. Second, when performing

correlation between several different techniques, the spatial resolution and sampling

involved in each technique must be considered. While having matching resolutions will

increase the integrity of the correlation, it is challenge to match the resolution of two

fundamentally different sampling methods (e.g. indentation vs X-ray imaging). Under

such circumstances, interpolation was used to assist in the matching of data spaces. This

approach highlights the capacity to underline the extension of state-of-the-art technology

on the same specimen and be able to map mechanistic processes by characterizing the

same specimen, however, using multiple complementary techniques. Additionally,

hierarchical considerations must be made when correlating data across different

magnification levels (**Fig. 4.6**). The DVC and correlation techniques presented in this

study allow a holistic approach to analyze and compare macroscopic biomechanics to

tissue level strains and biological effectors. However as was mentioned previously, the

magnification plays an important role in the separating material derived strain and must

be considered when interpreting results. Reiterating, results from this study provide

insights however with a hint of caution. This implies that when making inferences

concerning the effects of therapy (physical and/or pharmacological) on an organ or tissue,

caution should be warranted, in that the interpretation of results is limited to image

resolution (Zebaze and Seeman, 2015).

It was difficult map strain at a higher resolution while maintaining the hierarchical

integrity of the joint and the overall biomechanical loading scheme using the current state-

of-the-art X-ray bench-top technology. Sources of this limitation include a cap on

detectable speckle features, capacity of the optics to capture finer details in the

mineralized tissues without reducing the specimens and keeping the organ intact (most organs that are derived from mice – a commonly used animal model are small and can fit within the field of view of the latest x-ray microscopes), and parameters in the algorithms of the software used that have limited capacity to exploit detailed information despite its existence. This is a limitation of the current MicroXCT-200 that was used for the experiments described in this study and this limitation can be met with a higher flux capacity, optics and an equivalent detector with a higher spatial resolution. While the focus of the paper draws out the importance of using *in situ* loading schemes, current state-of-the-art dictates that both holistic and reduction approaches should be accounted for in order to couple organ-level biomechanics with tissue-level mechanobiological processes.

4.7.   Conclusions

In conclusion, deformation maps produced through DVC are influenced by the background noise resulting from instrumentation and experimental technique. Background noise reduction from instrumentation can be minimized by using physical filters during scanning and digital filters during post-processing of acquired images. Additionally, appropriate parameters for the DVC calculations (interrogation window size, window overlap, gage length, minimum fraction of valid pixel) should be optimized to increase the signal to noise ratio (Gillard et al., 2014).

DVC in tandem with higher resolution microscopy presents as a powerful tool for measuring strain within organs and related biological tissues. The mapped strains should be considered against calculated background noise through successive scans which is necessary for extrapolation of meaningful results from solutions. Results from DVC

solutions provide insights into form-derived and material-derived strains. The ratio of magnification used for imaging to feature density is key for differentiating form-derived strain from material-derived strain. Furthermore, through the correlation of DVC strains to complementary datasets such as histology or local material properties, a greater understanding of the mechanistic processes linking organ-level biomechanics to tissue-level mechanobiology can be drawn.

4.8. Supplemental Information

4.8.1. Image processing of scans prior to DVC calculations

After reconstruction of the tomograms, 3D images were further processed to optimize the strain calculation accuracy by filtering, rigid body registration, cropping, and masking. XRM tomograms were initially filtered using an anisotropic diffusion algorithm within Avizo (Avizo 8.1.0, FEI, Germany) to remove 'salt and pepper' noise while preserving features recognized by the DVC software (**Fig. 4.S1a**). Next, the scans of loaded and unloaded configurations were aligned using a rigid body registration (Avizo) using the internal alveolar bone to track the majority of the rigid body movement (**Fig. 4.S1b**). While rigid registration allows for easy visualization of internal deformation of an object, it is technically not necessary for strain calculation. Some specimens, such as PDMS, did not have reliable regions to perform rigid registration and therefore were not registered. Cropping was done to focus on particular regions and remove extraneous regions that would cause unnecessary noise (such as the beam hardening of the anvil). Finally, the tooth was removed digitally by masking away the regions of tooth structure (Which produced a significant amount of noise within the DVC solution) from the image space by using an intensity segmentation method (**Fig. 4.S1c**) with effects of masking on

strain shown in **Figure 4.S2**. This step differs from cropping (i.e. reducing the image's field of view) which is done to optimize computational time or exclude imaging artifacts.

4.8.2. Validation of DVC system using standard materials and recognizing potential sources of noise for DVC calculations

Prior to the *in situ* loading of animal specimens, a standard material was used to validate the DVC capabilities of our imaging acquisition and image processing methodologies.   PDMS specimens were fabricated with known dimensions and mechanical properties (1:30 crosslinker/base density) (**Fig. 4.2a**).   A high density of internal features was added to the PDMS through the embedding of small glass beads (50 μm diameter) within the material prior to curing. The setup of the specimen within the *in situ* load cell is shown in **Figure 4.2a**.

Results from unconfined compression of PDMS are shown in **Figure 4.2 and Figure 4.S4**. Strain values within PDMS at 2x and 4x (**Fig. 4.2b and c**) were comparable in magnitude (volumetric strain found in **Fig. 4.S6**). To further validate these solutions at different magnifications, maximum normal strains were compared with strains calculated using finite element method, and were found to be similar in magnitude and distribution (**Fig. 4.S4b and 4.S4c**).

Since the noise within the image (e.g. salt and pepper noise) and imaging artifacts may be misconstrued as deformable features, the first step was to calculate the background noise from the imaging setup (also referred to as "strain resolution" (Gillard et al., 2014)). This was done by taking consecutive scans of the specimen within the *in situ* load cell were taken and processed for strain. The interrogation volume for the DVC calculations were modulated until the background calculated strain was significantly

smaller than the calculated strain (>10% of the calculated strain resulting from *in situ* loading). Similar testing schemes for background noise was also performed on the alveolar bone of rats (**Fig. 4.S3**). Following consecutive scanning of the specimen within the load cell, the tomographies were treated with the same preprocessing methods used for *in situ* loaded strain calculations (see section 4.9.1). Optimum parameters for DVC calculation were determined by mapping strains using interrogation volumes from 16 x 16 x 16 pixels^3 to 256 x 256 x 256 pixels^3 with a 12%-87% (**Fig. 4.S3a and 4.S3b**) overlap for both 4X and 10X magnifications, respectively (**Fig. 4.S3c**). Because the data sets analyzed included masked regions, the minimum fraction of valid pixel (mfvp) was also toggled to find the best balance between data loss and solution confidence (Du et al., 2015).

Based on the testing of different permutations of overlap, interrogation window size, and mfvp (Du et al., 2015), the appropriate settings for alveolar bone at 10x and 4x (verified separately) are 50% overlap, 64 pixel interrogation window size, and 25% mfvp. Prior to loading within the DVC software, all images were filtered, registered, cropped, and masked (except for PDMS, in which only cropping and masking were done).

4.9. Figures
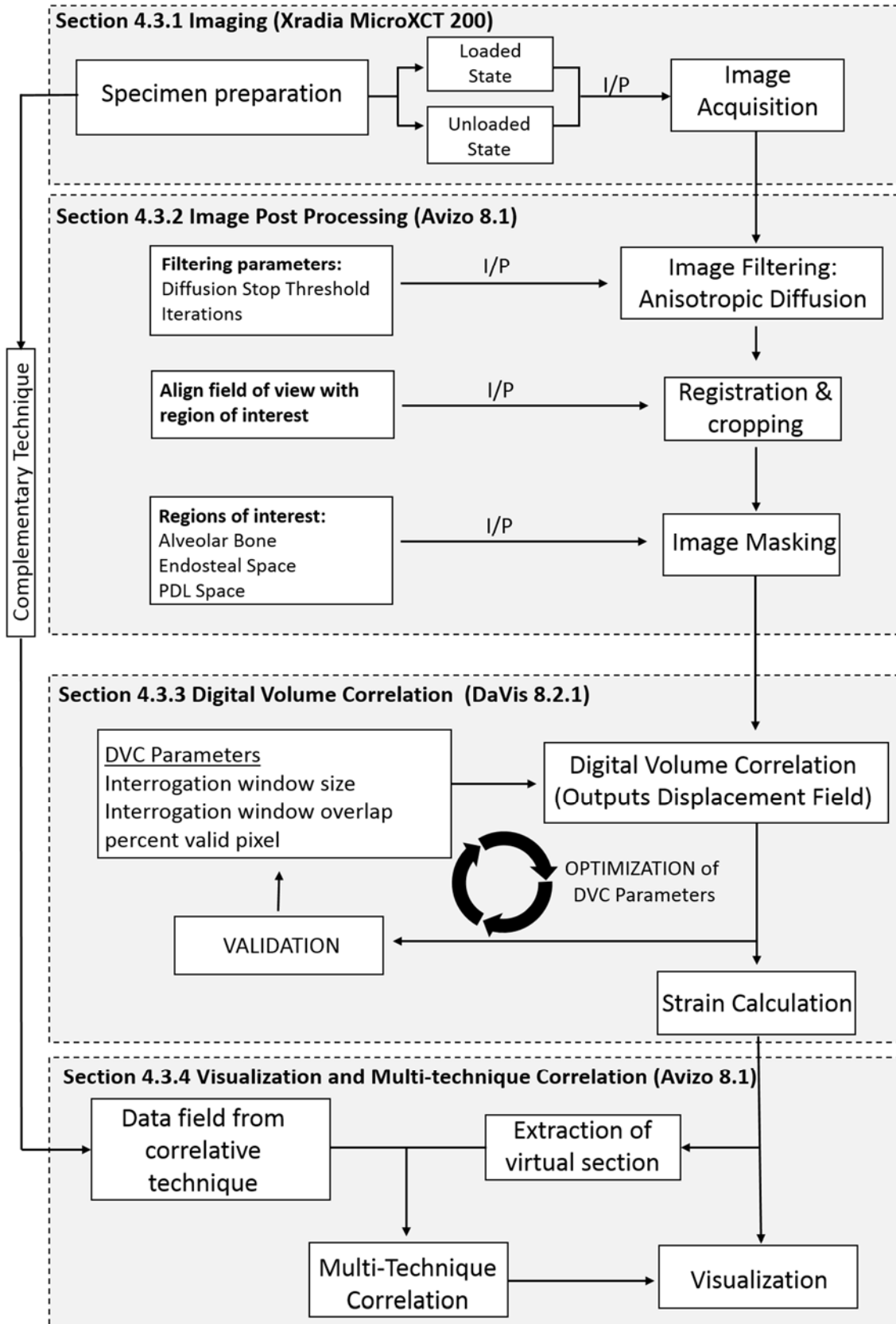
Figure 4.1. Flowchart of a workflow for digital volume correlation (DVC) includes specimen scanning using X-rays to acquire data (first block), post process the acquired data (second block) followed by digital correlation of the post-processed tomograms acquired at no load with loaded conditions (third block). The bottom block in the flow chart represents further correlation of processed data with other high resolution analytical techniques.
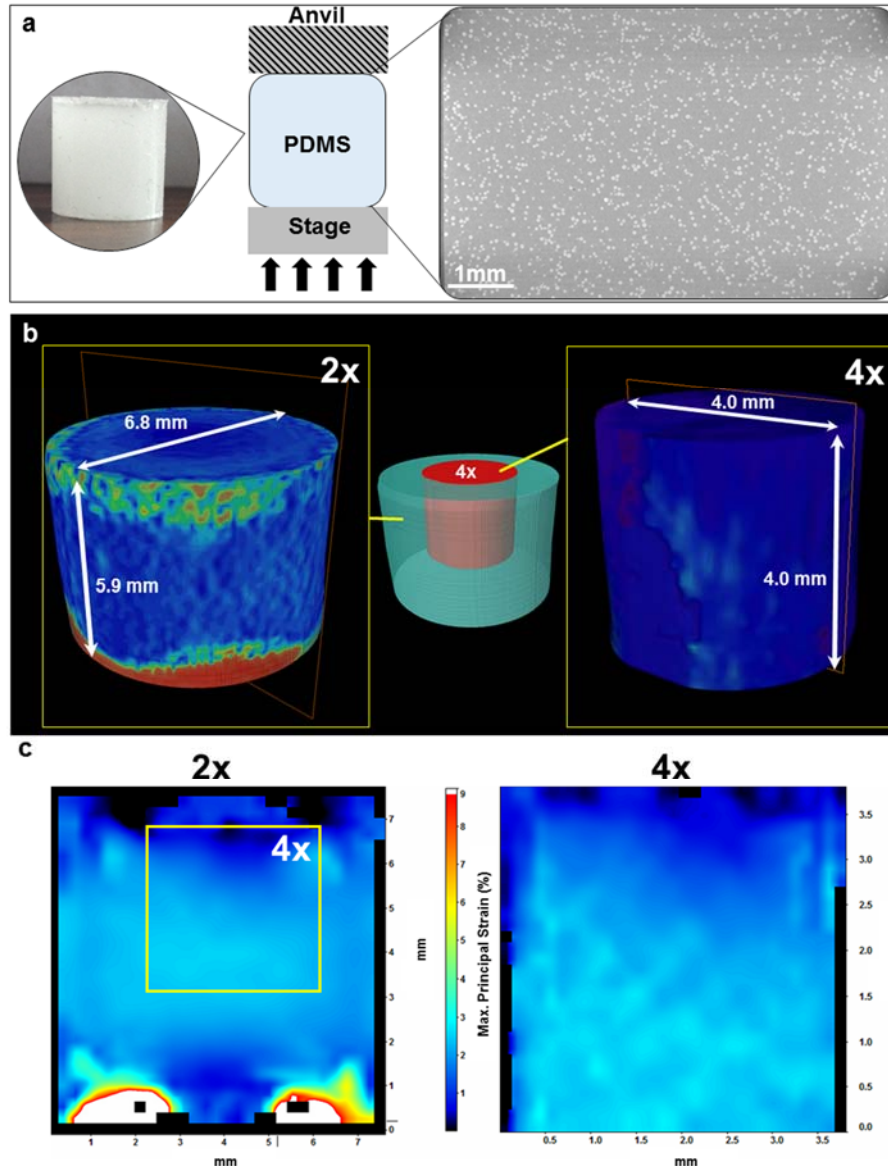
Figure 4.2. Illustration of DVC method using a PDMS cylinder a) with glass beads as trackable features within the specimen is shown. b) Maximum principal strain in volumes of PDMS at 2x and 4x magnifications illustrate regions from where 2D strain maps (c) were extracted. Strains were calculated using an interrogative window size of 64 pixels with a 50% overlap resulting in a gage length of 64 pixels and mapped using a minimum valid pixel threshold of 25%. Black boarders within 2D images are the result of regions in interrogation windows not calculated due to insufficient number of minimum fraction of valid voxels for accurate strain representation.
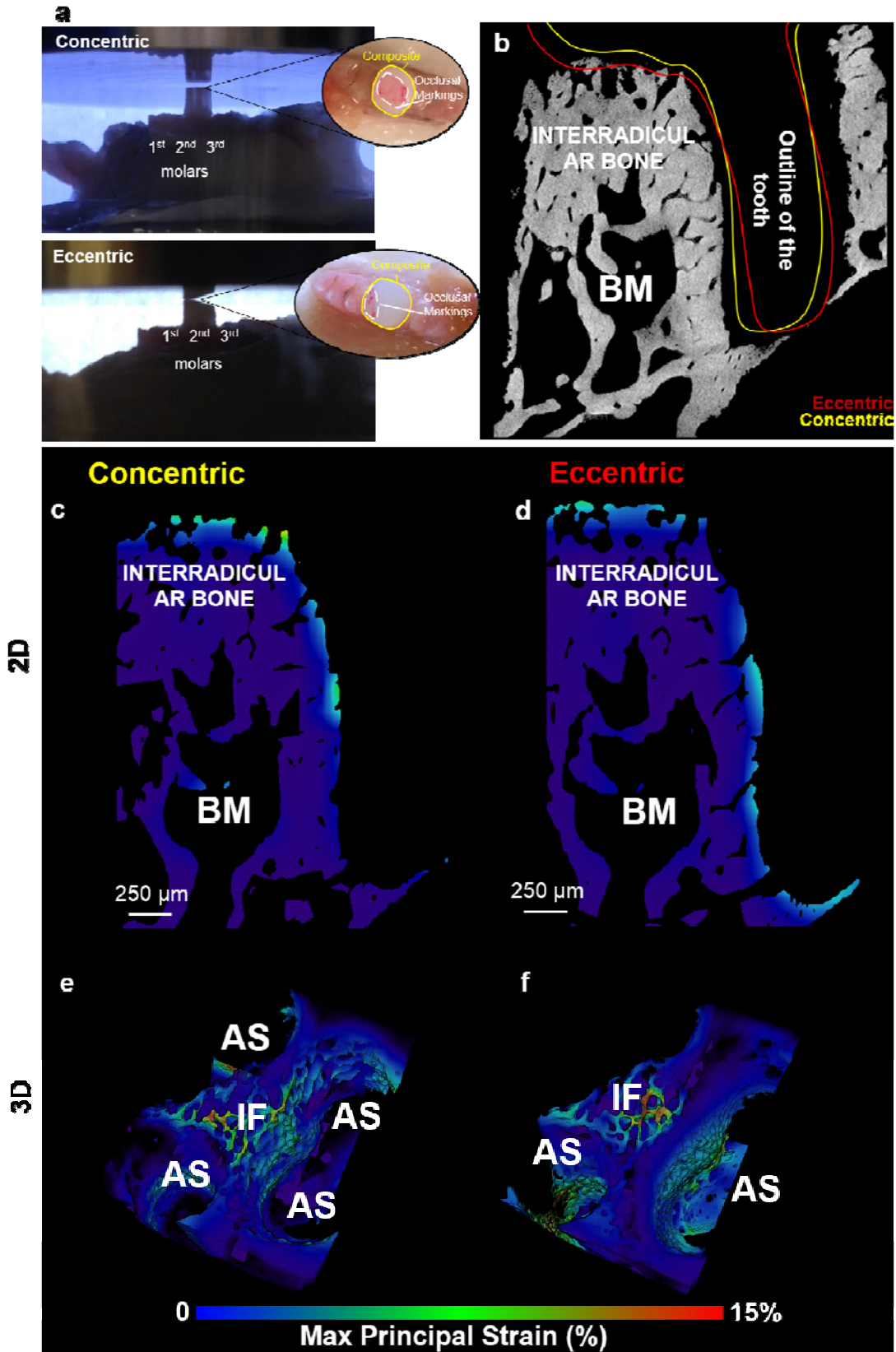
Figure 4.3. A change in loading scheme as denoted by the contact areas (a) is registered as a change in position of the tooth relative to the alveolar socket (b) and strain within bone (c –f). Strains within a section of an alveolar bone consisting bone marrow (BM) space are shown in the top panel (c and d). Strains within volumes of alveolar bone are concentrated at the interradicular fulcrum (IF) and subsurface regions of the alveolar socket (AS) surface (e and f). An interrogation window size of 64 pixels with a 50% overlap resulting in a gauge length of 64 pixels and 25% of minimum fraction of valid voxel were used for strain calculations
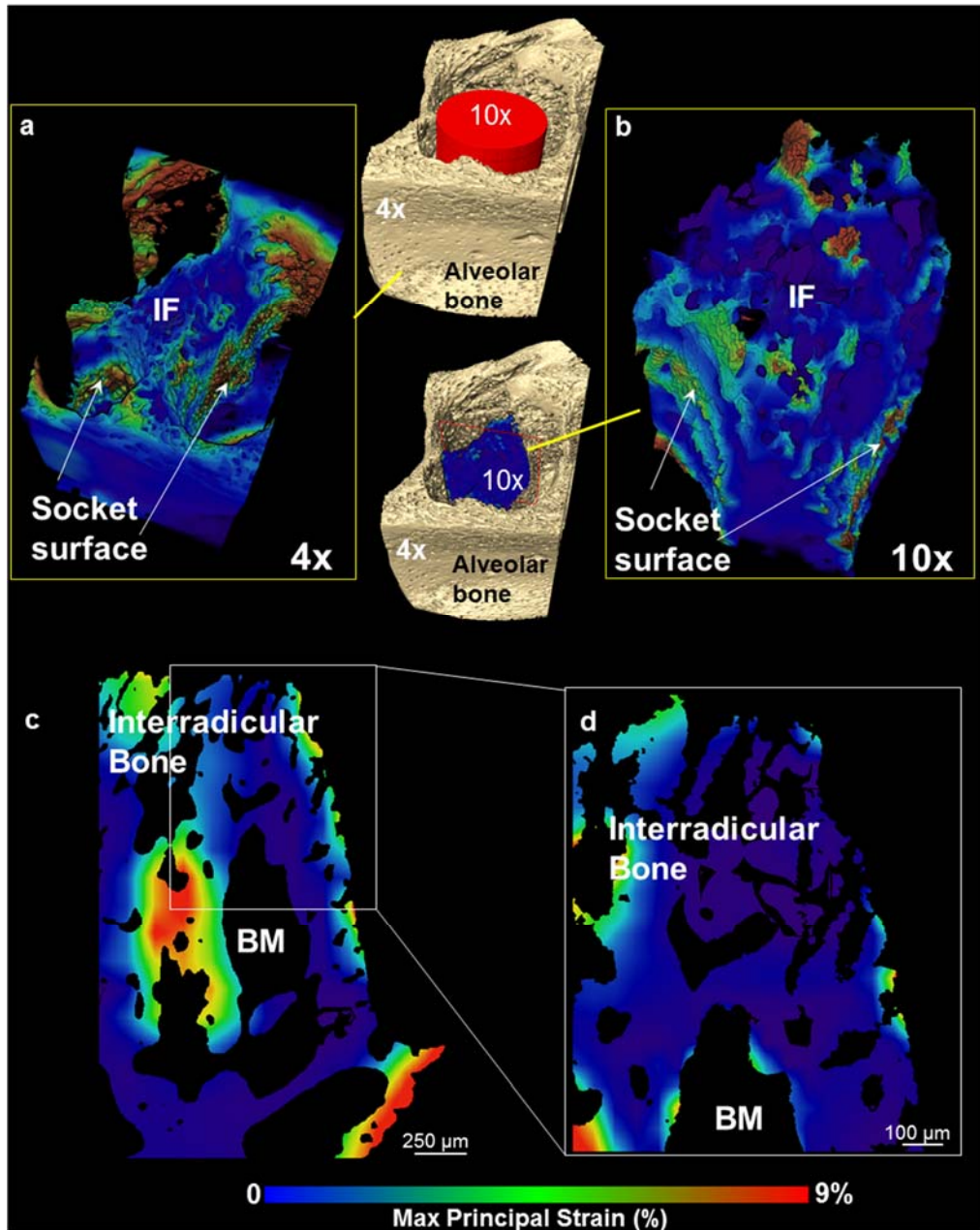
Figure 4.4. Comparison of volumetric strain maps at (a) 4x and (b) 10X magnifications following DVC of a concentric loaded bone-PDL-tooth fibrous joint. Differences in strains in the same virtual sections at magnification of 4X (c) and 10X (d) are illustrated.

a

Optical Micrograph

100μm

X-ray Radiograph

100μm

Strain Micrograph

100μm

0%　　　　　　　　　　　　　　　　1.5%+

b

Optical Micrograph

X-ray

Nanoind.

Topography

Strain Map

E (GPa)

x-axis (μm)

y-axis (μm)

Overlapped Interrogation Window

c

Nanoindent Spacing

Strain (%)

Elastic Modulus (GPa)

X-ray Attenuation (8bit)

Xray Attenuation　　strain (%)　　elastic modulus

distance (μms)
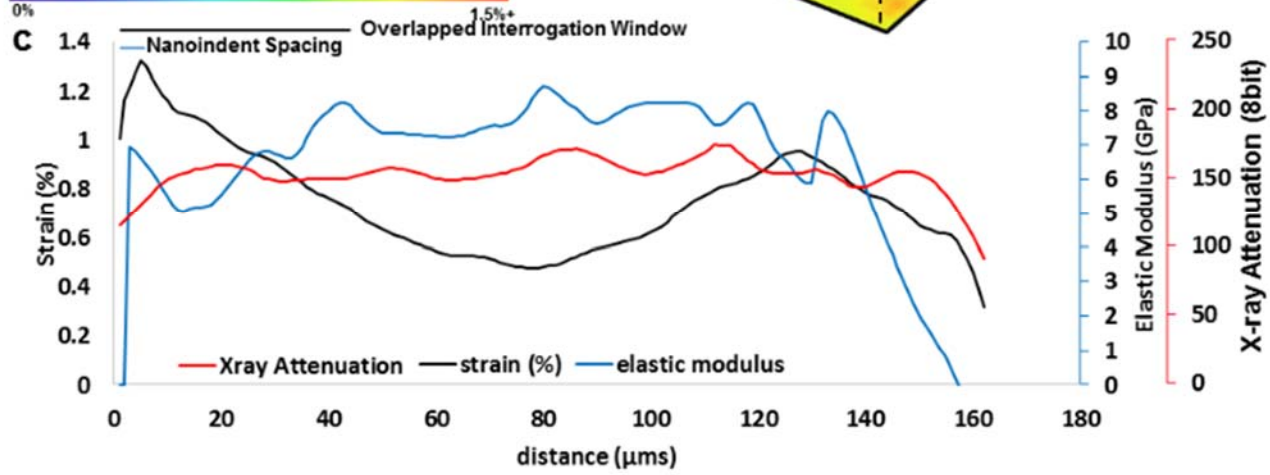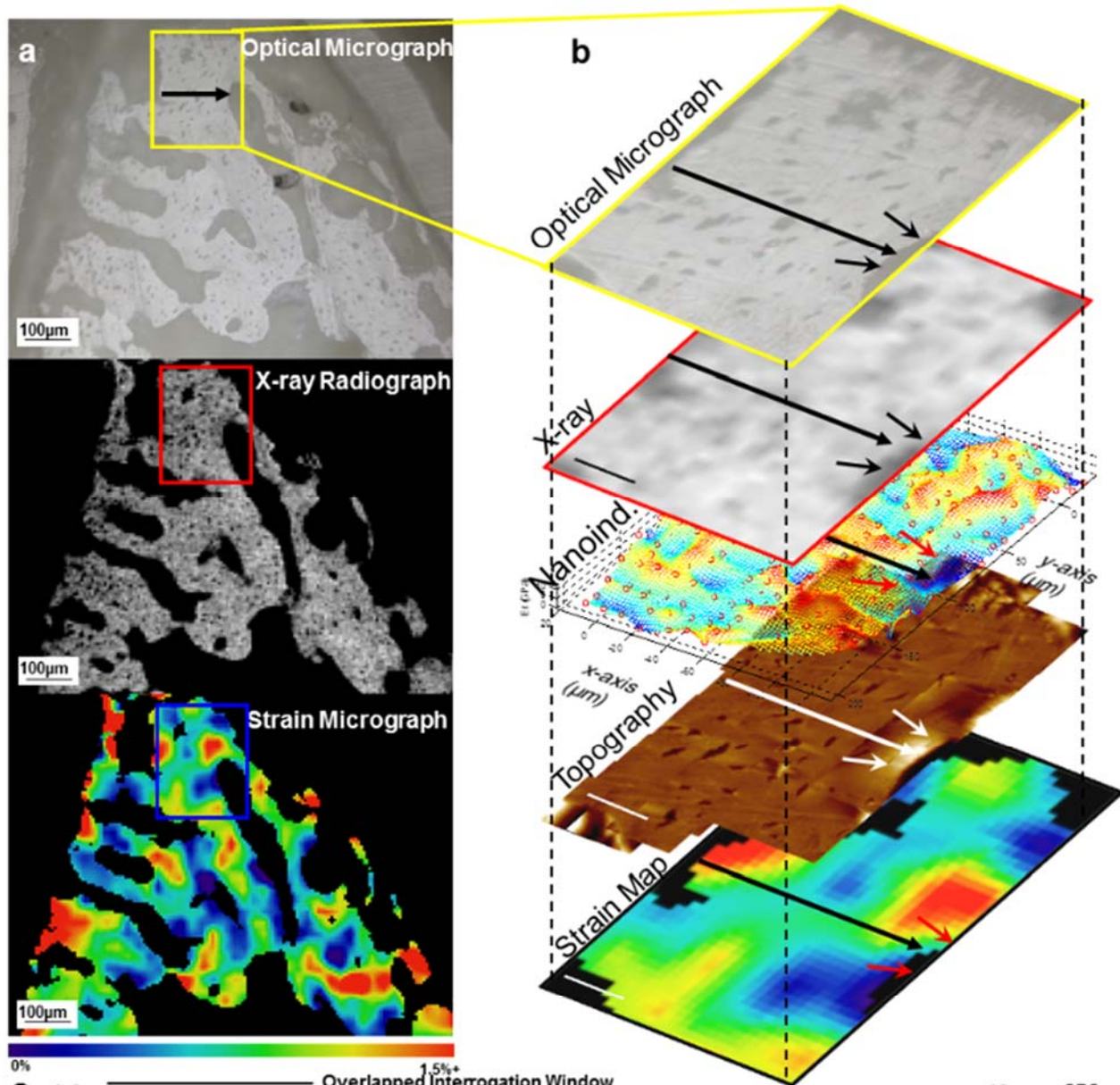
Figure 4.5. Correlative maps of various imaging and analytical modalities (optical, X-ray, nanoindentation, structure and DVC) on the same region of interradicular bone are shown in (a). Optical micrograph of a sectioned surface was aligned with an X-ray radiograph, modulus map, hygroscopic regions using atomic force microscope (AFM), and eventually with a strain map using a custom MATLAB code. Arrows represent the same region of interest in data spaces obtained using different characterization techniques. (c) Line profiles from various correlated micrographs of the same section illustrate site-specific physical and chemical relationships. Yellow, red and blue boxes represent analogous field of views in optical, radiographic and strain mapping spaces, respectively. While interpolation is needed to align the datasets, the differences in the spatial resolution is represented the line plots. Note: correlation is limited to spatial resolution of each characterization technique and corresponding data acquisition system.
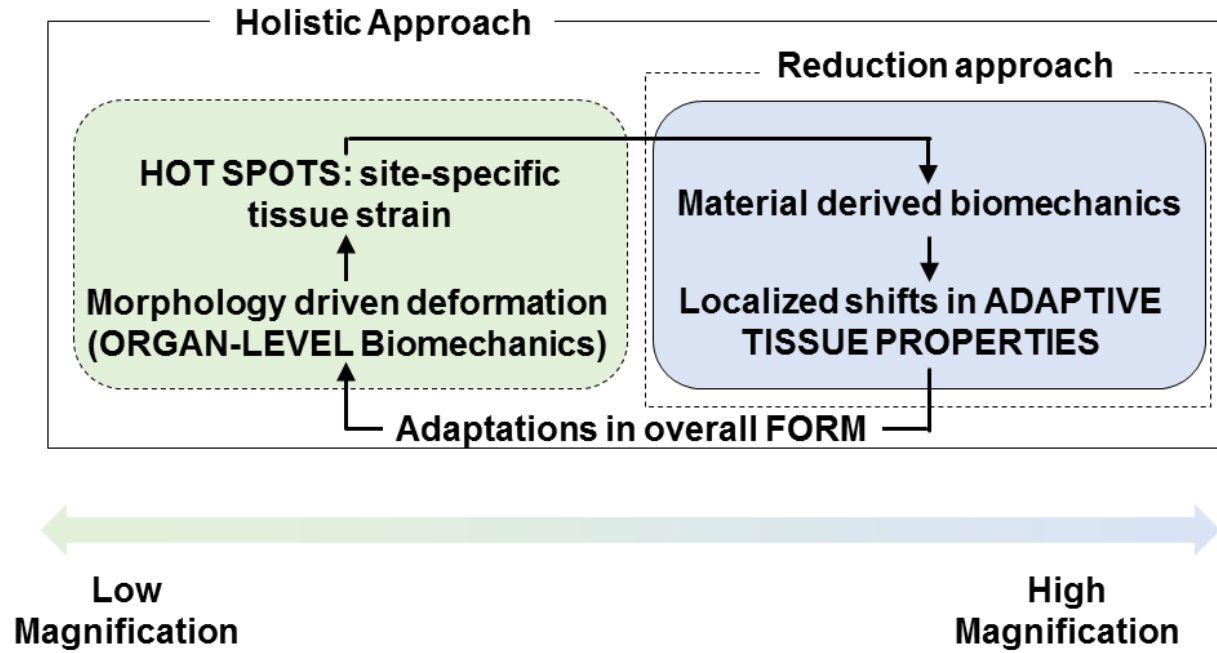
Figure 4.6. Graphical comparison of reductionist vs. holistic approach illustrating the effect of magnification on strain mapping within volumes of materials is shown.
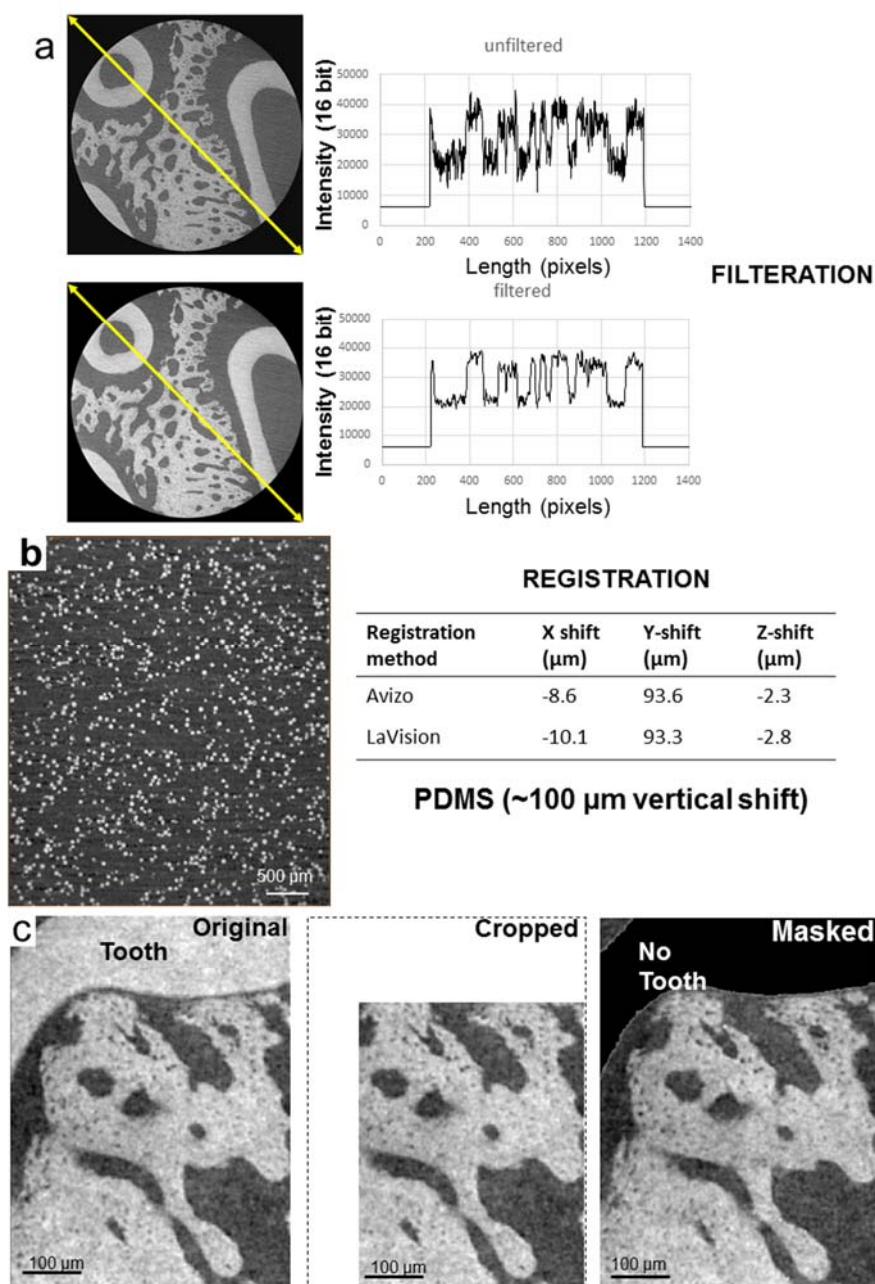
Supplemental Figure 4.1 (Fig. 4.S1). a) Example of anisotropic diffusion filtering method used to smoothen regions while preserving features of interest in alveolar bone. b) Image registration of scans taken before and after PDMS specimen translation resulted in similar values using AVIZO and DaVis softwares respectively. c) Example of tooth removal in two ways; cropping (middle) and masking (right) while the original image is shown in the far left.
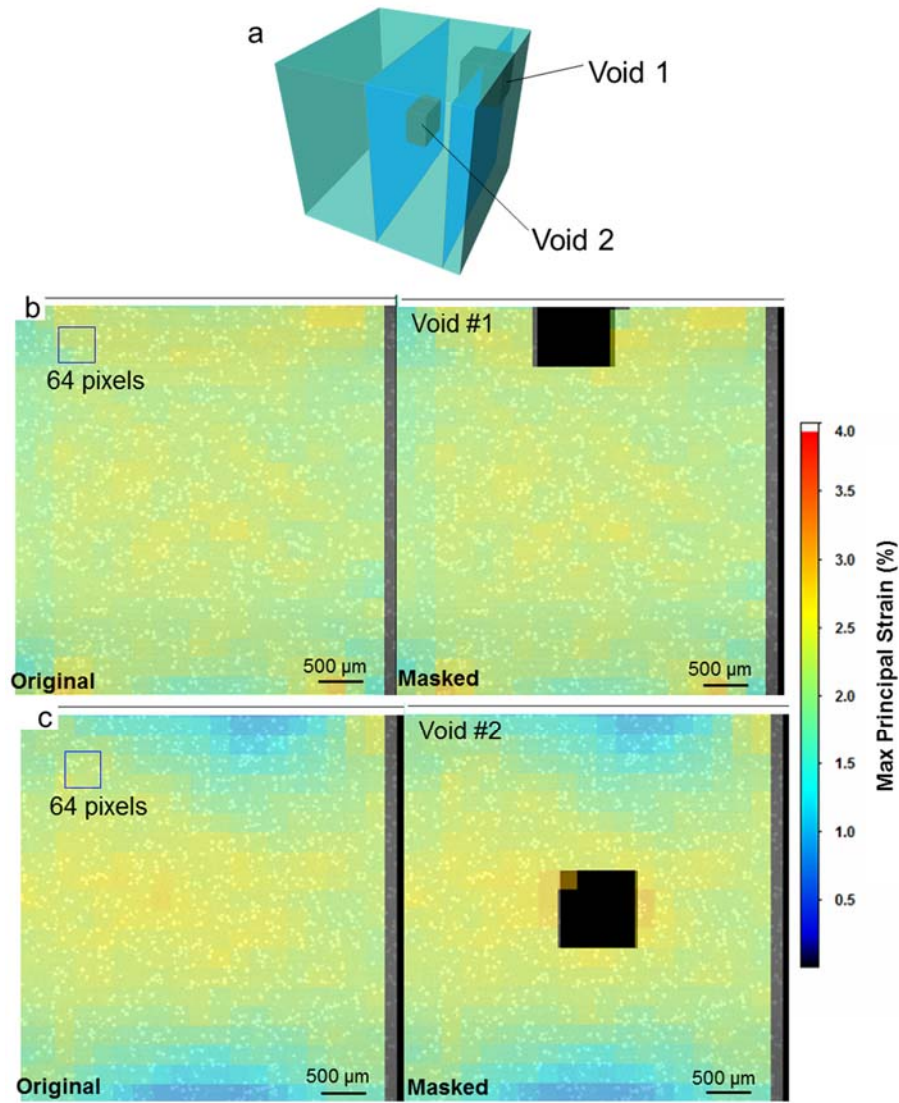
Supplemental Figure 4.2 (Fig. 4.S2). Effects of masking are demonstrated by masking regions (a) closer to the edge (b) and at the center (c) of a PDMS specimen. Comparisons with the original strain calculations and calculations with masked data (Void # 1 at the edge and Void #2 in the middle of the specimen) demonstrated small differences (<0.3% strain). Black boarders within 2D images are the result of regions in interrogation windows not calculated due to insufficient number of minimum fraction of valid voxels for accurate strain representation.
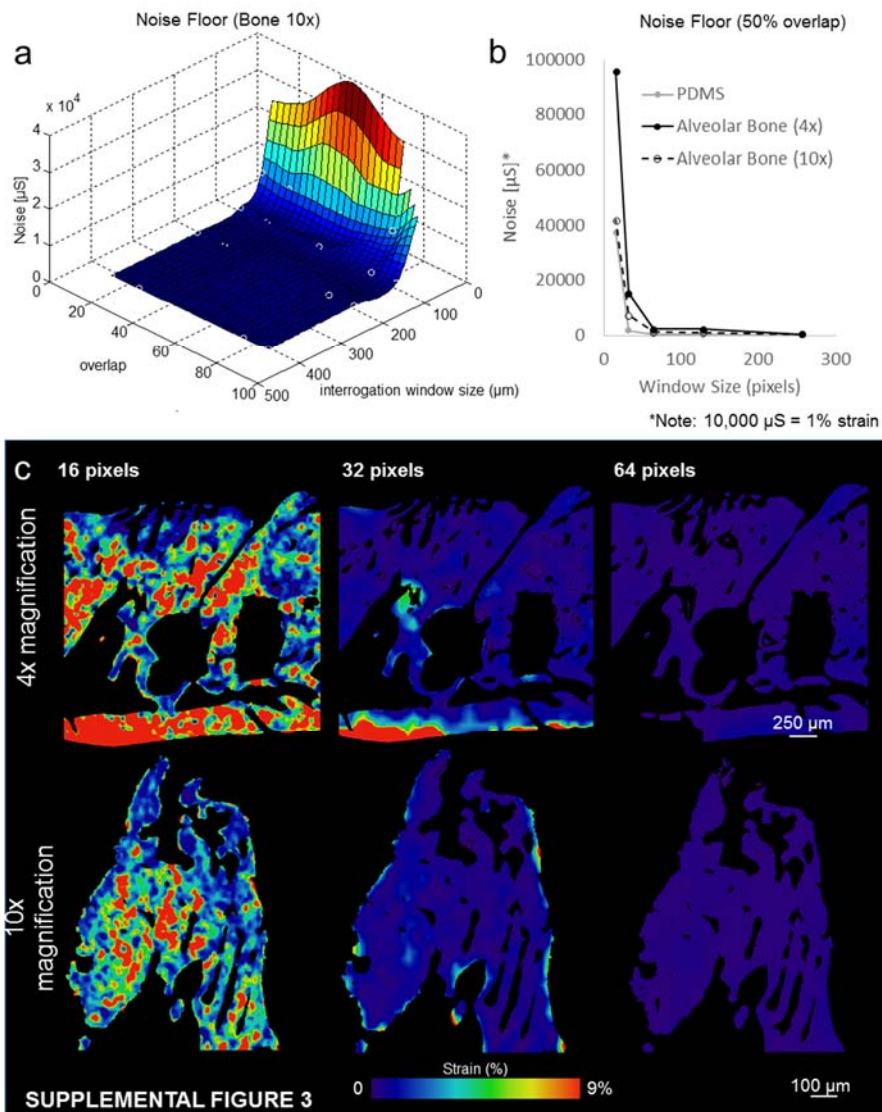
Supplemental Figure 4.3 (Fig. 4.S3). a) Noise Floor calculations by imaging specimen

consecutively at no load. b) Noise floor was calculated using interrogation volumes with

16, 32, 64, 128, and 256 pixel lengths for PDMS and alveolar bone (4X and 10X). An

inverse relationship between interrogation volume size (length) and noise floor was found.

b) DVC calculations of alveolar bone under load and no load demonstrated measurable

differences between measured strain and the noise floor. c) Noise floor calculations within

alveolar bone using different interrogation window sizes of 16, 32, and 64 pixel lengths

are shown.
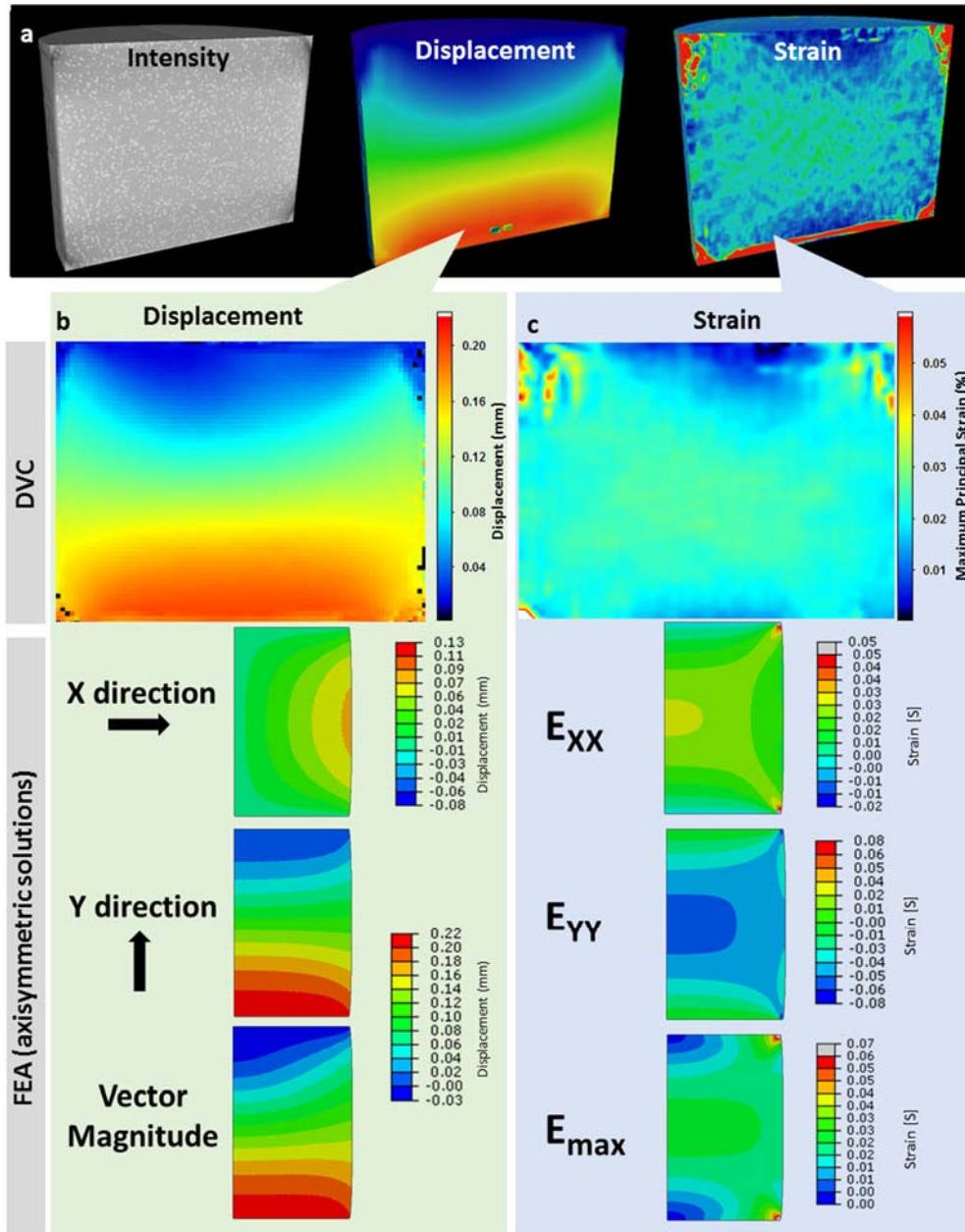
Supplemental Figure 4.4 (Fig. 4.S4). Validation of DVC solutions using finite element analysis. (a) 3D DVC solutions are shown for both displacement and strain. Virtual sections for both displacement (b) and strain (c) were comparable with solutions produced from finite element analysis.
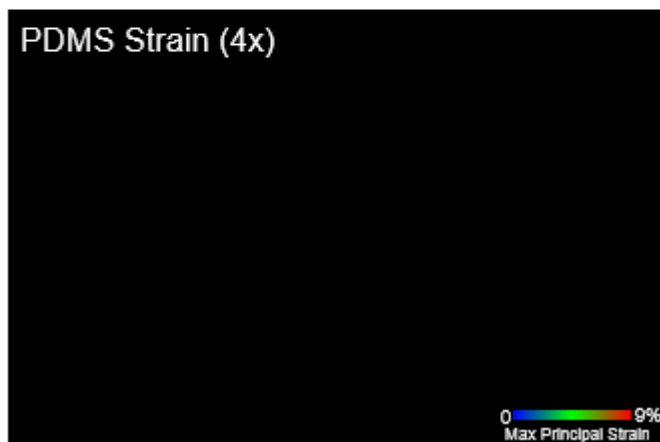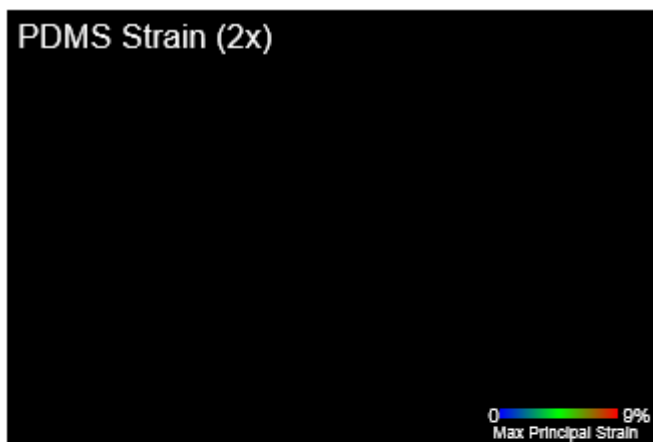
Supplemental Figure 4.5 (Fig. 4.S5). 2D slice progression generating a 3D distribution of strain in volumes of PDMS scanned at 2X (**Fig. 4.S5 2X, top**) and 4X (**Fig. 4.S5 4X, bottom**) magnifications are shown. Please refer to files "**Figure 4-S5 2x.avi**" and "**Figure 4-S5 4x.avi**" in the supplementary directory for respective movies.
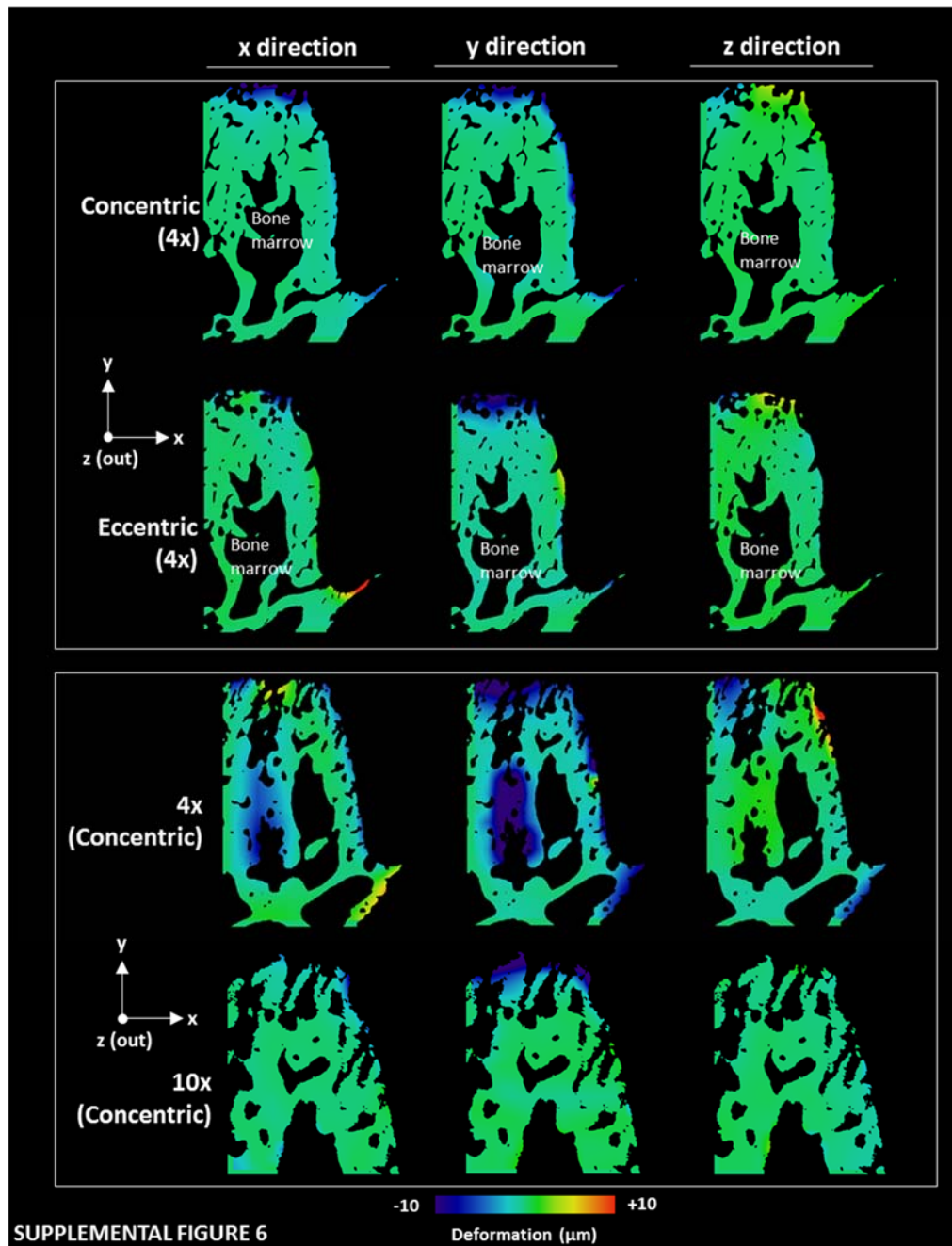
Supplemental Figure 4.6 (Fig. 4.S6). Deformation fields for concentric, eccentric loading configurations at 4X and concentric only at 10X are illustrated. Deformations calculated from DVC software were used to determine strain within alveolar bone under eccentric and concentric conditions as shown in **Figure 4.3**. Axis denotes positive direction for x, y, and z.
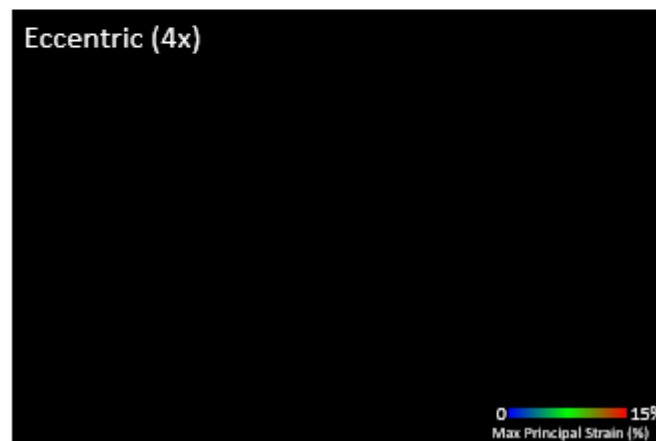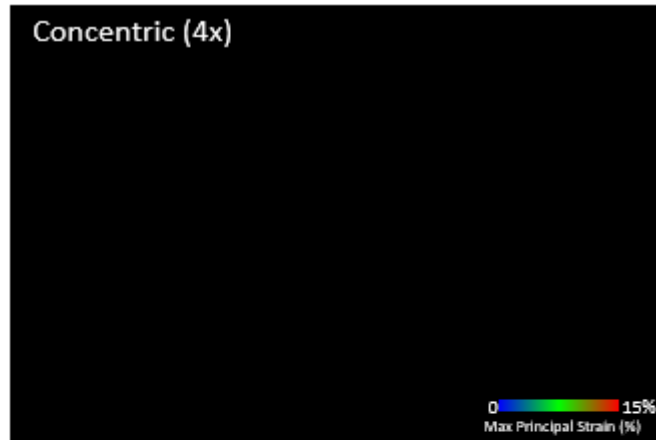
Supplemental Figure 4.7 (Fig. 4.S7). 2D slice progression generating a 3D distribution of strain in volumes of concentrically (**Fig. 4.S7 4X Concentric, top**) and eccentrically (**Fig. 4.S7 4X Eccentric, bottom**) loaded alveolar bone specimens are shown. Please refer to the publication for the video. Please refer to files "**Figure 4-S7 4x (Concentric).avi**" and "**Figure 4-S7 4x (Eccentric).avi**" in the supplementary directory for respective movies.
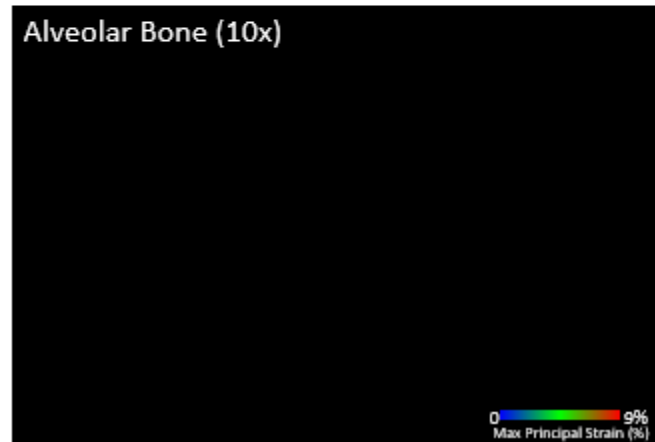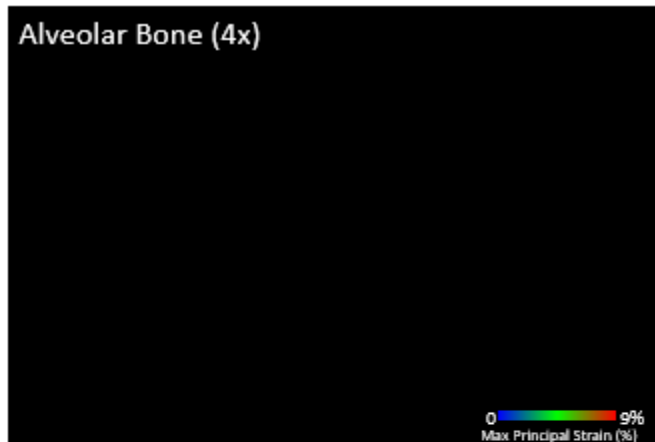
Supplemental Figure 4.8 (Fig. 4.S8). 2D slice progression generating a 3D distribution of strain in a volume alveolar bone imaged at 4X (**Fig. 4.S8 4X**) and 10X (**Fig. 4.S8 10X**) optical magnifications are shown. Please refer to the publication for the video. Please refer to the publication for the video. Please refer to files "**Figure 4-S8 4x.avi**" and "**Figure 4-S8 10x.avi**" in the supplementary directory for respective movies.

CHAPTER 5. MULTISCALE BIOMECHANICAL RESPONSES OF ADAPTED BONE-PERIODONTAL LIGAMENT-TOOTH FIBROUS JOINTS

5.1. Abstract

Reduced functional loads cause adaptations in organs. In this study, temporal adaptations of bone-ligament-tooth fibrous joints to reduced functional loads were mapped using a holistic approach. Systematic studies were performed to evaluate organ-level and tissue-level adaptations in specimens harvested periodically from rats given powder food for 6 months (N = 60 over 8,12,16,20, and 24 weeks). Bone-periodontal ligament (PDL)-tooth fibrous joint adaptation was evaluated by comparing changes in joint stiffness with changes in functional space between the tooth and alveolar bony socket. Adaptations in tissues included mapping changes in the PDL and bone architecture as observed from collagen birefringence, bone hardness and volume fraction in rats fed soft foods (soft diet, SD) compared to those fed hard pellets as a routine diet (hard diet, HD). *In situ* biomechanical testing on harvested fibrous joints revealed increased stiffness in SD groups (SD:239-605 N/mm) ($p<0.05$) at 8 and 12 weeks. Increased joint stiffness in early development phase was due to decreased functional space (at 8wks change in functional space was -33 µm, at 12wks change in functional space was -30 µm) and shifts in tissue quality as highlighted by birefringence, architecture and hardness. These physical changes were not observed in joints that were well into function, that is, in rodents older than 12 weeks of age. Significant adaptations in older groups were highlighted by shifts in bone growth (bone volume fraction 24wks: Δ-0.06) and bone hardness (8wks: Δ-0.04 GPa, 16 wks: Δ-0.07 GPa, 24wks: Δ-0.06 GPa). The response rate (N/s) of joints to mechanical loads decreased in SD groups. Results from the study

showed that joint adaptation depended on age. The initial form-related adaptation (observed change in functional space) can challenge strain-adaptive nature of tissues to meet functional demands with increasing age into adulthood. The coupled effect between functional space in the bone-PDL-tooth complex and strain-adaptive nature of tissues is necessary to accommodate functional demands, and is temporally sensitive despite joint malfunction. From an applied science perspective, we propose that adaptations are registered as functional history in tissues and joints.

5.2. Introduction

Functional loads arise from every day activities and are the primary environmental factors responsible for guiding tissue and organ development and growth (Carter, 1984; Carter et al., 1996). From a developmental standpoint, stiffness gradients due to passive stretch in matrices are thought to play a role in cell polarity, differentiation, organization, migration, and contribute to the synthesis and turnover of organic and inorganic constituents (Ingber, 1997). Subsequently, during growth, tissue maturation through increasing number of crosslinks in organic matrices and phase changes in mineral (Posner, 1969) occur based on functional cues throughout the lifespan of an organism (Carter, 1984).

In a bone-periodontal ligament (PDL)-tooth fibrous joint, the primary functional loads are enabled by the muscles of mastication, including the masseter, temporalis, medial pterygoid, and the upper/lower lateral pterygoid (Netter and Colacino, 1989; Dawson, 2006). Magnitudes and frequencies of functional loads are dependent on many intrinsic and extrinsic factors (Woda et al., 2006), including muscle efficiency (e.g. higher in men vs. women, higher in younger vs. older (Waltimo and Könönen, 1993; Kohyama et al., 2004; Palinkas et al., 2010)), diet hardness (e.g. softer foods and/or liquid diet vs. harder foods (Sako et al., 2002; Grünheid, 2010)), and other forms of behavioral loads (e.g. nail biting, tongue trusting, jaw clenching, bruxism (Hartsfield et al., 2004; Hartsfield Jr, 2009)). As a result, functional loads within the oral cavity are categorized as physiologic (e.g. food chewing), pathogenic (e.g. bruxism), and therapeutic (e.g. orthodontic loads). Hence, it is conceivable that a change in magnitude of functional loads due to one or more of these factors can change the axial and lateral loads on a

tooth and its relative position within the alveolar socket. In this study, functional adaptation by evaluating overall changes in biomechanics of a fibrous joint and adaptation of the respective tissues the makeup the joint were investigated by modulating chewing forces and frequencies through hardness of food given to rats.

Functional (i.e. overload, disuse, and directional load) adaptations in bone, cementum, and the PDL are often evaluated systematically using small-scale animal models, such as rodents. Studies focusing on muscle activity have noted a decrease in muscle contraction and an increase in contraction rate with a decrease in magnitude and an increase in loading frequency when hard pellet diet (HD) normally given to rats is replaced with either liquid, pudding, or powder soft diets (SD) (Thomas and Peyton, 1983; Nies and Young Ro, 2004). Studies leveraging the load-mediated response have mapped changes in mass of alveolar bone (Raadsheer et al., 1996; Mavropoulos et al., 2004b), bone architecture (Rubin, 1984), and PDL orientation and turnover rates. A previous study from our laboratory reported changes in hardness of alveolar bone and cementum, and mineral profile changes across the bone-PDL-cementum complex harvested from rats subjected to SD (Niver et al., 2011).

Considering the fibrous, hygroscopic, vascular, and innervated nature of the ligament between the tooth and the vascularized alveolar socket, the bone-PDL-cementum complex contains biophysical and biochemically graded fibrous PDL-bone and PDL-cementum entheses (Ho et al., 2010b). Early investigators isolated and performed biomechanical studies on transverse sectioned blocks of the bone-PDL-tooth complex and focused on the PDL's intrusive, extrusive and related viscoelastic/viscoplastic characteristics (Ralph, 1982; Mandel et al., 1986; Komatsu and Chiba, 1993; Tanaka et

al., 2006; Komatsu et al., 2007). Subsequently, by using an *in situ* mechanical loading device coupled to an x-ray microscope, biomechanical studies on intact bone-PDL-tooth fibrous joints , and geometric relationship of tooth with the alveolar socket in humans (Ho et al., 2013) and other mammalian models under normal (Naveh et al., 2012a; Lin et al., 2013; Jang et al., 2014b) and diseased conditions (Lin et al., 2014) were performed.

In this study, following reduced chewing forces on bone-PDL-tooth complexes of rats for a period of 20 weeks (24 weeks total age), the questions that were asked included: 1) is there a shift in biomechanics of fibrous complex exposed to reduced functional loads? 2) Do adaptive properties of tissues, i.e. physicochemical properties of bone, cementum, and PDL in reduced-function and normal-function groups converge to similar patterns with the age of the mammal? 3) What is the clinical significance in adaptive properties (physicochemical) of softer and harder tissues within the joint under prolonged reduced function? These questions were explored by designing experiments to identify shifts in stiffness of fibrous joints from HD and SD groups and correlating the shifts to tissue-level adaptations in respective groups. Hence the objective of the study was to use a holistic approach (as opposed to commonly adopted reductionist approach), in that, insights into tissue adaptations in rats aged 6 to 24 weeks were evaluated and discussed within the context of overall biomechanics of intact joints. Results demonstrated an altered biomechanical response of the fibrous joint through identifiable changes in: 1) joint reactionary response to *in situ* loading as seen by load-displacement and load-time relationships, and by comparing these readings to 2) changes in organization and structure of adapted hard/soft tissues and 3) bulk material properties of hard tissues.

5.3. Materials and methods

5.3.1. Reduced functional load animal model

All experimental protocols were compliant and followed the guidelines of the Institutional Animal Care and Use Committee (IACUC) (Niver et al., 2011). Sprague Dawley male rats (N = 60; Charles River Laboratories, Inc., Willmington, MA) at 4 weeks of age were divided into 2 groups and fed one of two nutritionally equivalent foods, which differed only in hardness, hard pellet food (Hard Diet = HD; N = 30) or soft powder chow (Soft Diet = SD; N = 30) (PicoLab 5058, LabDiet, Deans Animal Feeds, Redwood City, CA, USA).

To measure the effects of load-mediated changes due to food hardness across age groups, separate animal groups were grown to 8, 12, 16, and 24 weeks. Mandibles were harvested from sacrificed animals at each time point and separated into right and left hemimandibles (**Fig. 5.1**). Right hemimandibles were used to perform biomechanical testing using an *in situ* loading device coupled to a micro X-ray computed tomography/microscopy unit (Micro XCT-200, Carl Zeiss, Pleasanton, CA) (**Fig. 5.1a and b**). Specimens were stored in a tris-phosphate buffer solution supplemented with 50 µg/mL of penicillin and streptomycin (Chiba and Komatsu, 1993). Left hemimandibles were processed for histology.

5.3.2. Biomechanical testing and *in situ* imaging of functional-space in intact fibrous joints

The harvested hemimandibles were prepared for *in situ* biomechanical testing as described previously (Lin et al., 2013; Jang et al., 2014b). Prepared specimens were loaded *in situ* (MT500CT, Deben UK Ltd, Suffolk, UK) to several displacement rates (0.2, 0.5, 1.0, 1.5, 2.0 mm/min) and peak loads (5N, 6N, 8N, 10N, 15N) within the detectable

ranges of the mechanical testing device (**Fig. 5.2**). The load cell outputs of time, reactionary response to load, and displacement (**Fig. 5.1d**) were further processed to describe the biomechanical response of the dentoalveolar complex (stiffness and loading rate response) (Lin et al., 2013; Jang et al., 2014b). Joint stiffness (N/mm) was calculated by approximating the final 30% of the load vs. displacement graph (Fung, 1990; Popowics et al., 2009; Lin et al., 2013) with a linear regression model (**Fig. 5.1c**). Reactionary response of the joint to loads was calculated by evaluating load rate (N/s) from load vs. time gradient similar to stiffness. Relationships between parameters were evaluated statistically across age and diet groups and across the gradient within the specimens using a mixed effects regression model with random specimen effects. To highlight the multivariable effects of our data, 3D surface plots relating joint stiffness against a two dimensional axis (age and displacement, age and peak load) were generated using a custom MATLAB code (MATAB, Mathworks, Natick, MA).

Specimens used for biomechanical testing were also imaged using X-ray microscopy (XRM) (Micro XCT-200, Xradia, Pleasanton, CA) to identify structural changes within the dentoalveolar complex. A virtual sagittal plane bisecting the distal and mesial lingual roots of the 2nd molar was selected from tomograms taken at no load to evaluate changes in functional PDL-space. Functional PDL-spaces were measured between tooth and bone specifically in the interradicular region and the data was compared within and across HD and SD groups.

5.3.3. Hardness of bone, cementum, and dentin

Specimens were cut orthogonally to the occlusal plane (sagittal) of the molars into two halves and embedded in epoxy. The exposed surface containing the bone-PDL-tooth

complex was polished using a series of fine diamond suspension slurries (Buehler Ltd., Lake Bluff, IL) (Ho et al., 2004). Microindentation was performed on the secondary cementum (located at the apical 1/3 of the root) of the tooth, interradicular bone, and interdental bone of the alveolar complex using a Knoop indenter (Ho et al., 2004). Rows of microindents (10 seconds, 20 gf, dry conditions) were arranged according to ASTM E384-99 (ASTM - E04 Committee, 1999).

5.3.4. Collagen fiber birefringence and root-PDL directionality in adapted complexes

Histology sections containing an intact distal root from the 2nd molar were selected for PSR staining (n=3 at all-time points and diet groups) (Lin et al., 2014). Stained slides were analyzed using a directionality function of Fiji (Tinevez, 2015) to compute PDL directionality. PDL directionality measurements of the mid-root were taken on the mesial and distal sides and were analyzed for age and diet trends. Quantification of orientation through birefringence was performed by rotating the specimen stage until the region of interest illustrated maximum birefringence. Average intensities over tissue area were calculated in the following regions: interradicular bone (IR-B), interradicular PDL fibers (IR-PDL), and oblique PDL fibers along the root (R-PDL).

5.3.5. Bone volume fraction (BVF) of interradicular bone

Bone volume fraction (BVF) was calculated using XRM tomograms of specimens. Sub-volumes containing IR bone were isolated (**Fig. 5.6**), and bone volume fraction (Parfitt, 1988) equal to bone volume (BV) divided by the total volume (TV) (total volume (TV) = bone volume (BV) + endosteal space) (**Fig. 6b**) was calculated. The BV was isolated by using image segmentation (Avizo 8.1, FEI, Hillsboro, Oregon). Due to the

complex geometry of the interradicular space, the total bone volume was identified by applying a morphological closing algorithm to the bone volume space, effectively including the endosteal spaces. This method was chosen over sampling cube regions in order to reduce the risk of under sampling.

5.4.   Results

5.4.1. Changes in biomechanical response to *in situ* loads

The biomechanics of the bone-PDL-tooth joints from respective groups was evaluated for different permutations of displacement rates and peak loads within the detectable ranges of the loading device. Load-displacement relationships (**Fig. 5.1 and 5.S1**) were used to calculate joint stiffness by relating the displacement of the tooth within the socket to peak loads (**Fig. 5.2a**). Stiffness vs. displacement relationships revealed distinct regions based on the peak load. Higher peak loads resulted in a shift to the right shown in 2D (stiffness vs. displacement: **Fig. 5.2a**) and 3D (stiffness vs. displacement vs. age **Fig. 5.2b and c**). While both HD and SD groups demonstrated an overlap (**Fig. 5.2b-d**), fibrous joints from HD had an increased displacement response compared to SD for the same load (**Fig. 5.2a-c**).

Shifts in stiffness due to SD were plotted as a function of age and peak load with separate plots generated for different displacement rates (**Fig. 5.2d**).   Mixed linear regression models identified significant shifts in stiffness (SD-HD) as a result of reduced functional loading in younger groups (8 weeks and 12 weeks) and at higher loads (peak load = 15N, disp. rate = 0.2 mm/min) (**Fig. 5.2d**). However, comparisons at older ages and at other loading schemes showed no statistical difference between diet groups (**Fig. 5.2d**).

5.4.2. Functional space at interradicular regions of the complex

Functional spaces using tomograms were compared between HD and SD groups across all ages (**Fig. 5.3, 5.S1, and 5.S2**). In younger age groups (8, 12, 16 weeks), PDL functional space between and around the tooth furcation was significantly decreased in SD compared to HD group (p< 0.05; Student's t-test) (**Fig. 5.3b**). At older ages, functional space continued to decrease, but no statistical significance (p>0.05; Student's t-test) was observed between HD and SD starting at 20 weeks of age.

5.4.3. Collagen fiber birefringence and root-PDL directionality in adapted complexes

Overall, oblique fibers of the root PDL (R-PDL) were well-aligned and exhibited the most birefringence under polarized light microscopy (**Fig. 5.4c and d**). Within this region, the interfaces between the PDL and bone and cementum tended to have a higher birefringence compared with regions within the PDL *per se*. The PDL near the interradicular regions of the tooth furcation were spongy in nature and showed a significant decrease in birefringence compared with R-PDL fibers (**Fig. 5.4c**). Birefringence patterns within bone revealed distinct circular patterning of birefringence around the endosteal spaces (**Fig. 5.4c**).

Birefringence intensity values of IR-PDL or bone regions did not correlate with age using our method; however, the intensities increased as a function of age in both HD and SD groups within the R-PDL regions. At 8 weeks, intensities were significantly higher in HD groups compared to SD groups in R-PDL (p<0.05) (**Fig. 5.4c**). With an increase in age, the overall fiber angulation of the distal R-PDL decreased for both HD and SD groups (**Fig. 5.4e**).

5.4.4. Mechanical properties of secondary cementum, and interdental and interradicular bones

Within each specimen, the Knoop hardness of IR-bone was greater than that of interdental bone, which in turn was greater than secondary cementum (**Fig. 5.5**). Age-related trends for both HD and SD groups showed an increase in hardness for all tissues harvested from rats between 8 weeks and older. However, after 12 weeks of age, the hardness did not increase significantly with age. Tissues belonging to HD groups were harder than SD groups at 12, 16 and 24 weeks for both IR and interdental bone ($p < 0.05$ two-way ANOVA/Bonferroni ad post hoc test). Cementum from HD group was harder than cementum from SD groups at 12 and 16 weeks.

5.4.5. Interradicular bone volume fraction (BVF) as a function of age and diet

Within IR bone, bone separated from the endosteal space via segmentation is shown by comparing segmented endosteal space from IR-bone (**Fig. 5.6a and b**) and comparing identical sub-volumes of IR-bone, the apparent decrease in endosteal space (or increase in BVF) was seen (**Fig. 5.6c**). Volumetric measurements of segmented alveolar bone, showed an increase in BVF as a function of age (**Fig. 5.6d**). HD groups illustrated a significantly higher BVF compared to SD groups ($p < 0.05$) at 24 weeks.

5.4.6. Reactionary load rates of the dentoalveolar joint

Reactionary load response patterns of the joint increased with age for both HD and SD groups (**Fig. 5.7a**). In younger groups, SD groups had a slightly increased reactionary response compared to HD groups (**Fig. 5.7b**). However, with an increase in age, reactionary response was greater in HD groups compared with SD groups (**Fig. 5.7b**).

5.5. Discussion

The novel aspect of this study is demonstrated by mapping function-mediated adaptation of intact dentoalveolar complexes harvested from rats fed hard and soft diets respectively. The study seeks a multiscale approach, in that, stiffness of a macroscale fibrous joint and subsequently the physical properties of microscale regions within tissues that makeup the joint were evaluated and correlated.

The structural and chemical integrity of tissues is essential for joint function. In the case of a dentoalveolar fibrous joint, the cyclic chewing forces are absorbed and distributed to the surrounding tissues including the PDL, bone and cementum. The mechanically strained extracellular matrices will continue to signal cells and prompt changes in quality and architecture of respective tissues until an equilibrium is reached to meet functional demands. This is also known as functional adaptation and highlights strain-adaptive remodeling (Prendergast and Taylor, 1994), in that, the physicochemical properties of tissues that makeup the dentoalveolar joint change to accommodate functional demands. Results of this study will demonstrate this concept by 1) identifying a shift in joint stiffness due to reduced functional loads, and 2) by correlating the shift in joint biomechanics to a shift in physicochemical properties of tissues that makeup the joints exposed to reduced function. The experimental approach involved biomechanical testing of harvested joints at combinations of low to high displacement rates of low to high peaks loads using an *in situ* compression loading device. The experimental parameters to determine joint biomechanics are acceptable to identify differences in joint stiffness within and across groups, but do not mimic *in vivo* function.

113

The effect of reduced functional loads (SD group) on overall joint biomechanics was noted by decreased tooth displacement in the alveolar socket and was complemented by an increased joint stiffness upon compression of the tooth into the alveolar socket (**Fig. 5.2 and 5.S1**). Since there was a relationship between the tooth displacement and joint stiffness, we turned our attention to the functional space within the dentoalveolar complex. In general, the functional space between IR bone and its respective tooth is the least when compared to any other anatomical locations (Lin et al., 2014). As such, IR bone is the first contact region, as the tooth pivots about IR bone when under function, and from a biomechanics perspective is an area where strains are predominantly concentrated (Lin et al., 2013, 2014). Given that the unopposed tooth-molar model indicated cementum accretion (Murphy, 1959), it is conceivable that IR cementum growth due to reduced functional loads prompted an earlier contact between tooth and bone (**Fig. 5.3 and 5.S2**). However, the significant decrease in functional space as well as an increase in stiffness between the groups was only observed in the younger groups (8 and 12 weeks) with no observable changes in the older groups (16, 20, 24 weeks). Within the aforementioned argument lies a confounding factor, in that, it is plausible that the eruption rate of molars in the SD group was lower due to slower maturity of the rats. Hence, rats belonging to both groups were weighed periodically (**Fig. 5.S1**). No significant differences in body weights of rats were observed at earlier ages, and significant differences were observed at ages 16 weeks and older (**Fig. 5.S1**). Contrasting the body weight patterns were the observed significant differences in joint stiffness at earlier ages. Hence, should the differences in joint stiffness be correlated to differences

in growth rate of cementum in SD and HD groups, further scanning of the interradicular site at a higher resolution to visualize and measure cementum width is warranted.

Joint stiffness is a manifestation of shifts in adaptive physicochemical properties of bone, cementum, and the PDL. In this study, insights into the interplay between form and function at multiple length-scales were established by first coupling load response of joints harvested from SD group to tooth-bone association and subsequently to individual properties of tissues in the complex by contrasting with controls (joints harvested from HD group). The current model in dentoalveolar biomechanics is that compressive loads displace the tooth into the socket by first causing deformation in the softer ligament (Lin et al., 2013). Increased compressive loads on the tooth can cause hardening of the ligament prior to deforming mineralized tissues, primarily bone. The PDL, like many other soft tissues, from a biomechanical perspective can be modeled as a two phase system: solid and semisolid. The solid phase is composed primarily of fibrillar proteins and nonfibrillar matrix proteins, including proteoglycans which are fundamental structural elements that interact with each other and water (Ho et al., 2005; Nanci, 2007). The semisolid phase of the tissue is composed of bound interstitial fluid in the PDL. The mix of the two provides the characteristic feature, that is the load response rate of the organ (Lin et al., 2013). However, joint response can continue to change due to functional adaptation of the PDL as a result of altered turnover rate of various types of collagen which can be related to respective birefringence.

The architecture of the mesial PDL is significantly different from the distal PDL. This difference is due to the presence of large vasculature predominantly at the PDL-bone enthesis, passive strain due to innate hydrostatic pressure and the electrochemical

activity of the glycosaminoglycans that prompt water retention and tension within the tissue. Hence birefringence using PSR staining is specific to anatomical location within the complex and along a root. In general, the architecture of IR-PDL is heterogeneous compared to the polarized architecture of the oblique fibers of R-PDL. Heterogeneous organization of the IR-PDL could explain its lower birefringence regardless of magnitude and frequency of functional loads. Relatively, the PDL fibers in mesial and distal complexes illustrated higher birefringence (**Fig. 5.4c**); a semi-quantitative marker resulting from collagen orientation, collagen quality (crosslink density) and type of collagen. Hence, the changes in intensity could be related to functional adaptation of the PDL (**Fig. 5.4c**) as a result of a change in natural turnover rate of PDL due to a change in functional load. However, a confirmatory result for functional adaptation of the PDL should be addressed using spectroscopy techniques similar to that used for cartilage degeneration (Boskey and Pleshko Camacho, 2007).

The birefringence pattern in strained interradicular bone was illustrated by a circumferential pattern surrounding the endosteal spaces (**Fig. 5.4c**). Over time, it is likely that these regions will become osteons and can be termed as strain-induced adaptation underlined by circumferential collagen orientation interspersed with mineral as responsive events during remodeling (Bromage et al., 2003). These patterns increase with age as a result of increased birefringence in HD groups compared with SD groups. It is plausible that the formation of the observed birefringent rings is a response to function-mediated fluid flow over time. However, true birefringence of concentric circular or elliptical motifs (based on how the specimen was sectioned) is a challenge to measure quantitatively as polarized light is unidirectional in nature and can only capture a restricted angular range.

Additional limitations include measurement sensitivity due to interfering structures within a 5-6 micron-thick histology section and sectioning plane dependence of structural motifs.

Tissue structure in addition to ratio of organic to inorganic contents can affect its hardness. Rats experiencing reduced functional loads had significantly decreased hardness (**Fig. 5.5**) at older ages (12wks+) and corroborated with our previous study (Niver et al., 2011). In particular, the hardness of IR bone was greater than interdental bone and cementum, with cementum illustrating the least hardness (**Fig. 5.5**). These shifts in mechanical properties of bone can be attributed to mechanosensitive osteocytes (Qing and Bonewald, 2009) in IR-bone.

It has long been said, that shifts in functional loads will also affect the shapes (form) of bone (Wolff, 1982) and more recently was explained as an altered dynamics between blastic-and clastic-cellular activities (Frost, 1987, 2003). The resulting morphology can be a deviation in both the total volume and shape of the bone as indicated by a change in bone volume fraction (BVF) (**Fig. 5.6**). Since large-scale morphological changes are evident long-term effects in tissues, BVF shifts were only statistically significant at 24 weeks (**Fig. 5.6**). Altered fluid flow due to altered functional loads could have caused a change in the number and shape of the alveoli to total bone volume. It is important to note the shift in indicators with age, that is, from joint stiffness at an earlier age to a change in tissue hardness and morphological features at a later age. Results demonstrate the capacity of form-induced strain in older animals, compared to the dominance of material-induced differences in younger animals when compared to controls. The cumulative effect of form and material changes are better explained by illustrating a proof-of-concept on the decreased ability of joints from SD to react to simulated loads compared to HD which

can react at a faster rate. Therefore, we hypothesize that softer tissues could be more sensitive to shifts in mechanical strain caused by a shift in velocity. It should be noted that the shift in kinetic energy can be a dominant factor in maintaining the needed turnover rate of the ligament to meet functional demands. The results imply a higher risk of fracture and mechanical failure in SD adapted complexes compared to HD joints for the same loads and velocities (**Fig. 5.7**).

From a biomechanics perspective, the joint stiffness and reactionary response to load altered with age. Morphometric changes within the joint space included an increase in BVF and a decrease in the joint space, resulting in a restricted tooth movement in the alveolar socket. Tissue specific changes included an increase in hardness within IR-bone, ID-bone and cementum, and an increase in collagen organization within the oblique fibers of the root PDL. These changes can be collectively seen as an adaptation to prevent joint damage when chewing harder foods. When analyzing changes due to the soft diets, the measurement of shifts in outcomes related to functional adaptation are best done by revisiting the two growth phases encapsulated within this study (rapid growth and mature stages) (**Fig. 5.8a**). Within the earlier time points when the rat is undergoing rapid growth, shifts due to the soft diet included a decrease in functional space as well a decrease in collagen organization of the root PDL. Since strain (%deformation) has been shown to be essential for tissue homeostasis, the comparative reduction of functional space may be an attempt to maintain normal physiological strain within the region (**Fig. 5.8b and c**) in response to the environmental signal. It is interesting to note that the observed growth patterns in cementum and alveolar bone are opposing, indicating differing mechanisms for mechanotransduction and/or the growth of these respective

tissues (**Fig. 5.8d**). As the rat matures, shifts in joints stiffness as seen at earlier ages are not significant with age. It is suspected that the reduction in magnitude of functional loads might not be significant for continued joint adaptations albeit prompting changes in tissue architecture. Future experiments would need to be explored if a stronger stimulus (e.g. hypofunction) would produce stiffness changes in older rats. The focused timeframe of our study encapsulates observations over the period that is normally considered an active phase of laboratory rat (at and after 6 months these animals are normally retired and are minimally used for experiments).

In this study, experimental biomechanics under *ex vivo* conditions does not account for the hydrostatic pressure due to an active circulatory system (McCauley and Somerman, 2012). However, biomechanical testing under *ex vivo* conditions can detect shifts in joint biomechanics. These shifts can be due to form, material properties and reactionary responses of tissues to mechanical loads despite shifting the joint toward malfunction.

5.6.   Conclusions

A reduction in functional loads resulted in short term shifts in joint biomechanics. The effects on joint stiffness are short-lived and were not observed with rapid growth and as it plateaus with age. The fact that this study showed that joint adaptation is dependent on age and that the initial form-related adaptation (observed change in functional space) can challenge tissues to meet the functional demands with increasing age well into adulthood has important clinical implications. Additionally, the coupled effect between shape and tissue properties is necessary to accommodate functional demands, and that the shifts in shape as determined by the change in functional space and bone volume

fraction, and tissue properties as determined by hardness and semi-quantitative analysis

of collagen birefringence are temporally sensitive despite shifting the joint to malfunction.

5.7. Figures
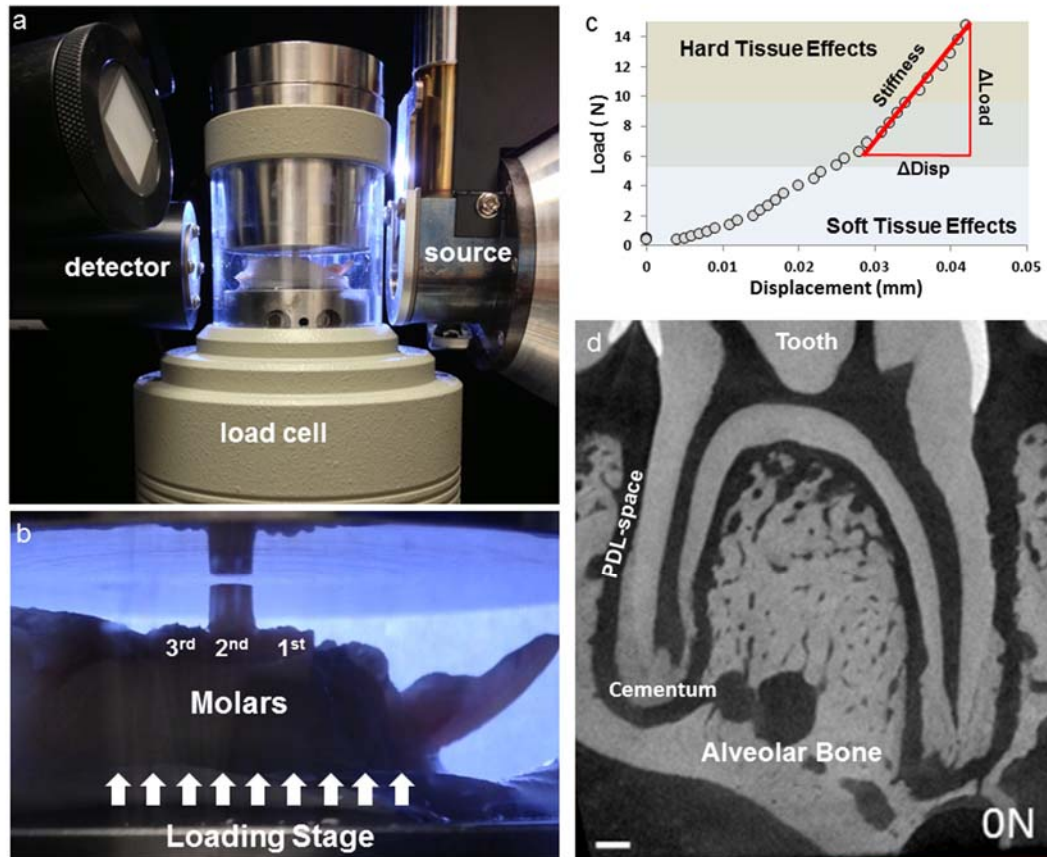
Figure 5.1. *In situ* loading device coupled to a XRM system to image tooth motion relative to the alveolar socket. a) Hemimandibles were prepared with composite buildups for mechanical testing and were placed in the load cell as shown. b) To ensure a parallel surface between the anvil and the composite buildup, occlusal marking paper was used (not shown) to mark uniform area of contact. c) The output of load displacement curve was analyzed by comparing the change in load (Δ Load) vs. the change in displacement (Δ Disp.). d) 2D virtual section relating tooth to the alveolar socket. Please note that 1d is a GIF file and should be viewed under slide show.

a

b

c

d

0.2 mm/min   0.5 mm/min   1.0 mm/min   1.5 mm/min

Blue – Upper Bound   Green – Lower Bound   Red – Zero Plane
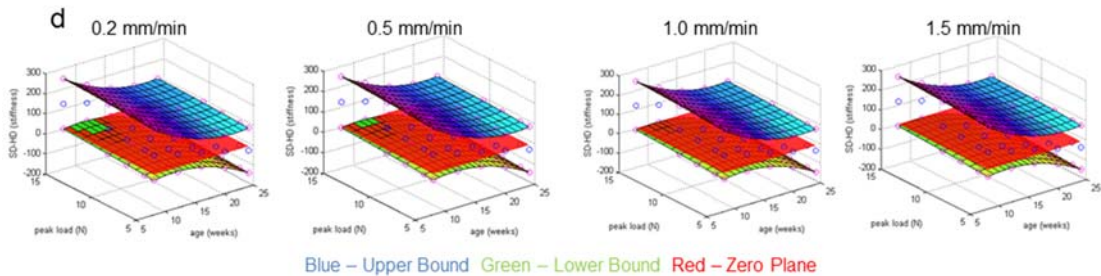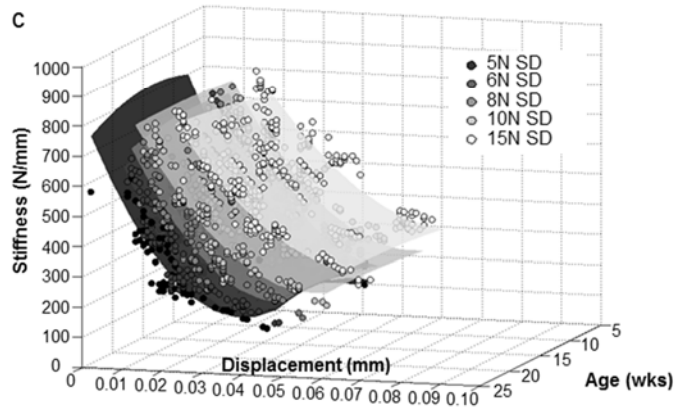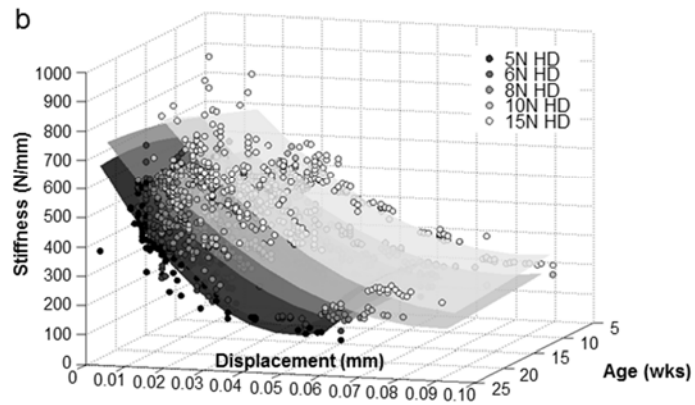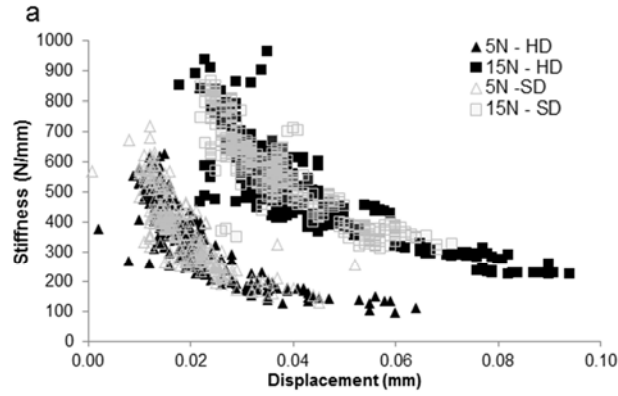
Figure 5.2. Stiffness values for fibrous joints obtained from those fed hard and soft diets respectively. a) The nonlinear plot illustrates joint stiffness values from all age groups when individually tested at different speeds (0.2, 0.5, 1.0, 1.5, 2.0 mm/min) and when loaded to 5 N (triangles – open and filled) and 15 N (squares – open and filled) respectively. Data for 6, 8, and 10 N are not shown but showed similar trends. The graph illustrates an increased range in displacement of the teeth from the HD group compared to displacement of teeth from SD group. 3D surface plots illustrate different spread of stiffness values with age (wks) and displacement (mm) when tested for peak loads of 5, 6, 8, 10, and 15 N in (b) HD groups and (c) SD groups. d) Statistical differences between stiffness values calculated from load-displacement relationships were analyzed using a mixed effects regression model and plotted as a function of age of the mammal. From the resulting 95% confidence intervals (blue – upper bound, green – lower bound, red – zero plane) the notable difference is that the joints from younger animals (8 and 12 week) in soft diet group were significantly stiffer than the joints from hard diet group under hard diet load-simulation conditions (higher load, lower displacement rate).
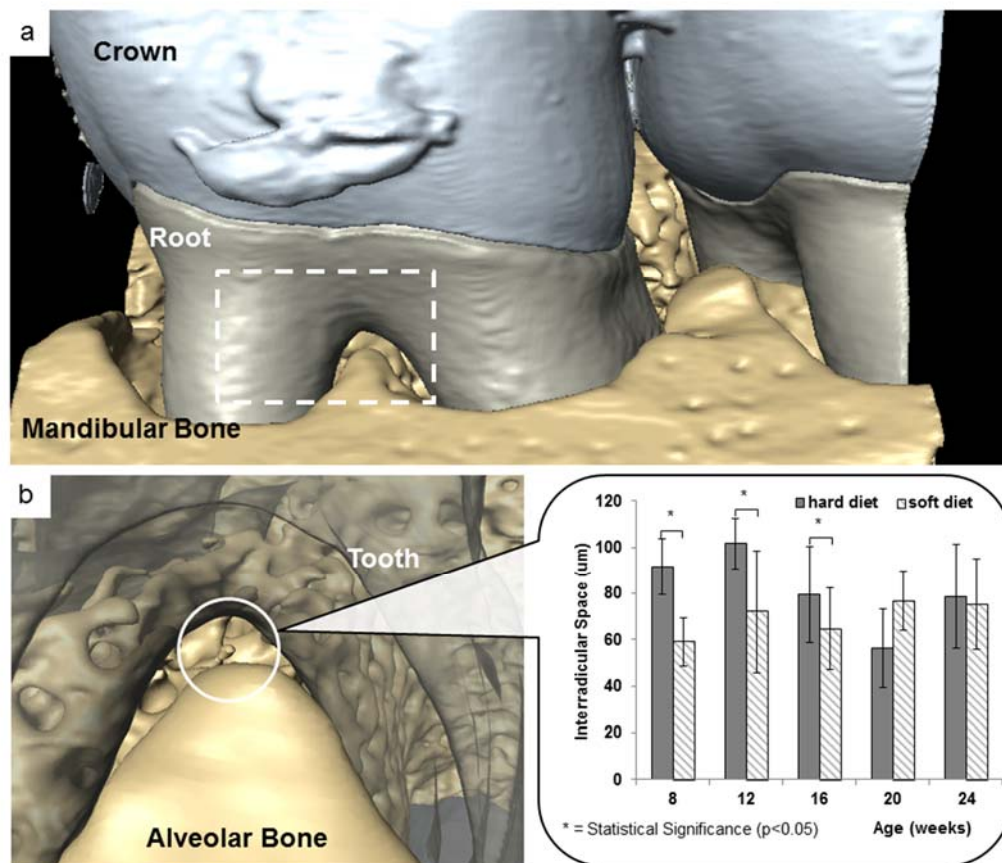
Figure 5.3. XRM tomography measurements of interradicular PDL-space. a) Representative tomogram illustrating a bone--PDL-tooth complex. Functional space was measured within the interradicular region (white dotted box). b) At younger groups, a narrower interradicular space was observed in soft diet groups compared with hard diet groups. However, with an increase in age, the difference between hard and soft diet groups became less significant.
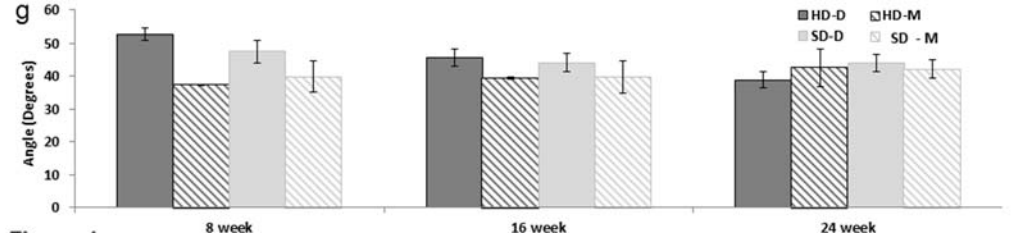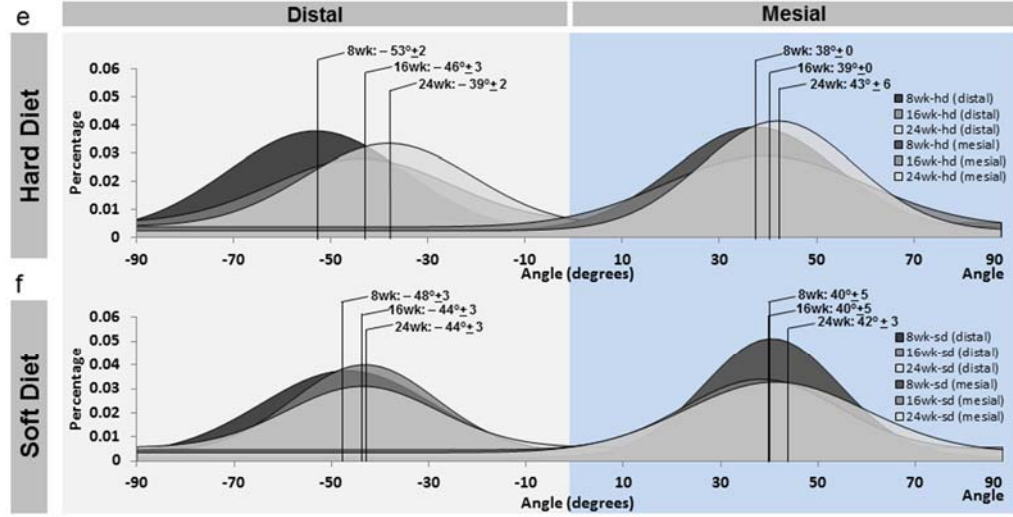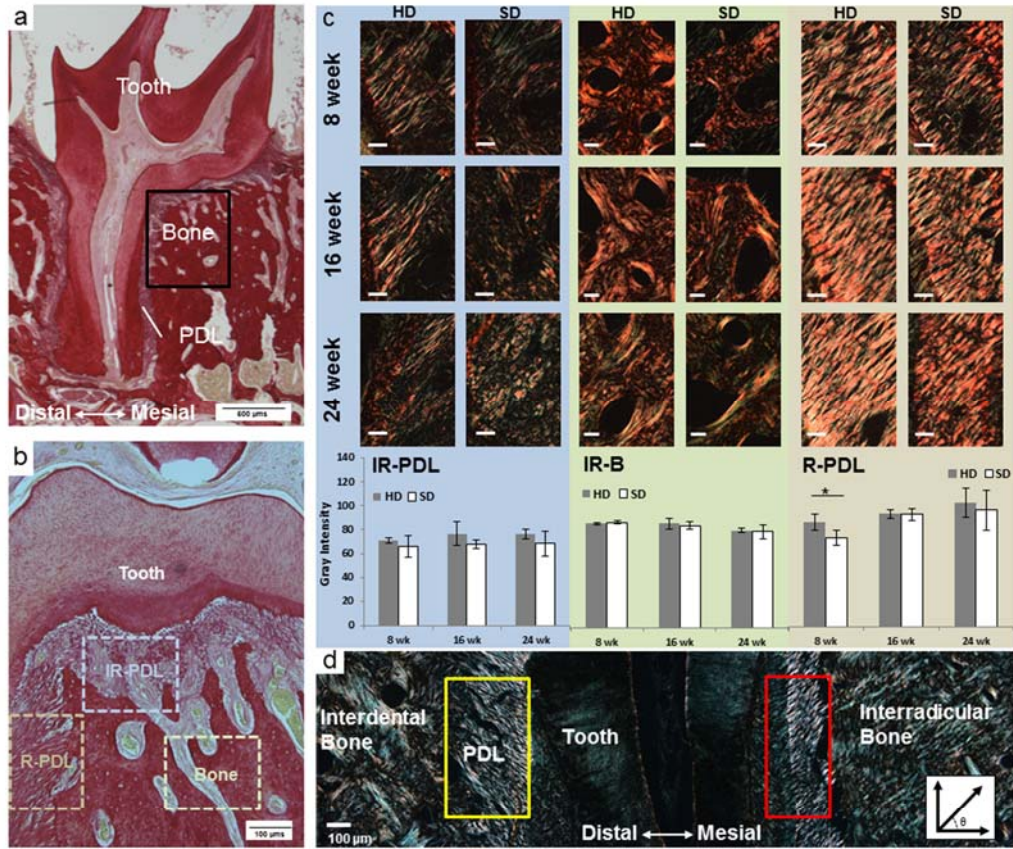
Figure 5.4. Collagen birefringence and PDL directionality across groups and age. a) Histology sections were stained with picrosirius red. b) Imaging was primarily focused around the furcation and root-PDL (R-PDL) surrounding the distal root of the 2nd molar. c) Birefringence signal was measured in the following regions: interradicular bone (IR-B), interradicular periodontal ligament (IR-PDL), and R-PDL. IR-PDL revealed a sponge-like configuration while R-PDL illustrated an increased collagen fiber orientation. Under polarized light, collagen orientation was quantified within IR-PDL, IR-B, and R-PDL. White bars are 100 µms. Trends show increased birefringence as a function of age within PDL regions and a decrease in birefringence as a function of age within interradicular bone. Statistical significance in birefringence between SD and HD is indicated with an (*) ($p<0.05$) and was only observed in the PDL of 8 week-old. Graphical representation of averages and standard deviations show no age-related trends for both hard and soft diet groups. (d) Images using polarized light microscopy show regions of distal (yellow box) and mesial (red box) regions used to calculate fiber orientation. Representative histogram distributions of fiber orientation in (e) hard diet and (f) soft diet are shown for 8, 16, and 24 weeks with total group average and standard deviations are shown. g) As a function of age trends included a decreasing difference in distal- and mesial-PDL orientation within and across hard and soft diet groups with age.
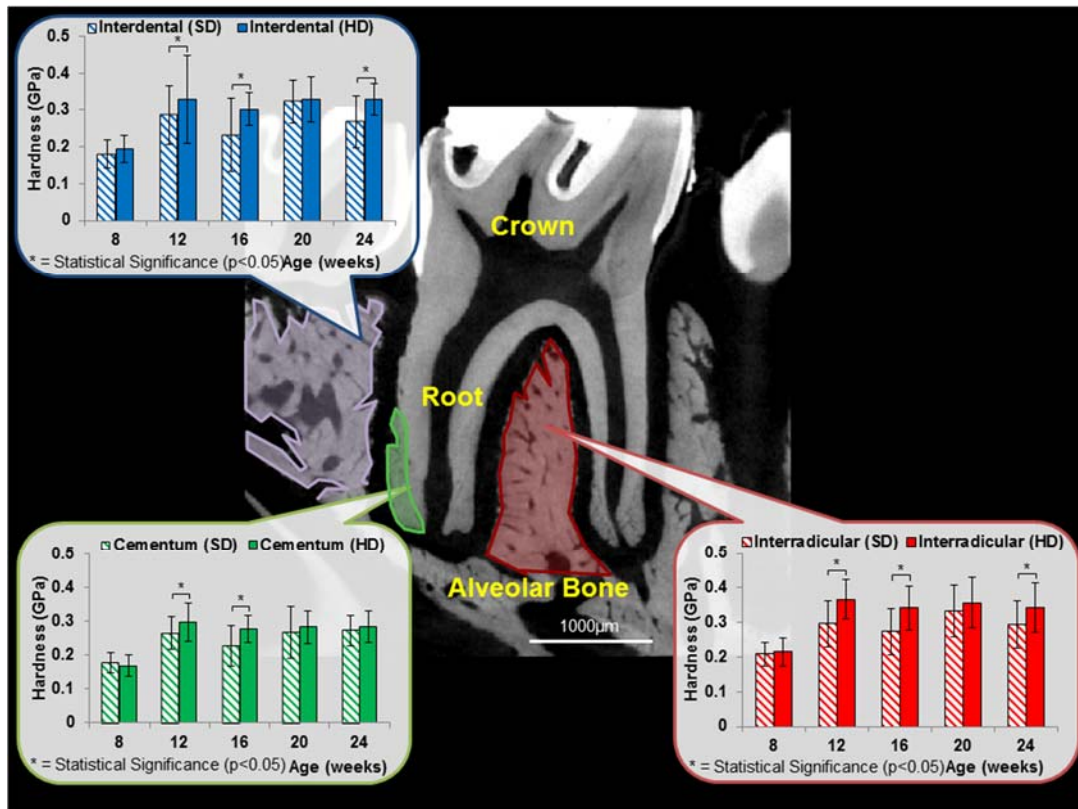
Figure 5.5. Microindentation and interradicular functional space of bone-PDL-tooth complexes. Microindentation was performed on cementum, interdental bone and interradicular bone. In general, interradicular bone was always harder than interdental bone which was always harder than cementum. While age-related trends were not found, hard diet groups illustrated an increased interradicular bone hardness compared to bone from rats on a softer diet. Additionally, interradicular functional space was measured by taking standard virtual sections between the distal and mesial buccal roots. Results show that interradicular space decreased in younger rats fed softer diet. *indicates statistically significant difference (p<0.05).
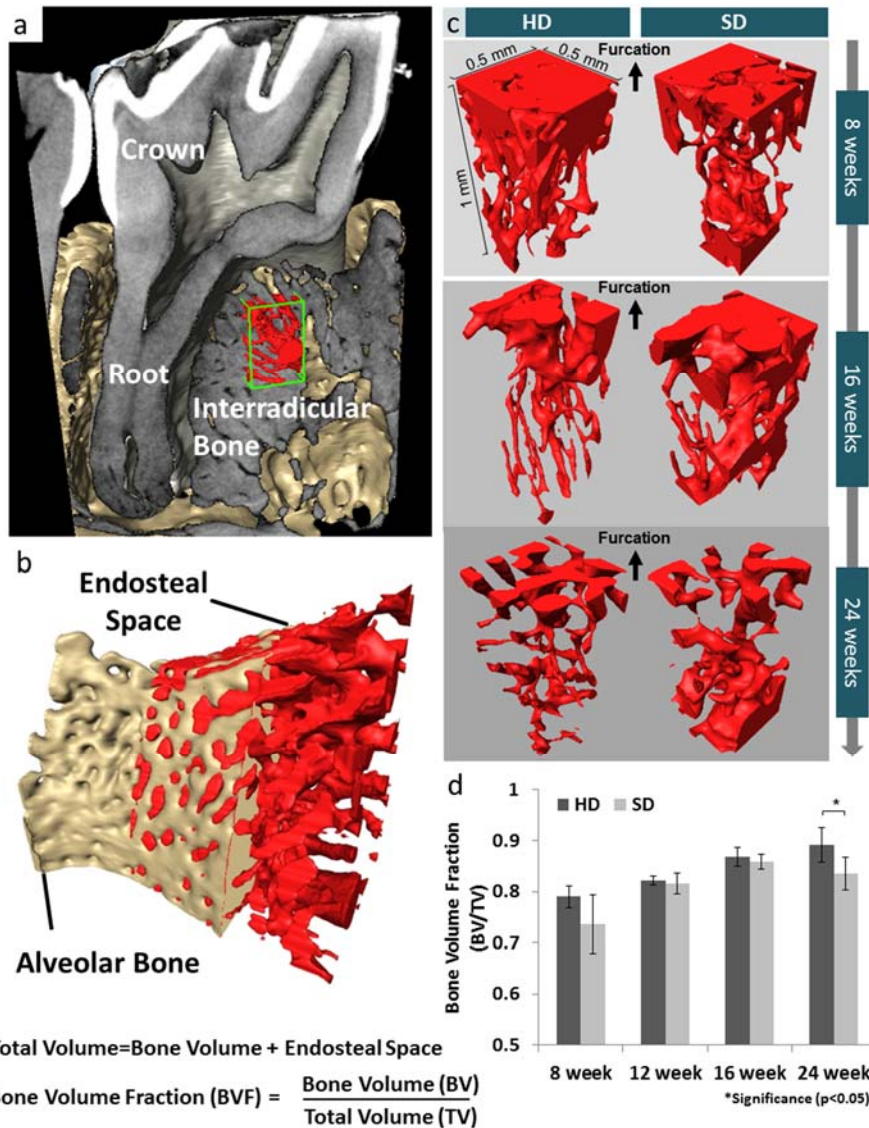
Figure 5.6. Comparison of bone volume fraction (BVF) of interradicular alveolar bone by using XRM tomography. (a) Digitally reconstructed structure of tooth in the alveolar socket illustrate the volume of interest in alveolar bone. (b) Bone volume fraction is illustrated as the ratio between bone volume to total volume (bone volume + endosteal volume (c)). (c) Endosteal volume decreased with age in both groups. However, greater endosteal volume in interradicular bone from those fed softer diet was observed. (d) BVF of HD was significantly higher than that of SD at 24 weeks.
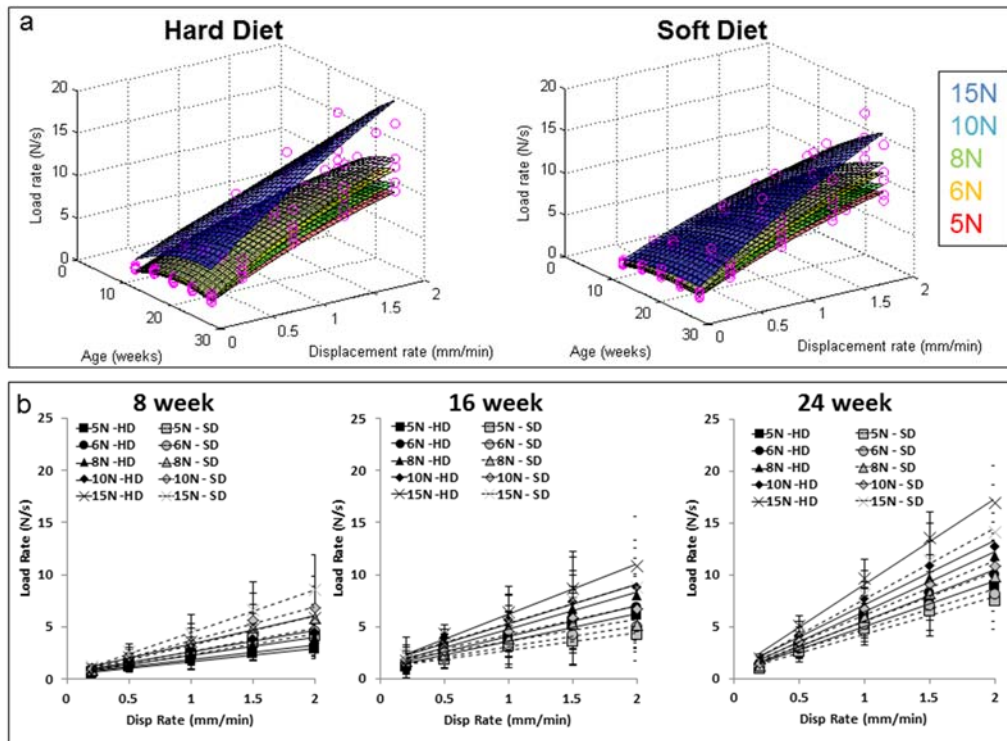
Figure 5.7. Comparison of reactionary responses of joints to loads. a) Higher reactionary response to load for HD older group was observed. b) Although similar trends were seen to a certain extent, the obvious trend was that the younger group fed SD demonstrated a higher reactionary response compared to its HD counterpart. Similar trend was not observed with an increase in age.
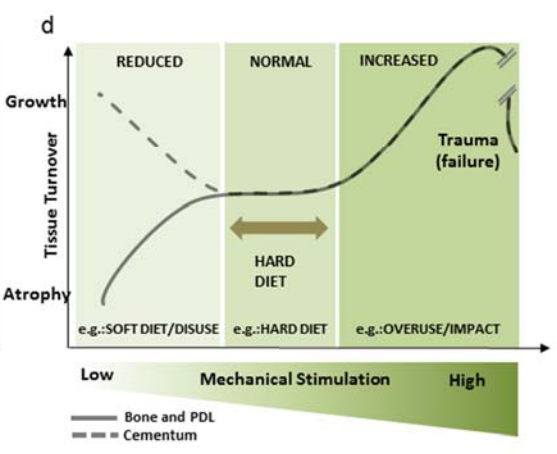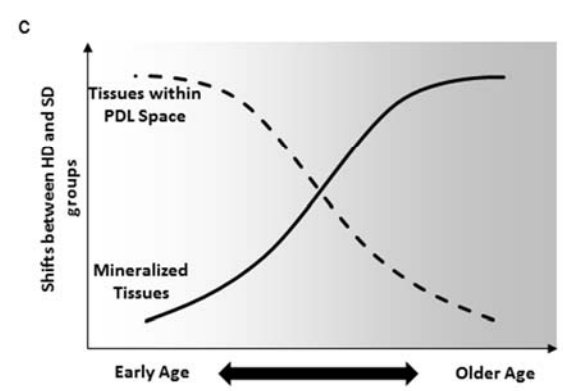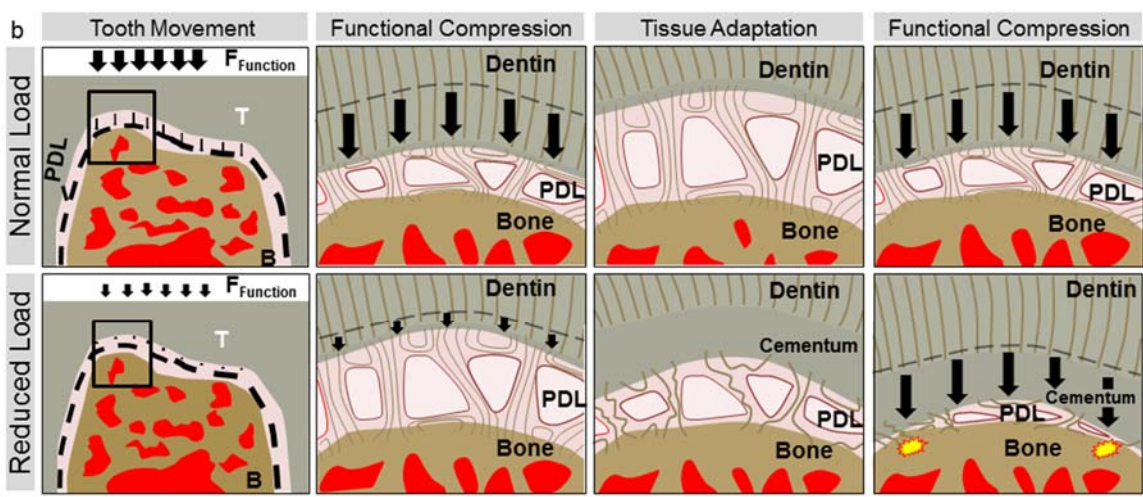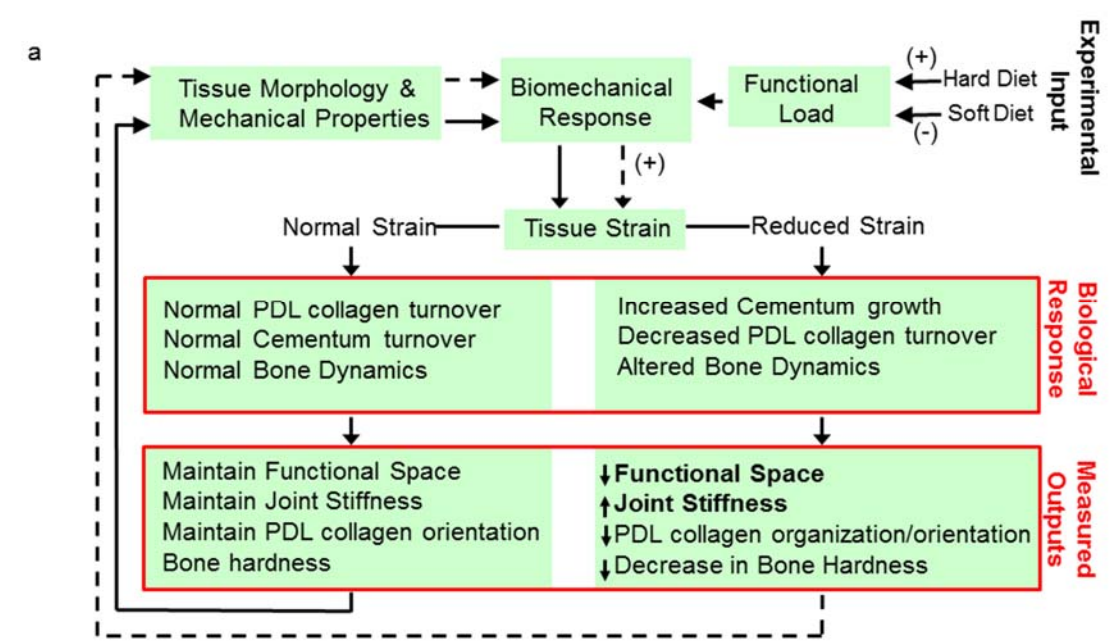
Figure 5.8. Postulated load-mediated adaptation of the dentoalveolar complex. a) Experimental workflow showing different food consistencies given to control (HD) and SD groups and changes in observed biological responses. (b) The fibrous joint compensates through decreased PDL-space through ingrowth of cementum and decreased orientation and organization of the collagen fibers. The shift in input signal prompts a shift in adaptive properties of tissues as indicated by site-specific measurements. However, if normal functional loads are placed on adapted tissues belonging to the SD diet group, they would likely be seen as traumatic loads prompting a damage response (yellow start bursts). (c) Shifts in outcomes due to load-mediated adaptations can be divided into two phases; early ages focused around the tissues within the PDL space, and shifts seen at later ages primarily as changes in bone mineral content and internal structure. (d) Normally chewing loads are accommodated by the dentoalveolar complex through compression of supporting tissues (PDL, bone, cementum) causing physiological strain due to tissue deformation (mixed-mode) and fluid flow from interstitial fluid movement. Mechano-responsiveness of localized cells in the regions of higher fluid flux and mechanical strain regulate a shift in tissue turnover in bone and the PDL morphology and material properties accordingly. A reduction of functional loads net a decrease in strain and is felt by the supporting tissue away from the physiological strain. Within bone, atrophy of tissue is usually seen, however, the opposite effect (growth) has been reported within cementum tissues.
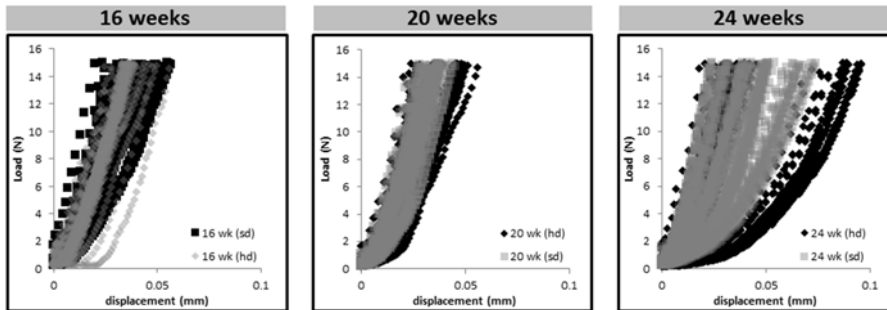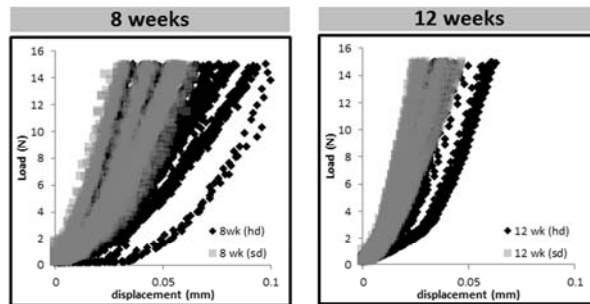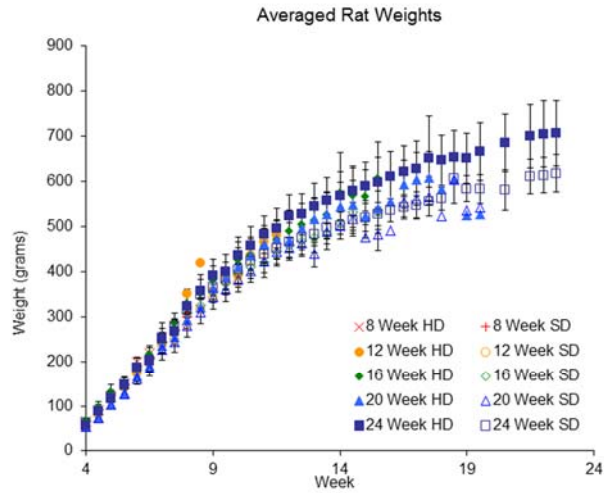
Supplementary Figure 5.1. (Fig. 5.S1). Average rat weights for HD and SD groups and load displacement curves from *in situ* compression tests. Rat weights from HD and SD groups fall within normal growth pattern boundaries from animal provider growth charts (www.criver.com). Load vs. displacement data for *in situ* loading tests for all displacement rates.
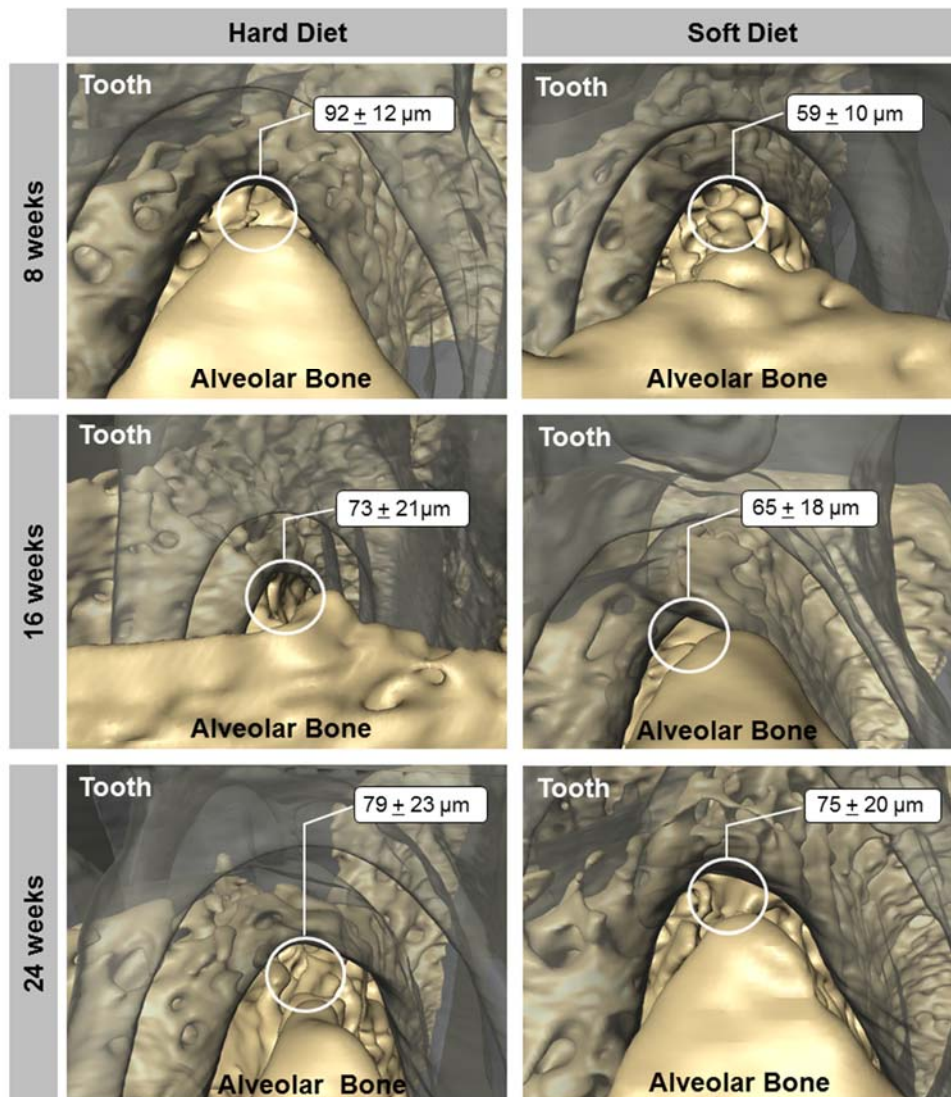
Supplementary Figure 5.2 (Fig. 5.S2). Representative images for interradicular functional space. Complementary images to **Figure 5.3** illustrate interradicular functional space with age (8-24 weeks) and between HD and SD groups.

CHAPTER 6. ADAPTATION OF ALVEOLAR BONE TO REDUCED FUNCTIONAL LOADS

6.1. Abstract

Objectives: Within this study, the shifts in biomechanics of the bone-periodontal ligament (PDL)-tooth fibrous joint due to reduced functional loads will be explained by providing insights into the coupled effect resulting from changes in form and material quality of the interradicular alveolar bone.

Methods: At 4 weeks of age, Sprague Dawley rats (N=60 total) were given either a hard pellet diet or a soft powdered chow. Changes in overall biomechanics of the bone-PDL-tooth fibrous joints were analyzed by raising the two groups to 8,12,16,20, or 24 weeks of age. An *in situ* loading device coupled to an X-ray computed tomography unit was used to highlight changes in functional space of the fibrous joint with age. Changes in natural occurrence of distal resorption across the two groups of rats were identified by mapping the distribution of osteoclasts as determined by staining for the expression of tartrate resistant acid phosphatase (TRAP). The architecture of alveolar bone was quantified by measuring bone volume fraction (BVF) from tomograms collected by performing micro X-ray computed tomography. Digital volume correlation (DVC) was performed on tomograms of fibrous joints from one hard and one soft diet rat at no load and under loaded conditions to investigate the maximum principal strain in adapted interradicular bones from respective groups. Elastic modulus values of interradicular bones from hard and soft diet groups were obtained under wet conditions using nanoindentation technique.

Results: A significant reduction in functional space (~90µm) was observed in the interradicular region of the fibrous joints subjected to reduced functional loads. Minimal changes in osteoclast resorption activity were observed within the interradicular bone, however significantly increased BVF (24 week mean BVF - HD:0.87 ± 0.02, SD:0.78 ± 0.05) and reduced elastic modulus (E_r) of interradicular alveolar bone (12 week mean Er - HD:14 ± 7 GPa, SD:10 ± 4 GPa) were seen as a function of age and diet. Increased maximum principal strain was observed in interradicular bone adapted to softer diet compared to HD specifically at lower loads.

Significance: Observed changes in bone volume fraction and elastic modulus indicate that adaptive processes within the interradicular region are mainly regulated during earlier ages of the mammal. Results demonstrate an optimization of form and material properties of the interradicular bone to meet functional demands placed on the bone-PDL-tooth fibrous joint. Although changes in form and material properties are mutually dependent, these physical properties could be inversely related to the age of a mammal.

6.2. Graphical abstract

a) Schematic of bone-tooth complex digitally reduced to illustrate tooth and alveolar bone configuration for *in situ* biomechanical testing. b) The furcation of the tooth saddles on interradicular bone and was identified as the region with the greatest reduction in functional space. c) The digital volume correlation (DVC) method was used to visualize differences in distributions of maximum normal strain within interradicular bone of rats adapted to hard and soft diets. d) From a multiscale perspective, changes in physical cues on organs resulting from the mechanical environment are transmitted through tissues to initiate biological responses in cells that over time can be related to biochemical processes leading to adaptations.

6.3. Introduction

The interradicular bone is a critical structural element that supports chewing forces. In a bone-periodontal ligament (PDL)–tooth fibrous joint, the functional space separating the tooth furcation and the alveolar bone is narrowest and therefore, from a biomechanics perspective, is the location of initial "contact" between the tooth and the alveolar bone (Chattah et al., 2009; Lin et al., 2013). During function, such as chewing, the interradicular bone serves as a natural fulcrum permitting "see-saw" and "screw-like" motions of the tooth (Chattah et al., 2009; Lin et al., 2013). Additionally, *in situ* loading data suggests interradicular alveolar bone as a major region experiencing deformation (Lin et al., 2013; Jang et al., 2014b). As such, given the morphology of the complex as well as its constituents including softer (gingival and PDL) and harder (cementum, dentin, enamel, and bone) elements, it is thought that the interradicular bone receives forces due to chewing, and that the tissues contained within the interradicular space experience increased biomechanical stimulation and adaptation.

Adaptation of interradicular bone is recorded as an increased metabolic activity in bone and often is related to resorption and formation dynamics (Baumhammers et al., 1965; Milne et al., 2009). However, to date, few studies have investigated the adaptations and functional optimization of interradicular bone due to shifts in functional loads. The effect of load-mediated changes with age due to a change in diet consistency was quantified as shifts in interradicular functional space, joint stiffness, and subsequent changes in alveolar bone hardness within the complex (Niver et al., 2011; Jang et al., 2015). Hence, the next step of the study was to investigate the interplay between form

and material properties specific to regions of increased compression that include the functionally active interradicular alveolar bone in the bone-PDL-tooth fibrous joint.

Subsequent shifts in the form and material properties of alveolar bone constitute the majority of adaptation and progress towards an optimized mechanical system to accommodate either reduced or increased functional demands. Hence, the objectives of this study were to: (1) demonstrate from a mechanical perspective that the interradicular interface with the tooth serves as a focal point for tissue compression; (2) correlate shifts in functional load with changes in formation/resorption dynamics within alveolar bone; and (3) characterize adaptations in morphology and material properties of bone when exposed to reduced chewing forces. To identify age related changes due to shifts in functional load, animals grown from 4 to 24 weeks of age were fed either a hard or soft diet. Computational methods highlighting site-specific loss of functional space and deformation of bony tissue were used to identify the interradicular bone as a hotspot for mechanical stimulation. The functional adaptations in form and material property shifts within the interradicular bone region was investigated as a function of age leading to a postulate discussing the interplay and optimization of form and material properties with age of the mammal.

6.4.   Materials and methods

6.4.1. Reduced functional load animal model

All experimental protocols were compliant and followed the guidelines of the Institutional Animal Care and Use Committee (IACUC). Male Sprague Dawley rats (N = 60; Charles River Laboratories, Inc., Willmington, MA) at four weeks of age were divided into two groups and fed one of two nutritionally equivalent foods: hard pellet food (Hard

Diet = HD; N = 30) or soft powdered chow (Soft Diet = SD; N = 30) (PicoLab 5058, LabDiet, Deans Animal Feeds, Redwood City, CA, USA); diets differed only in hardness (i.e. the soft diet was a pulverized version of the hard diet). Adaptations due to reduced function were studied at 8, 12, 16, 20, and 24 weeks. Hemimandibles were dissected and the right hemimandible was saved for *in situ* loading, micro X-ray computed tomography, and nanoindentation while the left hemimandible was processed for histology.

6.4.2. *In situ* biomechanical testing and XRM-tomography

Preparation of hemimandibles for *in situ* loading and X-ray computed tomography was done as previously described (Lin et al., 2013; Jang et al., 2014b). Prepared specimens were loaded using a load compression cell (MT500CT, Deben UK Ltd, Suffolk, UK) custom fitted to an XRM (Micro XCT-200, Carl Zeiss X-ray Microscopy, Pleasanton, CA). Each specimen was loaded 3 times to each permutation of peak load (5N, 6N, 8N, 10N, and 15N) and displacement rate (0.2 mm/min, 0.5 mm/min, 1.0 mm/min, 1.5 mm/min, 2.0 mm/min).

Two separate specimens (one 8wk HD and one 8wk SD) were prepared for *in situ* loading and X-ray tomography to perform digital volume correlation (DVC). Prior to loading, a tomogram was taken using the following parameters: 2500 projections, 75 KVp, optical magnifications: 4X and 10X, voxel size (~3.6 μm and ~1.6 μm for 4X and 10X magnifications respectively). After a period of rehydration (~1hr), the specimen was compressed at 0.2 mm/min to 7N of reactionary force. After target load was reached, displacement motors were locked in place and following specimen stabilization (~1hr), an additional tomogram was taken using the same scanning parameters. After scanning

was completed, the specimen was unloaded, hydrated, reloaded, and scanned at 15N of reactionary force and then the procedure was repeated at 20N of reactionary force.

6.4.3. Mapping functional-space shifts

Tomograms were analyzed using Avizo (Avizo 9.0.0, FEI Visualization Sciences Group, Burlington, MA). Segmentations of tooth and alveolar bone were calculated based on intensity cues as a result of X-ray attenuation and the segmented data were used to generate surface meshes. Morphological features within the alveolar bone and the tooth were used for rigid body registration and to define surface meshes at unloaded (0N) and loaded (7N) regions. For each node on the tooth surface mesh at the unloaded and loaded configurations, the distance to the closest node on the alveolar bone was determined. Loss of functional-space during *in situ* loading was calculated by taking the difference between loaded and unloaded functional-spaces (net change functional-space = [functional space at 0N] – [functional space at 7N]). The net change in functional-space was mapped on the tooth surface.

6.4.4. Mapping TRAP(+) regions within the complex

Left hemimandibles were fixed, decalcified, and embedded within paraffin as previously described (Lin et al., 2014). Tartrate-resistant acid phosphatase (TRAP) staining for osteoclasts was performed using an acetate buffer solution in conjunction with AS-MX phosphate and fast red TR salt. Tissue sections were counterstained using hematoxylin. More details have been reported previously (Lee et al., 2013). Individual multinucleated cells displaying a TRAP(+) response were tallied for each slide on the distal and within the interradicular alveolar bone. Statistically significant differences

between hard and soft diets were calculated for each age group using the Student's t-test.

6.4.5. Bone volume fraction analysis of interradicular bone

Bone volume fraction (BVF) was calculated using subvolumes within XRM tomograms (Parfitt, 1988; Bouxsein et al., 2010). Following segmentation of alveolar bone (Avizo 9.0.0), the total volume of the interradicular bone within the subvolume was calculated by applying a morphology closing algorithm allowing for the endosteal spaces to fill in. Values for BVF were generated by dividing the bone volume by the total volume (Parfitt, 1988; Bouxsein et al., 2010). Statistically significant differences between hard and soft diets were calculated for each age group using the Student's t-test.

6.4.6. AFM-based nanoindentation of interradicular bone

Hemimandibles (n=3 for each ageXdiet group) embedded in epoxy were sectioned under wet conditions using a diamond wafering blade and a low speed rotary cutter (ISOMET, Buehler Ltd., IL, USA). Cutting planes were set to be orthogonal to the occlusal plane of the molars. The sectioned surface was further polished using silicon carbide grit of sizes 800 and 1200 (Buehler Ltd., IL, USA) followed by sequential fine polishing using a diamond suspension slurry of grades 6,3,1, and 0.25 µm (Buehler Ltd., IL, USA) (Ho et al., 2009).

Nanoindentation (Nanoscan 4D, Nanounity, Moscow, Russia) on polished surfaces was performed under wet conditions using a Berkovich tip. Indents were made using 2000 µN load and were placed 16µm apart on the interradicular bone regions of the second molar. Reduced elastic modulus (Er) was calculated using Oliver-Pharr method (Oliver and Pharr, 1992).

Elastic modulus for age by diet was skewed so a nonparametric test of age X diet, overall diet, overall age, and age-specific diet effects was performed with stepdown Šidák tests to correct for multiple comparisons. Statistical analyses were performed with SAS version 9.4 (SAS Institute, Inc., Cary, NC).

6.4.7. Digital volume calculations for alveolar bone

Mapping of strain due to compression in interradicular alveolar bone was done on a single specimen from each diet group (8 weeks only). Piecewise digital volume correlation (DVC) was performed to compare deformations between 0N-7N, 7N-15N, and 15N-20N configurations as previously described (DaVis software, LaVision Inc., Ypsilanti, MI) (publication in review). Noise floor to determine the accuracy of strain calculations through DVC of alveolar bone at no load and loaded conditions is shown in **Figure 6.2**. DVC parameters were interrogation window size of 64 pixels, with 50% window overlap, and 64 pixels of gauge length where both masking and cropping was used to represent data with 25% minimum fraction of valid pixels and pixel size of 1.6μm.

6.4.8. SAWBONES™ preparation and experimentation

SAWBONES™ (SAWBONES™, Pacific Research Laboratories, Inc., Washington, USA) made from polyurethane with different porosities (10PFU and 20PFU) were cut into small cubes (~4.5mm length each side) and tested for using the same *in situ*/XRM setup utilized for bone-PDL-tooth imaging. Separate specimens were imaged at 0N and 14N or 25N (loaded at 0.2 mm/min). Images were analyzed using DVC software at 50% overlap and 128 pixel interrogation window size to accommodate for the large pore sizes. Similar method used to determine bone volume fraction was used to calculate volume density for SAWBONES™ (see section 2.7). Additionally, digital models were generated

from SAWBONES™ tomograms (MicroView, Parallax Innovations, Ilderon, ON, Canada; Meshlab 1.33, 3D-CoForm, Brighton, UK) and analyzed using finite element methods (ANSYS 16.2, ANSYS, Inc., Canonsburg, PA, USA) to test for differences in deformation as a function of size and density of pores (i.e. keeping the material properties of the model the same for each SAWBONES™ type).   Model conditions: [Elements: 331043 (SAWBONES™ 10); 540626 (SAWBONES™ 20)] [Nodes: 614837 (SAWBONES™ 10); 986674 (SAWBONES™ 20)], modulus of elasticity equal to 200 MPa, assuming elastic behavior.

6.4.9. Statistical modeling and significance

Nonlinear quadratic mixed effects regression models with normal random animal X replicate effects were used for each of 125 combinations of age X force X displacement rate to model the relationship of displacement on load (load displacement curve) between diets with a 3 degree of freedom (3 d.f.) test of the diet difference parameters (intercept, linear slope and quadratic slope). These models were also used to predict the difference between diets in displacement to yield 5N, 10N, and 15N loads as

$$\widehat{disp}_S - \widehat{disp}_H = \frac{-(\hat{b}_1+\hat{g}_1)+\sqrt{(\hat{b}_1+\hat{g}_1)^2-4(\hat{b}_2+\hat{g}_2)(\hat{b}_0+\hat{g}_0-load)}}{2(\hat{b}_2+\hat{g}_2)} - \frac{-\hat{b}_1+\sqrt{\hat{b}_1^2-4\hat{b}_2(\hat{b}_0-load)}}{2\hat{b}_2},$$

where b_0 is the intercept for hard diet, b_1 is the linear slope for hard diet, b_2 is the quadratic slope for hard diet, g_0 is the intercept difference from soft diet, g_1 is the difference in linear slope from soft diet, g_2 is the difference in quadratic slope from soft diet, and *load* is 5, 10, or 15N.

6.5.   Results

6.5.1. Changes in tooth-bone configuration during *in situ* loading of the tooth-PDL-bone complex

A load-displacement curve postulating reactionary forces due to various tissue contributions is shown in **Figure 6.1a**. Also shown are the virtual sections of the respective multi-load tomograms of tooth-PDL-bone. By tracking the tooth movement within the socket, the changes in functional space were measured, showing that the reduction in functional space was greatest around the interradicular alveolar bony crest (**Fig. 6.1b**). Additionally, visible deformation within alveolar bone was seen within the interradicular regions (**Fig. 6.1a and 6.S1**). Statistically significant differences between diets were seen from the 3 d.f. quadratic model tests of the load displacement curves in the vast majority (116 or 93%) of the 125 age X peak load X displacement rate combinations (**Fig. 6.1c**).

6.5.2. Osteoclast activity in the alveolar bone complex

The distribution of TRAP(+) cells within the regions of interest are shown in **Figure 6.2a**. Quantitative analysis of number of TRAP(+) cells showed preferential localization in the distal region within all specimens regardless of age or diet group. Within the distal portion of the root, TRAP(+) cell counts were significantly greater in the HD group compared with the SD group at 8 and 16 weeks of age ($p < 0.05$). The number of TRAP(+) cells decreased with an increase in age regardless of HD or SD groups. There was little to no presence of TRAP(+) cellular activity within interradicular bone which did not change with age or diet. Counterstaining of tissue sections revealed cement lines surrounding the endosteal spaces indicating an active remodeling process.

6.5.3. Age and diet change in bone volume fraction of interradicular bone

Relationship of tooth surface with alveolar socket was shown in **Figure 6.2b**. Regions segmented into either alveolar bone or endosteal space are shown in **Figure 6.2b**. Changes in BVF were seen as a function of age and diet. With an increase in age, the BVF was shown to increase. At 24 weeks, the HD alveolar bone had a higher BVF than alveolar bone of SD groups.

6.5.4. Elastic modulus changes in the interradicular alveolar bone as a function of age and diet

The histogram distribution of elastic modulus from nanoindentation is shown in **Figure 6.2c**. For elastic modulus of alveolar bone, the nonparametric age X diet interaction effect was statistically significant (p<0.001), indicating the diet effect differed between the age groups. At 12 weeks, the elastic modulus of alveolar bone within the HD (14$\pm$7 GPa) was significantly greater than that of SD (10$\pm$4 GPa). However, at 24 weeks, the elastic modulus of HD and SD groups were similar and did not show significant shifts.

6.5.5. Strain distribution within interradicular in response to *in situ* loads

Regions of alveolar bone highlighting the interradicular portion for digital volume correlation (DVC) is shown in **Figure 6.3a**. The 3D strain solutions produced from DVC of alveolar bones taken from 8 week old rats belonging to HD and SD at 8 weeks are shown in **Figure 6.3b** and **Figure 6.3c**, respectively. Major differences between HD and SD multi load deformations were seen primarily at the 0-7N regions where the SD showed increased strain at the crest of the interradicular bone compared with HD groups. Slight differences were seen between HD and SD at 7-15N and 15-20N and attributed to physiological variations between the animals.

145

6.5.6. Changes in the strain distribution as a function of modeled specimen porosity

Volume fraction, density, macro modulus, and nano modulus for SAWBONES™ 10 and 20 are shown in **Figure 6.4b**. Load displacement curves for *in situ* loading of DVC specimens are shown in **Figure 6.4c**. At 14N, max normal strain results (**Fig. 6.4d**) show an increase in strain in SAWBONES™10 (increased porosity) compared with strains within SAWBONES™ 20 (decreased porosity). At 25N, max normal strain magnitudes were similar, indicating that plastic deformation must have occurred at the higher loads. Finite element analysis (FEA) confirmed these results by showing an increased strain (**Fig. 6.4d**) within the large pore specimen compared small pore specimen under an equivalent loading conditions.

6.6. Discussion

Adaptations to functional loads occur at multiple hierarchical levels ranging from cellular- to organ-levels. Our previous study focused primarily on the shifts in organ-level biomechanics as a result of reduced function (Jang et al., 2015). This study investigates adaptations within the mechanically stimulated interradicular bone by relating to its material properties and form. Load-mediated or functional adaptation serves as a key epigenetic driving force for growth and development (Carter and Beaupré, 2007; Lieberman, 2011). In the musculoskeletal system including oral and craniofacial load bearing complexes, shifts in natural strain gradients within the supporting harder elements can result due to a change in function from daily activities (running, jumping, chewing, etc.) (Prendergast and Taylor, 1994). Shifts in physical stimuli (either in magnitude and/or frequency) produced from functional disturbances are finally "felt" by cells through a

series of events that include fluid flow, attachment to other cells, and with the extracellular matrix (ECM) (Duncan and Turner, 1995; Turner, 1998; Bonewald, 2006). As a result, the autoregulation "intelligence" that is naturally programmed in living organisms is what provides the organism with plasticity which can be leveraged to meet the functional demands. The response to functional demands is illustrated through output signals that include high expressions of biochemical markers until equilibrium to an input signal is reached. Several authors have described this as a feedback mechanism and have modeled it as a closed loop control system designed to optimize structure/form/morphology for a known mechanical stimulus (Frost, 1987; Prendergast and Taylor, 1994; Jaalouk and Lammerding, 2009). With respect to load-bearing bone, the regulation of tissue turnover including activation to resorption to formation (A$\rightarrow$R $\rightarrow$F), and activation-resorption (A$\rightarrow$F) has been described by several models (e.g. mechanostat model) where formation and resorption are dependent on the dynamics (gradual or abrupt shifts) in mechanical environment (Frost, 1987).

The bone-PDL-tooth complex is an excellent model for analyzing functional adaptation due to the presence of multiple biological interfaces within a functional space of 70 to 120 microns (in rodents), that permits distribution of consistent functional loads that are highly dynamic in nature (Berkovitz, 1990; Nanci, 2007; Niver et al., 2011). While loads placed on the complex are primarily generated from the muscles of mastication, shifts in load direction, magnitude, and frequency depend on a variety of factors both intrinsic and extrinsic. Adaptations resulting from shifts in pathologic (e.g. bruxing) (Mavropoulos et al., 2004a, 2004a), therapeutic (orthodontics) (Bondevik, 1984), and physiologic (e.g. chewing) (Tanaka et al., 2007) continue to be studied to underline

adaptive processes leading to clinical scenarios. In addition to shifts in input signal, site specific adaptations within the complex have been highlighted (Niver et al., 2011; Lin et al., 2013, 2014; Jang et al., 2015). Within the context of this study, adaptations specific to interradicular bone were studied as a response to shifts in diet consistency (hard diet vs soft diet). The interradicular bone was chosen as it is the structural element on which the tooth pivots when in function (Chattah et al., 2009). Previous studies within our group using a reduced functional load model on Sprague Dawley rats have highlighted age related adaptive shifts in bone-tooth biomechanics and associated tissue properties regardless of the biomechanical signals (Jang et al., 2015). It is plausible that the effect of reduced functional loads modeled by using a powdered diet is less than the effect from a hypo-function model (i.e. liquid diet or extracted opposing molar). However, such models introduce additional confounding factors such as those related to a change in nutrition/and super-eruption of teeth due to lack of an antagonist making it difficult to draw reasonable conclusions related to functional loads.

From a mechanics perspective, the dentoalveolar complex can be modeled as several tissues (tooth, alveolar bone, PDL) loaded in series (Naveh et al., 2012b). It is the intrinsic constitutive properties of the individual tissues and the collective nature that are constantly leveraged for clinical interventions including tooth movement and bone augmentation to maintain function. The constitutive properties of the tissues involved in functional maintenance of the bone-PDL-tooth complex differ greatly due to the mineral density and structural organization (Nanci, 2007). Therefore, it is conceivable that loads are distributed and transmitted in the order of softer to harder elements that include deformation in PDL followed by alveolar bone and tooth related tissues: cementum, dentin

and enamel (all grouped together as each of the tissues involved, i.e. dentin, enamel, cementum, have a greater mineral density and modulus than that of alveolar bone) (Nanci, 2007). This pattern of load travel is reflected in the multi-load data illustrating most PDL deformation in the 0-7N region followed by deformations in alveolar bone at higher loads (**Fig. 6.1 and 6.S1**). Deformation in alveolar bone is primarily seen within the crest of the alveolar bone, the region that serves as a fulcrum point for tooth rotation (Chattah et al., 2009). Further demonstrating this trend are the calculations illustrating differential strains in the interradicular crest as it is due to the region with the greatest amount of functional space reduction (~90μm) (**Fig. 6.1b**). While other portions of alveolar bone also undergo mechanical stimulation (e.g. interdental bone is deformed due to the rotational movement of the tooth within the socket), it is reasonable to conclude that the majority of alveolar bone deformation occurs within the crest of the interradicular bone. Additionally, statistical modeling of load-displacement curves (**Fig. 6.1c**) revealed statistically significant differences at all ages within all peak loads between soft and hard diet groups. It is our continued hypothesis that within lower loads, the main contributor to the mechanical response is the soft tissues (i.e. PDL) while the effect due to harder tissues is felt at higher peak loads (**Fig. 6.1a**). Therefore, it is reasonable to assume that adaptations within the PDL and alveolar bone occur at all ages, however it is recognized that a transducer sensitive to lower loads would provide soft tissue related biomechanical response.

The main mechanisms for functional adaptation within bone are regulated by formation and resorption dynamics (Frost, 1987). Bony tissues experiencing physiological loads will result in "normal" growth. Per the Utah paradigm, shifts in these

physiological loads in either positive or negative direction are met with a respective increase or decrease in bone metabolic activity and turnover (Frost, 1998, 1999). Since the dynamics of bone growth consists of resorption and formation processes, changes in the osteoclastic distribution was determined through staining for expression of TRAP. TRAP(+) cells were identified primarily on the distal side of the root in agreement with the natural distal drift process that occurs throughout a rodent's lifespan (Sicher and Weinmann, 1944; Macapanpan et al., 1954). Additionally, the reduction of osteoclasts on this distal PDL- bone interface in SD groups compared with HD groups suggests that this naturally occurring distal drift is linked to the mastication loads experienced by the PDL-bone interface. Few TRAP(+) cells were also seen within the interradicular crest and could possibly serve as a mechanism for the relatively narrowed functional space in SD groups compared with control animals (**Fig. 6.2a**). However, few or no TRAP(+) cells were seen within the interradicular bone proper suggesting that changes in bone turnover dynamics are mostly due to shifts in formation activities. To confirm this hypothesis, future studies identifying formation and mineralization activities (e.g. alkaline phosphatase, bone sialoprotein, osteocalcin) would be recommended.

The minimal osteoclastic activity within the interradicular alveolar bone was correlated with turnover dynamics along the endosteal spaces causing a change in internal architecture and material properties. Formation process results in the natural closing of the endosteal spaces subsequently leading to an increase in BVF (**Fig. 6.2b**). Relative to physiological loading, the reduced functional load group also showed an increase in BVF with an increase in age, albeit at a lower rate and was significantly lower in older groups. The resulting changes could be due to either an increase in formation

activity, decrease in resorption activity, or a combination of both. The lack of TRAP(+) cell activity within the region indicates that the adaptive process leading to a shift in BVF is primarily due to a shift in adaptation affected by mineral formation related events. Complementing these findings are the reductions in interradicular alveolar bone elastic modulus in SD groups compared with HD (**Fig. 6.2c**). This shift in elastic modulus could be due to a decrease in the local mineralization and osteocytic (perilacunar fluid flow that would prompt osteocyte activity) maintenance of the bone and its resulting physical properties, a process which could be controlled by (Rawlinson et al., 1996; Taylor et al., 2007) modulating the magnitude and frequency of functional loads. It is plausible that reduced functional loads can cause decreased fluid flow and consequently less mechanobiological activity to prompt and maintain formed alveolar bone.

To investigate adaptations in form and material properties from a biomechanics perspective, adapted joints at 8 weeks of age were loaded using similar loading schemes and peak loads as identified in Jang, et al. 2015 (Jang et al., 2015). The 8 week time point was primarily chosen due to the observed shift in organ level biomechanics (Jang et al., 2015). Differences in alveolar bone strain distributions demonstrated that these adaptations are noticeable from a biomechanics perspective as early as 4 weeks from weaning (i.e. 8 weeks of age). Increased strains in the interradicular bone from SD groups compared with HD groups were primarily seen at lower sections of the loading curve (0-7N) (**Fig. 6.3**). These results could primarily be due to the softer elements including the PDL and are a consequence of decrease in interradicular functional space in joints from SD group (Jang et al., 2015). Although an increase in strain in bone was observed, the change was minimal at higher load differentials (7-15N and 15-20N). This can be

explained by the lack of significant differences in the physicochemical properties of bone including the form at 8 weeks (Jang et al., 2015) (open compared to a closed configuration). While rats subjected to reduced functional loads for 4 weeks (following weaning at 4 weeks, rats were given softer diets) were only tested, it is plausible that the strain differences would likely be insignificant at loads lower and significant at higher loads in older groups. This is because of similarities in interradicular functional space at older age groups and a divergent behavior between groups at higher loads as a result of the significant differences in the form of bone and material properties between groups (Jang et al., 2015).

It is apparent that adaptation of interradicular bone to functional loads is shown as a change in material property (reduced elastic modulus) and a change in form (BVF). These two effects are coupled and to decouple within an *in vivo* or *ex vivo* model offers to be a challenge. However, by using standard materials, the effects of form and material properties toward mechanical response can be decoupled. In this study, we chose to use polyurethane foams with different porosity fractions (10 and 20 PFU) albeit different nanomechanical properties. Results indicated that an increase in volume fraction of pores (20 to 10) led to decreased stiffness and increased strain (**Fig. 6.4**). These results were also confirmed with computational modeling where for the same material properties of the SAWBONES™ increased deformations were observed in volumes with larger pores and lower pore density (**Fig. 6.4**). Although the nanomechanical properties are different, it is unlikely that the strain values would change given the dependency of DVC method on optical magnification (publication in review) and in turn the accuracy of resulting strains.

The processes by which form and material properties adapt to functional loads is highly dynamic and occur at multiple scales (Carter and Beaupré, 2007). From an organ-level perspective, functional loads for the dentoalveolar complex primarily originate from mastication cycles which are generated by the muscles of mastication to generate a food bolus (**Fig. 6.5**). The majority of functional loads generated from mastication are then absorbed by the tissues that permit function through micromotion within the alveolar socket, which is primarily vertical in nature, but also includes a rotational component with the interradicular bone serving as the fulcrum(Chattah et al., 2009). The micromotion of the tooth causes local deformations, which generates semiautonomous regions in perpetuity by stimulating nearby cells in the PDL-alveolar bone, PDL-cementum attachment sites and respective interfaces. In the interradicular region of alveolar bone, the primary forms of the mechanical stimulation are the fluid flow through the cannicular/osteonal network as well as deformations throughout the mineralizing extracellular matrices of cementum and alveolar bone (Bonewald, 2006). The cellular response to these local strain manifests primarily as a shift in remodeling rates within the interradicular region altering both the shape of the bone as well as its material properties. These changes result in adapted tissues which could behave differently when exposed to identical functional load. This generates feedback loops at multiple scales and the eventual optimization of the tissues/organ to enable form and tissue properties to meet functional demands.

Discretizing temporal changes in organ biomechanics as related to changes in load responses of individual tissues allows for new insights into adaptive responses of tissues and collectively the organs (data trends provided in **Fig. 6.5c**) (Jang et al., 2015). The

normal manifested adaptations to physiological loads in alveolar bone are the closing endosteal spaces in alveolar bone due to increased bone forming activities and hardening of the existing bone material due mechanosensitive osteocyte activities (**Fig. 6.5b**). Within alveolar bone, it should be noted that shifts in functional loads due to shifts in diet consistency (i.e. hard to soft) most likely regulate tissue quality through formation activities (**Fig. 6.5b**). Convergence patterns in biomechanical response (i.e. stiffness) (**Fig. 6.5**) suggests that early age adaptations occur within the PDL-space to the dynamics of lower magnitude of loads but applied at higher frequencies while a convergence in adaptations occurs due to slower metabolizing bone with an increase in age. From the changes seen in this model, it appears that there exists a cross over point between changes in morphology and material properties with an increase in age (**Fig. 6.5c**) and that this should be acknowledged when directing clinical intervention.

6.7. Conclusions

In conclusion, this study highlights adaptation of interradicular bone to meet the demands due to reduced mastication. In line with our previous results, it can be deduced that softer and harder tissues of the dentoalveolar complex are affected but at a different rate which can change with age. At younger ages, tissues and interfaces within the functional space tend to exhibit differences in properties while adaptations in form are more apparent in the alveolar bone with older ages. Specific to alveolar bone, it is highly probable that a regulation between osteoblast and osteocyte activities is the key in meeting functional demands and should be investigated by targeting molecules representative of a balanced act between formation and resorption related events not

limited to tissues per se, but interfaces within the biomechanical continuum of the bone-PDL-tooth complex.

In addition to identifying specific pathways linked to functional adaptation, we propose that the spatial distribution of functional adaptation activities can be associated with mechanical information from *ex vivo* simulated data. Using our current setup, connections between the spatial distribution of deformations with markers of resorption and formation can be made. However, it is recommended that significant advances in *ex vivo* biomechanical experimental modeling need to be made to direct physiological relevance of associating shifts in organ-level biomechanics to shifts in tissue-level mechanobiological events.

6.8.   Figures and Tables

a

4x Scans

(Joint Fracture)

Load

20N — Strain Hardening + Hard Tissue Effects
15N —
Mixed Effects
7N — Bulk Ligament Strain
0N —

Displacement

4x

10x

*4x images are 4mm x 4mm, 10x are 1.5mm x 1.5mm

b

Tooth

Alveolar Bone

Tooth at 0N
Tooth at 7N

Mesial   Distal

100

Loss in Functional Space (µm)

0

c

		Age (weeks)					
	Force (N)	8 # p<=0.05	12 # p<=0.05	16 # p<=0.05	20 # p<=0.05	24 # p<=0.05	all # p<=0.05
Hard	15	5	5	5	5	5	25
	10	5	5	5	5	5	25
Mixed	8	5	5	4	5	5	24
	6	5	5	4	3	4	21
Soft	5	4	5	4	4	4	21
	all	24	25	22	22	23	116

Figure 6.1. (a) A representative nonlinear load-displacement curve illustrates plausible biomechanical events as the tooth is compressed into the alveolar socket (refer to **Figure 6.S1** for gif animation). Identical virtual sections taken at 0N, 7N, 15N and 20N load increments illustrate tooth-alveolar socket relationships within increasing load. White bars = 200 μm. (b) The tooth and bony socket configuration shows the relative position of the tooth at 0N and 7N and a color map of narrowing and widening of functional space highlighting the furcation and the apex during mastication. (c) Analysis of load-displacement curves showing the number (out of 5) of statistically significant diet differences (for each displacement rate) at different peak loads and ages (3 d.f. test from nonlinear quadratic mixed models).

a

Distal

IR bone

AB

PDL

300µms

Distal

IR bone

CL

8wk – HD   16wk – HD   24wk – HD

8wk – SD   16wk – SD   24wk – SD

Osteoclasts

◇ HD □ SD

Age (weeks)

* - Sig. diff. (p<0.05) between HD and SD groups

b

Form Adaptations

Tooth

Endosteal Space

Interradicular Alveolar Bone

HD   SD

*Diet significance (p<0.05)

Bone Volume Fraction (BV/TV)

8 week   12 week   16 week   24 week

C

Material Property Adaptations

9   14

● 12wk HD   ○ 12wk SD

Frequency

Elastic Modulus (GPa)

9   10

● 24wk HD   ○ 24wk SD

Frequency

Elastic Modulus (GPa)

Age	Diet	Elastic Modulus (avg ± sd)
12 wk	HD	14±7
12 wk	SD	10±4
24 wk	HD	10±5
24 wk	SD	9±5

158

Figure 6.2. (a) TRAP(+) expression by osteoclasts is dominant on the distal side of the bone-PDL-tooth complex. Multinucleated TRAP(+)cells (indicated by arrows) can be observed at the PDL-bone enthesis. Osteoclast count along the distal edge of the dentoalveolar complex was significantly ($p < 0.05$) lower in 8 and 16 week old rats fed softer foods. Within the interradicular bone, cement lines (shown with the dotted lines) indicate a footprint of combined osteoclastic and blastic activities. However, TRAP activity within the interradicular bone region was minimal and did not vary with age or diet. Alveolar Bone (AB), Periodontal Ligament (PDL), Distal (D), Interradicular (IR), Cement Line (CL). Black bars are 100 μm. (b) XCT segmented image illustrates the surface of alveolar bone and the endosteal space in comparison to the furcation of the tooth. Adaptations in form were measured in interradicular bone by calculating bone volume fraction (BVF) from X-ray tomograms. BVF of interradicular bone increased with age and a significant difference between HD and SD at 24 weeks was observed. (c) Adaptations in physical properties of interradicular bone were in the form of decreased elastic modulus of alveolar bone from SD group compared to the HD group at 12 and 24 weeks of age, albeit the difference in elastic modulus values between the two groups was lower in the 24 week suggesting a converging pattern with an increase in age. Mean elastic modulus and standard deviation by diet for 12 and 24 week groups.

a *in situ* load

Coronal

Apical

tooth

bone

b

0N-7N   7N-15N   15N-20N

15%

Max Normal Strain (%)

1 mm   1 mm   1 mm

Hard Diet

0%

c

0N-7N   7N-15N   15N-20N

15%

Max Normal Strain (%)

1 mm   1 mm   1 mm

Soft Diet

0%

160
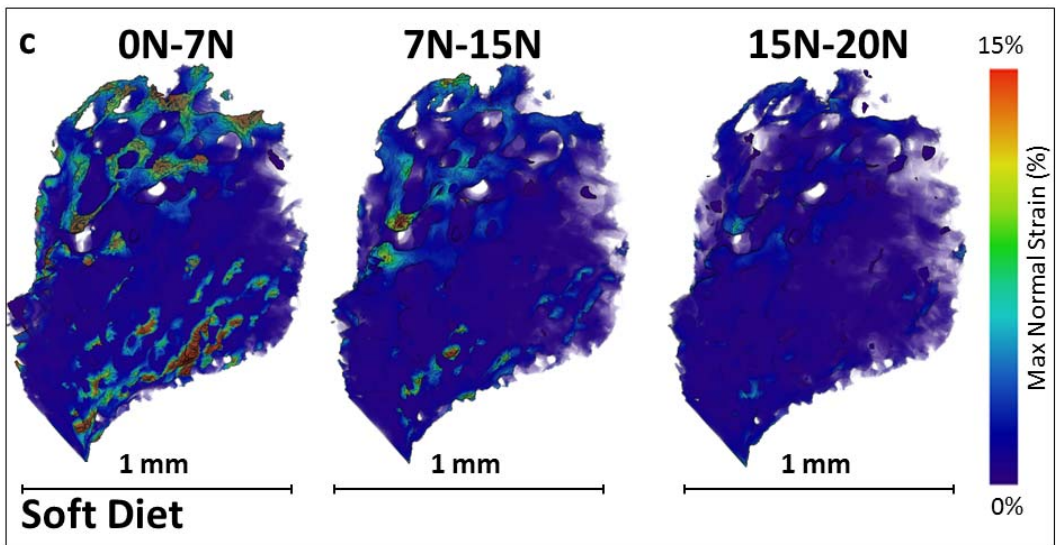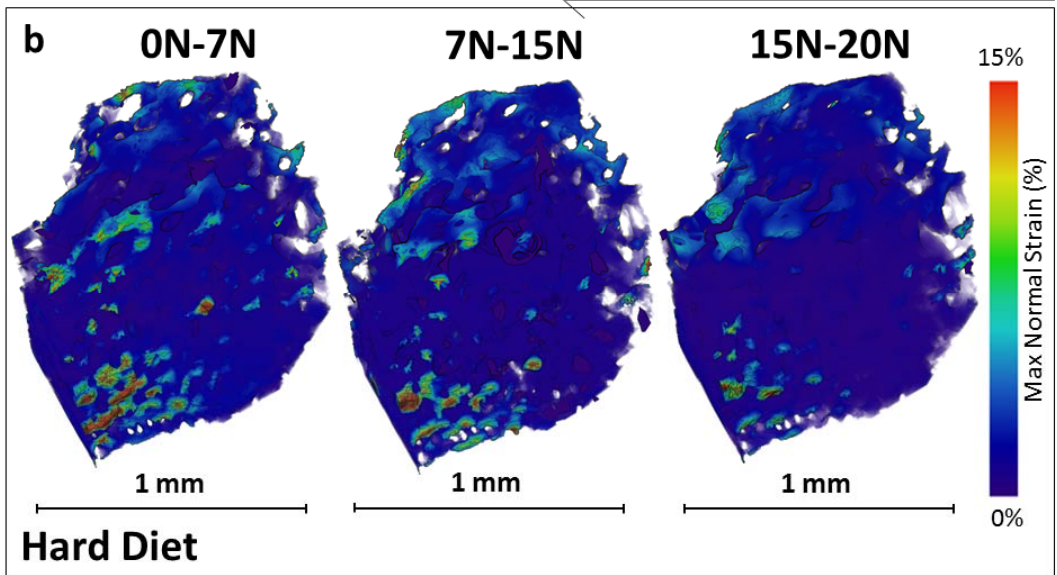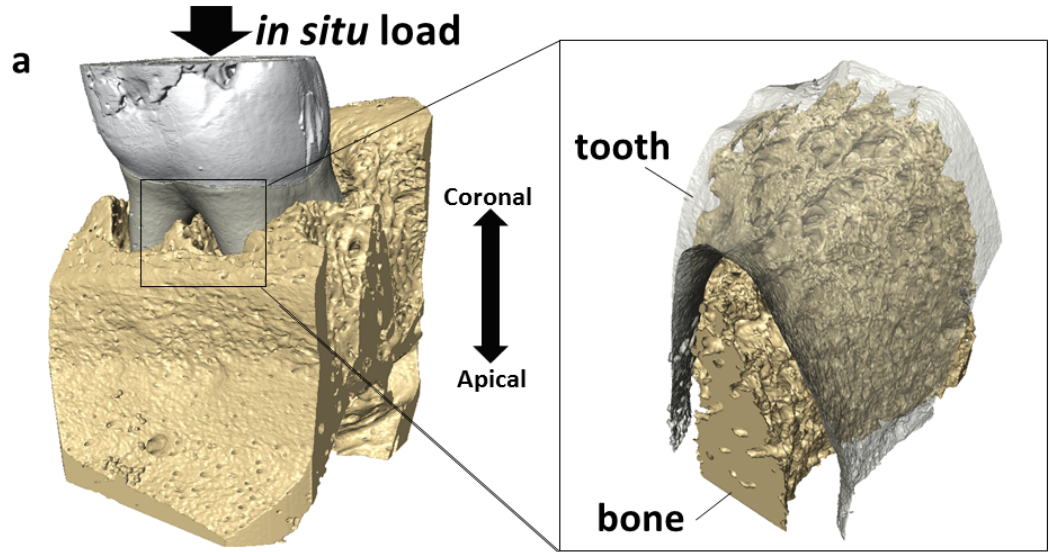
Figure 6.3.   Digital volume correlation (DVC) within interradicular bone of HD and SD (8 week old rats). (a) The tooth and alveolar bone configuration illustrates "saddling" of tooth furcation on interradicular bone. Multi load DVC was performed for HD (b) and SD (c) to represent the incremental strain between loads 0N, 7N, 15N, and 20N.   Differences between HD and SD were primarily found with a 7 N increase in load in which the SD specimen had greater deformation due a decreased functional space leading to premature contact. [DVC parameters: Masking with a 50% overlap between interrogation windows lengths of 64 pixels. Gauge length: 64 pixels. Pixel length = 1.6 μm; minimum fraction valid pixel: 25% see Supplemental information for optimization of parameters]

a ⬇ Functional Loads   Mechanical Response ⬆

HOT SPOTS: site-specific tissue strain

Morphology driven Deformation (ORGAN-LEVEL Biomechanics)

Material Derived Biomechanics

Localized shifts in ADAPTIVE BIOPHYSICAL PROPERTIES

Adaptations in overall FORM
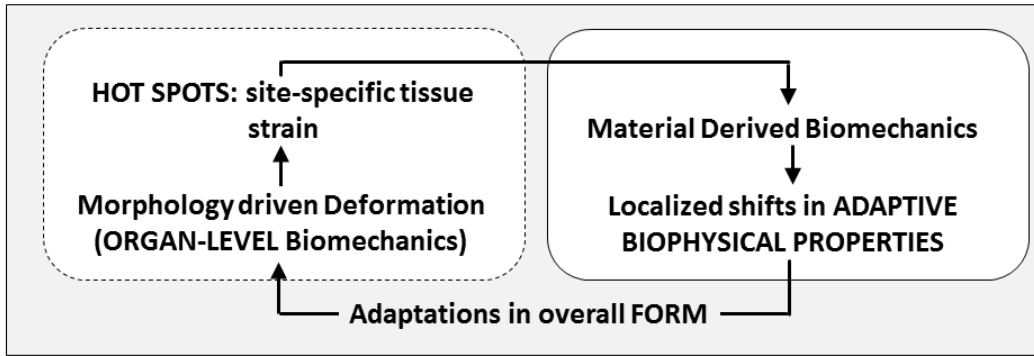
b

Adaptations in Form

SB (pcf)	Volume Fraction	Density (g/cc)	Modulus Macro (MPa)	Modulus Nano (MPa)
10	0.13	2.2	58	1688 ± 613
20	0.26	8.4	210	2572 ± 743

c

Load (N) vs Displacement (mm)

- - - SB 10
——— SB 20

25N, 14N

d

Sawbone 10 (higher porosity)   Sawbone 20 (lower porosity)

Digital Volume Correlation

14N

2mm

0% ▬▬▬ 1%
Max Normal Strain (%)

2mm

25N

2mm   2mm

Finite Element Analysis

0.5 mm

Strain
1,87
0,257
0,0354
0,00486
0,000667
9,17e-5
1,26e-6
1,73e-6
2,38e-7
3,26e-8
4,48e-9
6,16e-10
8,46e-11
1,16e-11
1,6e-12

162
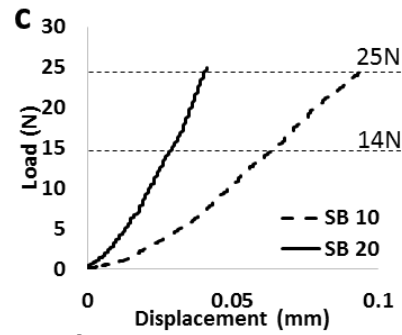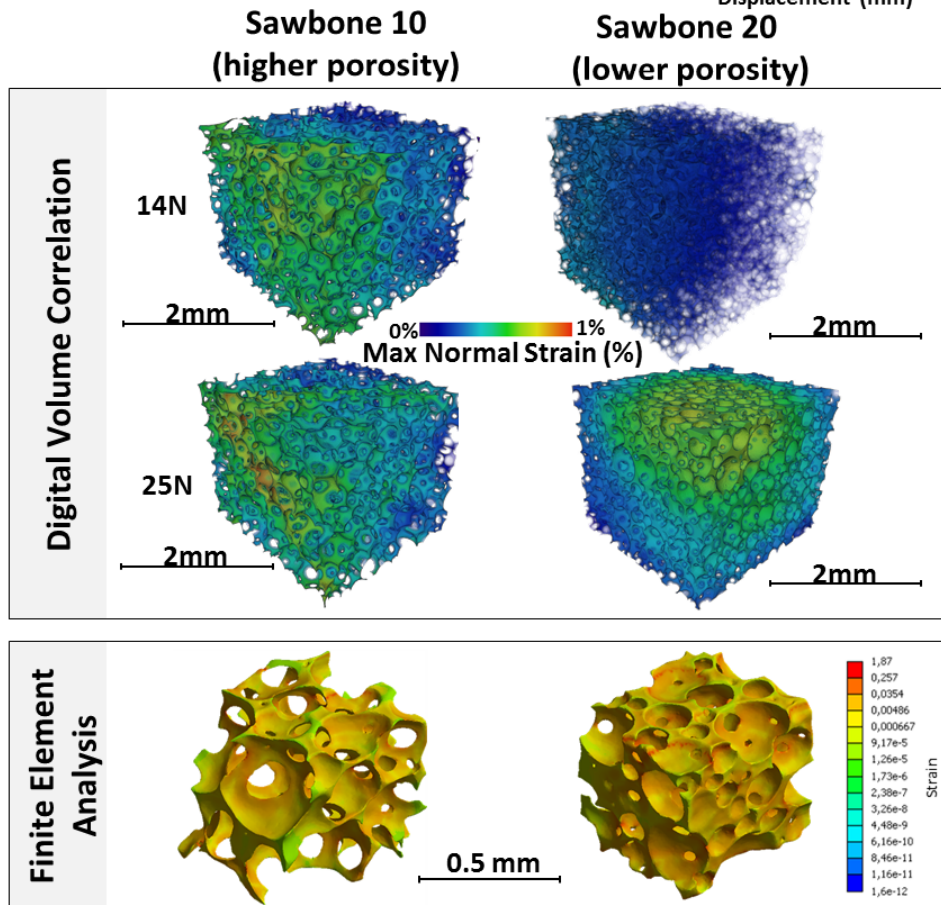
Figure 6.4. (a) As a tissue is loaded, contributions from both the material properties of a tissue and its architecture determine the overall biomechanical response. As the tissue is loaded over an extended period of time the mechano-responsiveness prompted by both form and tissue properties guides further adaptations. (b) To decouple form and material properties related effects, SAWBONES™ (polyurethane foam) differing primarily in pore density were used. (c and d) SAWBONES™ with lower porosity exhibited a higher macro modulus and a lower overall strain compared to SAWBONES™ of higher porosity at 14N, but exhibited plastic deformation at 25N. [DVC parameters: No masking was used, however, a 50% overlap between interrogation windows of length equal to 128 pixels and a gauge length of 128 pixels (1 pixel = 3.67 µm) with a minimum fraction valid pixel of 25% was used for mapping strains within saw bones of respective configurations]. Results showing differences in strain with changes porosity are also revealed in finite element analysis solutions. Logarithmic scale is shown for FEA results.
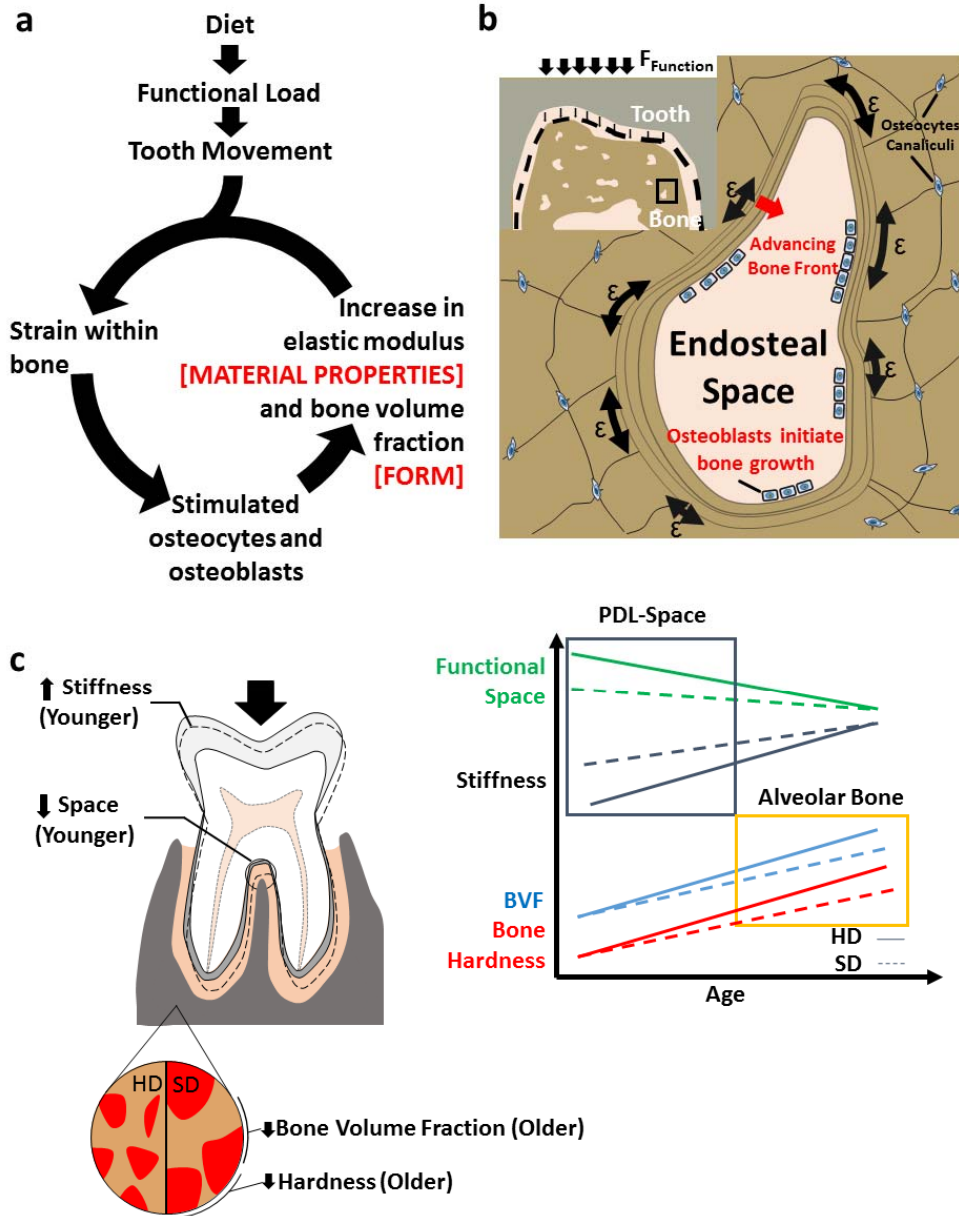
Physical Property	Age Effects	SD effect
Bone Volume Fraction	Increase with Age	Reduced rate
Bone Hardness	Increase over age	Reduced rate
Stiffness	Increase with age	Initial increase
Functional Space	Decrease with age	Initial decrease

Figure 6.5. (a) Mastication forces at varying frequencies cause strain within the alveolar bone. Within the interradicular alveolar bone, mechanical strain in tissues is transduced by cells cuing on ECM deformation and fluid flow thus stimulating osteocytes and osteoblasts and their network. The resulting effects include changes in ECM material properties and morphology which are often times noted as strain-adaptive properties of tissues. (b). Consequently, the strain-adaptive tissue properties that include form and material properties are optimized to accommodate functional demands the response of the adapted structure (c) Overall, measured adaptations in younger rats included a decrease functional space and an increase in joint stiffness while adaptations in older rats manifested as a decrease in BVF and bone hardness.

4x

10x

*4x images are 4mm x 4mm, 10x are 1.5mm x 1.5mm
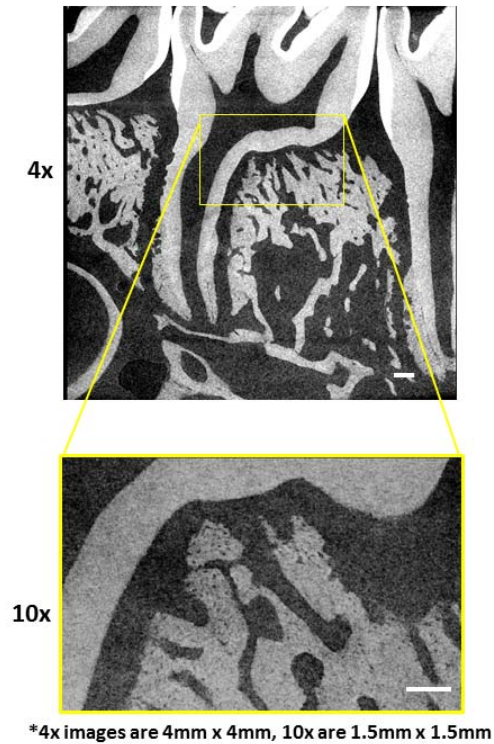
Figure 6.S1. Animated .gif images showing relative tooth displacement within the socket during *in situ* loading (0N→7N→15N→20N) at 4x and 10x. White bars = 200 μm. Please see "**Figure 6-S1.gif**" in the supplemental directory. Note: .gif files can be viewed in web browsers.
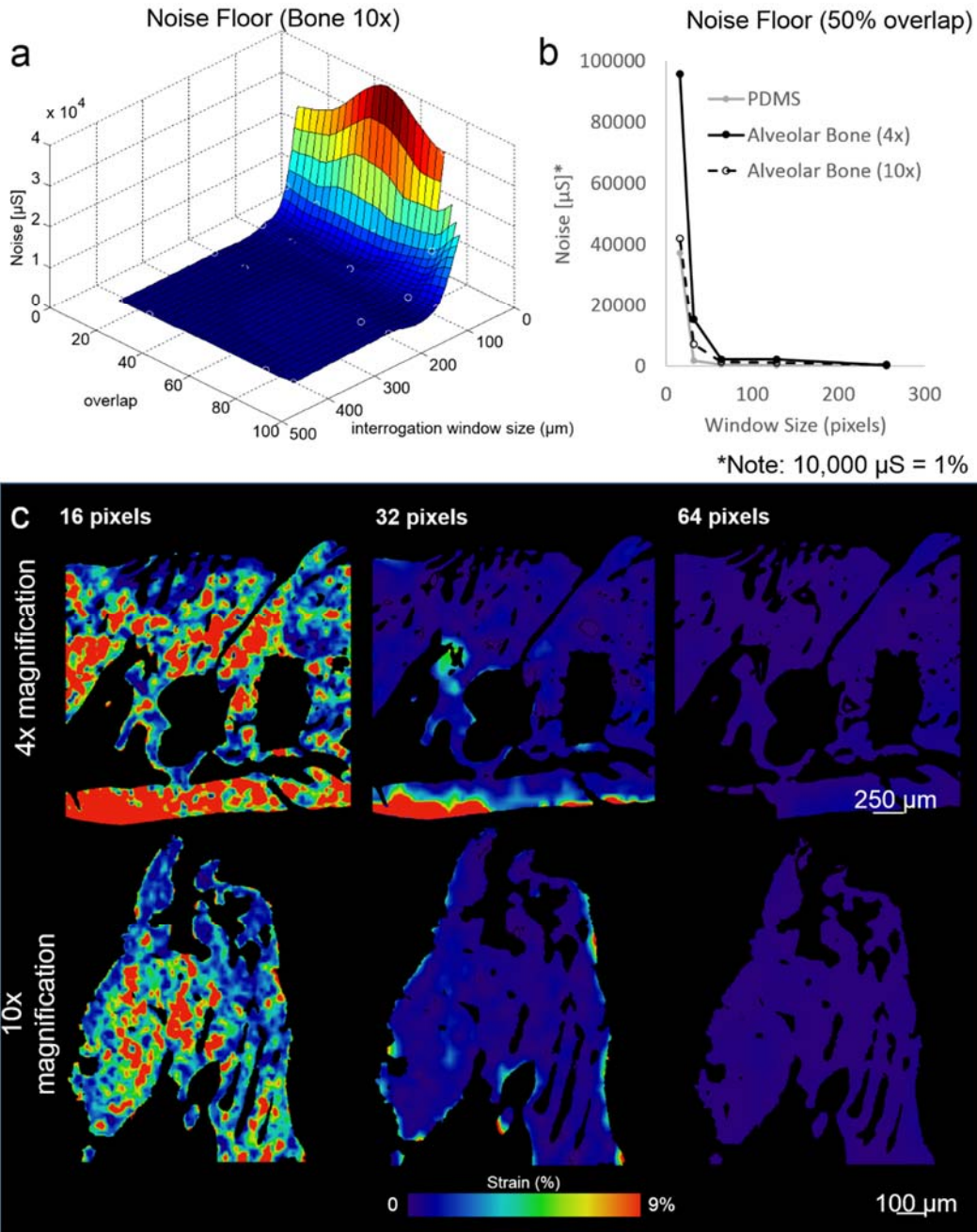
Figure 6.S2. Noise floor calculations for DVC for alveolar bone at different magnifications (alveolar bone 4x, alveolar bone at 10x, PDMS with 50μm beads at 2x). a) for alveolar bone at 4x, surface relationship describing effects of overlap percentage and interrogation window size on noise. b) at 50% overlap, relationship between window size and noise for different materials and magnifications. c) DVC output showing decrease in noise output with an increase in interrogation window size.
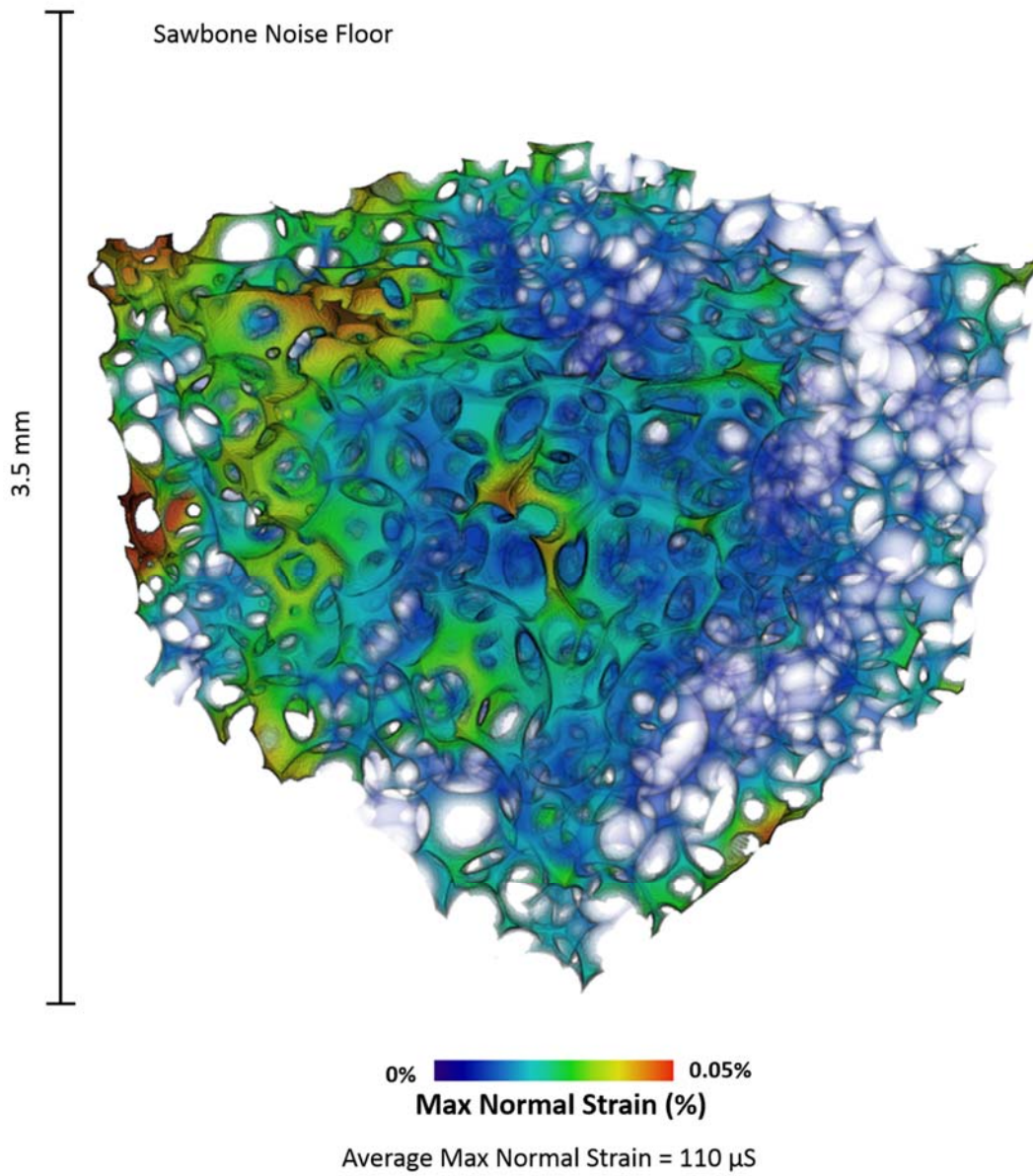
Figure 6.S3. Noise floor representation using consecutive scans. Average max normal strain = 110 µS.
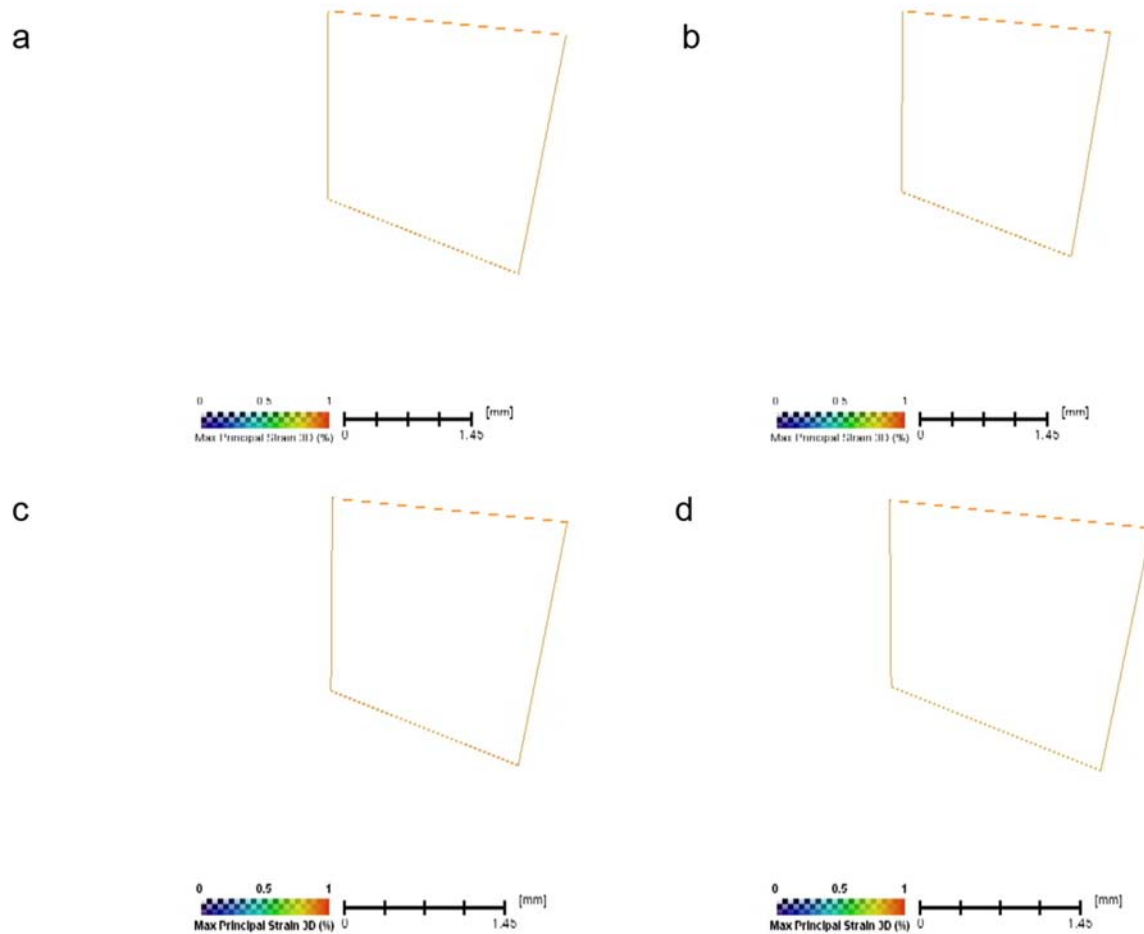
Figure 6.S4. Movie representations for SAWBONES™ specimens. (a) SB10: 14N (b) SB10: 25N (c) SB20: 14N (d) SB20: 25N. Please refer to files "**Figure 6-S4a (SB10 14N).avi**", "**Figure 6-S4b (SB10 25N).avi**", "**Figure 6-S4c (SB20 14N).avi**", and "**Figure 6-S4d (SB20 25N).avi**" in the supplementary directory for respective movies.

CHAPTER 7. AN OVERVIEW OF BIOMECHANICS AND MECHANOBIOLOGICALLY RELATED EVENTS IN THE BONE-PERIODONTAL LIGAMENT-TOOTH FIBROUS JOINT

7.1. Abstract

The biomechanics of bone-periodontal ligament (PDL)-tooth complex within the context of oral and craniofacial biomechanics is minimally investigated. This study investigates the correlation of tooth motion within the alveolar socket from a multiscale perspective. The bone-PDL-tooth complex of a rat was preserved within the craniofacial organ system to link the natural tooth-bone biomechanics to local mechanobiological activities at the PDL-bone and PDL-cementum interfaces. Digital tethers connecting the tooth and alveolar socket were used to measure deformations within the functional space between the tooth and the bone. Comparisons between loaded and unloaded configurations of the tooth and alveolar socket produced strain in the parallel and orthogonal (with respect to the tether) components. Components parallel to the tether were defined as similar in direction to compression and tension while orthogonal components were defined as similar to shear strain. Spatial distribution of biochemical factors related to formation (alkaline phosphatase - ALP) and resorption (tartrate resistant acid phosphatase - TRAP) activities as well as changes in the ultrastructure of the entheses regions (Transmission electron microscopy). Organ-level biomechanics illustrated that the tooth naturally rotates towards the distal side of the socket using the interradicular bone as a fulcrum and was correlated with increased ALP activity. The resulting motion produced an increase in shear and a decrease in functional space on the distal side of each root correlating with an increase in TRAP activity. Transmission electron microscopy on the distal socket revealed scallop-shaped surface characteristic

of Howship's lacunae. Imaging on the mesial boarder of the socket revealed mineral formations with the presence of bone sialoprotein (immunogold labeling) specifically between the collagen fibrils. Electron diffraction patterns of mineral forming regions showed mineral directionality in line with collagen fibrils while both regions illustrated diffraction from crystallographic planes characteristic of apatite crystals. Overall, these results indicate the functional loads generated from mastication as a major impetus for the natural tooth movement favored in the distal direction due to the form of the tooth relative to the form of the alveolar interradicular bone and socket. This relative motion due to narrowing and widening of the PDL-space on the distal and mesial surfaces of the bone-PDL-tooth complex perpetuates resorption and formation at the tethered end of the PDL with bone and is necessary to maintain a uniform PDL-space for joint function.

7.2. Introduction

The longstanding field of biomechanics can be traced all the way back to Aristotle. Since then, it has gained momentum through advances in technology and has allowed for an increased understanding of how structural elements in an organism interact within themselves and as a response to external environmental stimulus. A plethora of research studies using various types of *in vivo* models, have linked mechanical force to the growth and maturity of all tissues within the body (Carter et al., 1996; Frost, 1987; Wolff, 1982). Current studies focus on mechanobiology or how tissue mechanics contribute to development, maintenance, progression of disease, and therapy of organs specifically related to clinical interventions involving forces (including orthodontics and distraction osteogenesis). The oral and craniofacial complex is subjected to multiple sources of loads varying in both magnitude and frequency (chewing, speech, parafunction), and over the years has been studied from a biomechanics perspective in several (Herring and Wineski, 1986; Herring et al., 1991; Langenbach et al., 1992; Weijs et al., 1987; Westneat and Hal, 1992). Chewing forces not only act on the bone-PDL-tooth complex, but also on the sutures and the temporomandibular joint (TMJ), all of which put together was elegantly described as "craniofacial function and biology" to illustrate their adaptive nature (Vinyard et al., 2008). Despite several studies on the craniofacial complex from a biology perspective, there is a gap with regards to the involvement of mechanical forces on the bone-tooth complex and their effect on the entire craniofacial organ system that includes organs such as the temporal mandibular joint (TMJ) and subsequently other organs such as the sutures of the cranium and palette. It is known that function and its related adaptation within the jaw (function mainly being chewing) is required as a part of normal

development of skull morphology (Beecher and Corruccini, 1981; Bouvier and Hylander, 1984; Kiliaridis et al., 1985; Yamamoto, 1996) and its growth. This implies that the dimension and quality of structural components continuously change through developing mastication complexes (Biknevicius and Leigh, 1997; Cole III, 1992; Ravosa, 1991, 1998; Taylor et al., 2006). Previous authors have indicated shifts in mastication due to a changes in hardness of food (softer or harder foods) as a major contributor to the cranial shape and pathology by highlighting changes in the development of the jaw, sutures, as well as the TMJ through shifts in gene expression and elevated levels in glycosaminoglycan (GAG) content (Agarwal et al., 2001; Carvalho et al., 1995; Copray et al., 1985; Holmvall et al., 1995; Huang et al., 2002, 2003; Mao et al., 1998; Pirttiniemi et al., 1996). Additionally, activation of proteins involved in the regulation and resorption of inorganic matter have also been observed (Bouvier, 1988; Kim et al., 2003). Clinicians have utilized deliberate changes in jaw mechanics and shifts in tooth location (McDougall et al., 1982) as a therapeutic technique to produce desirable alveolar bone modeling (Chin and Toth, 1996; Ga, 1987) to facilitate function. Regardless of these studies, the link between the occlusal forces through the bone-PDL-tooth complex to the other load-bearing and seemingly non-load-bearing organs such as the sutures is yet to be established. As a fundamental first step from a biomechanics and mechanobiology perspective, creating a standardization of bone-PDL-tooth mechanics within the context of the craniofacial complex would provide researchers with the tools to systematically model mechanical stimulation on local tissues within the oral cavity as well study shifts due to pathological alterations such as degradation of the TMJ and/or parafunction. Given that there is a no standard protocol to observe the biomechanics of the bone-tooth

fibrous joint *per se*, it offers to be a challenge to link its contribution to the mechanics of the fibrocartilaginous organ, the TMJ and subsequently to other organs including the cranial and palatal sutures.

This study details a method that can be used to investigate biomechanics of the bone-tooth complex within the larger organ system, the craniofacial complex. Focusing on the bone-tooth complex, studies are limited to pieces reduced from a complete bone-PDL-tooth fibrous joint (Chiba and Komatsu, 1993) or have sought other numerical approaches that are limiting (Qian et al., 2001, 2009). In the pursuit of investigating the effect of mechanical loads and path of load transmittance in the oral and craniofacial organ system, a holistic approach was sought to model the biomechanics of the bone-tooth complex within the context of the craniofacial complex as a first step. This is accomplished by keeping the other fibrous joints such as the sutures and the fibrocartilaginous joints intact to be able to relate biomechanics of the bone-tooth complex to potential mechanobiological signals as identified through biochemical assays at the PDL-bone and PDL-cementum attachment sites.

The dentoalveolar complex is regarded as one of the most mechanically active tissues within the body and is highly dynamic due to a rich blood supply throughout the region (Gaengler, 2007; Nanci, 2007; Sodek and Ferrier, 1988; Sodek and Mckee, 2000). This complex consists of a ligament-filled space that connects the tooth to the alveolar bone and functions as the primary load-absorbing mechanism during mastication (chewing). At an organ level, the majority of mechanical stimulation within this complex originates from mastication and is generated through the activation of several muscle groups (temporalis, masseter, medial pterygoids) to rotate the maxilla and mandible

together (with the TMJ as the axis of rotation). As the upper and lower jaws articulate, the cusps of the teeth (primarily molars within rats) interdigitate allowing for specific points of contact on each tooth. The forces are transduced through teeth into the dentoalveolar complex which absorbs and distributes these forces locally.

The primary tissue responsible for accepting and distributing loads is the periodontal ligament (PDL) followed by the alveolar bone and cementum which forms soft/hard tissue interfaces with the PDL (Nanci, 2007). The mechanical response within the PDL is governed by the elastic (collagen and elastin) and viscous components (proteoglycans, non-collagenous proteins, and other parts of the ground substance bound to water) of the tissue allowing for time related response giving particular importance to modeling both compression, tension, and shear (Fung, 1990; Watanabe and Komatsu, 1997). Cells located locally are able to sense changes in active stretch of the extracellular matrix (ECM) in addition to interstitial fluid flow and respond by regulating ECM of both hard and soft tissue structural components (through tissue turnover and maturation).

Interfaces between mineralized and ligament tissues (entheses) are of particular importance when studying the mechanobiology paradigm within the dentoalveolar complex. From a materials and mechanics perspectives, interfaces between dissimilar materials initiate localized regions of increased strain gradients (Boresi et al., 1993). When applied to the fibrous joint, the attachment of disparate materials such as the PDL with cementum and alveolar bone should also create regions of increased strain gradients due to applied breakdown of occlusal load into compression, tension and shear related forces (Benjamin et al., 2006; Thomopoulos et al., 2006). The organization of the (ECM) leading to maturation of the tissues that constitute the joint is highly regulated by passive

or dynamic mechanical stimulation (Ingber, 1991, 2006, 1997; Wang et al., 1993). Studies comparing interfaces complexes either erupting or in function have indicated the presence of progenitors along the PDL-bone and cementum-PDL attachment sites identifying their function via cementum and bone apposition as a key for maintaining functional space in the interradicular regions as well as the apex (Lee et al., 2015) of the root. The ultrastructure of this region has been identified as having significant differences in the organization and diameter of collagen fiber bundles within the resorption and formation sites of alveolar bone (Kuroiwa et al., 1994). Specific to bone mechanobiology, the classical thought is that compression on the bone serves as a mechanical signal for osteoclastic (resorption) function while opposing tension serves as a stimulus for bone formation (Frost, 1987). While these trends have been studied in the bony socket within the bone-PDL-tooth complex using orthodontic models (Rody Jr et al., 2001; Rygh, 1974), these events have not yet been linked to the organ level biomechanical events resulting from physiological (chewing) loads.

Within the context of this study, it is hypothesized that the mechanical events generated with from a physiologically relevant *ex vivo* model of mastication will be spatially co-localized as indicated by biological activities that prompt mineral formation and resorption related events within the bone and cementum. To investigate this relationship, the objectives of this study were: 1) to further improve the current mastication model by including the articulation of all molars between the maxilla and the mandible by maintaining an intact TMJ. 2) To implement an "artificial PDL tether method" by using the tooth movement relative to the socket in order to model pseudo deformations within the

PDL. 3) To correlate formation and resorption related markers within the bone-PDL-tooth complex with respective strains as seen by the tethers.

7.3. Materials and methods

To maintain an organ level perspective, freshly harvested skulls from rats were loaded within physiologically relevant parameters within an *in situ* load cell coupled to an X-ray microscope (XRM) tomography unit. By applying an image registration in conjunction with an artificial digital tether system, the micromotion of the tooth was captured and used to estimate the local mechanical stimulus at the interfaces within the bone-PDL-tooth complex. Biomechanical signals were correlated with formation and resorption related biochemical events using conventional histology and immunogold labelling.

7.3.1. Animal model

All experimental protocols were compliant and followed the guidelines of the Institutional Animal Care and Use Committee (IACUC). Sprague Dawely rats (male) raised to 6 weeks were sacrificed and dissected making sure to preserve the structural integrity of the cranial base, temporomandibular joint (TMJ), and hemimandible attachments. Tris buffer solution (TBS) supplemented with 50 µg/mL of penicillin-streptomycin was used to maintain hydration of the specimen throughout the experiment (Chiba and Komatsu, 1993; Jang et al., 2014b; Lin et al., 2013). Floss was used to restrict the movement of the TMJ to purely rotational. To prepare the specimen for *in situ* loading, the skull was flipped and embedded within poly-methyl methacrylate (PMMA) as shown in **Figure 7.1**. PMMA was also used to secure the positioning of the hemimandibles within the anterior region (**Fig. 7.1**). Stereo optical microscopy (Olympus SZ61, Olympus,

Tokyo, Japan) was used to confirm the proper interdigitation of the molars on both the right and left side (**Fig. 7.1**).

7.3.2. Unconstrained compression and imaging using load cell coupled to XRM tomography unit.

Simultaneous compression and imaging of the specimen was done using an *in situ* load cell coupled to an XRM tomography unit (Jang et al., 2014b; Lin et al., 2013). Prior to loading and imaging, the specimen was wrapped in tissue papers soaked in TBS solution and loosely covered in Parafilm® to minimize evaporation and interference with the biomechanical testing. Specimen was initially scanned at an unloaded state (90 kVp, 2500 projections). Following image acquisition, the specimen was allowed to rehydrate (~1hr). The specimen was loaded by applying load to the mandible (**Fig. 7.1**) at a displacement rate of 0.2 mm/min to a peak load of 7N (Nies and Young Ro, 2004) and allowed for the equilibration of stress relaxation (~1hr). Following the stress relaxation period, an additional scan was taken at the identical parameters as the unloaded scan (See **Fig. 7.S2** for loading curves).

7.3.3. Post processing and artificial tether modeling

Tomographies were filtered using an anisotropic diffusion filter to improve image segmentation quality. Regions were then segmented into bone and tooth regions to define surface meshes (Avizo 9.0.1, FEI Company, Hillsboro, OR, USA). Rigid body registration was then used track the relative positioning of the tooth and alveolar bone (Avizo). A custom written MATLAB (Matlab r2007a, MathWorks, Natick, MA, USA) script was used to define tethers and as well as compute tether deformation using a cylindrical coordinate system (**Fig. 7.2a and b**). For a detailed explanation of the tether model

please see supplemental material. Results of the tether modeling were plotted on the surface of the tooth and visualized in Avizo. Correlation for virtual sections with respective histological slides and TEM ultrasectioning was done by sampling virtual sections with equivalent root diameter and distance between roots (**Fig. 7.S1**)

7.3.4. Separate animals used for histology (cryosectioning)

A separate animal at equivalent age and gender was sacrificed and dissected to isolate their hemimaxilla. Decalcification and fixation was done using a combination of 4% Paraformaldehyde and 0.5M Ethylenediaminetetraacetic acid (EDTA) (Doherty et al., 2010; Jang et al., 2015). Specimens were then placed in sequential sucrose solutions (15% for 2 hours, then 30% overnight) and processed for cryosectioning within the transverse plane (Lee et al., 2015).

7.3.5. Osteoclast identification using tartrate resistant acid phosphatase (TRAP) staining

Staining for tartrate resistant acid phosphatase (TRAP) was done following a previously published protocol (Erlebacher and Derynck, 1996). In brief, the method consisted of treating the rehydrated specimens with a 0.2 M acetate buffer and sodium tartrate dibasic dehydrate for 20 minutes at room temperature, added naphthol AS-MX phosphate and Fast Red TR, followed by incubation at 37°C for 15 minutes. Counterstaining was done using Meyers hematoxylin.

7.3.6. Osteoblast activity using alkaline phosphatase (ALP) staining

Staining for alkaline phosphatase (ALP) activity was done using a previously described method (Yoshiki et al., 1972; Miao and Scutt, 2002). In short, rehydrated slides

were pretreated overnight in an ALP substrate solution (100mM Trizima-maleate in DI water) with 1% added magnesium chloride. Slides were then transferred to a separate batch of ALP substrate solution with added naphthol AS-MX phosphate and Fast Red TR, followed by incubation at room temperature for 30 minutes. Counterstaining was done using Meyers hematoxylin.

7.3.7. Preparation and processing of specimens for transmission electron microscopy

The right maxilla of rat was dissected and fixed overnight in 10% neutral buffered formalin (NBF, Richard-Allan Scientific, Kalamazoo, MI). Afterwards, the specimen was washed twice in 1× phosphate-buffered saline (PBS) and then dehydrated through graded (50-100%) ethanol solutions. The specimen kept in 100% ethanol was scanned using a microCT (microXCT-200, Xradia) followed by infiltration of LR-white resin (hard grade; Electron Microscopy Sciences, Hatfield, PA). The infiltrated specimen was kept in gelatin capsule (Electron Microscopy Sciences, Hatfield, PA) and polymerized for about 2 days at 60°C. 90-100 nm thick tissue sections were cut with an ultramicrotome (Reichert Ultracut E, Leica Microsystems, Inc., Buffalo Grove, IL) then collected on formvar/carbon-coated Ni grids (Electron Microscopy Sciences). Immunogold labeling was adapted from a published protocol (Chen et al., 2015). Thin sections on grids were decalcified by incubation with 4% EDTA solution twice for 20 min each time. Decalcified sections were washed twice using Milli-Q water, twice with PBS, and then treated with blocking agent containing 2.5% bovine serum albumin (BSA, Sigma-Aldrich) in PBS for 10 min. Grids were incubated in primary antibody solutions (1:20 dilution in PBS) at 4°C overnight. After washing three times with PBS, sections were treated again with 2.5% BSA for 10 min

then incubated in a 10-nm-diameter protein G-gold nanoparticle solution (Electron Microscopy Sciences) for 1 hr. at room temperature. Following washing three times with PBS, grids were rinsed with Milli-Q water and air-dried overnight. No counterstaining had been applied on the sections. A JEOL 1400 transmission electron microscope (JEOL USA, Inc., Peabody, MA) operated at an accelerating voltage of 120 kV were used to image the sections

7.4. Results

7.4.1. Deformation output from tether model using standard shapes.

Examples of artificial tether model output using standard shapes are seen in **Figure 7.2.** The initial digital tethers connecting the inner surface node with the closest outer surface is visualized in **Figure 7.2a**. In order to mimic the natural rocking motion of the tooth within the socket (Chattah et al., 2009), the inner cylinder was tilted. Distributions of normalize tether changes in the parallel (**Fig. 7.2d**) and orthogonal (**Fig. 7.2e**) directions follow expected behavior patterns.

7.4.2. Shifts in tooth movement and tether change with *in situ* loading

A diagram showing the 3D surface of the tooth and a portion of the bony socket (extracted from the XRM tomography) is shown in **Figure 7.3a**. When looking into the functional space from the occlusal view the load induced shifts in the tooth position relative to the alveolar socket were found to be in the distal-buccal direction (**Fig. 7.3b**). The application of the tether model demonstrated a decrease in the functional space due to the distal-buccal shift of the tooth within the socket (**Fig. 7.3c and d**).

Normalized deformation of the tether in the parallel direction (**Fig. 7.4a**) showed an increase on the mesial lingual side with a decrease in the furcation as well as the distal

buccal side of each tooth root. Increases in the normalized shear (**Fig. 7.4b**) were found primarily within the furcation of the tooth as well as the distal buccal region of each tooth root. It should be noted that while results are plotted on the entirety of the tooth surface, only the root data is relevant.

7.4.3. Spatial distribution of bone resorption and formation activities within the alveolar socket

Increased activity of alkaline phosphates was seen primarily within the enthesis regions contacting the interradicular alveolar bone (**Fig. 7.5**) as well as within the endosteal spaces in the interradicular bone. ALP activity was present on all level root level, but was greatest near the crest (most coronal) region of the interradicular bone. Within each section, ALP was also seen bordering the endosteal space of interdental bone, albeit less distinct than interradicular bone. Minimal ALP was detected on the tooth-PDL interfaces.

Resorption activity as identified by TRAP(+) cell distribution was found to be primarily within the distal buccal side of each tooth root and opposing alveolar bone. TRAP staining was particularly high in distal lingual and distal buccal sockets (**Fig. 7.5**). Similar trends were seen on all transverse sections. Distribution of resorption activity spatially coordinated especially well with the locations of tether narrowing (**Fig. 7.5** center).

7.4.4. Ultrastructure of formation and resorption socket sites

Imaging from transmission electron microscopy is shown in **Figure 7.6** showing mineral nodule formation on the mesial complex and scalloped edges on the distal complex. Within the formation sites, electron diffraction of apatite crystal reveals the c-

axis of crystals alignment following the direction of the collagen fibrils (**Fig. 7.6ii**). On the distal side, diffraction patterns on the resorption sites suggest crystals more disordered (**Fig. 7.6iii**). Immunogold labeling (right) to bone sialoprotein reveals preferential labeling to sites containing apatite mineral (lighter colored blotches) in both formation and resorption sites of cementum and the alveolar bony socket interfaces with the PDL (**Fig. 7.7**).

7.5. Discussion

The inspiration for the study is within the need to meet the challenge of correlating organ-level biomechanics to tissue-level biochemical events commonly addressed as mechanobiological events especially within load bearing bone-PDL-tooth fibrous joint. Biochemical events within tissues and interfaces were mapped and results were inferred within the context of organ mechanics while accounting for occlusion that is relevant to physiological conditions.

To accomplish this, two novel approaches were used. The first is the approach to link biomechanical events on a system level to the mechanobiology events at localized tissues in 3D. Our goal was to simulate the system level mechanical apparatus of the TMJ and interdigitation between the opposing dentition to mimic the natural tooth movement within the socket. These organ level tooth motions were then used to extrapolate the localized deformations within the PDL space. Finally, these tissue level deformations were then correlated with local biochemical shifts in bone formation and resorption dynamics. The multiscale perspective described within this study also provided a framework to model perturbations to the system such as therapeutic loads as well as pathologic alterations to the constituents that makeup the complex (e.g.

hyperfunction models and degradation in the TMJ). Specific to the bone-PDL-tooth complex, distal resorption and mesial formation related events shown as natural occurrences within the rodent oral complex are correlated with narrowed and widened functional space. Previous research has predicted the rotational motion of the tooth in rats and pigs similar to our observations (Chattah et al., 2009; Naveh et al., 2012a). However, to date, challenges in connecting *ex vivo* and *in vivo* modeling has prevented the proper study of multiscale correlation between the anatomically specific mechanical events tooth mechanics and the formation and resorption activities at the PDL-bone and PDL-cementum interfaces and attachment sites.

The second novel aspect within this study is the attempt to mimic the overall mastication mechanics with our *in situ* system combined with the ability to measure resulting local deformations within the functional PDL space. Within a single mastication cycle, the closing of the jaw about the TMJ commonly known as a hinge joint initiates interdigitation of teeth at specific contacts areas on the occlusal surface of the crown (Wheeler, 1974). These topographical features on the contact areas combined with the rotational motion of the TMJ greatly influence the translational and rotational path that a tooth takes within the alveolar socket. Previous studies have postulated and identified a rocking motion of the tooth within the socket based on the socket and root morphology and association (Chattah et al., 2009). From our model, the contact points between the opposing dentition cause the tooth to rock in the distal direction (**Fig. 7.3**). Primary contributors to this motion are most likely due to the shape of the maxillary crown cusps (which point in the distal direction) and configuration of the roots whose apices point in the mesial direction. The resulting increase in shear and narrowing of the functional

space separating the tooth and alveolar bone is felt primarily as parallel and/or orthogonal deformations relative to the socket surface eventually initiating "blastic" or "clastic" responses at the interfaces. This study is the first of its kind to measure these movements while mimicking the occlusion in an intact craniofacial complex. It is recognized that the chewing behavior of rats (and humans) involve many complex behavior patterns which are difficult to model consistently (Hiiemäe and Ardran, 1968). However, the methods and subsequent results within this study provide a reasonable approximation and highlight the need for hierarchical biomechanical modeling to couple the effects of organ level events to tissue level adaptations.

The results from the tether model are in agreement with models of the dentoalveolar complex primarily at the region of the interradicular bone being the site of a see saw action and a fulcrum for rotational movement (**Fig. 7.3 and 7.4**) (Picton, 1962; Chattah et al., 2009). However, the patterns found in the orthogonal and parallel PDL deformations adds to the current dogma by indicating that *in vivo*, the tooth naturally tilts in a distal direction during the power stroke of a mastication cycle. Deformation in both the compression/tension and shear direction is important in mechanotransduction (Ingber, 1997; Alenghat and Ingber, 2002). Therefore, it was crucial to identify changes in the parallel direction as well as the orthogonal direction. From a conceptual standpoint, parallel effects in the defined tethers are similar to compression (narrowing) and tension (widening) of the functional space while orthogonal effects are seen as "shear strains". The measured deformations within the parallel and orthogonal directions indicate significant bias in mechanics towards the distal direction (**Fig. 7.4**). Using the definitions from the tether model, parallel trends observed were the narrowing of the functional space

on the distal side of each root to widening of the functional space of the mesial side. Additionally, the distal side of the roots also contained a greater orthogonal component indicating an increase in shear at local regions.

In this study, we largely focused on adaptation at the soft-hard tissue interfaces from the perspectives of functionally graded interfaces to deformations calculated from the tether model. From a mechanics standpoint, these interfaces serve as a key region for strain concentrations (Benjamin et al., 2006; Thomopoulos et al., 2006). From a biological standpoint, these interfaces have been shown increased vascular density for supplying nutrients and molecules for progenitor cell migration and differentiation (Lee et al., 2015). Various matrix molecules and nonaggregating molecules have been observed at the PDL-bone and PDL-cementum enthesial regions. These include BGN and DCN (SLRPs), NG2 – chondroitin sulfated neuroglial 2, OSX, BSP (globular proteins), various progenitors (hypertrophic cells) all of which seem to be activated specifically on the widening side (mesial) of the complex (Leong et al., 2012; Lee et al., 2015). On the narrowing side the release in pretension can prompt clastic cells which in turn can cause phosphatase production most likely activated by zinc (Ganss and Jheon, 2004; Drzazga et al., 2007; Garlet et al., 2007; Ho et al., 2013). On the widening side of the joint space, it is thought that the local factors orchestrate changes in mineral formation dynamics through the manipulation of Ca^{2+} and PO_4^{3-} charges to form local apatite relative to age-dependent presence or absence of carbonate ions (Blumenthal et al., 1975).

Narrowed functional space in the distal complex as well as the increased shear strain correlated with TRAP(+) cells (**Fig. 7.5**). While it is recognized that separate animals were used for the comparison (and is subject to differences in physiological

186

variances between animals), it should be noted that the common occurrences such as pits representing resorption activity were well aligned with the reduction in functional space and increase in shear which indicates a direct correlation between the tether model results and resorption related activities. Additionally, regions of increased mineral deposition visualized by ALP staining were primarily found in the crest interradicular alveolar bone (**Fig. 7.5 and 7.8**). This result is supported by the current dogma that the interradicular bone serves as the fulcrum (Chattah et al., 2009; Lin et al., 2013) and that the resulting mechanical stimulation serves as an input for internal bone growth and mineralization (Bonewald, 2006) through the activation of ECM deformation and fluid flow through the perilaccunar osteocyte and cementocyte networks in respective mineralized tissues. While the presence and distribution of these proteins have been characterized from a biological perspective, in this study as well as in other studies, we hypothesize that localized proteins at the interfaces are also aiding in the strain dampening and stimulation of progenitor cells and communication between progenitors and tissue specific cells through their inherent viscous properties. Regions identified in close association with the progenitor cells include osteoid and cementoid layers. As such, we continued our investigation at the next level to map nanoscale events that play a key role in maintaining functional space.

On the mesial border, mineralized nodules formed along the direction of the collagen fibrils from the tethered ends of the PDL with bone (**Fig. 7.6**). This observation demonstrates both guidance by the collagen fibril to form aggregates (additional information would be needed to differentiate sheets from bundles) aligned specific to the formation region but also from a materials standpoint, represents a process by which the

strained organic fibrillar structures are reinforced with rigid inorganic matter. It should be noted that the diffraction bands found on the mineralized collagen represented a dominance of apatite crystalline formation which was unexpected due to a historical characterization of poorly crystalline minerals as well as amorphous calcium phosphate on immature bone or the early stage of mineralization process in contrast to more crystalline apatite minerals on mature bone (Boskey and Posner, 1974; Blumenthal et al., 1975). On the distal region of the socket, resorption sites did not have highly orientated apatite crystals. Instead, the mineral resorption regions exhibited a scalloped nature characteristic of Howship's lacunae. The minerals contained within these scalloped regions are most likely native minerals which are constantly etched by the phosphatase enzymes and hydrochloric acids produced by osteoclasts. It should also be noted that the cement lines were seen on this region as well which were not as noticeable on the mineral formation side. The distribution of immunogold labels (**Fig. 7.7**) identifies a relationship between mineralized regions and BSP which has been shown to be important in the extrafibrillar mineralization of collagen (Landis and Jacquet, 2013; Chen et al., 2015). While the presence of immunogold particles does identify the localization of BSP associated with mineralized regions, it does not describe the exact functionality of the protein. The putative role of BSP is believed to nucleate apatite crystallization (Hunter and Goldberg, 1993). Previous studies (Chen et al., 1994; McKee et al., 1996; Bosshardt et al., 1998) have also shown the BSP distributed all over the mineralized region with a much higher expression in either cement line or mineralization front. Our results are in well agreement with these studies. However, it is intriguing to observe the presence of BSP in the resorption site as well. Since BSP and other matrix proteins including collagen

have been deposited by osteoblasts to form an extracellular matrix (ECM) to be mineralized, BSP and other noncollagenous proteins are embedded in the mineralized collagenous matrix. Therefore, removal of minerals from these mineralized matrices by osteoclast activities will help expose BSP while the BSP in the non-demineralized region remains intact. However, the decalcification process during immunogold labeling (Chen et al., 2015) is expected to reveal the BSP localized in such non-demineralized region. It is expected to see more BSP at the mineralization front or surface of newly mineralized regions, however but the data did not show this. It is suspected that the BSP has been embedded in the mineralized matrix during formation process. Therefore, these embedded BSP will be re-exposed after demineralization. As a result, we see BSP in formation site because it is helping mineralization, in resorption site it is unmasked by removal of mineral. Postulated as a mechanosensitive protein (Lee et al., 2015), it is somehow functionalized either directly or indirectly in the presence of mechanical stimulation; however, future experiments will be needed to confirm this. Overall, the formation and resorption processes occur in specific regions, and these activities are linked to mechanosensitive proteins which are controlled by tissue level deformations. Therefore, it is reasonable to deduce that all these formation and resorption events act in concert to produce organ level shifts and changes.

Over time, molars in rats have been shown to undergo distal functional drift (mesial in humans) (Belting et al., 1953). The involvement of mechanical loading in the natural physiological shift in teeth has been debated by previous authors (Moxham and Berkovitz, 1982; Luan and Diekwisch, 2007). Hypofunction studies have implied that functional load is related to the distal drift through the growth of secondary cementum on the mesial side

(Tsuchiya et al., 2013). It is known that an adequate functional space must be maintained as a part of physiological health within a joint (Ho et al., 2013). Therefore, this study fits into the current dogma by investigating from a joint mechanics and PDL-tooth mechanics perspective specifically and highlighting changes within the entheses regions of the alveolar socket. We hypothesize that distal drift is regulated by functional input from mastication and causes localized resorption through the site specific activation of osteoclasts on the distal boarder of the socket. Mineral formation is maintained around the surface of the socket experiencing causing a stretch in the PDL as shown by fluorochrome activity from other studies (Tsuchiya et al., 2013) and more at a nanoscale by localized events leading to micro and macro-scale formation of tissues. However, site specific activity on the distal side was due to the resorption activity (**Fig. 7.6**) and demonstrated the similar diffraction patterns indicated the presence of similar type of crystal as was the case at the formation sites. The site specificity of the resorption sites is governed by the distribution of functional loads. Evidence for this relationship is given from the co-localization of distal tooth tilting with the resorption activity (**Fig. 7.5**). Additionally the activation of TRAP(+) activity on the distal side of the socket can also be decreased through reduced stretch at the PDL-bone tethered ends (manuscript under review).

We propose two hypotheses which link the motion of the tooth to the increase in osteoclast activity within the distal region. The first is that osteoclasts are directly stimulated by the orthogonal (shear) strain at the alveolar bone socket which is produced from the screw like motion of the tooth within the socket. The shear strain on the distal side produces localized micro regions of tension and compression on the entheses

regions on both alveolar bone and cementum which, in turn, inhibits mineralization activities and activates osteoclast differentiation and activity. The second hypothesis is based off the concept that the oblique fibers lining the distal side are naturally in a prestrained state (Fung, 1990; Chen and Ingber, 1999). This prestrained state which is also strained during mastication naturally reduces the osteoclastic formation around the majority of the socket (Klein-Nulend et al., 1990; Kadow-Romacker et al., 2009). Within a single power stroke during mastication, the reduction in function space due to the tilting of the tooth in the distal direction would relieve the pretension within the PDL fibers (**Fig. 7.8e**). As tension based mechanical force is generally required for osteoblast function and subsequent osteoclast inhibition, the relief of the natural pretension would cause a reduction in the osteoblast activity thereby allowing for an increase in osteoclast proliferation. This particular model has also been suggested by other authors using different computational models (Melsen, 1999; Cattaneo et al., 2005). Additional experimentation involving in site specific modification of localized strain and the histological staining for resorption related activities can help provide additional support for both hypotheses.

7.6. Conclusions

During the physiological process of mastication, mechanical events which occur within the organ level cause the tooth to rotate about the interradicular bone within the socket. The micro motions within the tooth are shown to cause localized areas of deformations within the parallel and orthogonal directions to the surface of the root. These localized deformations at the PDL-alveolar bone interface and within the alveolar bone cause site specific pockets for bone mineralization and resorption. In concert, these

sites of mineralization and resorption provide the directionality which allow for the tooth to shift in the distal direction. While the results presented describe the relationship between jaw mechanics and local mechanobiology events within a healthy animal, the methods described within this study can be additionally used to model and explore conditions of pathological (e.g. joint malfunction, bruxism, periodontal disease) as well as therapeutic (e.g. orthodontic) loading.

It is recommended that several limitations within this study be overcome when exploring future studies related to this model. The first is that the *in situ* model be improved through comparison of the specific contact points of rats *in vivo* with the *in situ* model as well as the simulation of acting muscle groups and behaviors during mastication. This is difficult in smaller animals, but may be achieved in larger models. Secondly, while *in situ* load setup provides an adequate tomography for the tether model, the increased size of the specimen relative to the small field of view for the tomography results in a decreased signal to noise ratio for the dataset. Therefore, it is difficult to implement this methodology in conjunction with computational methods dependent on image quality such as digital volume correlation to measure bone strain. These limitations, however, may be overcome with improvements to imaging technologies. Finally, the implementation of 3D biochemical assays (e.g. light sheet technology (Keller et al., 2008)) will strengthen the correlation aspect of this study and allow for true 3D to 3D comparisons. However, it is particularly challenging to utilize such technologies within mineralized tissues which are naturally opaque to many imaging methodologies.

7.7. Supplemental Information

7.7.1. Tether model introduction

The dentoalveolar complex is composed of a tooth (enamel, dentin, and cementum) and alveolar bone which separated by a periodontal ligament (PDL)-space. Traditional X-ray microscopy techniques have been used for the visualization and measurement of mineralized tissues, allowing for the employment of modeling techniques such as digital volume correlation to measure deformation within. However, limitations within normal hard X-rays technology prove difficult to reliably image PDL tissues. Additionally x-ray contrasting enhancers (such as high percentage Lugol's solution) as well as contrasting agents such as iohexol only produce slightly better images (still not good enough for DVC) – they also dramatically change the material and mechanical properties of the tissues providing for inaccurate modeling.

Since, PDL is dramatically lower in elastic modulus compared with all the other hard tissues, therefore it can be assumed that all deformation within the soft tissue region occurs at relatively low loads (0-7N). Therefore a simple modeling technique can be used to capture this PDL deformation at early loads by considering the relatively rigid nature of the bone and tooth relative to the ligament space as well as the attached nature of the PDL into alveolar bone and cementum (Nanci, 2007).

7.7.2. Definition of tether model

Within the context of this study, tethers are defined between two surfaces. Within the perspective of this study, the surfaces will be referred to as either inner (e.g. tooth) or outer (e.g. bone) (**Fig. 7.S1a**). A mesh is calculated for each surface defining several vertices or nodes. The initial tethers are drawn during the unloaded state (0N). These tethers are made when by connecting each of the vertices on the inner surface with the closest vertices on the outer surface. Depending on the geometry, vertices will either

have zero, one, or more than one unique tether attached, but the inner surface vertices'

will all have only one tether attached (**Fig. 7.S1b**). Each tether is specifically indexed to

include the location of the first node (inner surface) and the second node (outer surface).

After a load is applied to the system, the spatial relationship of the inner and outer surface

of the tooth is changed. For each of the initial tethers drawn, a new tether connecting the

same nodes (new positions) is created (**Fig. 7.S1c**). This is a simple task since the

location and movement for each node is carefully indexed and recorded.

Shifts in the tethers are calculated relative to the inner surface node. For each set

of tethers drawn, the entire system is rotated such that the initial tether is in aligned in the

direction of the positive x-axis. Once rotated, the shift in the tether is calculated as the

movement of the outer surface node (**Fig. 7.S1d**). This tether shift is divided into shifts

by direction: either parallel with the original tether, or orthogonal with the original tether

(magnitude). The shifts are normalized by the length of the original tether and recorded

to the original index. After the shifts have been calculated for each node on the surface

of the tether and properly indexed, the resulting data can then be plotted on the surface

of the inner surface as a color map.

While the local coordinate system utilized for this study is the cylindrical coordinate

system, other systems such as the spherical coordinate system (**Fig. 7.S3**). It should be

noted that the local definitions of angles θ and φ are based on the orientation initial scan

of the tooth and arbitrary making it difficult to draw physiological conclusion.

While the tether model provides a good approximation of for the PDL deformation,

future advancements to the model can overcome the current limitations. The tether

system is able to capture gross changes in regional tissue mechanics; however, the

deformation is assumed to be homogenous across a single tether with the origin assumed

to be orthogonal to the surface plane. Future improvements can be made to the system

by accounting for the functionally graded interfaces at the enthesis regions as well as the

directionality of the PDL fibers (which can be approximated from 2D histology).

7.8. Figures
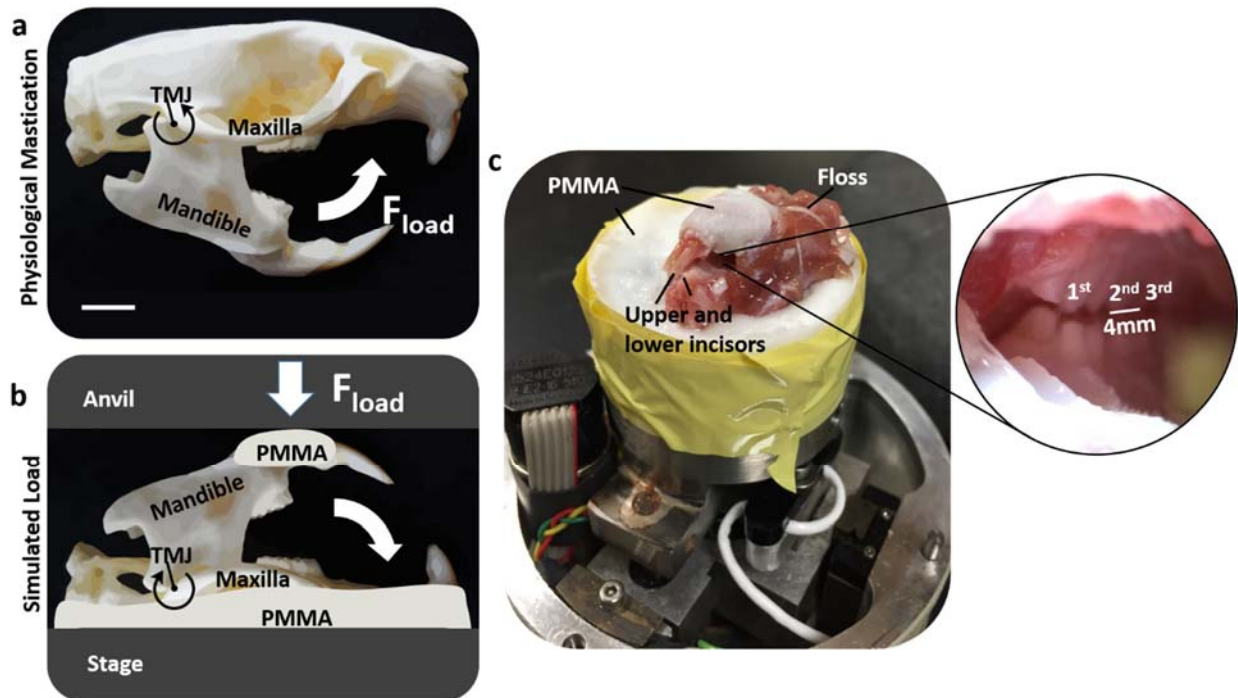
Figure 7.1. Mimicking occlusion. (a) Diagram of skeletal structural components including the maxilla, mandible, and the temporal mandibular joint (TMJ) illustrates maxilla/mandible relationship; white bar = 20 mm. b) The central goal of biomechanical testing was to preserve the natural articulation of maxillary and mandibular teeth. (c) This was done through the maintenance of rotational guidance of the TMJ by stabilizing the jaws with floss, and by inverting and loading a freshly dissected rat head using a mechanical testing device. Poly(methyl methacrylate) (PMMA) was added at the base to stabilize the structures for *in situ* loading.
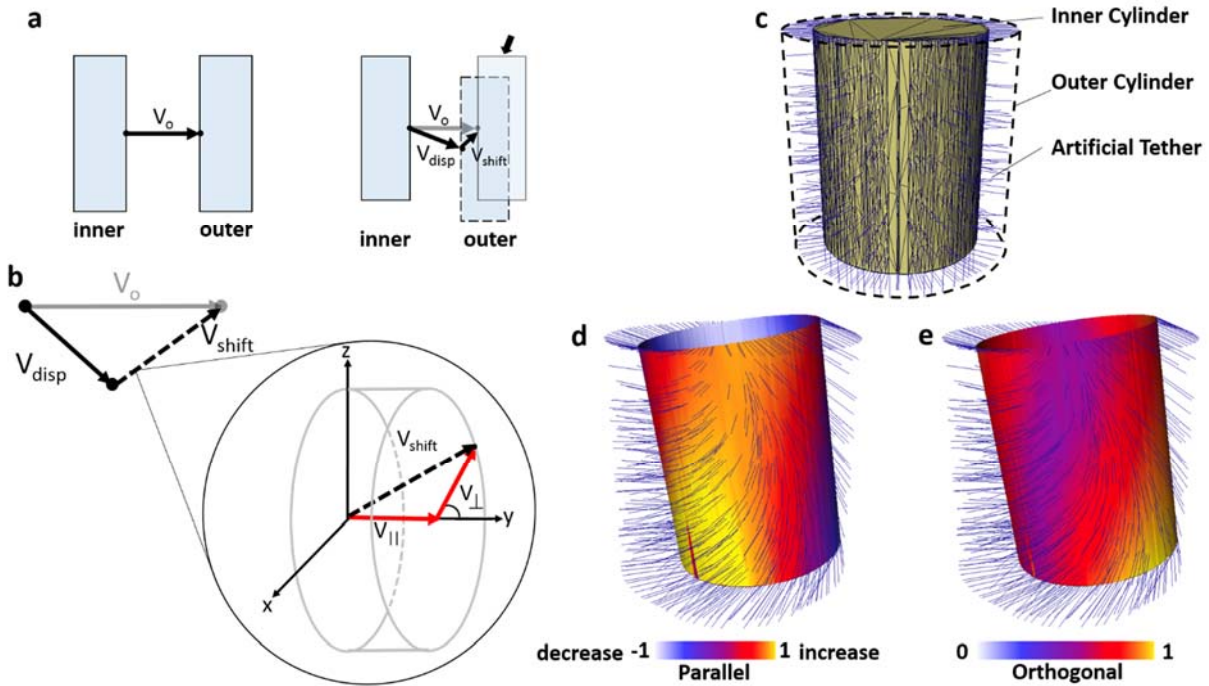
Figure 7.2. Diagram of an artificial tether model. (a) Spatial vectors also known as tethers were used to simulate deformations within the PDL. The tethers connect the surfaces of the tooth and the alveolar socket. During tooth movement, the shift of the vectors in the socket can be tracked. (b) Following displacement of the tether, the relative movement (V_{shift}) can be extracted by taking the difference between vectors at no load to those under loaded conditions. The V_{shift} can then be spilt into $V_{\parallel}$ (narrowing and widening of the PDL-space respectively) and $V_{\perp}$ (shear) to track shifts relative to the original vector V_o. (c) This model is first demonstrated using a solid cylinder within a larger hollow cylinder (dotted line). Artificial tethers are drawn between the surface nodes of the solid and hollow cylinders. Following simulation of inner cylinder movement, the compression/tension (d) and shear (e) components of each individual tether are mapped on the surface of the inner cylinder.
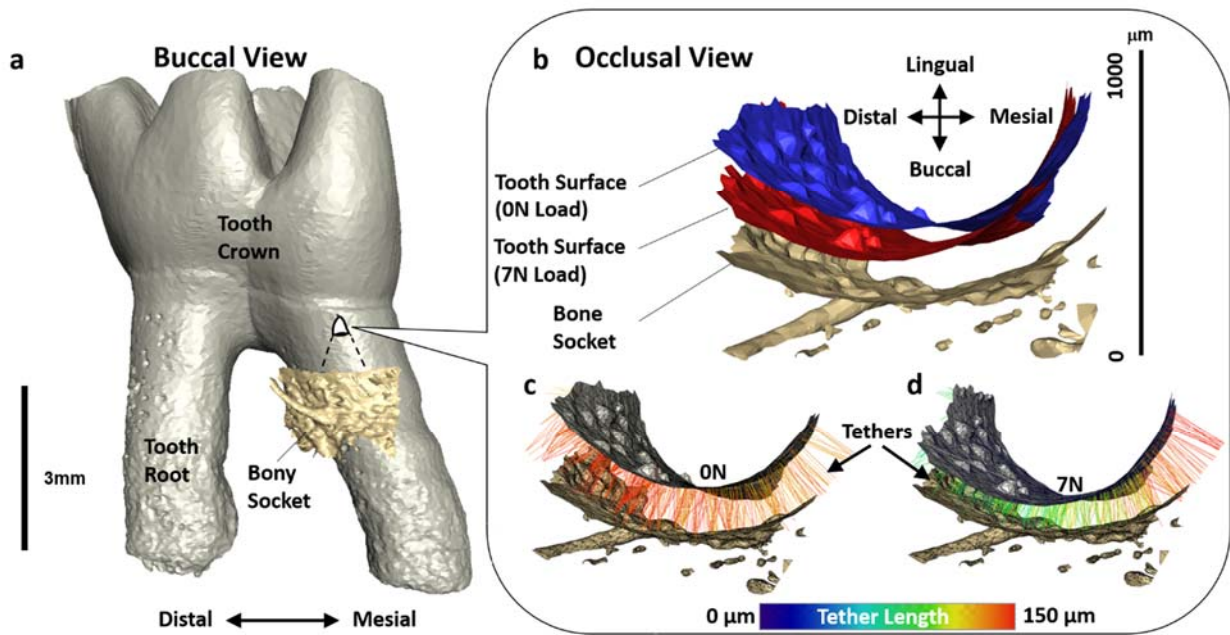
Figure 7.3. Tooth movement relative to the surface of the socket. (a) 3D surface rendering illustrates the position of a tooth relative to a portion of the root. (b) A magnified region of the bony socket with positions of the tooth relative to the alveolar socket surface at no-load (0N) (c) and loaded (7N) conditions (d) illustrates surface nodes and tethers.
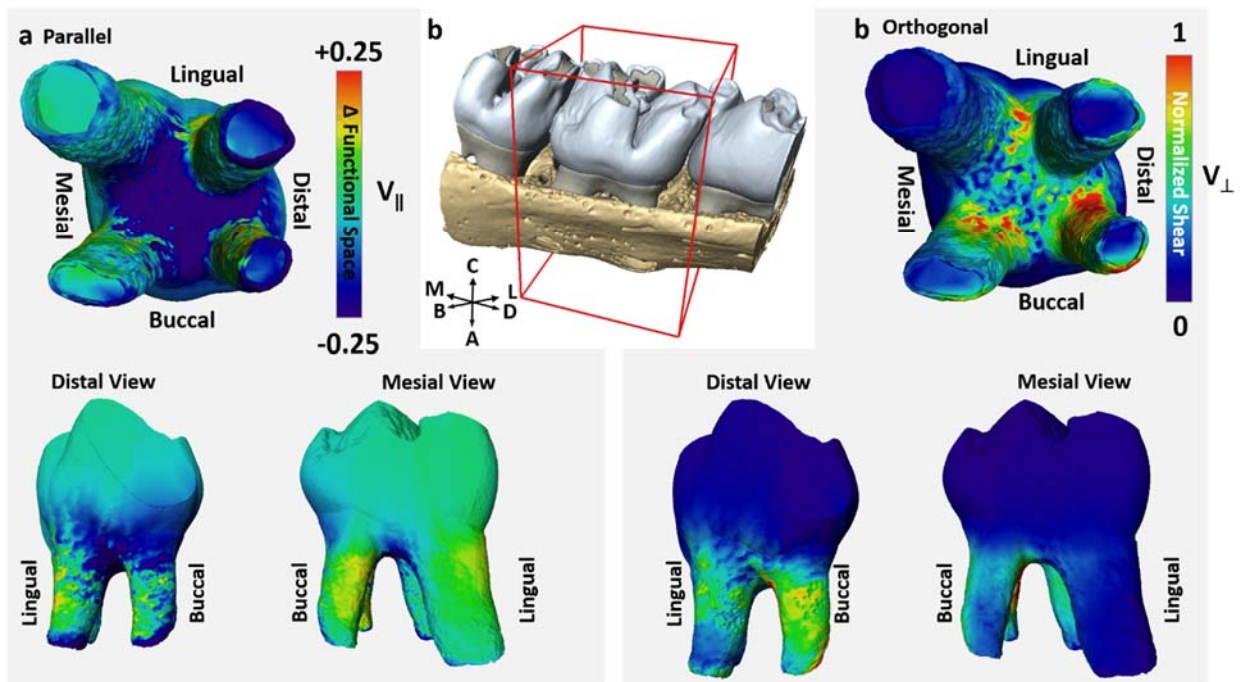
Figure 7.4. Surface mapping of $V_{\parallel}$ and $V_{\perp}$ vectors. (a) Narrowing and widening, and (c) shear components are illustrated as surface maps on a molar. Widening and less shear are seen on the mesial and lingual surfaces while increased narrowing and shear are seen at the distal l portions of the root of a molar. b) Model of tooth showing global directions [C-Coronal, L-Lingual, D-Distal, A-Apical, B-Buccal, M-Mesial].
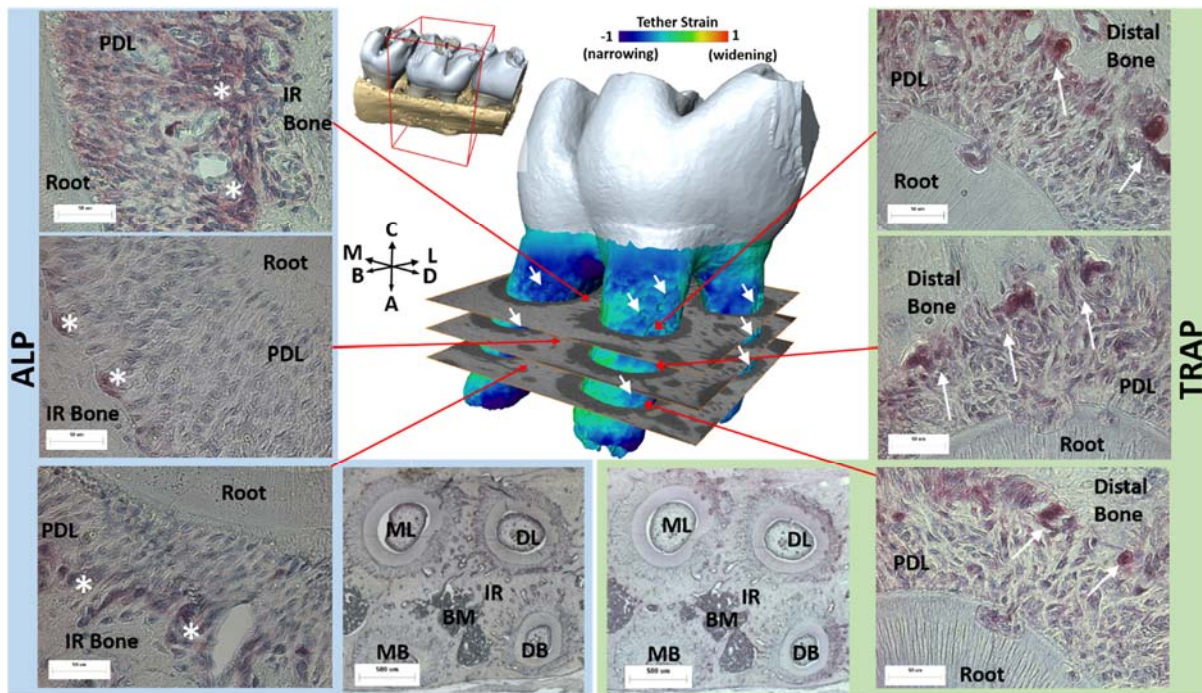
Figure 7.5. Spatial distribution of alkaline phosphatase (ALP) and tartrate resistant acid phosphatase (TRAP) staining. Transverse sections of the tooth-PDL-bone complex are shown to highlight spatial distributions of bone formation and resorption activities. ALP was mainly observed within the bone-PDL interfaces in the interradicular regions and within the interradicular endosteal spaces. TRAP was observed on the PDL-Bone interfaces on the distal regions of the complex.
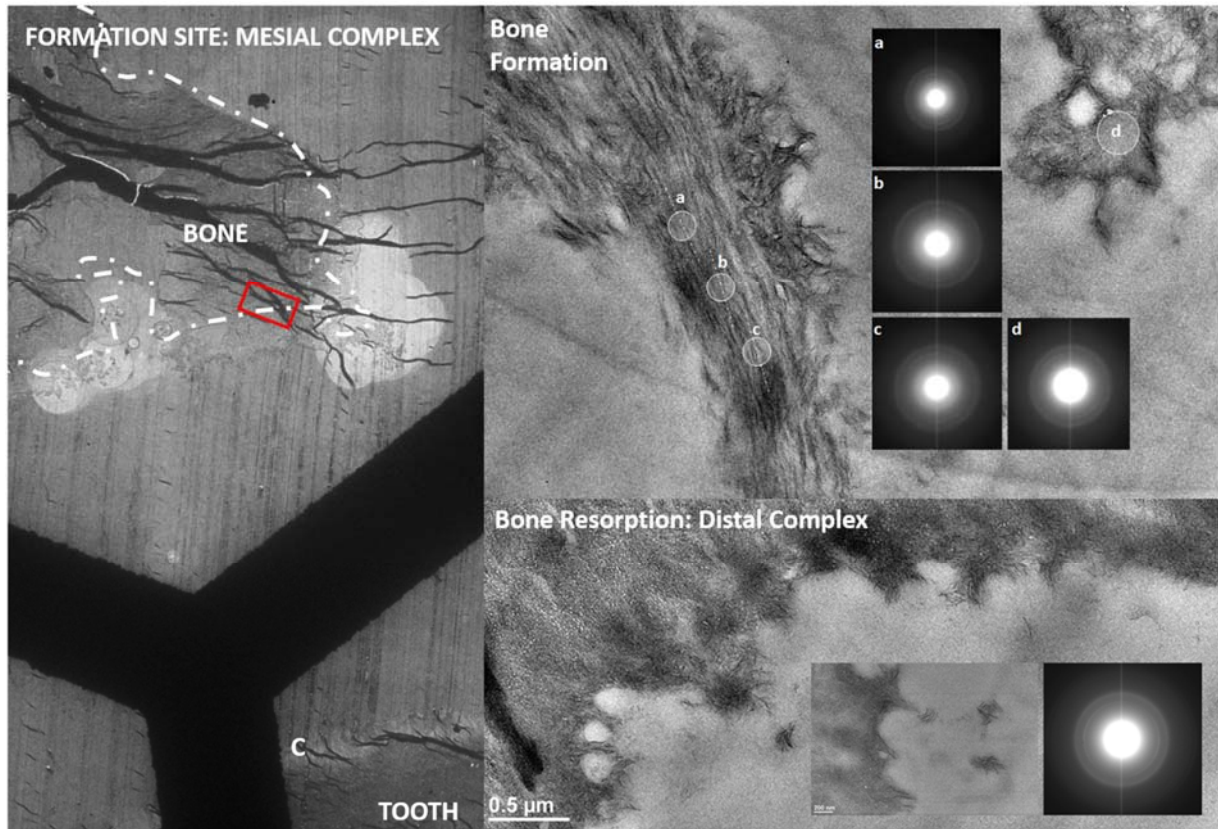
Figure 7.6. Transmission electron microscopy (TEM) of resorption and formation sites. Sites of formation (mesial distal complex) and resorption (distal complex) are shown. (ii) Sites of bone formation show hydroxyapatite crystal aligned with the collagen fibers. Alignment of hydroxyapatite crystal orientation is confirmed using the diffraction patterns of regions a-d. (iii) Sites of bone resorption on the distal complex show the classic scalloped pattern indicative of Howship's lacunae. Diffraction pattern shows decreased directionality of hydroxyapatite crystals.
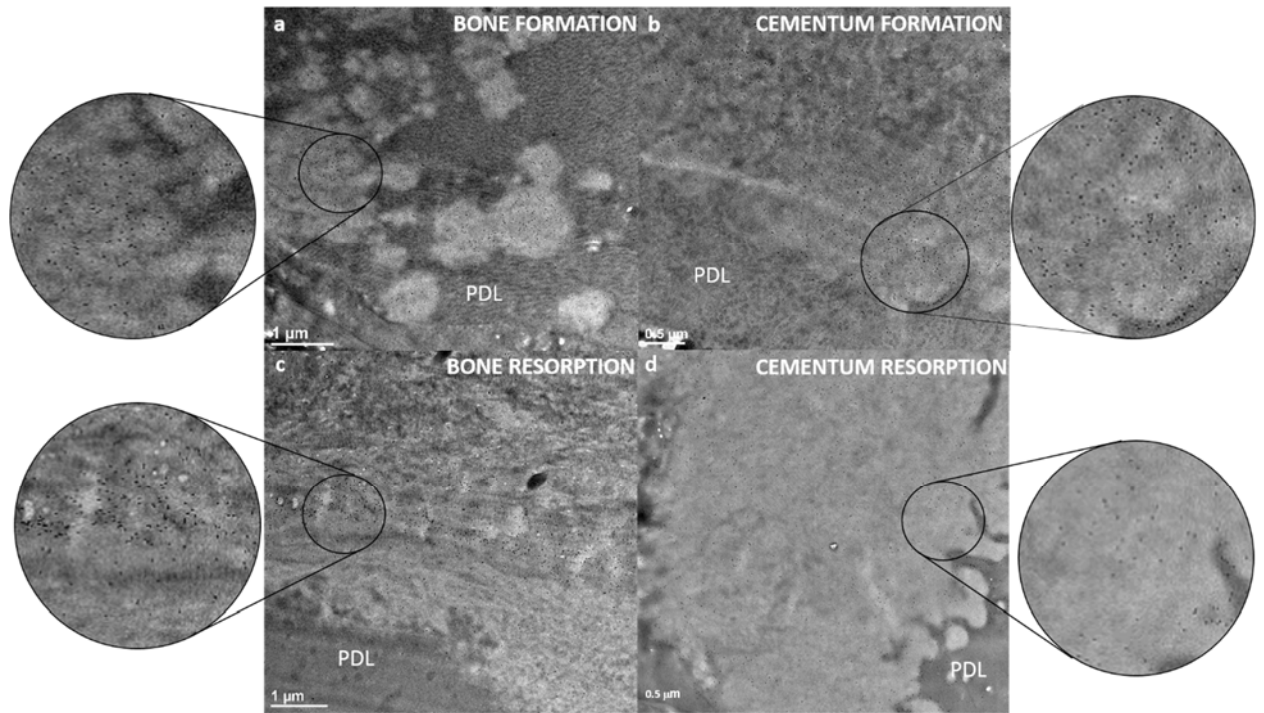
Figure 7.7. Immunogold labeling for bone sialoprotein within sites of (a) bone formation, (b) cementum formation, (c) bone resorption, and (d) cementum resorption. Lighter blotches represent previously calcified regions (removed by decalcification to allow for immunogold labeling). Within both formation and resorption sites, immunogold labeling (small black dots) highlight localization within regions previously containing mineral.

a Buccal View

Tooth Crown

F_load

DL Bone

Tooth Root

IR Bone

DB Bone

Mesial ⟷ Distal

b Occlusal View

D
L ⟷ B
M

Tooth Crown

Alveolar Bone

c

DL Bone

DB Bone

IR Bone

1mm

ALP activity
TRAP activity

d Interradicular Bone Compression

Tooth Surface

F_load

IR Bone

Activated bone fluid network

Increased ALP activity

Canniculi
Osteon

e Reduction of Distal Buccal PDL Space

Tooth Surface

Distal Buccal Bone

F_load

Tooth shift (DB direction)

Bone surface

Mastication Cycle

Strain

Mesial
Distal
prestrain

0

time

203

Figure 7.8.   A summary of spatial distribution of outcomes. (a-c) Results from the tether

model suggest that the tooth undergoes a combination of vertical movement as well as a

rotation in the distal-buccal direction.   Consequently, the affected primary regions by

mechanical motions are the IR bone as well as the distal-buccal (DB) and distal-lingual

(DL) roots. d) IR bone bears majority of compression during mastication as it first provides

a reactionary force by serving as a fulcrum prompting tooth rotation. The resulting

deformation causes shifts in mechanical strain within the ECM of porous bone and fluid

flow through the osteonal and canaliculi networks signaling local osteocytes and bone

lining cells to initiate mineral formation activities. e) Within the DB side of the tooth, the

space between the tooth and bone is narrowed, causing compression of the PDL –bone

and PDL-cementum interfaces and subsequent signaling of osteoclastic activities on the

cementum and alveolar bone surfaces. It is thought that the movement of the tooth

through mastication causes a reduction in the prestrain at the distal site creating the

necessary impetus for osteoclast activation.
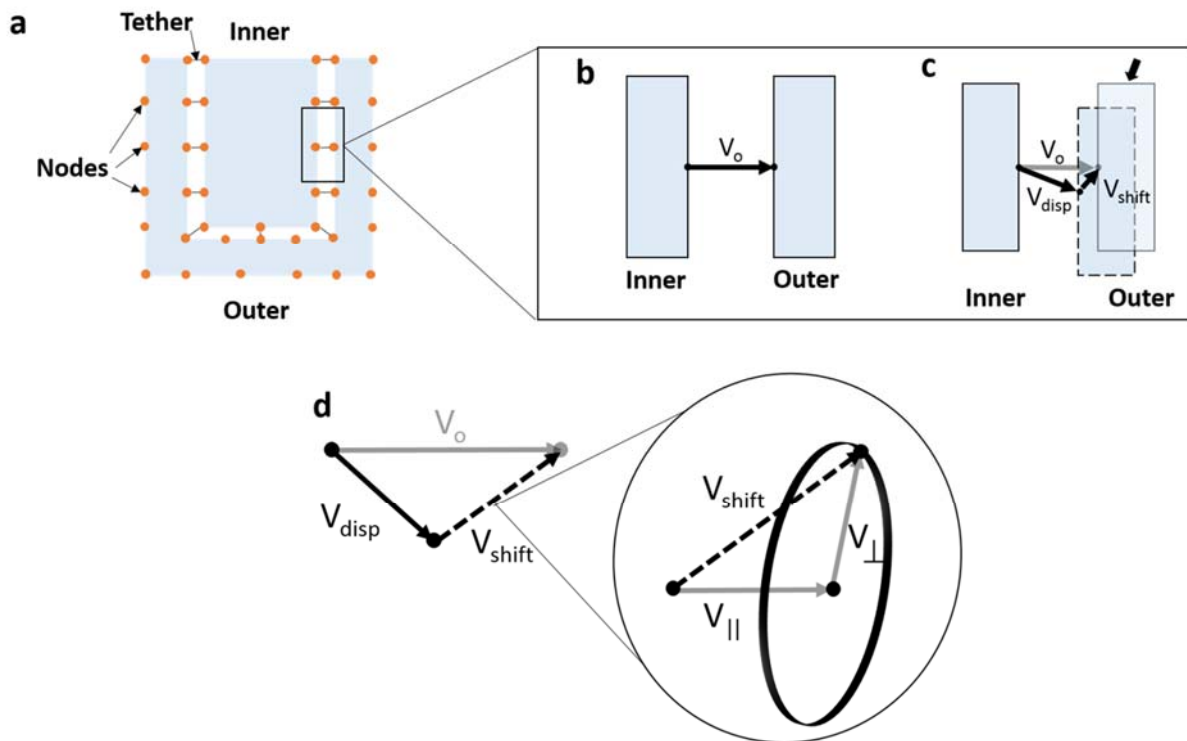
Figure 7.S1. Demonstration of tether generation. a) Surface of inner and outer regions illustrate nodes for the surface mesh. Tethers are formed between nodes of the inner and outer surfaces. b) The relative position of a single tether. c) Under loaded conditions is placed, the relative position of the inner and outer nodes change which shifts the tether. d) The tether displacement can further be broken down into vectors parallel and orthogonal to the original tether direction.
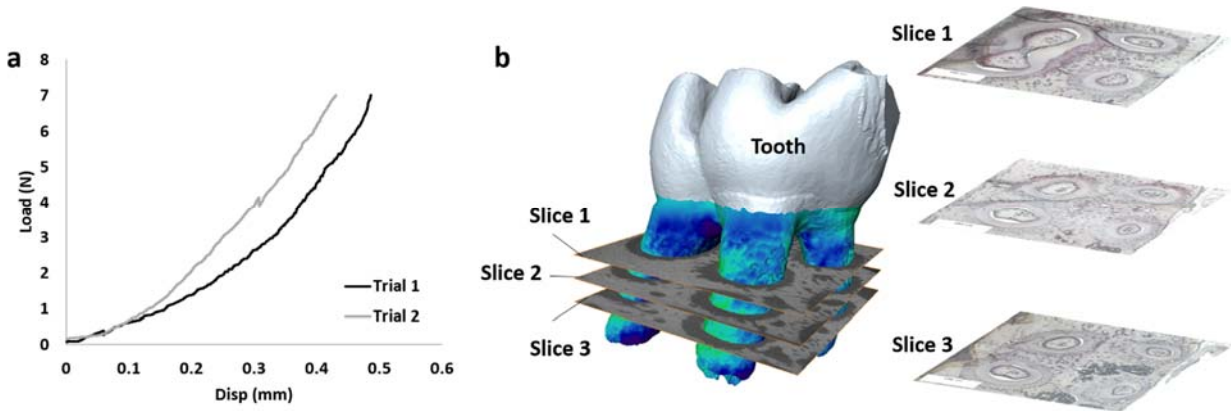
Figure 7.S2. Jaw mechanics, tooth motion and correlation with histology. (a) Load/displacement curves of the two whole jaw mechanics done using an *in situ* loading device. (b) Location of transverse sections for the correlation of biomechanical components, compression, tension and shear to provide insights into formation and resorption related biochemical events.
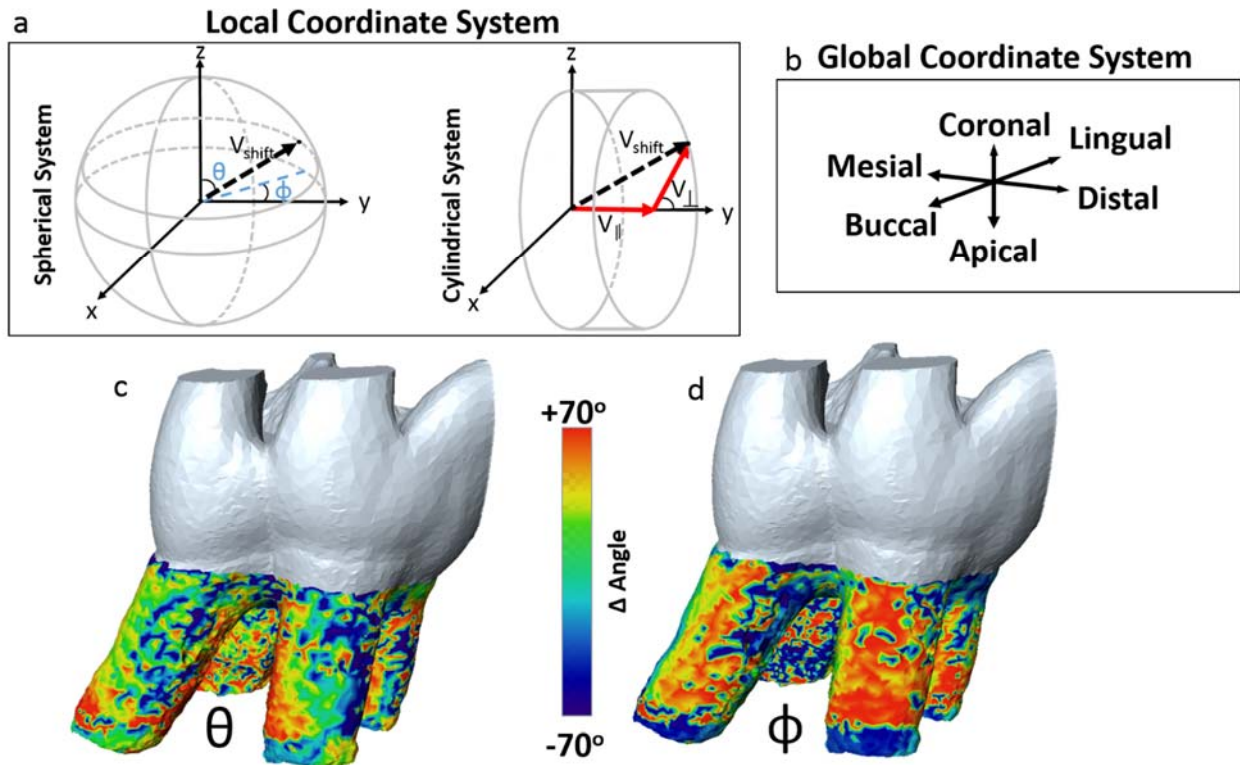
Figure 7.S3. Alternative to the current coordinate system for defining tether shifts. (a) Comparison of local coordinate systems (spherical and cylindrical) to (b) global coordinate systems. Using the spherical coordinate system can help define angulation changes through the definition of the φ and θ angles. Color maps of (c) θ and (d) φ show distributions of respective angle changes along the roots.
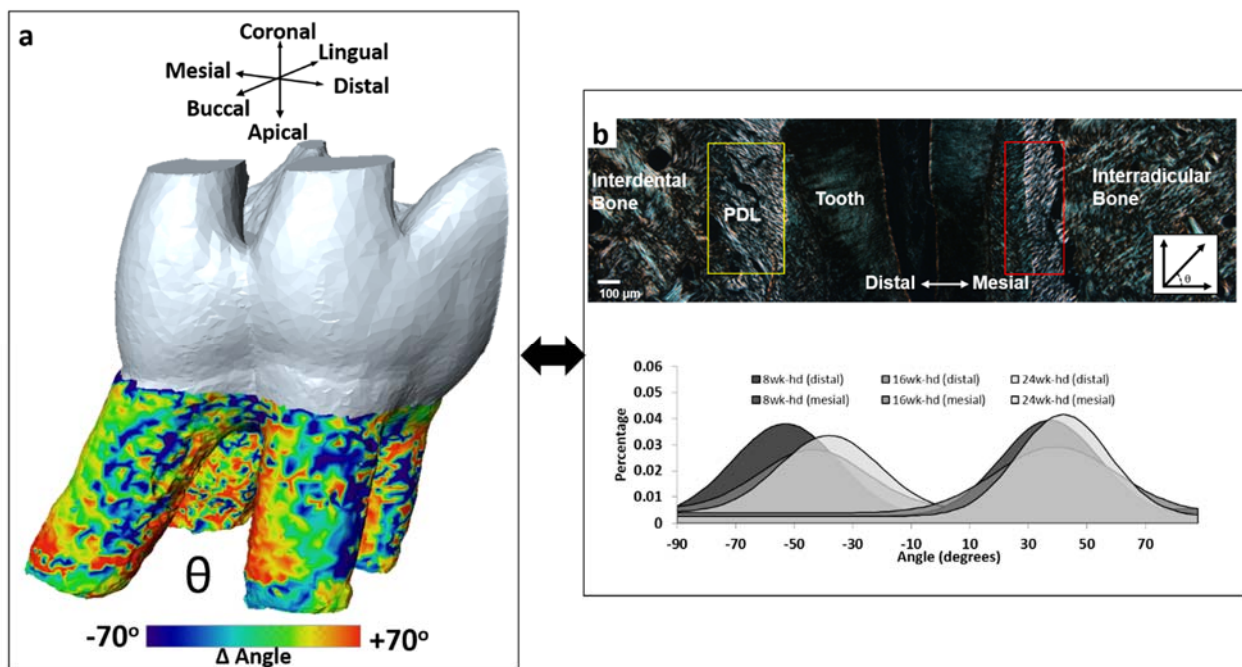
Figure 7.S4 Comparison of (a) spherical angulation in tether deformation to (b) directionality of PDL fibers taken from picrosirius red stains of histology sections. Sections were acquired from animals given a normal hard pellet diet over the course of 6 months. Histogram demonstrates general pattern for directionality measurements.

CHAPTER 8. LIMITATIONS AND FUTURE PERSPECTIVE

The mechanical stimulation arising from daily activities play an important role in the development, growth, and health of the supporting and load-bearing tissues. As an important epigenetic factor, the biological effects leading to functional adaptation has been studied from different perspectives ranging from macroscopic changes in shape of a human skull (Lieberman, 2011) to identifying shifts in production and regulation of mechanosensitive transcription factors (Nakashima et al., 2002). In addition, it has been documented that our bodies also respond to the cumulative effects of functional load, meaning that the nature of adaptation is influenced by the history of mechanical stimulation (Prendergast and Taylor, 1994; Turner, 1998). Studies from our group and others have confirmed the effects of mechanical stimulation on the dentoalveolar complex, highlighting its ability to change morphology and material properties of tissues (Niver et al., 2011). While previous publications have used reduction approach to analyze discrete tissues or interfaces *per se*, few have attempted to draw out the hierarchical nature of functional adaptation through a multiscale experimental perspective specifically using intact organs. Therefore, the major goal of this dissertation was to relate the spatiotemporal functional adaptation of the dentoalveolar tissues to clinical observations.

One of the primary functions of the dentoalveolar complex is to accept and dissipate the functional loads generated by mastication. Within chapter 5, shifts in the organ level biomechanics in response to reduced functional loads were investigated using an *in situ* loading setup which was calibrated within our lab (chapter 3 and (Lin et al., 2013)). The adaptations seen as a function of age were short lived and depended

primarily on the shifts in functional space. Additionally, the spatiotemporal aspect of the study demonstrated that the manifestation of adaptations within the complex depended on the tissue-types: changes in harder tissues can be recorded at a later time than changes in PDL within the functional space. The coupled effects between the change in morphology of the joint and the material properties of its individual tissues highlight the observed shift in biomechanics and the capacity of the joint to adapt to its local functional needs. In addition, the temporal nature of the study emphasized a plausible route for traumatic failure should the joint adapted to reduced functional loads be exposed to normal loads for rats, that is harder foods.

The dynamics between adaptations in both morphology and material properties of dentoalveolar tissues were analyzed in chapter 6. Through the use of *in situ* loading method, it was determined that the interradicular portion of the complex was significantly mechanically stimulated and this observation corroborated with that observed by others. The interradicular bone is the fulcrum for tooth rotation (Chattah et al., 2009; Christiansen and Burstone, 1969). Local strain distributions as observed using DVC (chapter 4) of control (normal harder pellets) and those adapted to reduced functional loads highlighted the effect due to a change in biomechanics as a result of a change in functional loads on the interradicular bone. Shifts in both material properties as well as changes in interradicular bone morphology could be due to a shift in mineral resorption activity in adapted systems from reduced functional load group compared to control. Finally, it was postulated that collective optimization of form and material properties within the interradicular bone are needed, and that these changes in physical properties could be inversely related to functional optimization of the joint.

Within chapter 7, a multiscale approach was used to apply direct physiological relevance of functional loads through correlation of local deformations produced from organ-level biomechanical events to site specific shifts in tissue-level mechanobiological events. To increase the physiological relevance of simulated loads, improvements to our standard *in situ* model were made by modeling the influence of the temporal mandibular joint's rotational path and the interdigitating pattern of the maxillary and mandibular occlusal surfaces on the micro motion of the tooth within the alveolar socket. Deformations within the functional PDL-space of the dentoalveolar complex were taken by utilizing a novel digital tether method. Observed patterns in PDL deformation were then related to the shifts in the TRAP and ALP distributions representing resorption and formation activities of bone specifically at PDL-bone and PDL-cementum tethered ends. Of particular interest was the correlation between the increased compression/shear within the PDL and the increased resorption at the distal portions of the alveolar socket. In conjunction with the results that this distal resorption response was attenuated when reducing functional loads, it was hypothesized that the distal drift that naturally occurs within rats is primarily initiated by osteoclastic activities which resorb the distal boarder of the alveolar socket and that the functional loads produced from mastication provided the necessary impetus for this resorption activity.

In summary, the work within this dissertation represents work that expands on the current dogma of functional adaptation within the dentoalveolar socket through the inclusion of a multiscale perspective. While the research within attempted to push the boundaries in correlative microscopy and biomechanics, future studies and technological advancements are needed to overcome the limitations of our experiments and better

understand the complete hierarchical story connecting organ level loads to mechanobiological events specifically within *in vivo* models (current study is limited to measurements in ex vivo systems). The described *in situ* biomechanical experiments did not account for temperature and effects of vessel pressure of an *in vivo* model. While considered extremely difficult by today's standards due to resolution and penetration constraints, the measurement of deformation within a living functionally active joint at the resolution attempted in this study could theoretically be achieved should the *in* vivo three dimensional imaging modalities including ultrasound be challenged. Additionally, the usage of fluorescent microscopy techniques designed to produce three dimensional images (e.g. light sheet) would be advantageous over the current 2D to 3D correlations which were primarily utilized within this dissertation. Improvements to the digital tether model can include supplementing the model with anisotropic organization, directionality of the PDL fibers and constitutive properties to the tethers and tethered ends that include interfaces (properties are significantly different from bulk tissues *per se*). Finally, the results and methods described provide a scientific baseline in which future multiscale studies can be performed.   Examples include testing of known and novel mechanosensitive proteins using transgenic models and the exploration at multiple scales on the effects due to diseases and therapies within the oral cavity.

REFERENCES

Agarwal, S., Long, P., Gassner, R., Piesco, N.P., and Buckley, M.J. (2001). Cyclic tensile strain suppresses catabolic effects of interleukin-1β in fibrochondrocytes from the temporomandibular joint. Arthritis Rheum. *44*, 608–617.

Aghaloo, T.L., Chaichanasakul, T., Bezouglaia, O., Kang, B., Franco, R., Dry, S.M., Atti, E., and Tetradis, S. (2010). Osteogenic Potential of Mandibular vs. Long-bone Marrow Stromal Cells. J. Dent. Res. *89*, 1293–1298.

Ahlgren, J., and Öwall, B. (1970). Muscular activity and chewing force: A polygraphic study of human mandibular movements. Arch. Oral Biol. *15*, 271–IN1.

Alenghat, F.J., and Ingber, D.E. (2002). Mechanotransduction: all signals point to cytoskeleton, matrix, and integrins. Sci STKE *119*.

Alhashimi, Frithiof, L., Brudvik, P., and Bakhiet, M. (2000). Orthodontic Movement Induces High Numbers of Cells Expressing IFN-gamma at mRNA and Protein Levels. J. Interferon Cytokine Res. *20*, 7–12.

Alhashimi, Frithiof, L., Brudvik, P., and Bakhiet, M. (2001). Orthodontic tooth movement and de novo synthesis of proinflammatory cytokines. Am. J. Orthod. Dentofacial Orthop. *119*, 307–312.

Asbell, M.B. (1990). A brief history of orthodontics. Am. J. Orthod. Dentofacial Orthop. *98*, 176–183.

ASTM - E04 Committee (1999). Test Method for Microindentation Hardness of Materials (ASTM International).

Asundi, A., and Kishen, A. (2000). A strain gauge and photoelastic analysis of in vivo strain and in vitro stress distribution in human dental supporting structures. Arch. Oral Biol. *45*, 543–550.

Asundi, A., and Kishen, A. (2001). Advanced digital photoelastic investigations on the tooth–bone interface. J. Biomed. Opt. *6*, 224–230.

Baud, C.A.M.D. (1968). Submicroscopic Structure and Functional Aspects of the Osteocyte*. Clin. Orthop. *56*, 227–236.

Baumhammers, A., Stallard, R.E., and Zander, H.A. (1965). Remodeling of alveolar bone. J. Periodontol. *36*, 439–442.

Bay, B.K., Smith, T.S., Fyhrie, D.P., and Saad, M. (1999). Digital volume correlation: Three-dimensional strain mapping using X-ray tomography. Exp. Mech. *39*, 217–226.

Beecher, R.M., and Corruccini, R.S. (1981). Effects of Dietary Consistency on Craniofacial and Occlusal Development in the Rat. Angle Orthod. *51*, 61–69.

Bellows, C.G., Melcher, A.H., and Aubin, J.E. (1982). Association between tension and orientation of periodontal ligament fibroblasts and exogenous collagen fibres in collagen gels in vitro. J. Cell Sci. *58*, 125–138.

Belting, C.M., Schour, I., Weinmann, J.P., and Shepro, M.J. (1953). Age Changes in the Periodontal Tissues of the Rat Molar. J. Dent. Res. *32*, 332–353.

Benjamin, M., Kumai, T., Milz, S., Boszczyk, B.M., Boszczyk, A.A., and Ralphs, J.R. (2002). The skeletal attachment of tendons—tendon "entheses." Comp. Biochem. Physiol. A. Mol. Integr. Physiol. *133*, 931–945.

Benjamin, M., Toumi, H., Ralphs, J.R., Bydder, G., Best, T.M., and Milz, S. (2006). Where tendons and ligaments meet bone: attachment sites ("entheses") in relation to exercise and/or mechanical load. J. Anat. *208*, 471–490.

Berkovitz, B.K.B. (1990). The structure of the periodontal ligament: an update. Eur. J. Orthod. *12*, 51–76.

Biknevicius, A.R., and Leigh, S.R. (1997). Patterns of growth of the mandibular corpus in spotted hyenas (Crocuta crocuta) and cougars (Puma concolor). Zool. J. Linn. Soc. *120*, 139–161.

Bing, P., Hui-min, X., Tao, H., and Asundi, A. (2009). Measurement of coefficient of thermal expansion of films using digital image correlation method. Polym. Test. *28*, 75–83.

Blumenthal, D.N.C., Betts, F., and Posner, A.S. (1975). Effect of carbonate and biological macromolecules on formation and properties of hydroxyapatite. Calcif. Tissue Res. *18*, 81–90.

Bondevik, O. (1980). Tissue changes in the rat molar periodontium following application of intrusive forces. Eur. J. Orthod. *2*, 41–49.

Bondevik, O. (1984). Tissue changes in the rat molar periodontium following alteration of normal occlusal forces. Eur. J. Orthod. *6*, 205–212.

Bonewald, L.F. (2006). Mechanosensation and transduction in osteocytes. BoneKEy-Osteovision *3*, 7–15.

Boresi, A.P., Schmidt, R.J., and Sidebottom, O.M. (1993). Advanced mechanics of materials (Wiley New York).

Boskey, A.L., and Posner, A.S. (1974). Magnesium stabilization of amorphous calcium phosphate: A kinetic study. Mater. Res. Bull. *9*, 907–916.

Boskey, A., and Pleshko Camacho, N. (2007). FT-IR imaging of native and tissue-engineered bone and cartilage. Biomaterials *28*, 2465–2478.

Bosshardt, D.D., and Selvig, K.A. (1997). Dental cementum: the dynamic tissue covering of the root. Periodontol. 2000 *13*, 41–75.

Bosshardt, D.D., Zalzal, S., Mckee, M.D., and Nanci, A. (1998). Developmental appearance and distribution of bone sialoprotein and osteopontin in human and rat cementum. Anat. Rec. *250*, 13–33.

Bouvier, M. (1988). Effects of Age on the Ability of the Rat Temporomandibular Joint to Respond to Changing Functional Demands. J. Dent. Res. *67*, 1206–1212.

Bouvier, M., and Hylander, W.L. (1984). The effect of dietary consistency on gross and histologic morphology in the craniofacial region of young rats. Am. J. Anat. *170*, 117–126.

Bouxsein, M.L., Boyd, S.K., Christiansen, B.A., Guldberg, R.E., Jepsen, K.J., and Müller, R. (2010). Guidelines for assessment of bone microstructure in rodents using micro–computed tomography. J. Bone Miner. Res. *25*, 1468–1486.

Boyle, W.J., Simonet, W.S., and Lacey, D.L. (2003). Osteoclast differentiation and activation. Nature *423*, 337–342.

Braun, S., Bantleon, H.-P., Hnat, W.P., Freudenthaler, J.W., Marcotte, M.R., and Johnson, B.E. (1995). A study of bite force, part 2: Relationship to various cephalometric measurements. Angle Orthod. *65*, 373–377.

Braun, S., Hnat, W.P., Freudenthaler, J.W., Marcotte, M.R., Hönigle, K., and Johnson, B.E. (1996). A study of maximum bite force during growth and development. Angle Orthod. *66*, 261–264.

Bromage, T.G., Goldman, H.M., McFarlin, S.C., Warshaw, J., Boyde, A., and Riggs, C.M. (2003). Circularly polarized light standards for investigations of collagen fiber orientation in bone. Anat. Rec. B. New Anat. *274B*, 157–168.

Carter, D. (1984). Mechanical loading histories and cortical bone remodeling. Calcif. Tissue Int. *36*, S19–S24.

Carter, D. (1987). Mechanical loading history and skeletal biology. J. Biomech. *20*, 1095–1109.

Carter, D.R., and Beaupré, G.S. (2007). Skeletal function and form: mechanobiology of skeletal development, aging, and regeneration (Cambridge University Press).

Carter, D., Van der Meulen, M.C.H., and Beaupré, G.S. (1996). Mechanical factors in bone growth and development. Bone *18*, S5–S10.

Carvalho, R.S., Yen, E.H.K., and Suga, D.M. (1995). Glycosaminoglycan synthesis in the rat articular disk in response to mechanical stress. Am. J. Orthod. Dentofacial Orthop. *107*, 401–410.

Cattaneo, P.M., Dalstra, M., and Melsen, B. (2005). The Finite Element Method: a Tool to Study Orthodontic Tooth Movement. J. Dent. Res. *84*, 428–433.

Chattah, N.L.-T., Shahar, R., and Weiner, S. (2009). Design Strategy of Minipig Molars Using Electronic Speckle Pattern Interferometry: Comparison of Deformation under Load between the Tooth-Mandible Complex and the Isolated Tooth. Adv. Mater. *21*, 413–418.

Chen, C.S., and Ingber, D.E. (1999). Tensegrity and mechanoregulation: from skeleton to cytoskeleton. Osteoarthritis Cartilage *7*, 81–94.

Chen, J., McKee, M.D., Nanci, A., and Sodek, J. (1994). Bone sialoprotein mRNA expression and ultrastructural localization in fetal porcine calvarial bone: comparisons with osteopontin. Histochem. J. *26*, 67–78.

Chen, L., Jacquet, R., Lowder, E., and Landis, W.J. (2015). Refinement of collagen–mineral interaction: A possible role for osteocalcin in apatite crystal nucleation, growth and development. Bone *71*, 7–16.

Chiba, M., and Komatsu, K. (1993). Mechanical responses of the periodontal ligament in the transverse section of the rat mandibular incisor at various velocities of loading in vitro. J. Biomech. *26*, 561–570.

Chin, M., and Toth, B.A. (1996). Distraction osteogenesis in maxillofacial surgery using internal devices: Review of five cases. J. Oral Maxillofac. Surg. *54*, 45–53.

Christiansen, R.L., and Burstone, C.J. (1969). Centers of rotation within the periodontal space. Am. J. Orthod. *55*, 353–369.

Civitelli, R. (2008). Cell–cell communication in the osteoblast/osteocyte lineage. Arch. Biochem. Biophys. *473*, 188–192.

Cole III, T.M. (1992). Postnatal heterochrony of the masticatory apparatus in Cebus apella and Cebus albifrons. J. Hum. Evol. *23*, 253–282.

Copray, J., Jansen, H.W.B., and Duterloo, H.S. (1985). Effects of compressive forces on proliferation and matrix synthesis in mandibular condylar cartilage of the rat< i> in vitro</i>. Arch. Oral Biol. *30*, 299–304.

Cornelis, M.A., Scheffler, N.R., De Clerck, H.J., Tulloch, J.F.C., and Behets, C.N. (2007). Systematic review of the experimental use of temporary skeletal anchorage devices in orthodontics. Am. J. Orthod. Dentofacial Orthop. *131*, S52–S58.

Cowin, S.C., Moss-Salentijn, L., and Moss, M.L. (1991). Candidates for the Mechanosensory System in Bone. J. Biomech. Eng. *113*, 191–197.

Crabtree, W., and Murphy, W. (1979). The value of ethanol as a fixative in urinary cytology. Acta Cytol. *24*, 452–455.

Dawson, P.E. (2006). Functional occlusion: from TMJ to smile design (Elsevier Health Sciences).

Doherty, A.H., Lowder, E.M., Jacquet, R.D., and Landis, W.J. (2010). Murine Metapodophalangeal Sesamoid Bones: Morphology and Potential Means of Mineralization Underlying Function. Anat. Rec. Adv. Integr. Anat. Evol. Biol. *293*, 775–785.

Dong-Xu, L., Hong-Ning, W., Chun-Ling, W., Hong, L., Ping, S., and Xiao, Y. (2011). Modulus of elasticity of human periodontal ligament by optical measurement and numerical simulation. Angle Orthod. *81*, 229–236.

Dougherty, E.R., Lotufo, R.A., and SPIE, T.I.S. for O.E. (2003). Hands-on morphological image processing (SPIE press Bellingham).

Drzazga, Z., Michalik, K., Maciejewska, K., Trzeciak, H., and Kaszuba, M. (2007). Role of endogenous zinc in bones of newborn rats. BioFactors Oxf. Engl. *30*, 243–248.

Du, J., Lee, J., Jang, A., Gu, A., Hossaini-Zadeh, M., Prevost, R., Curtis, D., and Ho, S. (2015). Biomechanics and strain mapping in bone as related to immediately-loaded dental implants. J. Biomech.

Duncan, R.L., and Turner, C.H. (1995). Mechanotransduction and the functional response of bone to mechanical strain. Calcif. Tissue Int. *57*, 344–358.

Embery, G., Waddington, R., and Hall, R. (1995). The ground substance of the periodontal ligament. Periodontal Ligament Health Dis. 83–106.

Endo, B. (1966). Experimental studies on the mechanical significance of the form of the human facial skeleton. J. Fac. Sci. Univ. Tokyo Sect. 5 Anthropol. *3*, 1–106.

Engler, A.J., Sen, S., Sweeney, H.L., and Discher, D.E. (2006). Matrix Elasticity Directs Stem Cell Lineage Specification. Cell *126*, 677–689.

Enokida, M., Kaneko, S., Yanagishita, M., and Soma, K. (2005). Influence of Occlusal Stimuli on the Remodelling of Alveolar Bone in a Rat Hypofunction-Recovery Model. J. Oral Biosci. *47*, 321–334.

Erlebacher, A., and Derynck, R. (1996). Increased expression of TGF-beta 2 in osteoblasts results in an osteoporosis-like phenotype. J. Cell Biol. *132*, 195–210.

Evans, S.L., and Holt, C.A. (2009). Measuring the mechanical properties of human skin in vivo using digital image correlation and finite element modelling. J. Strain Anal. Eng. Des. *44*, 337–345.

Foster, B.L., Popowics, T.E., Fong, H.K., and Somerman, M.J. (2007). Advances in defining regulators of cementum development and periodontal regeneration. Curr. Top. Dev. Biol. *78*, 47–126.

Fox, S.W., Chambers, T.J., and Chow, J.W. (1996). Nitric oxide is an early mediator of the increase in bone formation by mechanical stimulation. Am. J. Physiol. - Endocrinol. Metab. *270*, E955–E960.

Frost, H.M. (1964). Mathematical Elements of Lamellab Bone Remodeling. Plast. Reconstr. Surg. *34*, 315.

Frost, H.M. (1987). Bone "mass" and the "mechanostat": A proposal. Anat. Rec. *219*, 1–9.

Frost, H.M. (1998). Changing concepts in skeletal physiology: Wolff's Law, the Mechanostat, and the "Utah Paradigm." Am. J. Hum. Biol. *10*, 599–605.

Frost, H.M. (1999). Why do bone strength and "mass" in aging adults become unresponsive to vigorous exercise? Insights of the Utah paradigm. J. Bone Miner. Metab. *17*, 90–97.

Frost, H.M. (2003). Bone's mechanostat: A 2003 update. Anat. Rec. A. Discov. Mol. Cell. Evol. Biol. *275A*, 1081–1101.

Frost, H.M., Villanueva, A.R., Roth, H., and Stanisavljevic, S. (1961). Tetracycline Bone Labeling. J. New Drugs *1*, 206–216.

Fung, Y.C. (1990). Biomechanical Aspects of Growth and Tissue Engineering. In Biomechanics, (Springer New York), pp. 499–546.

Ga, I. (1987). The principles of the Ilizarov method. Bull. Hosp. Jt. Dis. Orthop. Inst. *48*, 1–11.

Gaengler, P. (2007). 12 Evolution of tooth attachment in lower vertebrates to tetrapods. Dev. Funct. Evol. Teeth 173.

Ganss, B., and Jheon, A. (2004). ZINC FINGER TRANSCRIPTION FACTORS IN SKELETAL DEVELOPMENT. Crit. Rev. Oral Biol. Med. *15*, 282–297.

Garlet, T.P., Coelho, U., Silva, J.S., and Garlet, G.P. (2007). Cytokine expression pattern in compression and tension sides of the periodontal ligament during orthodontic tooth movement in humans. Eur. J. Oral Sci. *115*, 355–362.

George, A., Sabsay, B., Simonian, P.A., and Veis, A. (1993). Characterization of a novel dentin matrix acidic phosphoprotein. Implications for induction of biomineralization. J. Biol. Chem. *268*, 12624–12630.

Gibson, J.M., King, G.J., and Keeling, S.D. (1992). Long-term orthodontic tooth movement response to short-term force in the rat. Angle Orthod. *62*, 211–215.

Gillard, F., Boardman, R., Mavrogordato, M., Hollis, D., Sinclair, I., Pierron, F., and Browne, M. (2014). The application of digital volume correlation (DVC) to study the microstructural behaviour of trabecular bone during compression. J. Mech. Behav. Biomed. Mater. *29*, 480–499.

Grandfield, K., Herber, R.-P., Chen, L., Djomehri, S., Tam, C., Lee, J.-H., Brown, E., Woolwine III, W.R., Curtis, D., Ryder, M., et al. (2015). Strain-guided mineralization in the bone–PDL–cementum complex of a rat periodontium. Bone Rep. *3*, 20–31.

Grünheid, T. (2010). The masticatory system under varying functional load.

Hallmon, W.W. (1999). Occlusal Trauma: Effect and Impact on the Periodontium. Ann. Periodontol. *4*, 102–107.

Hals, E., and Selvig, K.A. (1977). Correlated electron probe microanalysis and microradiography of carious and normal dental cementum. Caries Res. *11*, 62–75.

Hardisty, M.R., and Whyne, C.M. (2009). Whole Bone Strain Quantification by Image Registration: A Validation Study. J. Biomech. Eng. *131*, 064502–064502.

Hartsfield, J.K., Everett, E.T., and Al-Qawasmi, R.A. (2004). Genetic Factors in External Apical Root Resorption and Orthodontic Treatment. Crit. Rev. Oral Biol. Med. *15*, 115–122.

Hartsfield Jr, J. (2009). Pathways in external apical root resorption associated with orthodontia. Orthod. Craniofac. Res. *12*, 236–242.

Hemae, K.M. (1967). Masticatory Function in the Mammals. J. Dent. Res. *46*, 883–893.

Herber, R.-P., Fong, J., Lucas, S.A., and Ho, S.P. (2012). Imaging an Adapted Dentoalveolar Complex. Anat. Res. Int. *2012*, e782571.

Herring, S.W., and Mucci, R.J. (1991). In vivo strain in cranial sutures: The zygomatic arch. J. Morphol. *207*, 225–239.

Herring, S.W., and Wineski, L.E. (1986). Development of the masseter muscle and oral behavior in the pig. J. Exp. Zool. *237*, 191–207.

Herring, S.W., Anapol, F.C., and Wineski, L.E. (1991). Motor-unit territories in the masseter muscle of infant pigs. Arch. Oral Biol. *36*, 867–873.

Hiiemäe, K. (2004). Mechanisms of food reduction, transport and deglutition: how the texture of food affects feeding behavior. J. Texture Stud. *35*, 171–200.

Hiiemäe, K.M., and Ardran, G.M. (1968). A cinefluorographic study of mandibular movement during feeding in the rat (Rattus norvegicus). J. Zool. *154*, 139–154.

Hiiemäe, K.M., and Houston, W.J.B. (1971). The structure and function of the jaw muscles in the rat (Rattus norvegicus L.). Zool. J. Linn. Soc. *50*, 75–99.

Ho, S.P., Balooch, M., Marshall, S.J., and Marshall, G.W. (2004). Local properties of a functionally graded interphase between cementum and dentin. J. Biomed. Mater. Res. A *70A*, 480–489.

Ho, S.P., Sulyanto, R.M., Marshall, S.J., and Marshall, G.W. (2005). The cementum–dentin junction also contains glycosaminoglycans and collagen fibrils. J. Struct. Biol. *151*, 69–78.

Ho, S.P., Yu, B., Yun, W., Marshall, G.W., Ryder, M.I., and Marshall, S.J. (2009). Structure, chemical composition and mechanical properties of human and rat cementum and its interface with root dentin. Acta Biomater. *5*, 707–718.

Ho, S.P., Kurylo, M.P., Fong, T.K., Lee, S.S.J., Wagner, H.D., Ryder, M.I., and Marshall, G.W. (2010a). The biomechanical characteristics of the bone-periodontal ligament-cementum complex. Biomaterials *31*, 6635–6646.

Ho, S.P., Kurylo, M.P., Fong, T.K., Lee, S.S.J., Wagner, H.D., Ryder, M.I., and Marshall, G.W. (2010b). The biomechanical characteristics of the bone-periodontal ligament-cementum complex. Biomaterials *31*, 6635–6646.

Ho, S.P., Kurylo, M.P., Grandfield, K., Hurng, J., Herber, R.-P., Ryder, M.I., Altoe, V., Aloni, S., Feng, J.Q., Webb, S., et al. (2013). The plastic nature of the human bone–periodontal ligament–tooth fibrous joint. Bone *57*, 455–467.

Holmvall, K., Camper, L., Johansson, S., Kimura, J.H., and Lundgren-Åkerlund, E. (1995). Chondrocyte and Chondrosarcoma Cell Integrins with Affinity for Collagen Type II and Their Response to Mechanical Stress. Exp. Cell Res. *221*, 496–503.

Huang, Q., Opstelten, D., Samman, N., and Tideman, H. (2002). Experimentally induced unilateral tooth loss: histochemical studies of the temporomandibular joint. J. Dent. Res. *81*, 209–213.

Huang, Q., Opstelten, D., Samman, N., and Tideman, H. (2003). Experimentally induced unilateral tooth loss: expression of type II collagen in temporomandibular joint cartilage 1, 2. J. Oral Maxillofac. Surg. *61*, 1054–1060.

Huelke, D.F., and Castelli, W.A. (1965). The blood supply of the rat mandible. Anat. Rec. *153*, 335–341.

Hunt, H.R., Rosen, S., and Hoppert, C.A. (1970). Morphology of Molar Teeth and Occlusion in Young Rats. J. Dent. Res. *49*, 508–514.

Hunter, G.K., and Goldberg, H.A. (1993). Nucleation of hydroxyapatite by bone sialoprotein. Proc. Natl. Acad. Sci. *90*, 8562–8565.

Hurng, J.M., Kurylo, M.P., Marshall, G.W., Webb, S.M., Ryder, M.I., and Ho, S.P. (2011). Discontinuities in the human bone–PDL–cementum complex. Biomaterials *32*, 7106–7117.

Hylander, W.L. (1985). Mandibular Function and Biomechanical Stress and Scaling. Am. Zool. *25*, 315–330.

Hylander, W.L., and Johnson, K.R. (1992). Strain gradients in the craniofacial region of primates. Biol. Mech. Tooth Mov. Craniofacial Adapt. 559–569.

Hylander, W.L., and Johnson, K.R. (1997). In vivo bone strain patterns in the craniofacial region of primates. Sci. Pract. Occlusion 165–178.

Hylander, W.L., Johnson, K.R., and Picq, P.G. (1991). Masticatory-stress hypotheses and the supraorbital region of primates. Am. J. Phys. Anthropol. *86*, 1–36.

Ingber, D. (1991). Integrins as mechanochemical transducers. Curr. Opin. Cell Biol. *3*, 841–848.

Ingber, D. (2003). Mechanobiology and diseases of mechanotransduction. Ann. Med. *35*, 564–577.

Ingber, D. (2006). Cellular mechanotransduction: putting all the pieces together again. FASEB J. *20*, 811–827.

Ingber, D.E. (1997). Tensegrity: the architectural basis of cellular mechanotransduction. Annu. Rev. Physiol. *59*, 575–599.

Ingber, D.E. (2005). Tissue adaptation to mechanical forces in healthy, injured and aging tissues. Scand. J. Med. Sci. Sports *15*, 199–201.

Itoiz, M.E., Carranza Jr, F.A., and Cabrini, R.L. (1963). Histologic and histometric study of experimental occlusal trauma in rats. J. Periodontol. *34*, 305–314.

Jaalouk, D.E., and Lammerding, J. (2009). Mechanotransduction gone awry. Nat. Rev. Mol. Cell Biol. *10*, 63–73.

Jang, A.T., Lin, J.D., Choi, R.M., Choi, E.M., Seto, M.L., Ryder, M.I., Gansky, S.A., Curtis, D.A., and Ho, S.P. (2014a). Adaptive properties of Human cementum and cementum dentin junction with age. J. Mech. Behav. Biomed. Mater.

Jang, A.T., Lin, J.D., Seo, Y., Etchin, S., Merkle, A., Fahey, K., and Ho, S.P. (2014b). In situ Compressive Loading and Correlative Noninvasive Imaging of the Bone-periodontal Ligament-tooth Fibrous Joint. J. Vis. Exp.

Jang, A.T., Merkle, A.P., Fahey, K.P., Gansky, S.A., and Ho, S.P. (2015). Multiscale biomechanical responses of adapted bone–periodontal ligament–tooth fibrous joints. Bone *81*, 196–207.

Jantarat, J., Palamara, J.E.A., and Messer, H.H. (2001a). An investigation of cuspal deformation and delayed recovery after occlusal loading. J. Dent. *29*, 363–370.

Jantarat, J., Panitvisai, P., Palamara, J.E.A., and Messer, H.H. (2001b). Comparison of methods for measuring cuspal deformation in teeth. J. Dent. *29*, 75–82.

Johnson, R.B. (1990). Effect of altered occlusal function on transseptal ligament and new bone thicknesses in the periodontium of the rat. Am. J. Anat. *187*, 91–97.

Kadow-Romacker, A., Hoffmann, J.E., Duda, G., Wildemann, B., and Schmidmaier, G. (2009). Effect of Mechanical Stimulation on Osteoblast- and Osteoclast-Like Cells in vitro. Cells Tissues Organs *190*, 61–68.

Kaneko, S., Ohashi, K., Soma, K., and Yanagishita, M. (2001). Occlusal hypofunction causes changes of proteoglycan content in the rat periodontal ligament. J. Periodontal Res. *36*, 9–17.

Kanzaki, H., Chiba, M., Sato, A., Miyagawa, A., Arai, K., Nukatsuka, S., and Mitani, H. (2006). Cyclical Tensile Force on Periodontal Ligament Cells Inhibits Osteoclastogenesis through OPG Induction. J. Dent. Res. *85*, 457–462.

Katebi, N., Kolpakova-Hart, E., Lin, C.Y., and Olsen, B.R. (2012). The mouse palate and its cellular responses to midpalatal suture expansion forces. Orthod. Craniofac. Res. *15*, 148–158.

Kawarizadeh, A., Bourauel, C., and Jager, A. (2003). Experimental and numerical determination of initial tooth mobility and material properties of the periodontal ligament in rat molar specimens. Eur. J. Orthod. *25*, 569–578.

Keller, P.J., Schmidt, A.D., Wittbrodt, J., and Stelzer, E.H.K. (2008). Reconstruction of Zebrafish Early Embryonic Development by Scanned Light Sheet Microscopy. Science *322*, 1065–1069.

Kiliaridis, S., Engstr m, C., and Thilander, B. (1985). The relationship between masticatory function and craniofacial morphology. Eur. J. Orthod. *7*, 273–283.

Kim, S.-G., Park, J.-C., Kang, D.-W., Kim, B.-O., Yoon, J.-H., Cho, S.-I., Choe, H.-C., and Bae, C.-S. (2003). Correlation of immunohistochemical characteristics of the craniomandibular joint with the degree of mandibular lengthening in rabbits. J. Oral Maxillofac. Surg. *61*, 1189–1197.

King, G., Keeling, S.D., McCoy, E.A., and Ward, T.H. (1991). Measuring dental drift and orthodontic tooth movement in response to various initial forces in adult rats. Am. J. Orthod. Dentofacial Orthop. *99*, 456–465.

Kingsmill, V.J., Boyde, A., Davis, G.R., Howell, P.G.T., and Rawlinson, S.C.F. (2010). Changes in Bone Mineral and Matrix in Response to a Soft Diet. J. Dent. Res. *89*, 510–514.

Klein-Nulend, J., Paul Veldhuijzen, J., Van Strien, M.E., Jong, M.D., and Burger, E.H. (1990). Inhibition of osteoclastic bone resorption by mechanical stimulation in vitro. Arthritis Rheum. *33*, 66–72.

Klein-Nulend, J., Bacabac, R.G., and Mullender, M.G. (2005). Mechanobiology of bone tissue. Pathol. Biol. *53*, 576–580.

Kohyama, K., Hatakeyama, E., Sasaki, T., Dan, H., Azuma, T., and Karita, K. (2004). Effects of sample hardness on human chewing force: a model study using silicone rubber. Arch. Oral Biol. *49*, 805–816.

von Kölliker, A. (1873). Die normale Resorption des Knochengewebes: und ihre Bedeuting für die Entstehung der typischen Knochenformen (FCW Vogel).

Komatsu, K., and Chiba, M. (1993). The effect of velocity of loading on the biomechanical responses of the periodontal ligament in transverse sections of the rat molar in vitro. Arch. Oral Biol. *38*, 369–375.

Komatsu, K., Sanctuary, C., Shibata, T., Shimada, A., and Botsis, J. (2007). Stress–relaxation and microscopic dynamics of rabbit periodontal ligament. J. Biomech. *40*, 634–644.

Kumar, G.S. (2014). Orban's Oral Histology & Embryology (Elsevier Health Sciences).

Kuroiwa, M., Chihara, K., and Higashi, S. (1994). Light and Electron-Microscopic Observation of Attachment between the Periodontal Ligament and Alveolar Bone in Rat Molars. Showa Univ. J. Med. Sci. *6*, 165–170.

Landis, W.J., and Jacquet, R. (2013). Association of Calcium and Phosphate Ions with Collagen in the Mineralization of Vertebrate Tissues. Calcif. Tissue Int. *93*, 329–337.

Langenbach, G.E., Brugman, P., and Weijs, W.A. (1992). Preweaning feeding mechanisms in the rabbit. J. Dev. Physiol. *18*, 253–261.

Langenbach, G.E.J., Weijs, W.A., and Koolstra, J.H. (1991). Biomechanical changes in the rabbit masticatory system during postnatal development. Anat. Rec. *230*, 406–416.

Langenbach, G.E.J., Weijs, W.A., Brugman, P., and van Eijden, T.M.G.J. (2001). A longitudinal electromyographic study of the postnatal maturation of mastication in the rabbit. Arch. Oral Biol. *46*, 811–820.

Lanyon, L.E. (1992). Control of bone architecture by functional load bearing. J. Bone Miner. Res. *7*, S369–S375.

Lee, J.-H., Lin, J.D., Fong, J.I., Ryder, M.I., and Ho, S.P. (2013). The Adaptive Nature of the Bone-Periodontal Ligament-Cementum Complex in a Ligature-Induced Periodontitis Rat Model. BioMed Res. Int. *2013*, e876316.

Lee, J.-H., Pryce, B.A., Schweitzer, R., Ryder, M.I., and Ho, S.P. (2015). Differentiating zones at periodontal ligament–bone and periodontal ligament–cementum entheses. J. Periodontal Res. n/a – n/a.

Lehoux, S., and Tedgui, A. (2003). Cellular mechanics and gene expression in blood vessels. J. Biomech. *36*, 631–643.

Leong, N.L., Hurng, J.M., Djomehri, S.I., Gansky, S.A., Ryder, M.I., and Ho, S.P. (2012). Age-Related Adaptation of Bone-PDL-Tooth Complex: Rattus-Norvegicus as a Model System. PLoS ONE *7*, e35980.

Li, J., Li, H., Fok, A.S.L., and Watts, D.C. (2009). Multiple correlations of material parameters of light-cured dental composites. Dent. Mater. *25*, 829–836.

Lieberman, D. (2011). The evolution of the human head (Harvard University Press).

Lin, J.D., Özcoban, H., Greene, J.P., Jang, A.T., Djomehri, S.I., Fahey, K.P., Hunter, L.L., Schneider, G.A., and Ho, S.P. (2013). Biomechanics of a bone–periodontal ligament–tooth fibrous joint. J. Biomech. *46*, 443–449.

Lin, J.D., Lee, J., Özcoban, H., Schneider, G.A., and Ho, S.P. (2014). Biomechanical adaptation of the bone-periodontal ligament (PDL)-tooth fibrous joint as a consequence of disease. J. Biomech. *47*, 2102–2114.

Lu, H.H., and Thomopoulos, S. (2013). Functional Attachment of Soft Tissues to Bone: Development, Healing, and Tissue Engineering. Annu. Rev. Biomed. Eng. *15*, 201–226.

Luan, X., and Diekwisch, T.G. (2007). Vienna–Chicago: The cultural transformation of the model system of the un-opposed molar. Bioessays *29*, 819–830.

Macapanpan, L.G., Weinmann, J.P., and Brodie, A.G. (1954). Early Tissue Changes Following Tooth Movement In Rats*. Angle Orthod. *24*, 79–95.

Mandel, U., Dalgaard, P., and Viidik, A. (1986). A biomechanical study of the human periodontal ligament. J. Biomech. *19*, 637–645.

Mao, J.J. (2002). Mechanobiology of Craniofacial Sutures. J. Dent. Res. *81*, 810–816.

Mao, J.J., Rahemtulla, F., and Scott, P.G. (1998). Proteoglycan expression in the rat temporomandibular joint in response to unilateral bite raise. J. Dent. Res. *77*, 1520–1528.

Marshall, S.J., Balooch, M., Habelitz, S., Balooch, G., Gallagher, R., and Marshall, G.W. (2003). The dentin–enamel junction—a natural, multilevel interface. J. Eur. Ceram. Soc. *23*, 2897–2904.

Matsubara, T., Suardita, K., Ishii, M., Sugiyama, M., Igarashi, A., Oda, R., Nishimura, M., Saito, M., Nakagawa, K., Yamanaka, K., et al. (2005). Alveolar Bone Marrow as a Cell Source for Regenerative Medicine: Differences Between Alveolar and Iliac Bone Marrow Stromal Cells. J. Bone Miner. Res. *20*, 399–409.

Matsuura, T., Tokutomi, K., Sasaki, M., Katafuchi, M., Mizumachi, E., Sato, H., Matsuura, T., Tokutomi, K., Sasaki, M., Katafuchi, M., et al. (2014). Distinct Characteristics of Mandibular Bone Collagen Relative to Long Bone Collagen: Relevance to Clinical Dentistry, Distinct Characteristics of Mandibular Bone Collagen Relative to Long Bone Collagen: Relevance to Clinical Dentistry. BioMed Res. Int. BioMed Res. Int. *2014, 2014*, e769414.

Mavropoulos, A., Kiliaridis, S., Bresin, A., and Ammann, P. (2004a). Effect of different masticatory functional and mechanical demands on the structural adaptation of the mandibular alveolar bone in young growing rats. Bone *35*, 191–197.

Mavropoulos, A., Bresin, A., and Kiliaridis, S. (2004b). Morphometric analysis of the mandible in growing rats with different masticatory functional demands: adaptation to an upper posterior bite block. Eur. J. Oral Sci. *112*, 259–266.

Mavropoulos, A., Ödman, A., Ammann, P., and Kiliaridis, S. (2010). Rehabilitation of masticatory function improves the alveolar bone architecture of the mandible in adult rats. Bone *47*, 687–692.

McCauley, L.K., and Somerman, M.J. (2012). Mineralized Tissues in Oral and Craniofacial Science: Biological Principles and Clinical Correlates (John Wiley & Sons).

McDougall, P.D., McNamara Jr., J.A., and Dierkes, J.M. (1982). Arch width development in Class II patients treated with the Fränkel appliance. Am. J. Orthod. *82*, 10–22.

McKee, M.D., Zalzal, S., and Nanci, A. (1996). Extracellular matrix in tooth cementum and mantle dentin: localization of osteopontin and other noncollagenous proteins, plasma proteins, and glycoconjugates by electron microscopy. Anat. Rec. *245*, 293–312.

Melsen, B. (1999). Biological reaction of alveolar bone to orthodontic tooth movement. Angle Orthod. *69*, 151–158.

Metscher, B.D. (2009). MicroCT for comparative morphology: simple staining methods allow high-contrast 3D imaging of diverse non-mineralized animal tissues. BMC Physiol. *9*, 11.

Meyer, G.H. (1867). Archief fur den anatomische und physiologischen Wissenschaften im Medizin. Archit. Spongiosa *34*, 615–628.

Miao, D., and Scutt, A. (2002). Histochemical Localization of Alkaline Phosphatase Activity in Decalcified Bone and Cartilage. J. Histochem. Cytochem. *50*, 333–340.

Miller, A., and Parker, S.B. (1984). Collagen: The Organic Matrix of Bone [and Discussion]. Philos. Trans. R. Soc. Lond. B Biol. Sci. *304*, 455–477.

Milne, T.J., Ichim, I., Patel, B., McNaughton, A., and Meikle, M.C. (2009). Induction of osteopenia during experimental tooth movement in the rat: alveolar bone remodelling and the mechanostat theory. Eur. J. Orthod. *31*, 221–231.

Mohr, T., Pødenphant, J., Biering–Sørensen, F., Galbo, H., Thamsborg, G., and Kjær, M. (2014). Increased Bone Mineral Density after Prolonged Electrically Induced Cycle Training of Paralyzed Limbs in Spinal Cord Injured Man. Calcif. Tissue Int. *61*, 22–25.

Morey, E.R., and Baylink, D.J. (1978). Inhibition of bone formation during space flight. Science *201*, 1138–1141.

Moxham, B.J., and Berkovitz, B.K.B. (1982). The periodontal ligament and physiological tooth movements. In The Periodontal Ligament in Health and Disease, (Pergamon Press Oxford), pp. 215–247.

Murakami, T., Nakagaki, H., Sakakibara, Y., Weatherell, J.A., and Robinson, C. (1987). The distribution pattern of fluoride concentrations in human cementum. Arch. Oral Biol. *32*, 567–571.

Murphy, T. (1959). Compensatory mechanisms in facial height adjustment to functional tooth attrition. Aust. Dent. J. *4*, 312–323.

Nakagaki, H., Weatherell, J.A., Strong, M., and Robinson, C. (1985). Distribution of fluoride in human cementum. Arch. Oral Biol. *30*, 101–104.

Nakashima, K., Zhou, X., Kunkel, G., Zhang, Z., Deng, J.M., Behringer, R.R., and de Crombrugghe, B. (2002). The Novel Zinc Finger-Containing Transcription Factor Osterix Is Required for Osteoblast Differentiation and Bone Formation. Cell *108*, 17–29.

Nakata, T.M., Stepnick, R.J., and Zipkin, I. (1972). Chemistry of human dental cementum: the effect of age and fluoride exposure on the concentration of ash, fluoride, calcium, phosphorus and magnesium. J. Periodontol. *43*, 115.

Nanci, A. (2007). Ten Cate's Oral Histology-Pageburst on VitalSource: Development, Structure, and Function (Elsevier Health Sciences).

Nanci, A., and Bosshardt, D.D. (2006). Structure of periodontal tissues in health and disease*. Periodontol. 2000 *40*, 11–28.

Natali, A.N., Pavan, P.G., Schrefler, B.A., and Secchi, S. (2002). A Multi-Phase Media Formulation for Biomechanical Analysis of Periodontal Ligament*. Meccanica *37*, 407–418.

Natali, A.N., Pavan, P.G., and Scarpa, C. (2004). Numerical analysis of tooth mobility: formulation of a non-linear constitutive law for the periodontal ligament. Dent. Mater. *20*, 623–629.

Natali, A.N., Carniel, E.L., Pavan, P.G., Sander, F.G., Dorow, C., and Geiger, M. (2008). A Visco-Hyperelastic-Damage Constitutive Model for the Analysis of the Biomechanical Response of the Periodontal Ligament. J. Biomech. Eng. *130*, 031004–031004.

Naveh, G.R.S., Shahar, R., Brumfeld, V., and Weiner, S. (2012a). Tooth movements are guided by specific contact areas between the tooth root and the jaw bone: A dynamic 3D microCT study of the rat molar. J. Struct. Biol. *177*, 477–483.

Naveh, G.R.S., Lev-Tov Chattah, N., Zaslansky, P., Shahar, R., and Weiner, S. (2012b). Tooth–PDL–bone complex: Response to compressive loads encountered during mastication – A review. Arch. Oral Biol. *57*, 1575–1584.

Netter, F.H., and Colacino, S. (1989). Atlas of human anatomy (Ciba-Geigy Corporation).

Nies, M., and Young Ro, J. (2004). Bite force measurement in awake rats. Brain Res. Protoc. *12*, 180–185.

Nijweide, P.J., Burger, E.H., and Feyen, J.H. (1986). Cells of bone: proliferation, differentiation, and hormonal regulation. Physiol Rev *66*, 855–886.

Niver, E.L., Leong, N., Greene, J., Curtis, D., Ryder, M.I., and Ho, S.P. (2011). Reduced functional loads alter the physical characteristics of the bone–periodontal ligament–cementum complex. J. Periodontal Res. *46*, 730–741.

Noble, B.S. (2008). The osteocyte lineage. Arch. Biochem. Biophys. *473*, 106–111.

Ochareon, P., and Herring, S.W. (2011). Cell replication in craniofacial periosteum: appositional vs. resorptive sites. J. Anat. *218*, 285–297.

Okada, Y., Naka, K., Kawamura, K., Matsumoto, T., Nakanishi, I., Fujimoto, N., Sato, H., and Seiki, M. (1995). Localization of matrix metalloproteinase 9 (92-kilodalton gelatinase/type IV collagenase = gelatinase B) in osteoclasts: implications for bone resorption. Lab. Investig. J. Tech. Methods Pathol. *72*, 311–322.

Okane, H., Yamashina, T., Nagasawa, T., and Tsuru, H. (1979). The effect of anteroposterior inclination of the occlusal plane on biting force. J. Prosthet. Dent. *42*, 497–501.

Oliver, W. c., and Pharr, G. m. (1992). An improved technique for determining hardness and elastic modulus using load and displacement sensing indentation experiments. J. Mater. Res. *7*, 1564–1583.

Palinkas, M., Nassar, M.S.P., Cecílio, F.A., Siéssere, S., Semprini, M., Machado-de-Sousa, J.P., Hallak, J.E.C., and Regalo, S.C.H. (2010). Age and gender influence on maximal bite force and masticatory muscles thickness. Arch. Oral Biol. *55*, 797–802.

Papachroni, K.K., Karatzas, D.N., Papavassiliou, K.A., Basdra, E.K., and Papavassiliou, A.G. (2009). Mechanotransduction in osteoblast regulation and bone disease. Trends Mol. Med. *15*, 208–216.

Parfitt, A.M. (1988). Bone histomorphometry: Proposed system for standardization of nomenclature, symbols, and units. Calcif. Tissue Int. *42*, 284–286.

Parfitt, G.J. (1960). Measurement of the Physiological Mobility of Individual Teeth in an Axial.

Perona, P., and Malik, J. (1990). Scale-space and edge detection using anisotropic diffusion. IEEE Trans. Pattern Anal. Mach. Intell. *12*, 629–639.

Picton, D.C.A. (1962). Tilting movements of teeth during biting. Arch. Oral Biol. *7*, 151–159.

Pirttiniemi, P., Kantomaa, T., Salo, L., and Tuominen, M. (1996). Effect of reduced articular function on deposition of type I and type II collagens in the mandibular condylar cartilage of the rat. Arch. Oral Biol. *41*, 127–131.

Pittenger, M.F., Mackay, A.M., Beck, S.C., Jaiswal, R.K., Douglas, R., Mosca, J.D., Moorman, M.A., Simonetti, D.W., Craig, S., and Marshak, D.R. (1999). Multilineage Potential of Adult Human Mesenchymal Stem Cells. Science *284*, 143–147.

Popowics, T.E., and Herring, S.W. (2007). Load transmission in the nasofrontal suture of the pig, Sus scrofa. J. Biomech. *40*, 837–844.

Popowics, T., Yeh, K., Rafferty, K., and Herring, S. (2009). Functional cues in the development of osseous tooth support in the pig, Sus scrofa. J. Biomech. *42*, 1961–1966.

Posner, A.S. (1969). Crystal chemistry of bone mineral. Physiol Rev *49*, 760–792.

Prendergast, P.J., and Taylor, D. (1994). Prediction of bone adaptation using damage accumulation. J. Biomech. *27*, 1067–1076.

240

Qian, H., Chen, J., and Katona, T.R. (2001). The influence of PDL principal fibers in a 3-dimensional analysis of orthodontic tooth movement. Am. J. Orthod. Dentofacial Orthop. *120*, 272–279.

Qian, L., Todo, M., Morita, Y., Matsushita, Y., and Koyano, K. (2009). Deformation analysis of the periodontium considering the viscoelasticity of the periodontal ligament. Dent. Mater. *25*, 1285–1292.

Qin, C., D'Souza, R., and Feng, J.Q. (2007). Dentin Matrix Protein 1 (DMP1): New and Important Roles for Biomineralization and Phosphate Homeostasis. J. Dent. Res. *86*, 1134–1141.

Qing, H., and Bonewald, L.F. (2009). Osteocyte Remodeling of the Perilacunar and Pericanalicular Matrix. Int. J. Oral Sci. *1*, 59–65.

Quintarelli, G., Zito, R., and Cifonelli, J.A. (1971a). On phosphotungstic acid staining. I. J. Histochem. Cytochem. *19*, 641–647.

Quintarelli, G., Cifonelli, J.A., and Zito, R. (1971b). On phosphotungstic acid staining. II. J. Histochem. Cytochem. *19*, 648–653.

Quintarelli, G., Bellocci, M., and Geremia, R. (1973). On phosphotungstic acid staining IV. Selectivity of the staining reaction. J. Histochem. Cytochem. *21*, 155–160.

Raadsheer, M.C., Kiliaridis, S., Van Eijden, T.M.G.J., Van Ginkel, F.C., and Prahl-Andersen, B. (1996). Masseter muscle thickness in growing individuals and its relation to facial morphology. Arch. Oral Biol. *41*, 323–332.

Ralph, W.J. (1982). Tensile behaviour of the periodontal ligament. J. Periodontal Res. *17*, 423–426.

Ravosa, M. (1996). Mandibular form and function in North American and European Adapidae and Omomyidae. J. Morphol. *229*, 171–190.

Ravosa, M. (1999). Anthropoid Origins and the Modern Symphysis. Folia Primatol. (Basel) *70*, 65–78.

Ravosa, M.J. (1991). The ontogeny of cranial sexual dimorphism in two old world monkeys:Macaca fascicularis (Cercopithecinae) andNasalis larvatus (Colobinae). Int. J. Primatol. *12*, 403–426.

Ravosa, M.J. (1998). Cranial allometry and geographic variation in slow lorises (Nycticebus). Am. J. Primatol. *45*, 225–243.

Rawlinson, S.C.F., Pitsillides, A.A., and Lanyon, L.E. (1996). Involvement of different ion channels in osteoblasts' and osteocytes' early responses to mechanical strain. Bone *19*, 609–614.

Reichert, J.C., Gohlke, J., Friis, T.E., Quent, V.M.C., and Hutmacher, D.W. (2013). Mesodermal and neural crest derived ovine tibial and mandibular osteoblasts display distinct molecular differences. Gene *525*, 99–106.

Robling, A.G., Niziolek, P.J., Baldridge, L.A., Condon, K.W., Allen, M.R., Alam, I., Mantila, S.M., Gluhak-Heinrich, J., Bellido, T.M., Harris, S.E., et al. (2008). Mechanical

Stimulation of Bone in Vivo Reduces Osteocyte Expression of Sost/Sclerostin. J. Biol. Chem. *283*, 5866–5875.

Rody Jr, W.J., King, G.J., and Gu, G. (2001). Osteoclast recruitment to sites of compression in orthodontic tooth movement. Am. J. Orthod. Dentofacial Orthop. *120*, 477–489.

Roelofsen, J., Klein-Nulend, J., and Burger, E.H. (1995). Mechanical stimulation by intermittent hydrostatic compression promotes bone-specific gene expression in vitro. J. Biomech. *28*, 1493–1503.

Roux, W. (1905). Die Entwickelungsmechanik; ein neuer Zweig der biologischen Wissenschaft: Eine Ergänzung zu den Lehrbüchern der Entwickelungsgeschichte und Physiologie der Tiere. Nach einem Vortrag gehalten in der ersten allgemeinen Sitzung der Versammlung Deutscher Naturforscher und Ärzte zu Breslau am 19. September 1904 (W. Engelmann).

Rubin, C.T. (1984). Skeletal strain and the functional significance of bone architecture. Calcif. Tissue Int. *36*, S11–S18.

Rygh, P. (1974). Elimination of hyalinized periodontal tissues associated with orthodontic tooth movement. Eur. J. Oral Sci. *82*, 57–73.

Rygh, P. (1976). Ultrastructural changes in tension zones of rat molar periodontium incident to orthodontic tooth movement. Am. J. Orthod. *70*, 269–281.

Rygh, P., Bowling, K., Hovlandsdal, L., and Williams, S. (1986). Activation of the vascular system: A main mediator of periodontal fiber remodeling in orthodontic tooth movement. Am. J. Orthod. *89*, 453–468.

S, W., Sc, C., and Y, Z. (1994). A model for the excitation of osteocytes by mechanical loading-induced bone fluid shear stresses. J. Biomech. *27*, 339–360.

Saffar, J.-L., Lasfargues, J.-J., and Cherruau, M. (1997). Alveolar bone and the alveolar process: the socket that is never stable. Periodontol. 2000 *13*, 76–90.

Sako, N., Okamoto, K., Mori, T., and Yamamoto, T. (2002). The hardness of food plays an important role in food selection behavior in rats. Behav. Brain Res. *133*, 377–382.

Salmon, C.R., Tomazela, D.M., Ruiz, K.G.S., Foster, B.L., Paes Leme, A.F., Sallum, E.A., Somerman, M.J., and Nociti Jr., F.H. (2013). Proteomic analysis of human dental cementum and alveolar bone. J. Proteomics *91*, 544–555.

Sato, T., Ovejero, M. del C., Hou, P., Heegaard, A.M., Kumegawa, M., Foged, N.T., and Delaisse, J.M. (1997). Identification of the membrane-type matrix metalloproteinase MT1-MMP in osteoclasts. J. Cell Sci. *110*, 589–596.

Shaw, S.R., Vailas, A.C., Grindeland, R.E., and Zernicke, R.F. (1988). Effects of a 1-wk spaceflight on morphological and mechanical properties of growing bone. Am. J. Physiol. - Regul. Integr. Comp. Physiol. *254*, R78–R83.

Shore, R.C., Berkovitz, B.K.B., and Moxham, B.J. (1985). The effects of preventing movement of the rat incisor on the structure of its periodontal ligament. Arch. Oral Biol. *30*, 221–228.

Short, E., and Johnson, R.B. (1990). Effects of tooth function on adjacent alveolar bone and Sharpey's fibers of the rat periodontium. Anat. Rec. *227*, 391–396.

Sicher, H., and Weinmann, J.P. (1944). Bone growth and physiologic tooth movement. Am. J. Orthod. Oral Surg. *30*, C109–C132.

Silva, M.A., and Merzel, J. (2004). Alveolar bone Sharpey fibers of the rat incisor in normal and altered functional conditions examined by scanning electron microscopy. Anat. Rec. A. Discov. Mol. Cell. Evol. Biol. *279*, 792–797.

Smith, T.S., Bay, B.K., and Rashid, M.M. (2002). Digital volume correlation including rotational degrees of freedom during minimization. Exp. Mech. *42*, 272–278.

Sodek, J., and Ferrier, J.M. (1988). Collagen Remodelling in Rat Periodontal Tissues: Compensation for Precursor Reutilization Confirms Rapid Turnover of Collagen. Coll. Relat. Res. *8*, 11–21.

Sodek, J., and Mckee, M.D. (2000). Molecular and cellular biology of alveolar bone. Periodontol. 2000 *24*, 99–126.

Steigman, S., Michaeli, Y., Yitzhaki, M., and Weinreb, M. (1989). A Three-dimensional Evaluation of the Effects of Functional Occlusal Forces on the Morphology of Dental and Periodontal Tissues of the Rat Incisor. J. Dent. Res. *68*, 1269–1274.

Suresh, S. (2001). Graded Materials for Resistance to Contact Deformation and Damage. Science *292*, 2447–2451.

Suresh, S., and Mortensen, A. (1998). Fundamentals of functionally graded materials (The Institut of Materials).

Tanaka, E., Inubushi, T., Koolstra, J.H., Eijden, T.M. van, Sano, R., Takahashi, K., Kawai, N., Rego, E.B., and Tanne, K. (2006). Comparison of Dynamic Shear Properties of the Porcine Molar and Incisor Periodontal Ligament. Ann. Biomed. Eng. *34*, 1917–1923.

Tanaka, E., Sano, R., Kawai, N., Langenbach, G.E.J., Brugman, P., Tanne, K., and Eijden, T.M.G.J. van (2007). Effect of Food Consistency on the Degree of Mineralization in the Rat Mandible. Ann. Biomed. Eng. *35*, 1617–1621.

Taylor, A.B., Jones, K.E., Kunwar, R., and Ravosa, M.J. (2006). Dietary consistency and plasticity of masseter fiber architecture in postweaning rabbits. Anat. Rec. A. Discov. Mol. Cell. Evol. Biol. *288A*, 1105–1111.

Taylor, A.F., Saunders, M.M., Shingle, D.L., Cimbala, J.M., Zhou, Z., and Donahue, H.J. (2007). Mechanically stimulated osteocytes regulate osteoblastic activity via gap junctions. Am. J. Physiol. - Cell Physiol. *292*, C545–C552.

Teitelbaum, S.L. (2000). Bone Resorption by Osteoclasts. Science *289*, 1504–1508.

Ten Cate, A.R., Freeman, E., and Dickinson, J.B. (1977). Sutural development: Structure and its response to rapid expansion. Am. J. Orthod. *71*, 622–636.

Thomas, N.R., and Peyton, S.C. (1983). An electromyographic study of mastication in the freely-moving rat. Arch. Oral Biol. *28*, 939–945.

Thomopoulos, S., Marquez, J.P., Weinberger, B., Birman, V., and Genin, G.M. (2006). Collagen fiber orientation at the tendon to bone insertion and its influence on stress concentrations. J. Biomech. *39*, 1842–1851.

Thompson, D.W. (1961). On form and mechanical efficiency. Growth Form JT Bonber Ed. Camb. Univ. Press Camb. UK.

Thongudomporn, U., Chongsuvivatwong, V., and Geater, A. (2009). The effect of maximum bite force on alveolar bone morphology. Orthod. Craniofac. Res. *12*, 1–8.

Tinevez, J.-Y. (2015). Fiji.

Tsuchiya, S., Tsuchiya, M., Nishioka, T., Suzuki, O., Sasano, Y., and Igarashi, K. (2013). Physiological Distal Drift in Rat Molars Contributes to Acellular Cementum Formation. Anat. Rec. *296,* 1255–1263.

Turner, C.H. (1998). Three rules for bone adaptation to mechanical stimuli. Bone *23*, 399–407.

Turner, C.H., and Burr, D.B. (1993). Basic biomechanical measurements of bone: a tutorial. Bone *14*, 595–608.

Turner, C.H., Forwood, M.R., and Otter, M.W. (1994a). Mechanotransduction in bone: do bone cells act as sensors of fluid flow? FASEB J. *8*, 875–878.

Turner, C.H., Forwood, M. r., Rho, J.-Y., and Yoshikawa, T. (1994b). Mechanical loading thresholds for lamellar and woven bone formation. J. Bone Miner. Res. *9*, 87–97.

Turner, C.H., Takano, Y., and Owan, I. (1995). Aging changes mechanical loading thresholds for bone formation in rats. J. Bone Miner. Res. *10*, 1544–1549.

Turner, R.T., Bell, N.H., Duvall, P., Bobyn, J.D., Spector, M., Holton, E.M., and Baylink, D.J. (1985). Spaceflight Results in Formation of Defective Bone. Exp. Biol. Med. *180*, 544–549.

Umemura, Y., Ishiko, T., Yamauchi, T., Kurono, M., and Mashiko, S. (1997). Five Jumps per Day Increase Bone Mass and Breaking Force in Rats. J. Bone Miner. Res. *12*, 1480–1485.

Urist, M.R., DeLange, R.J., and Finerman, G.A. (1983). Bone cell differentiation and growth factors. Science *220*, 680–686.

Verhulp, E., Rietbergen, B. van, and Huiskes, R. (2004). A three-dimensional digital image correlation technique for strain measurements in microstructures. J. Biomech. *37*, 1313–1320.

Vinyard, C.J., and Ravosa, M.J. (1998). Ontogeny, function, and scaling of the mandibular symphysis in papionin primates. J. Morphol. *235*, 157–175.

Vinyard, C., Ravosa, M.J., and Wall, C. (2008). Primate Craniofacial Function and Biology (Springer Science & Business Media).

Wada, H., Hosomichi, J., Shimomoto, Y., and Soma, K. (2008). Influence of occlusal hypofunction on the elastic property and bone formation of rat alveolar bone. Orthod. Waves *67*, 9–14.

Waltimo, A., and Könönen, M. (1993). A novel bite force recorder and maximal isometric bite force values for healthy young adults. Eur. J. Oral Sci. *101*, 171–175.

Wang, J.H.-C. (2006). Mechanobiology of tendon. J. Biomech. *39*, 1563–1582.

Wang, R.Z., and Weiner, S. (1997). Strain–structure relations in human teeth using Moiré fringes. J. Biomech. *31*, 135–141.

Wang, N., Butler, J.P., and Ingber, D.E. (1993). Mechanotransduction across the cell surface and through the cytoskeleton. Science *260*, 1124–1127.

Wang, N., Tytell, J.D., and Ingber, D.E. (2009). Mechanotransduction at a distance: mechanically coupling the extracellular matrix with the nucleus. Nat. Rev. Mol. Cell Biol. *10*, 75–82.

Watanabe, Y., and Komatsu, K. (1997). Biomechanical and Morphological Studies on the Periodontal Ligament of the Rat Molar after Treatment with α-amylase in vitro. Connect. Tissue Res. *36*, 35–49.

Weijs, W.A., and de Jongh, H.J. (1977). Strain in mandibular alveolar bone during mastication in the rabbit. Arch. Oral Biol. *22*, 667–675.

Weijs, W.A., Brugman, P., and Klok, E.M. (1987). The growth of the skull and jaw muscles and its functional consequences in the New Zealand rabbit (Oryctolagus cuniculus). J. Morphol. *194*, 143–161.

Westneat, M.W., and Hal, W.G. (1992). Ontogeny of feeding motor patterns in infant rats: An electromyographic analysis of suckling and chewing. Behav. Neurosci. *106*, 539–554.

Wheeler, R.C. (1974). Dental anatomy, physiology, and occlusion (WB Saunders Company).

Wheeless, C.R. (1996). Wheeless' textbook of orthopaedics (DataTrace Internet Pub.).

Woda, A., Foster, K., Mishellany, A., and Peyron, M.A. (2006). Adaptation of healthy mastication to factors pertaining to the individual or to the food. Physiol. Behav. *89*, 28–35.

Wolff, J. (1892). Das gesetz der transformation der knochen. DMW-Dtsch. Med. Wochenschr. *19*, 1222–1224.

Wolff, J. (1982). Das Gesetz iiber die Transformation der Knochen. Hirschwald Berl.

Wolff, J. (1986). The Law of Bone Remodeling (translation of the German 1892 edition). Berl. Heildelberg N. Y. Springer.

Wood, J.D., Wang, R., Weiner, S., and Pashley, D.H. (2003). Mapping of tooth deformation caused by moisture change using moiré interferometry. Dent. Mater. *19*, 159–166.

Wronski, T.J., and Morey, E.R. (1983). Effect of spaceflight on periosteal bone formation in rats. Am. J. Physiol. - Regul. Integr. Comp. Physiol. *244*, R305–R309.

Xiaofeng, H., Guixin, Z., and Herring, S.W. (1994). Age changes in mastication in the pig. Comp. Biochem. Physiol. A Physiol. *107*, 647–654.

Yamamoto, S. (1996). The effects of food consistency on maxillary growth in rats. Eur. J. Orthod. *18*, 601–615.

Yasuda, H., Shima, N., Nakagawa, N., Yamaguchi, K., Kinosaki, M., Mochizuki, S., Tomoyasu, A., Yano, K., Goto, M., Murakami, A., et al. (1998). Osteoclast differentiation factor is a ligand for osteoprotegerin/osteoclastogenesis-inhibitory factor and is identical to TRANCE/RANKL. Proc. Natl. Acad. Sci. *95*, 3597–3602.

Yoshiki, S., Umeda, T., and Kurahashi, Y. (1972). An effective reactivation of alkaline phosphatase in hard tissues completely decalcified for light and electron microscopy. Histochemie *29*, 296–304.

Zauel, R., Yeni, Y.N., Bay, B.K., Dong, X.N., and Fyhrie, D.P. (2005). Comparison of the Linear Finite Element Prediction of Deformation and Strain of Human Cancellous Bone to 3D Digital Volume Correlation Measurements. J. Biomech. Eng. *128*, 1–6.

Zebaze, R., and Seeman, E. (2015). Cortical Bone: A Challenging Geography. J. Bone Miner. Res. *30*, 24–29.

Zhang, D., and Arola, D.D. (2004). Applications of digital image correlation to biological tissues. J. Biomed. Opt. *9*, 691–699.

Zhang, D., Mao, S., Lu, C., Romberg, E., and Arola, D. (2009). Dehydration and the dynamic dimensional changes within dentin and enamel. Dent. Mater. *25*, 937–945.

PUBLISHING AGREEMENT

It is the policy of the University to encourage the distribution of all theses, dissertations, and manuscripts. Copies of all UCSF theses, dissertations, and manuscripts will be routed to the library via the Graduate Division. The library will make all theses, dissertations, and manuscripts accessible to the public and will preserve these to the best of their abilities, in perpetuity.

I hereby grant permission to the Graduate Division of the University of California, San Francisco to release copies of my thesis, dissertation, or manuscript to the Campus Library to provide access and preservation, in whole or in part, in perpetuity.

Author Signature_____ Date __12-4-2015__